PIEZOELECTRIC AND ELECTROSTRICTIVE MATERIALS
FOR TRANSDUCERS APPLICATIONS

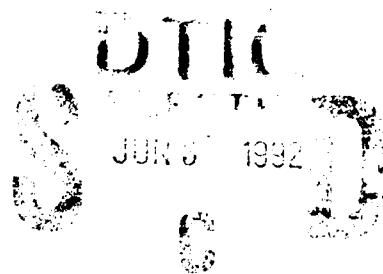Period February 1, 1991 to January 31, 1992

Final Report

AD-A250 890

VOLUME II

APPROVED FOR PUBLIC RELEASE – DISTRIBUTION UNLIMITED

L. E. Cross
R. E. Newnham
A. S. Bhalla
J. P. Dougherty
J. H. Adair
V. K. Varadan
V. V. Varadan

92-14490

PENNSTATE

1855

THE MATERIALS RESEARCH LABORATORY
UNIVERSITY PARK, PA

92 6 01 157

REPORT DOCUMENTATION PAGE

Form Approved
OMB No. 0704-0188

1a. REPORT SECURITY CLASSIFICATION	1b. RESTRICTIVE MARKINGS
2a. SECURITY CLASSIFICATION AUTHORITY	3. DISTRIBUTION/AVAILABILITY OF REPORT
2b. DECLASSIFICATION/DOWNGRADING SCHEDULE	Reproduction in whole or in part is permitted for any purpose of the United States Governmen

4. PERFORMING ORGANIZATION REPORT NUMBER(S)	5. MONITORING ORGANIZATION REPORT NUMBER(S)
N00014-89-J-1689	

6a. NAME OF PERFORMING ORGANIZATION	6b. OFFICE SYMBOL (If applicable)	7a. NAME OF MONITORING ORGANIZATION
MATERIALS RESEARCH LABORATORY		

6c. ADDRESS (City, State, and ZIP Code)	7b. ADDRESS (City, State, and ZIP Code)
THE PENNSYLVANIA STATE UNIVERSITY UNIVERSITY PARK, PA 16802	

8a. NAME OF FUNDING/SPONSORING ORGANIZATION	8b. OFFICE SYMBOL (If applicable)	9. PROCUREMENT INSTRUMENT IDENTIFICATION NUMBER

8c. ADDRESS (City, State, and ZIP Code)	10. SOURCE OF FUNDING NUMBERS			
	PROGRAM ELEMENT NO.	PROJECT NO.	TASK NO.	WORK UNIT ACCESSION NO.

11. TITLE (Include Security Classification)
PIEZOELECTRIC AND ELECTROSTRICTIVE MATERIALS FOR TRANSDUCER APPLICATIONS

12. PERSONAL AUTHOR(S)
L. E. Cross, R. E. Newnham, A. S. Bhalla, J. P. Dougherty, J. H. Adair, V.K. Varadan, V.V.Vara

13a. TYPE OF REPORT	13b. TIME COVERED	14. DATE OF REPORT (Year, Month, Day)	15. PAGE COUNT
FINAL	FROM 2/1/91 TO 1/31/92		

16. SUPPLEMENTARY NOTATION

17. COSATI CODES			18. SUBJECT TERMS (Continue on reverse if necessary and identify by block number)
FIELD	GROUP	SUB-GROUP	

19. ABSTRACT (Continue on reverse if necessary and identify by block number)

SEE REVERSE SIDE OF PAGE.

20. DISTRIBUTION/AVAILABILITY OF ABSTRACT	21. ABSTRACT SECURITY CLASSIFICATION
☐ UNCLASSIFIED/UNLIMITED ☐ SAME AS RPT. ☐ DTIC USERS	
22a. NAME OF RESPONSIBLE INDIVIDUAL	22b. TELEPHONE (Include Area Code) 22c. OFFICE SYMBOL

ABSTRACT

This report documents work carried out in the Materials Research Laboratory of The Pennsylvania State University on the third and final year of the program on "Piezoelectric and Electrostrictive Materials for Transducers Applications" sponsored by the Office of Naval Research (ONR) under grand No. N00014-89-J-1689. This marks the termination of a very long and highly productive sequence of contracts and grants focusing on the development of new materials for Piezoelectric and Electrostrictive transducer applications carried through under core ONR funding. Fortunately many elements of the work will be continuing on a new University Research Initiative (URI) program under ONR sponsorship.

Highlights of the past year's activities include: An increased emphasis upon the flextensional (moonie) type actuators, modeling both the internal stress distribution as a function of geometry, and the very interesting resonant mode structure of the composites; A more refined focus upon the performance of piezoelectric ceramic transducers, particularly under high drive levels is developing with concern for the extrinsic domain and phase boundary contributions to response. Measurement and modelling are being used to explore the nonlinearity and the frequency response and to examine the phase partitioning at the rhombohedral : tetragonal morphotropic phase boundary in the PZT system. Phenomena limiting lifetime in polarization and phase switching actuators are being explored to separate surface and volume effects and those due to grain size and flaw population differences. New work has been initiated to examine Acoustic Emission as a technique, in combination with Barkhausen current pulse analysis, to separate and evaluate domain switching and microcracking in polarization switching systems.

From work on this program it has now become clear that the relaxor ferroelectrics are in fact close analogues of the magnetic spin glasses, so that the spin glass formalism can be used to explain the very wide range of dielectric, elastic and electrostrictive properties. The remaining outstanding fundamental problem is that of the detailed interrelationship between the known nano-heterogeneity in the structure and chemistry and the nanopolar regions which contribute the electrical response.

Of very high practical interest is the manner in which the relaxor can be field biased into extremely strong piezoelectric response. Work is going forward to examine this response in detail and to explore the possibility that such "super-responses" can be induced by chemical (solid solution) means.

Processing studies have focused upon new lower temperature consolidations for relaxors, and upon new compositions for high temperature piezoelectric ceramics.

In parallel with the ONR Transducer Program the Laboratory has extensive DARPA sponsored research on ferroelectric thin films. Since the films structures frequently involve materials like the PZT, PMN : PT, PLT and PLZT families of compositions and do explore piezoelectric effects and applications, a small group of the most relevant papers form this program are appended to the report.

PIEZOELECTRIC AND ELECTROSTRICTIVE MATERIALS
FOR TRANSDUCERS APPLICATIONS

Period February 1, 1991 to January 31, 1992

Final Report

VOLUME II

OFFICE OF NAVAL RESEARCH
Contract No. N00014-89-J-1689

APPROVED FOR PUBLIC RELEASE – DISTRIBUTION UNLIMITED

Reproduction in whole or in part is permitted for any purpose
of the United States Government

L. E. Cross
R. E. Newnham
A. S. Bhalla
J. P. Dougherty
J. H. Adair
V. K. Varadan
V. V. Varadan

PENNSTATE

THE MATERIALS RESEARCH LABORATORY
UNIVERSITY PARK, PA

TABLE OF CONTENTS

APPENDICES

General Summary Papers

1.   L. Eric Cross. "Ferroelectric Ceramics Tailoring Properties for Specific Applications."

2.   R. E. Newnham and T. R. Shrout. "Advanced Ceramics," Electronic Ceramics 1, 601-620.

Composite Materials

3.   R. E. Newnham "Tunable Transducers: Nonlinear Phenomena in Electroceramics," National Institute of Standards and Technology Special Publication 804, Chemistry of Electonic Ceramic Materials, Proceedings of the International Conference held in Jackson, WY, August 17-22, 1990, issued January 1991.

4.   R. E. Newnham. "Composite Electroceramics," International Encyclopedia of Composites, Vol. 6, 158-173.

TABLE OF CONTENTS
(continued)

Phenomenological Studies (continued)

Relaxors and Related Systems

TABLE OF CONTENTS
(continued)

APPENDIX 7

CERAMIC-METAL COMPOSITE ACTUATOR

Q.C. Xu, A. Dogan, J. Tressler,
S. Yoshikawa, and R. E. Newnham
Materials Research Laboratory
The Pennsylvania State University
University Park, PA 16802

ABSTRACT

The main objective of this work was to develop a new type of actuator. It consists of a piezoelectric ceramic disk or multilayer stack and two metal end plates with a crescent-shaped cavity on the inner surface. The plates are used as mechanical transformers for converting and amplifying the lateral displacement of the ceramic into a large axial motion in the plates. Both d_{31} and d_{33} contribute to the axial displacement. Sizeable strains were obtained with both PZT-metal and PMN-metal actuators. Displacement amplification principle, fabrication, and measurement results are presented.

INTRODUCTION

In recent years, piezoelectric and electrostrictive ceramics have been used in many actuator applications. The two most common types of actuator are a multilayer ceramic actuator with internal electrodes and a cantilevered bimorph actuator[1]. A frame structure for displacement amplifier in impact printer head has also been developed using piezoelectric multilayer actuators [2].

This paper describes a new type of ceramic-metal composite actuator which is based on the concept of a flextensional transducer[3]. The ceramic is excited in an extensional mode and the metal plates in a flexure mode. The metal plates are used as a mechanical transformer for transforming the high mechanical impedance of the ceramic to the low mechanical impedance of the load. Therefore, a large effective piezoelectric coefficient, d_{33}, exceeding 4000 pC/N as well as a hydrostatic piezoelectric coefficient d_h, exceeding 800 pC/N can be obtained from a single PZT disk-metal (brass) composite[4].

PRINCIPLE

The extensional mode of the piezoelectric ceramic element is characterized by a large generated force, a high electromechanical coupling, a high resonant frequency, and a small displacement. Often it is desirable to use a compact structure to magnify the displacement of the ceramic element. Figure 1 shows the basic configuration of the ceramic-metal composite
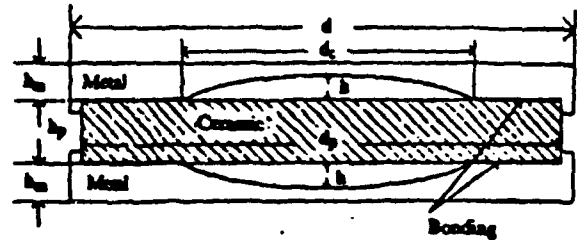
Figure 1. The geometry of composite.

actuator. The ceramic element can either be a piezoelectric ceramic or an electrostrictive ceramic with single layer or multilayer. Low driving voltages can be used for the multilayer ceramic element. The electrostrictive ceramic is expected to reduce hysteresis as well as exhibit a nonlinear relationship between the voltage and the displacement.

The "Moonie" metal plates are used as displacement magnifiers. The relationship between the displacement of the metals and the geometry of the metals and the ceramic is explained below. For simplicity, consider a curved beam with small curvature bonded to a ceramic bar (Figure 2). According to elastic theory [5], the bending moment M under an electroactive force from the ceramic is as eq. (1):

$$M = \frac{-T_d[(b^2-a^2)^2 - 4a^2b^2(\ln\frac{b}{a})^2]}{4[\frac{-a^2b^2}{r^2}\ln\frac{b}{a} + b^2\ln\frac{r}{b} + a^2\ln\frac{a}{r} + b^2-a^2]} \tag{1}$$
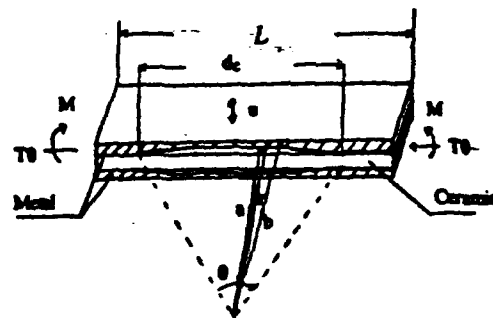
Figure 2. Simplified model for displacement magnification.

The electroactive force will be transmitted to the Moonie metal. The stress in the metal is:

$$T_\theta = \frac{dE_3 Y_c A_c}{A_m} \qquad (2)$$

where d =   piezoelectric strain coefficient of the ceramic,
E_3 =   electric field in the ceramic,
Y_c =   Young's modulus of the ceramic,
A_c, A_m =   cross sectional area of the ceramic and metal, respectively,

and $r \sim a \sim b$.

The normal displacement of the metal produced by the piezoelectric effect of the ceramic is:

$$U_{pi} = \frac{-M \left(\frac{h_m}{2}\right)^2}{2 Y_m I_m} \sim \frac{3}{4} \frac{d Y_c d_c}{h_m Y_m \theta} V \qquad (3)$$

b_m =   thickness of the metal
Y_m =   Young's modulus of the metal
V =   applied voltage
I_m =   moment of inertia of the metal

$$d_{33}\Big|_{eff} = \frac{U_{pi}}{V} = \frac{3}{4} \frac{d Y_c d_c}{h_m Y_m \theta} \qquad (4)$$

For the electrostrictive effect:

$$T_\theta = \frac{Q \epsilon^2 E^2 Y_c A_c}{A_m} \qquad (5)$$

Q =   electrostrictive coefficient of the ceramic
ϵ =   permittivity

The displacement of the metal by the electrostrictive effect is then:

$$U_{el} = \frac{3}{4} \frac{Q \epsilon^2 Y_c d_c}{h_m h_c Y_m \theta} V^2 \qquad (6)$$

The transverse displacement at the end of the ceramic bar is:

$$\delta = \frac{dV}{h_c} L$$

and the displacement conversion ratio is:

$$\frac{U}{\delta} = \frac{3}{4} \frac{d_c}{L\theta} \frac{Y_c}{Y_m} \frac{h_c}{h_m} \qquad (7)$$

Equations (3) and (6) explain how the normal displacement U of the metal is related to the transverse piezoelectric or electrostrictive effect of the ceramic. The total displacement is the sum of the displacement described above and the displacement due to longitudinal effects.

The lowest resonant frequency of the actuator is a flextensional mode which is determined mainly by the stiffness of the ceramic in a planar mode and the equivalent mass of the metal plate. The equivalent mass is much larger than the real mass of the metal plate because the vibration velocity of the metal part is much larger than the reference velocity of the PZT. The equivalent mass is

$$M_e = \frac{\int_0^L \frac{1}{2} \rho_m b h_m U^2 \omega^2 dX}{\frac{1}{2} \delta^2 \omega^2} \sim M_m \frac{d_c^2 Y_c^2 h_c^2}{L^2 \theta^2 Y_m^2 h_m^2}$$

$$M_m = \rho_m V_m = \rho_m b h_m L$$

When the h_c/h_m ratio is high and $k_m \ll k_c$, the resonant frequency of the lowest flextensional mode is:

$$f_a = \frac{1}{2\pi \sqrt{(M_e + M_o)(k_c + k_m)^{-1}}} \sim \frac{f_c}{\sqrt{1 + (2\pi f_o)^2 M_o k_c^{-1}}}$$

$$= [1 + (2\pi f_o)^2 \frac{M_o k_c^{-1} Y_c^2 h_c^2 d_c^2}{L^2 \theta^2 Y_m^2 h_m^2}]^{\frac{1}{2}} f_c \qquad (8)$$

The M_e is much larger than the real mass of the metal.
Here k_c=stiffness of ceramic
k_m=stiffness of metal plate
f_c=resonant frequency of planar mode of the ceramic itself.

$$f_c = \frac{1}{2\pi \sqrt{M_c k_c^{-1}}}$$

From equation (8) the lowest flextensional frequency f_{ft} is proportional to $\sqrt{h_m}$.

SAMPLE PREPARATION

The composite actuators were made from electroded PZT5A or PMN-PT ceramic disks (11 mm in diameter and 1 mm thick) and brass end caps (from 11 mm to 13 mm in diameter with thicknesses ranging from 0.2 to 3 mm). Shallow cavities from 6 mm to 8.5 mm in diameter and about 150 μm center depth were machined into the inner surface of each brass cap. The ceramic disk and the end caps were bonded around the circumference, taking care not to fill the cavity or short circuit the ceramic electrodes. Three kinds of bonding materials have been utilized:

1. Silver foil (25 μm thickness) and silver paste bonding.

This composite was heated to 600°C under stress to solidify the bond. After cooling, the actuator was encapsulated using Spurr's epoxy resin, followed by curing at 70°C for 12 hours. Electrodes were attached to the brass end caps and the PZT ceramic was poled at 2.5 MV/m for 15 minutes in an oil bath held at 120°C.

2. Pb-Sn-Ag Solder Bonding.

The PMN-PT or poled PZT and the brass end caps with the Pb-Sn-Ag solder ring (thickness 50 μm) were heated to 190°C under pressure. After cooling, the composite was encapsulated using epoxy resin.

3. Epoxy Resin Bonding.

The brass end caps and the ceramic were bonded by Emerson & Cuming epoxy resin around the rim at room temperature.

An electrostrictive actuator was made from a multilayer ceramic stack and a brass beam and bonded to the Moonie inner surface with an epoxy (Figure 3). This composite demonstrates that a sizeable displacement can be produced under low driving voltage using a multilayer ceramic stack.
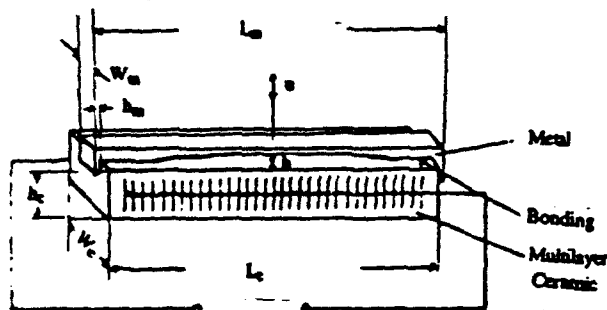
Figure 3. Another type of ceramic-metal composite actuator with multilayered ceramic part.

EXPERIMENT RESULTS

The displacement of the composite actuator in the low frequency range was measured with a Linear Voltage Differential Transducer (LVDT) having a resolution of approximately 0.05 μm. The direct piezoelectric coefficient d_{33} was measured at a frequency of 100 Hz using a Berlincourt d_{33} meter. The displacement-frequency dependence was measured with a double beam laser interferometer. Resonant frequencies were obtained with a Hewlett-Packard Spectrum Analyzer (HP-3585A) or Network Analyzer (HP-3577A).

1. Displacement Measurement

Figure 4 shows the displacements versus electric field curves for composite actuators driven by PZT and PMN ceramics. Displacements for the uncapped ceramics are shown for comparison. PMN does not need to be poled because it utilizes the electrostrictive effect rather than piezoelectricity. Dimensions of the PMN composite sample in Figure 4 are as follows: d=13 mm, d_p=11 mm, h=150 μm, d_c=6 mm, h_p=1 mm, and h_m=0.4 mm. The dimensions of the PZT composite-1 sample are: d=d_p=11 mm, h=50 μm, d_c=7 mm, h_p=1 mm, and h_m=0.5 mm. Both of the uncapped PZT and PMN ceramics have the same size, d_p=11 mm and h_p=1 mm. The experimental results show that the composites produce a strain amplification of about 10 times. A displacement of about 10 μm can be obtained under a field of 1 kV/mm. By loading these actuators with weights, it is capable of exerting forces in excess of 2 kgf.

As shown in Equation 3 and Equation 6, the displacement amplification is dependent on the thickness of metal h_m and cavity diameter d_c. The sample PZT composite-2 with dimensions d=d_p=11 mm, h_p=1 mm, h=200 μm, h_m=0.3 mm, and d_c=8.5
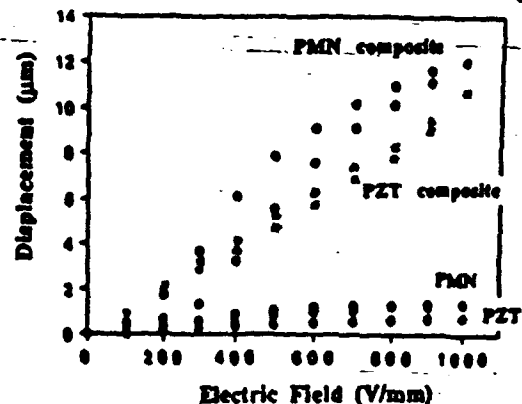
Figure 4. Displacements measured for composite actuators driven by PZT and PMN ceramics. Displacement for the uncapped ceramics are shown for comparison.

mm exhibits sizeable displacements - as large as 20 μm with a force capability of 0.15 kgf (see Figure 5).
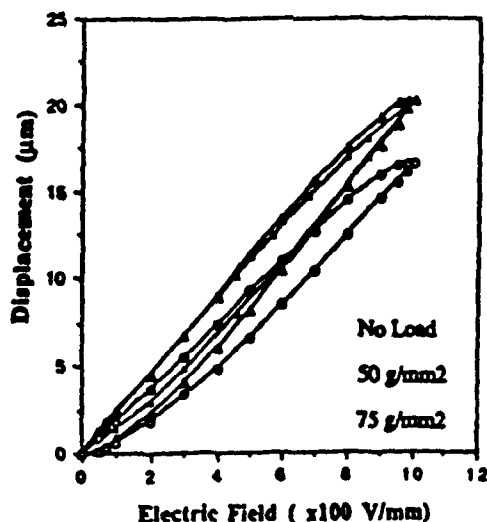
Figure 5. Displacement vs. field curves under different exerty forces for the sample PZT composite-2.

The 124 layer electrostrictive composite actuator shown in Figure 3 gave the displacement exhibited in Figure 6. More than 15 μm displacement can be obtained under an applied voltage of 150V. Notice that this experimental result is obtained with only one metal end-cap on the ceramic stack. If the convex or concave metal end-caps are placed on both sides of the ceramic stack, more than 30 μm displacement will be obtained under the applied voltage of 150V. Displacements for the uncapped multilayer ceramic in the same direction are shown for comparison. The lowest flextensional resonant frequency for the composite is 6.4 kHz.
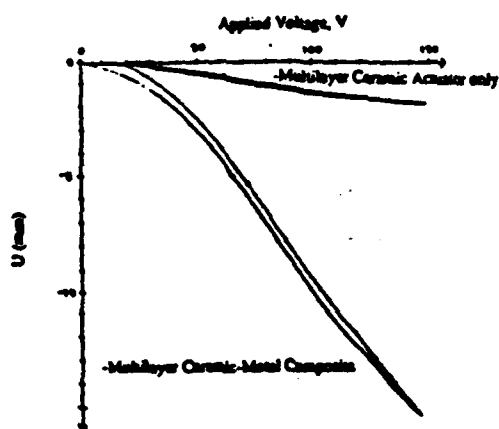
Figure 6. Displacement with increase in applied voltage of the multilayer ceramic-metal composite actuator using an electrostrictive ceramic stack and a brass end cap.

2 Thickness Dependence

Figure 7 shows the effective d_{33} coefficient and resonant frequency plotted as a function of the brass thickness. As expected in Eq. (4) and Eq. (8), the effective d_{33} is proportional to $1/h_m$ and the lowest resonant frequency is proportional to $\sqrt{h_m}$. The d_{33} values were measured at the center of the brass end caps using a Berlincourt d_{33} meter. Values as high as 4000 pC/N, approximately 10 times that of PZT5A, were obtained with the Moonie actuator.
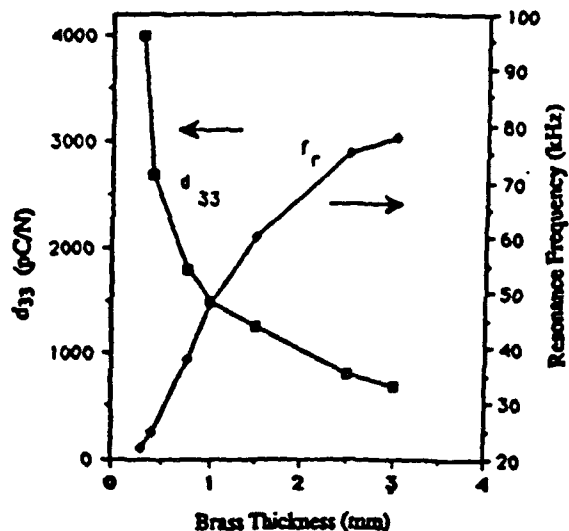
Figure 7. Resonance frequency f_r and d_{33} coefficient plotted as a function of the thickness of the brass endcaps.

Piezoelectric effects are largest near the center of the transducer where the flexural motion is largest. The effective values measured as a function of position with a Berlincourt meter are shown in Figure 8. Plots are shown for two brass thicknesses of 0.4 and 5.0 mm. Ample working areas of several mm² are obtained with the actuators.
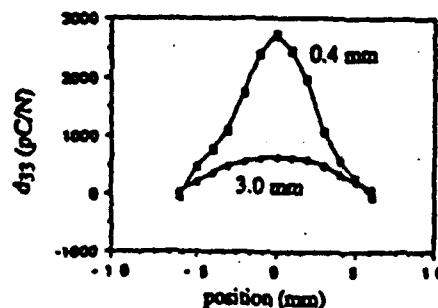
Figure 8. Positional dependence of the d_{33} coefficient for two actuators with brass thickness of 0.4 mm and 3.0 mm.

3. Resonant Frequency-Temperature Dependence

The lowest flextensional frequency of the PZT-brass composite with Pb-Sn-Ag solder bond and without epoxy encapsulation decreases with temperature as shown in Figure 9. This is probably due to the high stress in the PZT ceramic arising from thermal stresses set up by the metal.
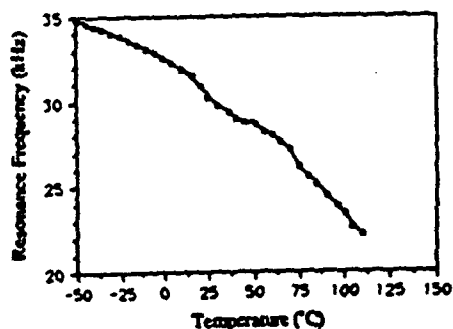
Figure 9. Resonance Frequency vs. Temperature

4. Electrode Effect

Figure 10 shows the effective piezoelectric d_{33} coefficient of the composite increases with electrode area of PZT. This means that all the PZT is contributing uniformly to the displacement.
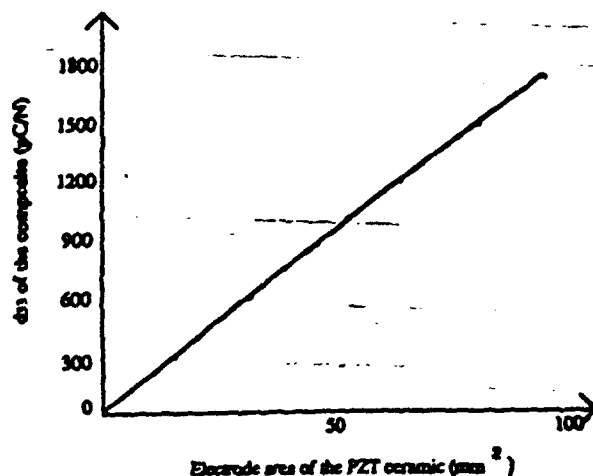
Figure 10. Effective d_{33} vs. electrode area of the ceramic.

5. Creep

Keeping a field of 1 kV/mm on the composite sample with epoxy bonding for two hours, no displacement change was observed by LVDT measurement (see Figure 11) after one hour.
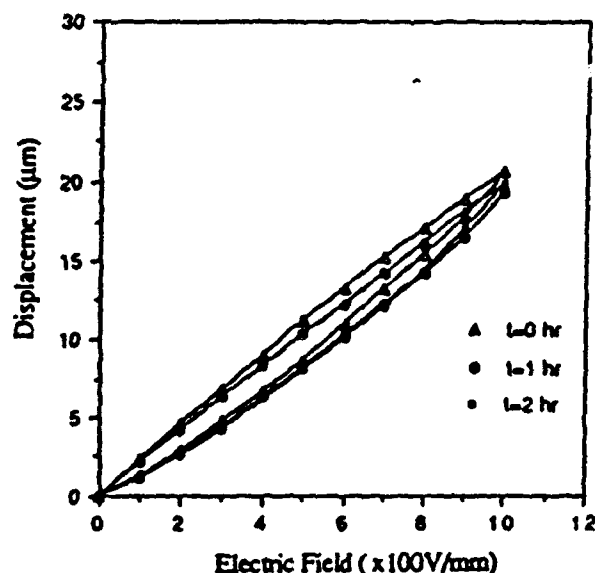
Figure 11.   Creep under field 1KV/mm.

CONCLUSIONS

A new type of actuator has been constructed from piezoelectric PZT ceramics bonded to metal end caps. Shallow spaces under the end caps produce substantial increases in strain by combining the d_{33} and d_{31} contributions of the ceramic. Even larger displacements were obtained using PMN electrostrictive ceramics.

The displacement is inversely proportional to the metal thickness.

The lowest resonant frequency is proportional to the square root of the metal thickness.

The displacement is proportional to the area of the driving ceramic.

The creep under 1 kV/mm is very small after one hour.

Further improvements in actuator performance are expected using improved materials and design. Driving voltages can be reduced using multilayer ceramics, and larger displacements can be obtained using multimoonie stacks (Figure 12).
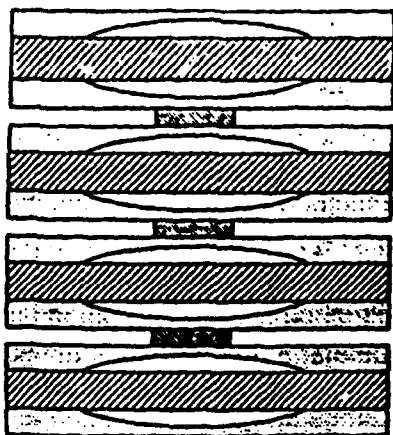
Figure 12.   Illustration of Stacked Composite.

ACKNOWLEDGEMENTS

REFERENCES

1. K. Uchino, "Piezoelectric/Electrostrictive Actuator," Morikita Publishers, Tokyo, Japan(1986)

2. K. Yoda , H. Morita, T. Mori, T. Shibuya, "Frame Structure for Impact Print Head," Spring Meeting of IECE of Japan, 7-96 (1990) (in Japanese).

3. Q.C. Xu, J. Belsick, S. Yoshikawa, and R. E. Newnham, "Piezoelectric Composites with High Sensitivity and High Capacitance for Use at High Pressure," IEEE Transactions on UFFC (in press).

4. R.E. Newnham, Q.C. Xu, and S. Yoshikawa, (patent) "Transformed Stress Direction-Acoustic Transducer (to the Pennsylvania Research Corporation) U.S. 4,999,819 (March 12, 1991).

5. S. Timoshenko and J. N. Goodier, "Theory of Elasticity," Chapters 4 and 10, 2d ed., New York, McGraw-Hill, 1951.

6. Y. Sugawara, K. Onitsuka, S. Yoshikawa, Q.C. Xu, R.E. Newnham, and K. Uchino, "Piezoelectric and Electrostrictive Composite Actuators," Proceedings of the 1991 International Symposium on Active Materials and Adaptive Structures, Alexandria, VA (in press).

PIEZOELECTRIC CERAMICS

APPENDIX 8

Effects of Surface Layers on the Physical Properties of Lanthanum Doped Lead Zirconate Titanate Ceramic

Q. Y. Jiang, Wenwu Cao and L. E. Cross

Materials Research Laboratory

The Pennsylvania State University

University Park PA. 16802

ABSTRACT

Dielectric measurements in the temperature range of -20 °C to 160 °C have been performed on lanthanum doped lead zirconate titanate ceramic samples with rough ground, polished and chemically etched surfaces, respectively. It is found that the observed dielectric constants, dielectric loss, polarization and pyroelectric coefficient are the smallest in the ground samples and the largest in the etched samples. The difference is more pronounced near the permittivity maximum temperature T_{max}. The measured dielectric constant was found to depend on sample thickness in the ground and polished samples but not in samples with etched surfaces. The results are explained in terms of a simple surface layer model. A nonferroelectric layer is produced during lapping, which has dielectric constant of the order of 100 and the capacitance of this layer in the investigated temperature range is $0.2 - 0.7 \ \mu F/cm^2$. Through post-annealing, the contributions from the nonferroelectric nature of this surface layer and from the two dimensional tensile stress generated by lapping were also separated and quantified.

1

I. INTRODUCTION

Surface layers have special effects on many physical properties of ferroelectric materials, such as dielectric constant, dielectric loss[1,2], pyroelectric current[3], remnant polarization, domain switching time, coercive field[4] and optical properties.[5] The existence of a surface layer can introduce many artifacts to electric measurements, causes misleading in the property evaluation of ferroelectric materials.

Recent technology advances in the thin film deposition have made the practical application of ferroelectric thin film possible, the most promising applications include non-volatile memory and electro-optical devices.[6] Since ferroelectric films have thickness of only several thousand angstroms to a few microns, the surface to volume ratio is two to four orders of magnitude larger than that in bulk ferroelectric material. Therefore, the surface layer behavior has a critical influence to the properties of the ferroelectric thin film. It has been realized that in order to improve the performance of the ferroelectric thin film, one must understand and control the surface behavior. The same is true also for the bulk ferroelectric ceramic, especially when the sample thickness becomes very thin. An induced surface layer from mechanical processing could strongly affect the performance of the ceramic. In comparison a ceramic system is easier to study than thin film because one can manipulate the dimensions and a well densified ceramic is readily produced while there are still many unsolved technical problems in the thin film processing and its surface effect can not be easily separated. Therefore we choose to study a ceramic system, the results could also be instructive for a thin film system.

The study of surface layer can be traced back in the 1950's. Kanzig[7] found that in very small $BaTiO_3$ particles a discrepancy exists in the symmetries of a surface layer (about 100 Å in thickness) and the bulk. From X-Ray and

electron diffraction experiments he also found that a tetragonal strain presents in this surface layer even above Curie temperature. He proposed that a space charge layer at sample surface is responsible for these results. Chynoweth[3] observed a polarized surface in $BaTiO_3$ crystals above Curie temperature and provided some evidence to support the space charge layer model. Merz[4] demonstrated that the switching time and the coercive field depend on sample thickness, which can be explained by the fact that there exists a surface layer in which the domain wall mobility is less than those in the bulk of the crystal.[8] Since then, many experiments have verified the existence of the surface layer on ferroelectric samples, these experiments includes: thickness dependence of the dielectric constant and loss[1,2], optical absorption coefficient[9] and refractive index.[5,10] The thickness dependence of dielectric constant and loss were first studied by Schlosser and Drougard[1], their experiments showed that the measured dielectric constant from a thin sample of $BaTiO_3$ single crystal is consistently smaller than that from a thick sample. The effect was ascribed to the presence of a surface layer with lower dielectric constant. The relaxation time of this layer was measured to be about 10^{-4} second at 120 °C. Thickness dependence of dielectric constant was also found in many other ferroelectric crystals, including TGS^{11}, $Pb_5Ge_3O_{11}{}^2$, KDP and Rochelle salt[12]. The electric impedance of the surface layer is much higher than that of the interior of the bulk. An interesting fact is that this surface layer seems to be insensitive to the change of temperature.

The existence of the surface layer was explained as due to the presence of intense space charge field near the ferroelectric-electrode interface, which modifies the ferroelectric behavior.[13] The characterization of this surface layer is not so simple, there are at least three different types of surface layers: (a) the as grown layer; (b) the lapped layer; (c) the chemically etched layer. Each of

these layers may have different structure and contribute differently to material properties. Previous studies on the thickness dependence of dielectric constant and loss did not incorporate the effect of different surface conditions. Although Schlosser and Drougard[1] did use samples with both etched and polished surfaces, the difference in their experimental results from these two surfaces was not explained. Jyomura et al[14] have studied the influence of the surface layers produced by mechanical lapping (grinding and polishing) on the physical properties in $(Pb_{0.8}Ba_{0.1}Sr_{0.1})(Zr_{0.8}Ti_{0.2})O_3$ ceramics. Their results show that after these lapped surface layers were etched off, the dielectric properties of the ceramic were improved. They concluded that the lapped surface layer (about 0.1-0.2 μm thick) seems to be non-ferroelectric, so that near the Curie temperature (at which the dielectric constant reaches maximum in mornal ferroelectrics) the dielectric constants of this layer is much smaller than that of the bulk material. They also found a 2-dimensional tensile stress in the order of 5-15Kbar inside this surface layer. Unfortunately, none of the above mentioned investigators have studied the thickness dependence of dielectric properties in a ceramic system.

In order to gain a better understanding of the nature of these surface layers it is necessary to evaluate the contributions from different type of surfaces. In this paper we present some experimental results which quantify the contributions of three types of surfaces: ground, polished and chemically etched. The effects of the lapping generated two-dimensional tensile stress were also singled out through post-annealing. The physical properties being studied include dielectric constant, dielectric loss and pyroelectric coefficients, and the material being studied is Lanthanum doped lead zirconate titanate(PLZT), a relaxor ferroelectric ceramic . The reason for chosen PLZT

4

ceramic as our subject material is because its excellent electro-optical property which has found many practical applications.[15,16]

II. EXPERIMENTMENTAL PROCEDURE

2.1 Surface Preparation

Ceramic PLZT specimens were fabricated from mixed oxides by hot pressing technique as described by Yao et al.[17] The compositions are represented by the formula $Pb_{1-x}La_x(Zr_yTi_z)_{1-x/4}O_3$. Conventionally, this formula is simplified to a form 100x/100y/100z representing the mole ratio La/Zr/Ti. For instance, $Pb_{0.92}La_{0.08}(Zr_{0.65}Ti_{0.35})_{0.98}O_3$ is simply represented by 8/65/35. Three different compositions were used in this study, they are 7/68/32, 8/65/35 and 8.4/65/35. The grain size for these three compositions are $5\mu m$, $5\mu m$ and $10\mu m$, respectively. At room temperature, 7/68/32 is rhombohedral, 8/65/35 and 8.4/65/35 are also mainly rhombohedral but very close to the morphotropic phase boundary (a structural phase boundary between tetragonal and rhombohedral phases) composition.

The samples used in the experiments were cut into platelets with their thickness ranging from $45\mu m$ to $2000\mu m$ and areas of about 2-20 mm^2. Three types of surface were prepared by the following methods: a) Grinding with $3\mu m$ silicon nitride abrasive. b) Polishing with $1\mu m$ diamond paste after grinding. c) Etching in H_3PO_4 acid for 2 minutes at 140°C after grinding or polishing. Surface obtained from method c) is relatively rougher than the polished surface but better than the ground surface. After surface processing, some of the samples were annealed at 600°C for 1 hour to release the mechanical stress generated during polishing and grinding in the surface layer. Gold electrodes were either sputtered or evaporated onto the surfaces of these samples.

2.2 Measurements

The dielectric properties were measured using a computerized system produced by Hewlett-Packard. A HP 9825A desktop computer was used for the on-line control of automated measurements through a HP 6904B multiprogrammer interface. The temperature and frequency dependence of capacitance and loss tangent were measured by LCR meter, HP4274A and 4275A impedance analyzers, respectively. The frequency range in our study is 10^2—10^7 Hz, and the total system accuracy is estimated to be 0.3%. The pyroelectric currents vs. temperature were measured using the HP4140B picoampere meter. A Delta Design model 2300 environment chamber was used for temperature control, which can regulate temperature from -150 °C to 200 °C by using liquid nitrogen as coolant. Temperatures were measured with a Fluke 8502A digital multimeter via a platinum resistance thermometer mounted directly on the ground electrode of the sample holder. The rate of temperature change is fixed at 3 °C/min for all the runs. In order to avoid aging effect, the starting temperature is set at 160 °C and the finishing temperature is -160 °C in all the dielectric measurements.

III. RESULTS AND DISCUSSIONS

In order to separate different contributions, the study was carried out in two steps: first, we only change the surface conditions while keeping the sample thickness fixed, then we change the thickness for each type of surface conditions.

3.1 Effects of surface conditions

Temperature dependence of the measured dielectric constant and loss tangent for 7/68/32 are shown in Fig.1 for three types of surfaces, i.e., ground, polished and chemically etched respectively. Near the dielectric maximum
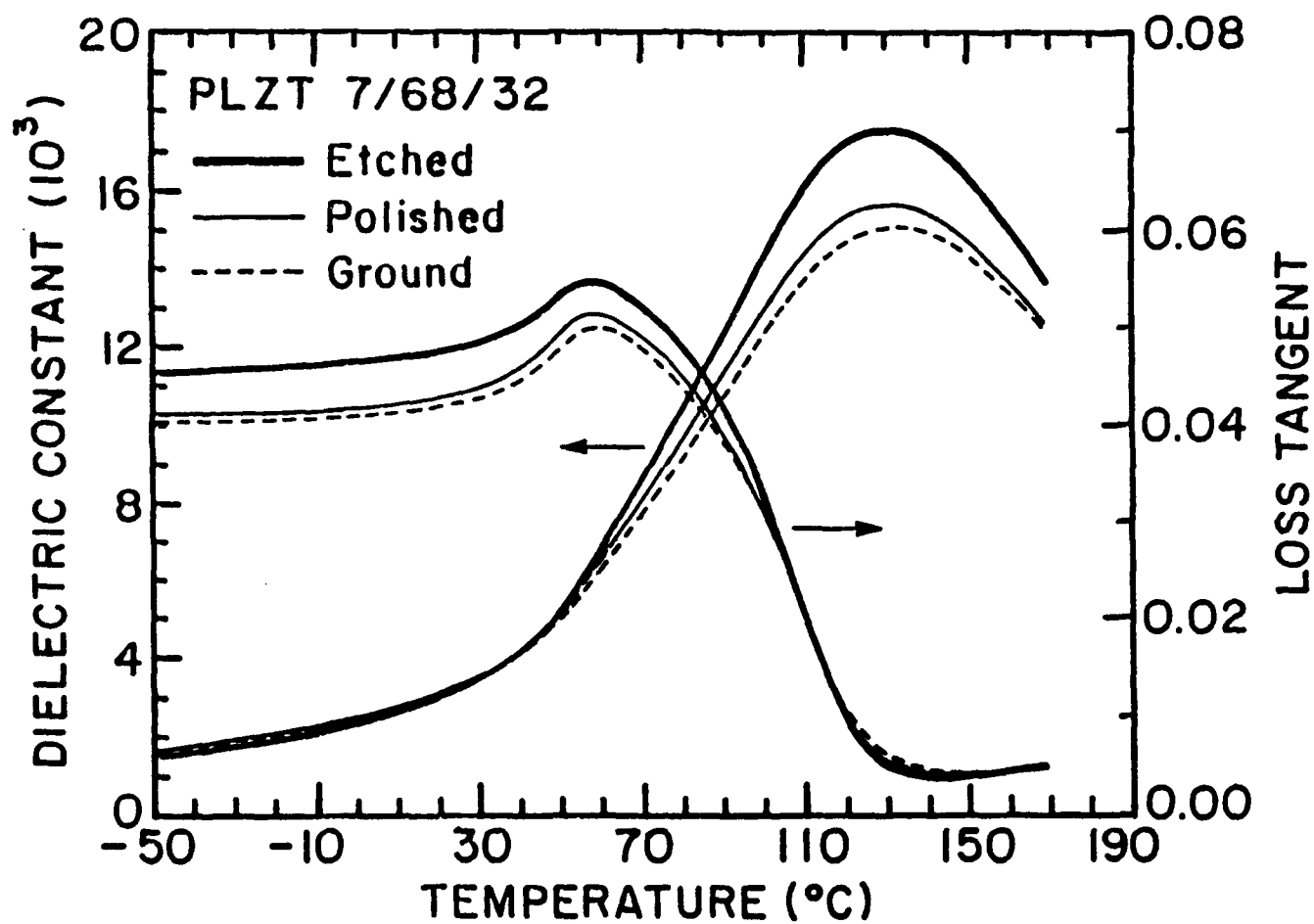
Figure 1   Dielectric constant and loss tangent vs temperature measured at 1 kHz for PLZT 7/68/32 hot pressed samples with three different surface conditions. The results for etched, polished and ground surfaces are represented by thick, thin and dashed lines respectively.

temperature($T_{max} \sim 140°C$), the specimen with etched surface gives the highest dielectric constant, and the one with ground surface(roughest surface) has the lowest dielectric constant. However, it has been noticed that the higher the dielectric constant of the ferroelectric the stronger the surface effects, below 50 °C the dielectric constants are almost the same for all three surface conditions. This anomalous behavior suggests that a surface layer might be produced by the lapping process, which has different dielectric characteristic. This surface layer is about $0.1\mu m$ to $2\mu m$ thick[14], which is two to three orders of m. itud smaller than the thickness of the specimen ($200\mu m$). Therefore, the capacitance ($\propto 1/d$) of the surface layer is very large compared with the bulk material. Considering the fact that the surface layer is a capacitor in series with the bulk, it contributes very little to the observed total capacitance C_m, $C_m = \dfrac{C_s C_b}{C_s + C_b} \sim C_b$, when $C_s \gg C_b$, where C_s and C_b are the capacitance of the surface layer and the bulk respectively. However, when the dielectric constant K_b becomes very large near T_{max}, C_b ($\propto K_b$) becomes comparable to C_s, hence according to the formula for two capacitances in series, the total capacitance C_m would reflect strong contributions from C_s. The dielectric losses also show some differences among these three surfaces (Fig.1). Above 110 °C the e the same, but below T_{max} the specimen with etched surface shows the highest loss and the one with ground surface has the lowest loss. This phenomena may also be explained by the existence of a non-ferroelectric surface layer and will be discussed further below.

Fig.2 is the temperature dependence of the dielectric constant and the loss tangent for PLZT 8/65 /35 (T_{max} is $\sim 90°$ C) with both etched and ground surfaces at three different frequencies. The two set of measurements have been conducted on the same sample, i.e., after the measurements were done

8
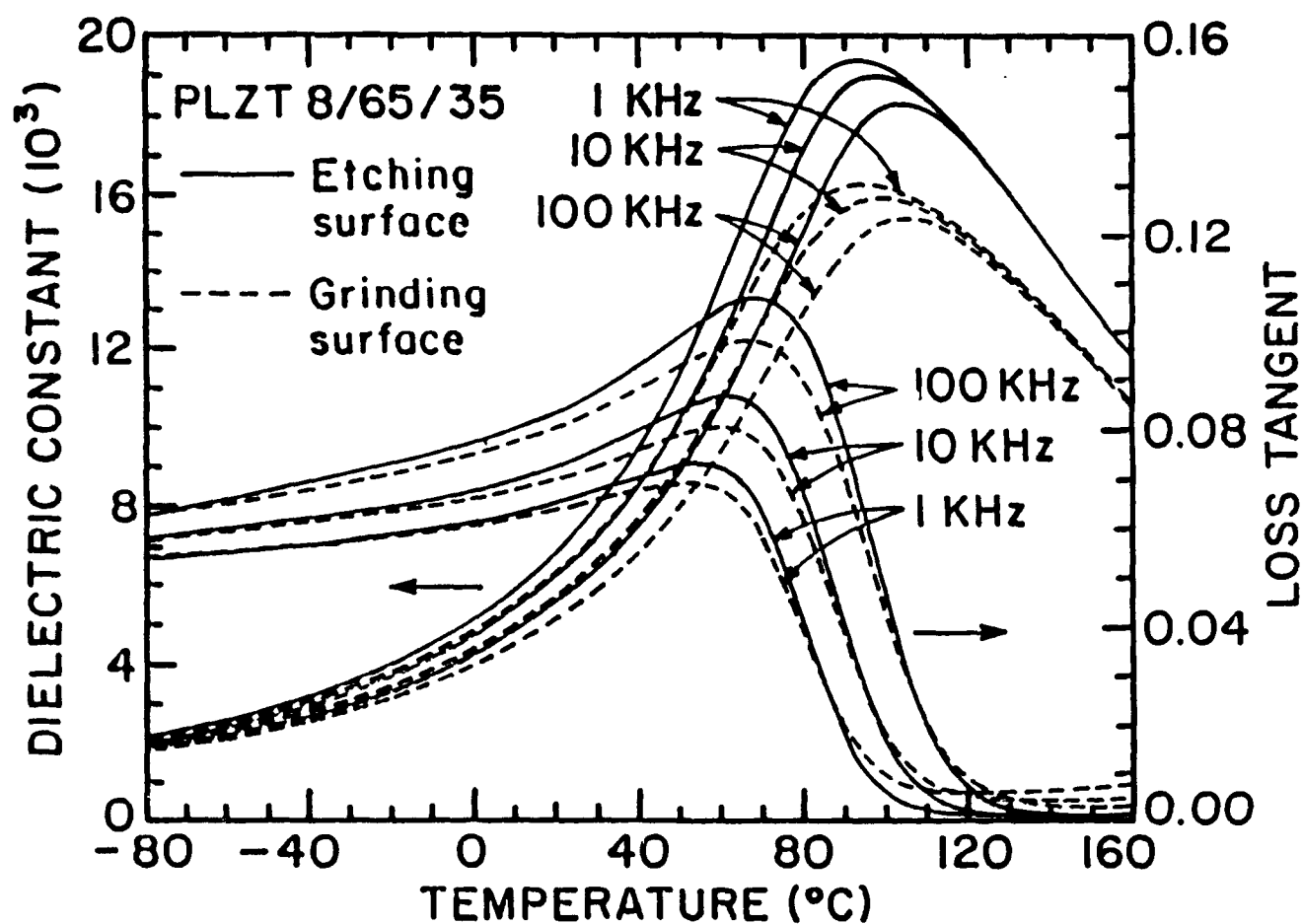
Figure 2   Dielectric constant and loss tangent vs temperature for PLZT 8/65/35 hot pressed specimen of ground and etched surfaces respectively at three different frequencies.

with the ground surface, the same sample was etched to remove the lapped surface layer then do the dielectric measurements again.

Polishing and grinding are mechanical processes, two consequences may result from these processes: One is the mechanical damage to the sample surface which creates a structurally distorted surface layer; the other is the introduction of a mechanical stress to the surface of the specimen, the nature of this stress is usually a two dimensional tensile stress.[14] In order to study how this surface stress contributes to the change of dielectric properties, we have carried out pre-processing and post-processing heat treatment for the samples. First, all samples were annealed before lapping to remove the bulk stresses produced during material processing and cutting, then these annealed samples were either polished or ground, and finally after polishing or grinding, some of the samples were annealed again to remove the surface stresses produced from lapping process. Dielectric measurements were carried out on all of these different heat treated samples. Typical results are shown in Fig.3a which is for PLZT 7/68/32. We can see that the dielectric constant and loss tangent are quite different for the samples being post-annealed and for those without being post-annealed, especially close to the dielectric maximum temperature T_{max}. One can see that the dielectric constant becomes larger at higher temperature (> 40 ° C) but becomes smaller for temperatures below 40 °C after post-annealing for samples with polished surfaces. The loss tangent is also changed by the post-annealing for the polished sample, it becomes larger for temperatures below T_{max} but smaller for temperature above T_{max}. Fig (3b) lists the results before and after post-annealing respectively for sample with etched surface, no change was found for the dielectric properties in this case within the experimental error. In Fig.4 are the temperature dependence of spontaneous polarization and pyroelecrtric coefficient, respectivel   fore and after post-

10
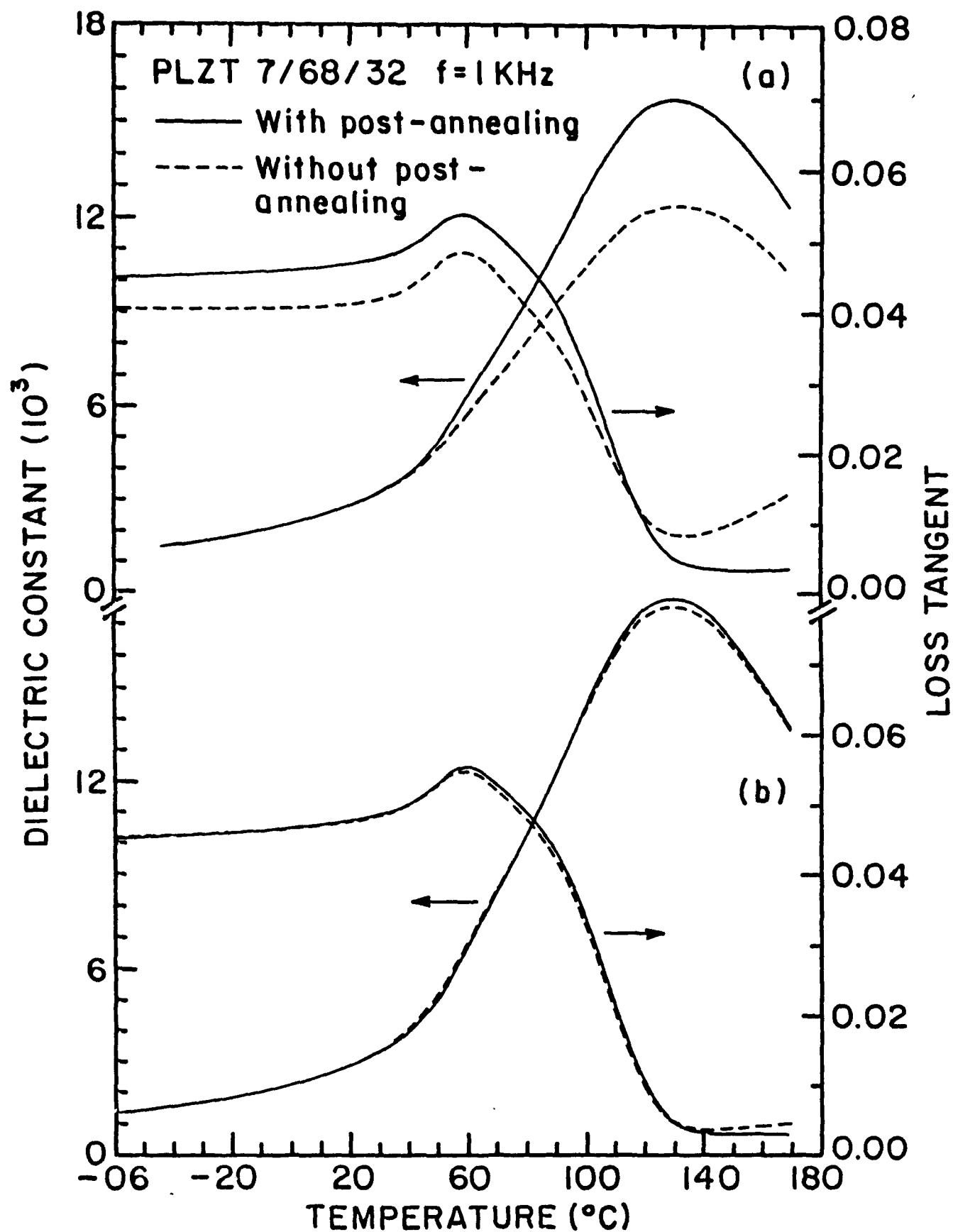
Figure 3   The effects of post-annealing on the dielectric constant and loss tangent measured at 1 kHz in the temperature range of -60°C - 170°C for PLZT 7/68/32 hot pressed ceramic specimens. (a) Results for samples with polished surfaces. (b) Results for etched samples.
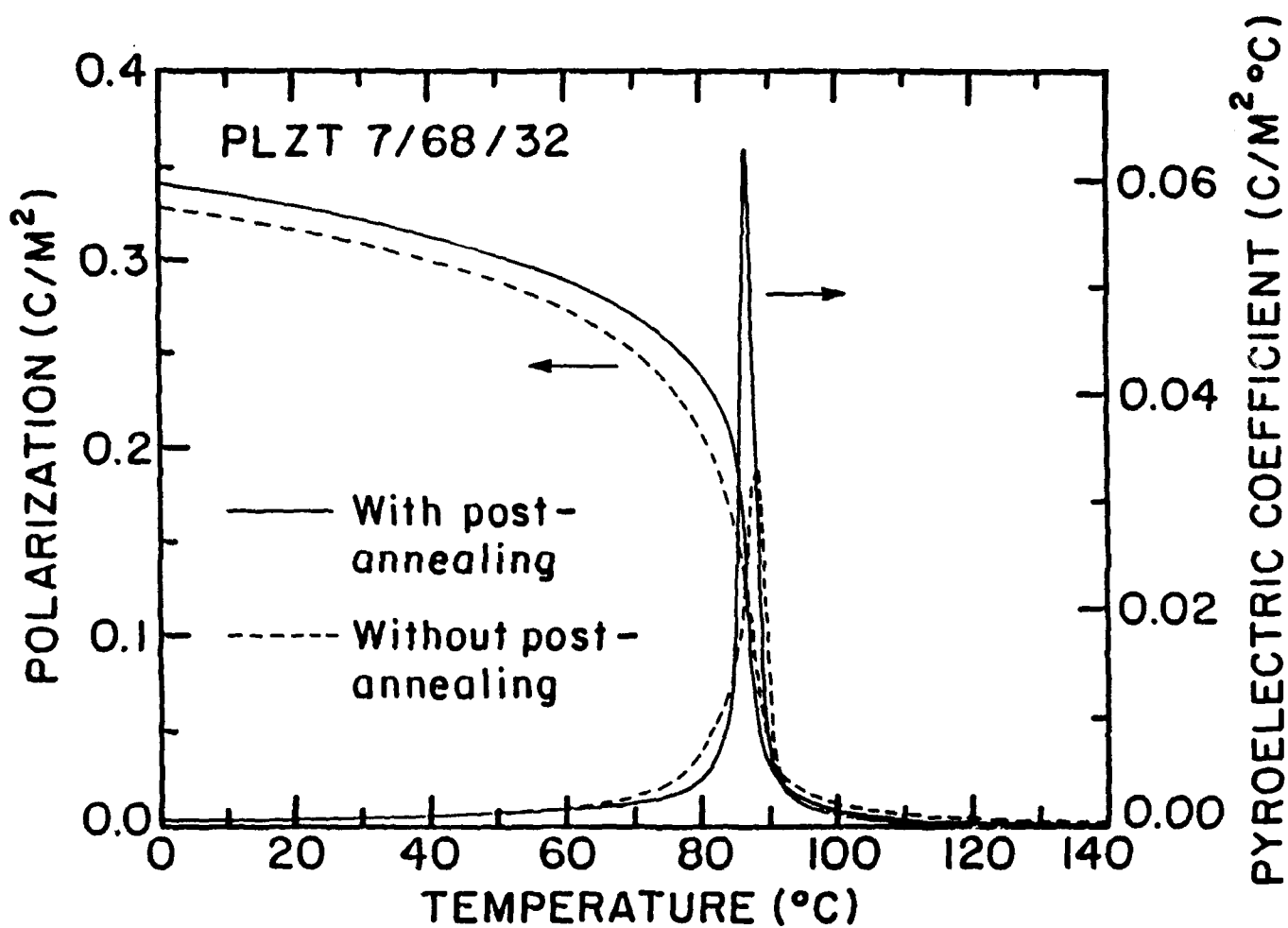
Figure 4   Polarization and pyroelectric coefficient vs temperature for polished PLZT 7/68/32 hot pressed ceramic samples with and without post-annealing, respectively.

annealing for a sample with polished surface. One can see that both quantities are increased by the post-annealing. We also found that the depolarization temperature is 2 °C lower for the post-annealed samples due to the elimination of surface stress.

Since the results in Figs. 3(a) & 4 were obtained from two samples of exactly the same chemical composition and geometry, the difference shown in in the figures are solely caused by the post-annealing, in other words, by the elimination of surface stresses produced during lapping process.

3.2 Thickness Dependence of Physical Properties

As pointed out in section 3.1, the surface layers produced from lapping on the PLZT hot pressed ceramic samples will contribute to the measured physical properties. The nature of these layers depend only on the preparation techniques, it should not change with the sample thickness. From this argument and the fact that the surface layer is actually a large capacitor in series with the bulk, it is expected that the surface layers should contribute more to the measured physical properties in thinner sample whose capacitance is comparable to the surface layer capacitance than in thicker samples whose capacitance is much smaller than C_s. This is indeed the case observed in our experiments.

In order to quantify the surface layer contributions, we have studied the influence of sample thickness to the measured dielectric properties. The specimens used for this study have been annealed at 650 °C for 1 hour after polishing to relieve the surface stress, hence the effects observed on these samples are mainly due to the non-ferroelectric nature of the surface layers. As shown in Fig.5 (a) the measured dielectric constant and the loss tangent for a PLZT 8.4/65/35 decrease with decreasing sample thickness, which is consistent

13
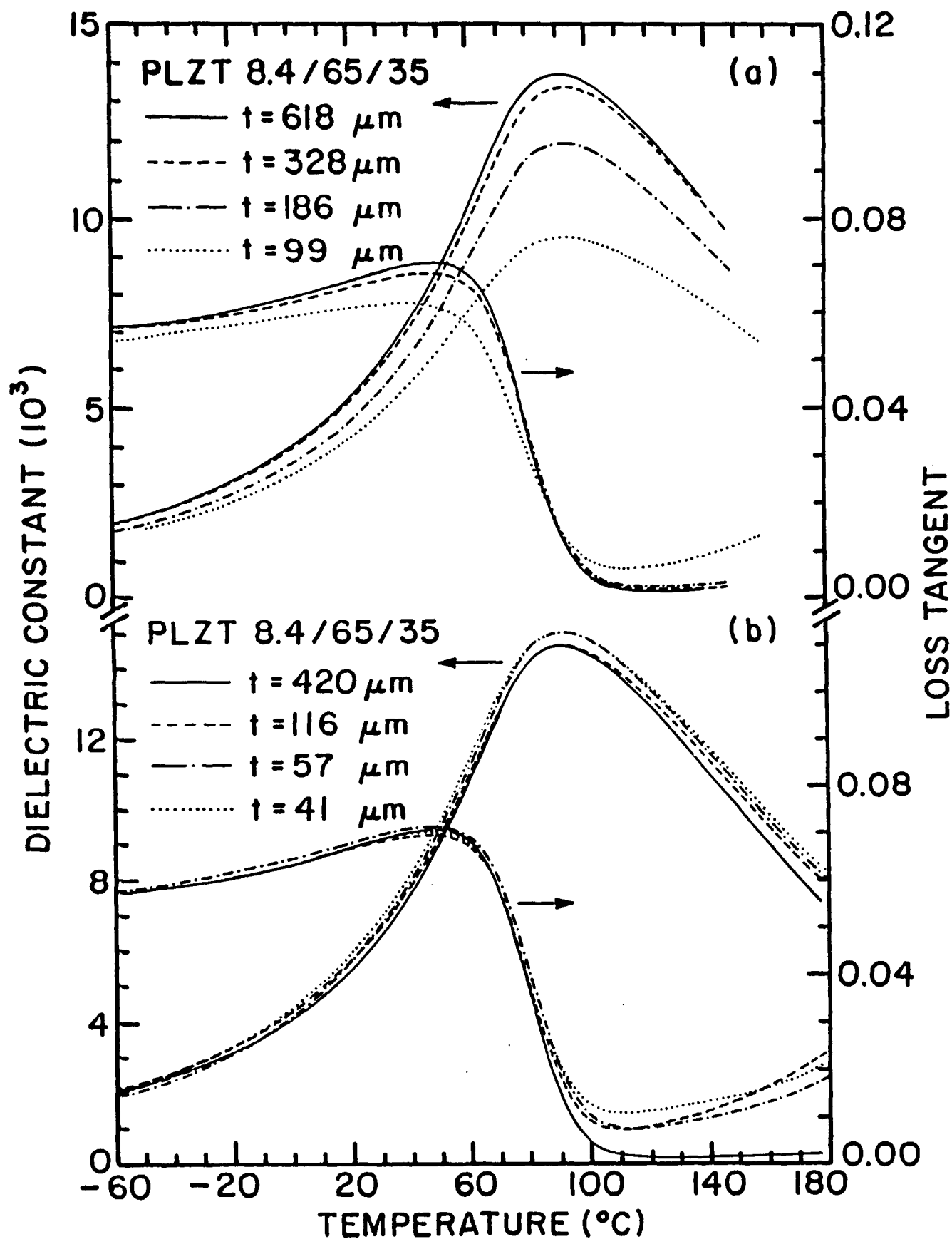
Figure 5   Temperature dependence of dielectric constant and loss tangent at 1 kHz for PLZT 8.4/65/35 hot pressed specimens of different thickness. (a) Results for samples with polished surfaces; (b) Results for samples with etched surfaces.

14

with some reported results on other ferroelectric single crystals[1,2]. Our results show that the thickness effect is not very obvious until the sample thickness is below 200μm. The dielectric maximum reduces about 30% when the sample thickness decreases from 618 μm to 99μm. We have performed the thickness dependent testing experiments in several compositions of the PLZT system, including 8/65/35, 8.6/65/35 and 9.5/65/35, similar results as in Fig. 5 were obtained for all of these compositions.

It may be intriguing to make a comparison of the results in Figs.1 &5. One finds that at low temperature (< 40 °C) the three curves (representing the temperature dependence of the dielectric constants for ground, polished and etched surfaces) in Fig.1 merge into a single curve, but in Fig. 5 the thickness effect does not completely go away even at very low temperatures.

A simple explanation may be given as follows for the thickness dependence of the measured dielectric constant values: Lapping produces a thin surface layer which has different dielectric characteristic. This surface layer is only about 0.1— 2 μm in thickness, therefore, the capacitance of this surface layer is very large although its dielectric constant may be relatively low. When the sample is thick (> 200 μm), the capacitance of the bulk part is much smaller than that of the surface layer, so that the measured dielectric constant value is very close to the true value of the bulk interior. As the thickness of the sample decreases, the capacitance of the bulk becomes more and more comparable to the capacitance of the surface layer so that the measured capacitance is influenced more and more by the surface layer. At temperatures close to T_{max} the dielectric constant of the bulk interior becomes very large, which in turn makes the capacitance of the interior very large, in this case surface layer could contribute substantially to the measured values. Since each sample consists of two surface layers and the bulk interior which are three capacitors in series, the

15

total capacitance and hence the measured dielectric constant should decrease with sample thickness. If the sample is thin enough this effect will not vanish even at very low temperature. Fig. 5 precisely shows this characteristic.

The most interesting results are show in Fig. 5 (b) which are for samples with chemically etched surfaces. We can see that the thickness dependence is completely eliminated even for sample as thin as 41 μm! Although the etched surface is rougher than the polished surface, a better result could be achieved with those etched samples. This is a very important result from the application standpoint for ferroelectric ceramics. Fig. 5 (b) also shows that there is a slight increase of the loss factor for temperatures above T_{max}, which may be due to the increase of DC conductivity in some of the samples at higher temperatures.

3.3 Model for Ferroelectric Surface Layer

A simple theoretical treatment to the problem is to consider the lapped surface layer to be a homogeneous dielectric layer which has different dielectric nature than the interior. Each sample being measured is a sandwich with the PLZT ceramic in between two such surface layers. The total capacitance C_T of this sandwich structure is

$$1/C_T = 1/C_b + 2/C_s \qquad (1)$$

where C_b, C_s are the capacitances of the bulk interior and the surface layer, respectively. We have shown that the dielectric constants do not depend on sample thickness for those samples with etched surface, therefore results on these etched samples are taken to be the bulk values in our calculations. C_T is the measured value for a sample with lapped surfaces. The surface capacitance C_s calculated from Eq. (1) for both ground and polished samples is plotted in Fig.6 as a function of temperature. We can see from Fig.6 that the surface capacitance is a linear function of temperature within the experimental error. In

16
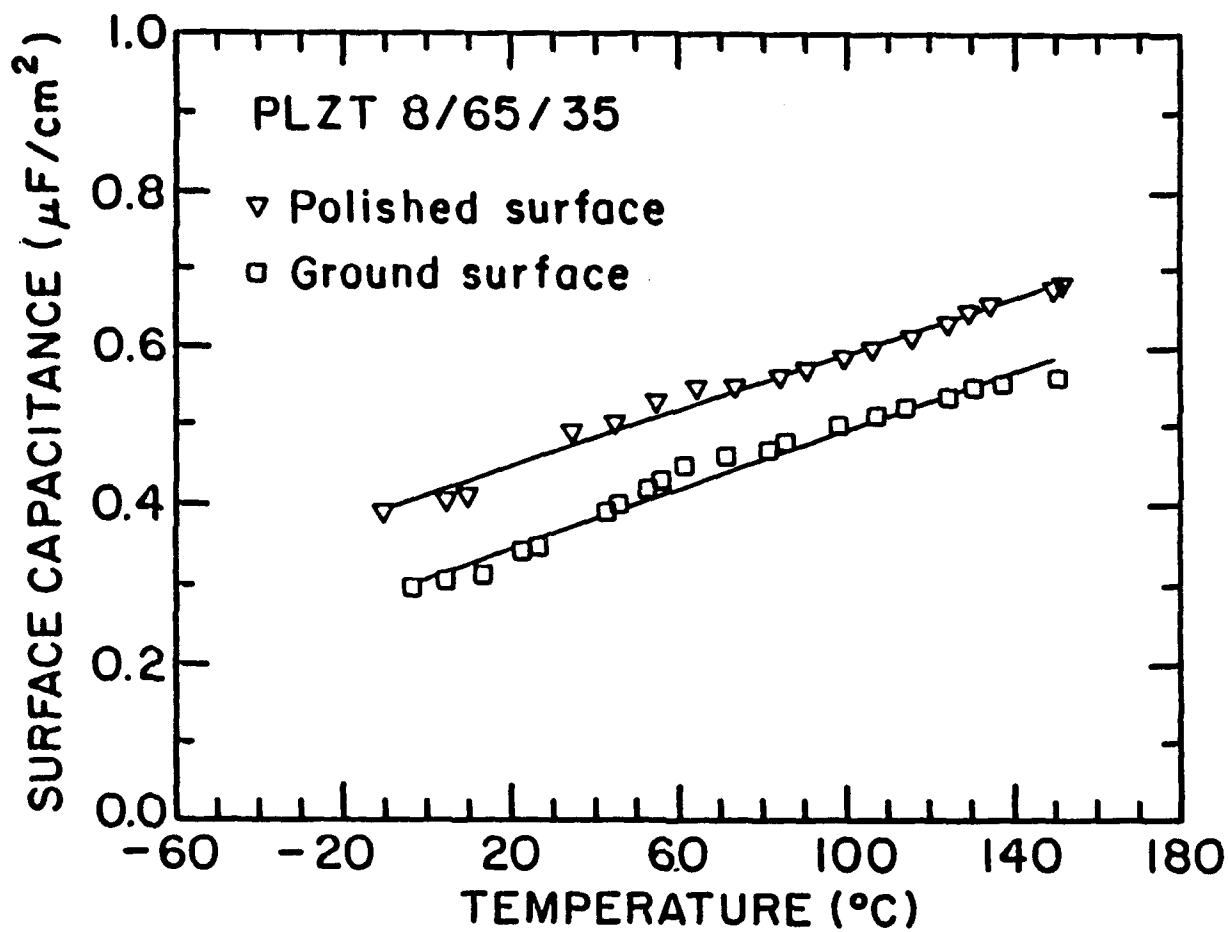
Figure 6   Capacitance of the surface layer vs temperature at 1 kHz for PLZT 8/65/35 hot pressed samples with polished and ground surfaces.

the measured temperature range, -20 °C — 160 °C, the surface capacitances C_s^G and C_s^P for the cases of ground and polished surfaces respectively may be expressed by the following linear functions

$$C_s^G = (1.848 * 10^{-3} T + 0.30632) \ \mu F/cm^2 \qquad (2a)$$

$$C_s^P = (1.796 * 10^{-3} T + 0.40979) \ \mu F/cm^2 \qquad (2a)$$

One can see from Fig. 6 that the surface capacitance of the polished sample C_s^P is consistently larger than the surface capacitance of the ground sample C_s^G, which may be explained from the fact that the mechanical damaged surface layer is thinner for the polished sample than for the ground sample.

An important point should be mentioned for the results in Fig. 6: There is no peak or any other types of anomalies observed at $T_{max} \sim 90°$ C for the surface capacitance! This result provides a strong support for the non-ferroelectric nature of the surface layer even below T_{max}. It has been reported that a surface capacitance of $\sim 0.5 \ \mu F/cm^2$ exists for polished single crystal barium titanate and strontium titanate,[1,14] which is in the same order of magnitude as our results in Fig.6.

Because the thickness is much smaller than the lateral dimensions in all our samples, it is quite accurate to treat them as plane capacitors, from Eq.(1) we have

$$1/K_m = 1/K_b + (2d_s/d) \ (1/K_s). \qquad (3)$$

Where K_m, K_b and K_s are the measured, bulk and surface layer dielectric constants respectively, d and d_s are the sample thickness and the surface layer thickness. The plot of K_m^{-1} versus d^{-1} for PLZT 8.4/65/35 with polished surface is shown in Fig.7 at three different frequencies, where K_m is the dielectric constant at T_{max} (note in relaxor materials T_{max} and K_m are both function of frequency). The straight lines are obtained from least squares fitting. There are different intercepts (K_b^{-1}) for different frequencies which are due to the dielectric

18
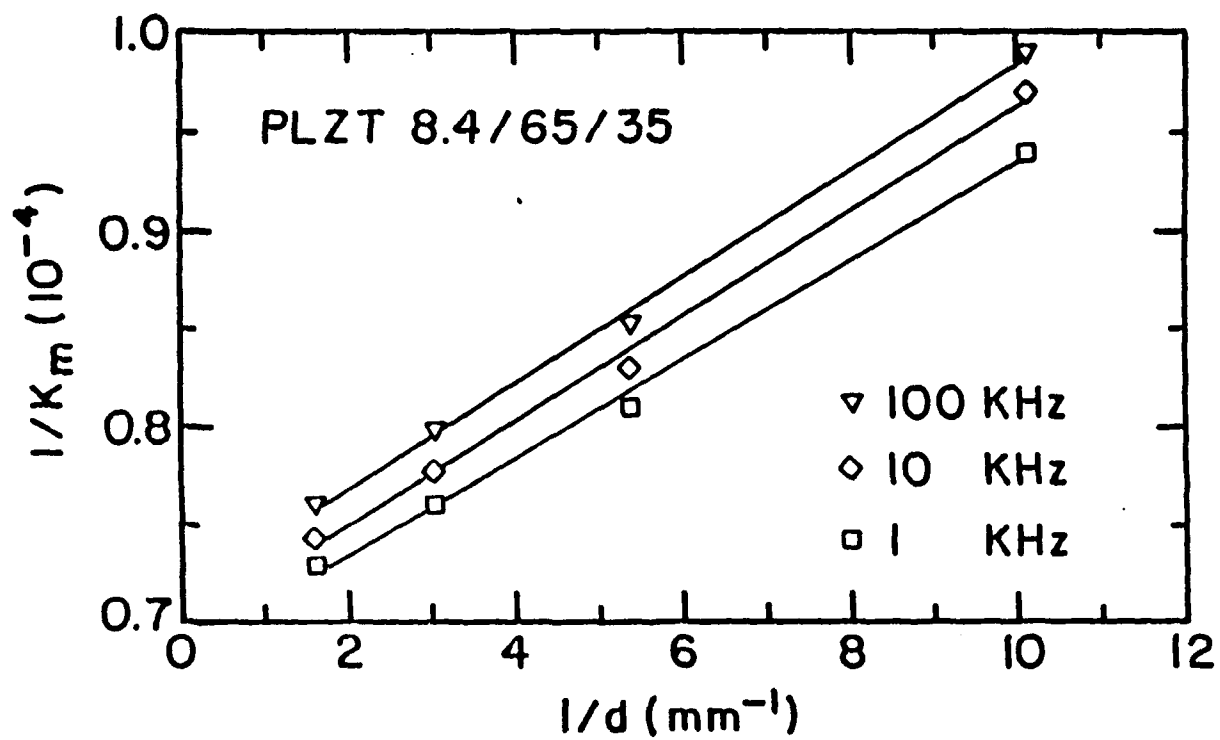
Figure 7 $1/K_m$ as a function of $1/d$ at three different frequencies: 1 kHz, 10 kHz and 100 kHz, for polished PLZT 8.4/65/35 hot pressed ceramic.

TABLE 1

f (kHz)	1/Km (intercept)	2ds/Ks (mm)	Ks (cal.)	Kb (cal.)	Kb (etched)
1	6.83e-5	2.51e-6	120	14634	14660
10	6.96e-5	2.67e-6	112	14370	14338
100	7.22e-5	2.70e-6	111	13850	13840

dispersion of relaxor materials. The fitted parameters are listed in Table 1 for all three frequencies. In addition, the bulk dielectric constants calculated from these intercepts are given in Table 1, which agree very well with those obtained directly from measurements on etched samples (see Table 1). The dielectric constants of the surface layer listed in Table1 are calculated   n the slopes ᵢ the fitted straight lines and using the thickness value of $d_s = 0.15$ μm for ᵗʰⁿ polished samples, which was the value estimated by Jyomura et al.[14] The typical value of the dielectric constant for the surface layer is in the order of 100, which is much smaller than the dielectric constants of the bulk that could be more than 15000 near T_{max}.

The loss tangent can also be separated into contributions from the bulk, $(\tan\delta)_b$, and from the surface layers, $(\tan\delta)_s$, respectively. Based on the surface layer model, the total measured dielectric loss $(\tan\delta)_m$ may be represented by[14]

$$(\tan\delta)_m - (\tan\delta)_b = [(\tan\delta)_s - (\tan\delta)_b] / (1 + C_s/2C_b) \quad (4)$$

Below T_{max} the bulk is in ferroelectric state, $(\tan\delta)_b$ is ge due   ᵢe contribution from hysteretic domain processes. Since the surface layer is in non-ferroelectric state, $(\tan\delta)_b$ is usually larger than $(\tan\delta)_s$, hence $(\tan\delta)_s - (\tan\delta)_b$ is negative. From equation (3) one concludes that $(\tan\delta)_m$ is smaller

than $(\tan\delta)_b$, which explains why the ground and polished samples appear to have lower dielectric loss than the etched samples at temperatures below T_{max} (see Figs.1 and 2).

The post-processing heat treatment results are consistent with that of Jyomura et al,[14] who found that a two-dimensional tensile stress of about 5-15 kbars was generated on sample surface during lapping. This surface tensile stress can reduce the total effective dielectric constants, polarization and pyroelectric coefficient , in addition, it may also cause the increase of depolarization temperature, similar to the effects of compressional stress and hydrostatic stress on ferroelectric properties reported by other investigators[18,19,20].

IV. SUMMARY AND CONCLUSIONS

In summary, a systematic study has been carried out on the effects of surface layer in PLZT relaxor ferroelectric ceramic system. This surface layer is produced by lapping process, its thickness is about 0.1-1 μm. Our results show that the dielectric constant of this surface layer is about 100 and only changes slightly with temperature, no dielectric maximum was observed at T_{max} for this surface layer. The capacitance of this surface layer is very large and change linearly with temperature in the investigated temperature range (-20 °C — 160 ° C) from 0.2 μF/cm^2 to 0.7 μF/cm^2. Since the surface layer and the bulk interior are capacitance in series, the large surface capacitor can show its effects only when the interior capacitance becomes comparable, i.e., when the sample is very thin (< 200 μm) or at temperatures close to T_{xam}. In addition to some degree of amorphism in this surface layer, lapping also produces a two dimensional tensile stress in this layer, we show that the tensile stress can be relieved through post-annealing. It is found that the surface effects can be reduced by as much as 60—80 % through the post-annealing.

21

One of the most encouraging results is that the surface effects can almost be eliminated through chemical etching although some surface roughness may be introduced. In a real application one may chose either post-annealing or chemical etching, or may even the combination of the two, to eliminate the surface effects depending on the requirements. Direct application of as polished thin ceramic sample can cause substantial degradation of many physical properties.

It may be necessary to point out that the dielectric properties we have reported here are obtained under weak electric field, it is conceivable that the effects of surface layer could be quite different under strong electric field. In fact, we have already noticed that the coercive field, the saturated and remnant polarizations measured from hysteresis loops show strong sample thickness dependence even in etched samples, which suggests that the surface layer from lapping may not be important under strong electric field, instead, a space charge layer may form at the metal dielectric interface. We will not address the space charge layer problem in this paper.

ACKNOWLEGEMENTS

REFERENCES

1. H. Schlosser and M. E. Drougard, J. Appl. Phys., **32**,1227 (1961).

2. Abhaimansing, K.N. Srivastava and Bachchan Singh, J. Appl. Phys., **50**, 4314 (1979).

3. A. G. Chynoweth, Phys. Rev., **102**, 705 (1956).

4. W. J. Merz, J. Appl. Phys., **27**, 938 (1956).

5. Philip D. Thacher, Applied Optics, **16**, 3210 (1977).

6. M. Okuyama, T. Usuk and Y. Hamakawa, Appl. Phys., **21**, 339(1980).

7. W. Kanzig, Phys. Rev., **98**, 549 (1955).

8. D. R. Callaby, J. Appl. Phys., **36**, 2751(1965).

9. P. Coufova and H. Arend, Czech. J. Phys., **B11**, 663 (1960).

10. V. Afanasjev, S. Korpela and T. Tuomi, Ferroelectrics, **65**, 175 (1985).

11. Abhai Mansing and Eswar Prasad SRJ, J. Appl. Phys., **48**, 1379 (1977).

12. Abhai Mansing and Eswar Prasad SRJ, J. Phys. D: Appl. Phys, **9**, 3399 (1976).

13. M. E. Lines and A. M. Glass, in Principles and Applications of Ferroelectrics and Related Materials, Oxford, Clarendon Press, 118 (1977).

14. Shigeru Jyomura, Iwao Matsuyama and Gyozo Toda, J. Appl. Phys. **51** 5838 (1980).

15. C. E. Land, Sandia National Laboratories, SC-R-67_1219, October, 1967.

16. C. E. Land and W. D. Smith, Appl. Phys. Lett., **23**, 57 (1973).

17. Yao Xi, Chen Zhili and L. E. Cross, J. Appl. Phys., **54**, 3399 (1983).

18. G. Shirane and K. Sato, J. Phys. Soc. Jpn., **6**, 29 (1951).

19. I. N. Polandov and V. P. Mylov, Sov. Phys. Solid state, **9**, 1816 (1968).

APPENDIX   9

THE INFLUENCE OF SURFACE CONTAMINATION ON ELECTRIC FATIGUE OF FERROELECTRICS

Qiyue Jiang, Wenwu Cao and L.E. Cross

Materials Research Laboratory

The Pennsylvania State University

ABSTRACT

Electric fatigue is a major obstacle for some potential applications of ferroelectric materials based on the reversals of spontaneous polarization, such as making memory devices and actuators. It is found that the observed fatigue in small grain ceramics is not intrinsic but significantly related to the surface conditions. Studies on hot pressed lead zirconate titanate (PLZT) of composition 7/68/32 show that the fast fatigue is actually caused by contaminated surfaces instead of intrinsic structure deterioration or the change of domain states. All the specimens with conventionally cleaned surfaces show significant fatigue after 10^5 switching cycles, but specimens cleaned with a new cleaning procedure did not fatigue even after more than 10^8 switching cycles. The fatigue initiated by the surface contamination under a high AC field is explained in terms of the degradation of the interface between ferroelectric and electrode, which leads to an inhomogeneous field distribution causing microcracking in the ceramic.

I. INTRODUCTION

Many applications of ferroelectric materials, such as making piezoelectric, electro-optical and electrostrictive devices, involve repeated reversals of the polarization. One critical limitation on the performance of these devices is the fatigue associated with repeated electrical cycling. Fatigue mainly refers to the degradation of the ferroelectric properties with respect to repeated reversals of the polarization, which appears in the hysteresis loop in the form of a decrease in remnant polarization(P_r) or saturated polarization(P_m) and often accompanied by an increase of the coercive field(E_c).

In 1953, Mcquarrie[1] first reported the time dependence of the P-E hysteresis loop in a BaTiO$_3$ ceramic. He found that after several weeks of switching at 60 Hz, the square shaped hysteresis loop was changed to a distinct propeller shape with some obvious decrease in both the maximum polarization and the remnant polarization. Merz and Anderson[2] studied fatigue behavior in a single BaTiO$_3$ crystal, a gradual reduction of polarization after a few million switching cycles was observed and the fatigue behavior was related to the wave patterns of the electric field(sine wave or pulse train wave). The ambient atmosphere had an effect on the switching stability of BaTiO$_3$ single crystal[3], a loss of squareness of the hysteresis loop was found when the crystal was switched in vacuum, N$_2$, H$_2$, or He gases, and the deteriorated hysteresis loop could restore its original shape under AC cycling in O$_2$, or dry air.

Fatigue experiments were also carried out on other ferroelectrics in the 1960's. Taylor[4] studied fatigue phenomena in 24 compositions of niobium-doped Pb(Zr,Sn,Ti)O$_3$ ceramics and discovered that the fatigue rate depended on the composition. However, he found little difference in fatigue behavior when the AC electric field pattern was changed from a sine wave to a pulse train wave. A more detailed study of fatigue was carried out by Stewart and Cosentino on La or Bi doped PZT ceramics[5], they showed that the polarization decreased rapidly and was reduced to half of its original value after 5x10^6 switching cycles. They concluded that the patterns of electric field, the types of electrodes,

and the ambient conditions had no significant effects on the fatigue behavior. Stewart and Cosentino[5] also reported an interesting result: when a fatigued sample was heated above the paraelectric-ferroelectric phase transition temperature Tc, the fatigued properties could be restored. Contrary to Stewart and Cosentino, Fraser and Maldonado[6] also studied the same La doped PZT ceramics and reported significant effects of the electrodes. They found that when indium was used as electrode material instead of gold or silver, there was still 85% of the original remnant polarization left after 10^9 switching cycles, but fatigue occurred much faster when using lead, aluminum, gallium, silver and gold as electrode material. Carl[7] observed significant degradation in the La or Mn doped $PbTiO_3$ ceramics, after only a few thousand switching cycles the polarization dropped to 30% of its original value together with some increase of the coercive field, and some cracks were also observed on the surfaces of the samples under SEM.

Although the fatigue phenomena in ferroelectrics have been studied for over thirty years, its origin is still not clear. Some possible causes of the fatigue under high AC field are:1) the gradual reorientation of domains into a more stable, i.e. minimum energy configuration[1] [8] ; 2) injection of charge carriers into the ferroelectrics which provide pinning for domain wall movement[9] ;3) structural inhomogeneity which produces traps for the domain walls, which can reduce the domain wall mobility[10]; 4) the appearance of microcracking caused by the large change of strain during switching[7][11].

Despite the fact that the fatigue effect is the key factor which prevents some potential applications of ferroelectrics, only a limited number of papers have been published on this subject. In addition, these published results by different investigators are often in contradiction, and there are no explanations for these discrepancies. Therefore a systematic study on this subject is needed in order to understand the origin and mechanism of fatigue behavior. We report here an extensive study of the fatigue behavior on La doped lead zirconate titanate(PLZT) ceramic system. The reason for choosing PLZT ceramic system is because its relatively low coercive field, large polarization and square shaped hysteresis

3

loop. Moreover, hot pressed PLZT ceramics are transparent, therefore have potential applications in non-volatile memory, electro-optical, and electrostrictive devices. In this paper, the focus will be on the effect of surface contamination on the fatigue behavior. We believe that different surface conditions was one of the main reasons for the inconsistencies of those reported experimental results.

II. EXPERIMENT PROCEDURES

Lanthanum doped lead zirconate titanate ceramic specimens were fabricated from mixed oxides by hot pressing technique. The composition used in this study is $Pb_{0.93}La_{0.07}(Zr_{0.68}Ti_{0.32})_{0.9825}O_3$. Conventionally, this formula is simplified to a form 7/68/32 according to the mole ratio of La/Zr/Ti. The average grain size is about $5\mu m$. At room temperature 7/68/32 is in rhombohedral phase. Samples were first cut into platelets with the areas of about $10 \, mm^2$ and thicknesses in the range of $150-300\mu m$, then annealed at $600 \, ^oC$ for 1 hour to release the mechanical stress generated during cutting, grinding and polishing processes.

Three different surface conditions were prepared: a) ground by $3\mu m$ abrasive, b) polished by $1\mu m$ diamond paste, c) etched in H_3PO_4 acid for 2 minutes at 140^oC. In conventional cleaning procedure, organic solvents (alcohol or acetone) are used to rinse the samples and then the samples are dried in air at room temperature. An improved cleaning method used in our experiments is described as follows: first the samples are cleaned by conventional procedure, then they are further cleaned ultrasonically in solvent, and finally the samples are heated in a furnace for 1 hour at $500-600^oC$. Gold electrodes were sputtered onto the sample surfaces.

The properties studied here are the remnant polarization P_r, the maximum polarization P_m, coercive field Ec, and the dielectric constant ϵ in depoled state. High voltage sine wave AC field was used to switch the polarization, and the hysteresis loops were measured though a conventional Sawyer-Tower circuit and a Nicolet 214 digital oscilloscope. The

temperature dependence of dielectric constant was measured by Hewlett Pacakard 4274A
LRC meter, and the temperature was measured using a Fluke 8502A digital multimeter.
The heating rate was set at 3 °C/min.

III. RESULTS AND DISCUSSION

3.1 Fatigue in PLZT Specimens Cleaned by Conventional Procedure.

In order to compare the results from different specimens and to emphasize the
changes of the measured properties, relative polarization and coercive field are used in this
paper, they represent the percentages of the polarization and coercive field with respect to
the initial polarization and coercive field obtained at 10^2 or 10^3 switching cycles. Fig.1
shows the typical results obtained from specimen cleaned by conventional procedure. The
AC field was kept at only 10 Hz in order to avoid heating effect. One can see that the
fatigue started at about 10^3 switching cycles, and proceeded very rapidly between 10^5 -10^6
cycles. The polarization P_r dropped to a value below 40% of the initial values after 10^6
switching cycles. The changes of the saturated polarizations which were not show here
have similar behavior as that of the remnant polarization P_r. Fig.2(a) and 2(b) are typical
hysteresis loops before and after the fatigue test, respectively, from a sample with polished
surfaces. The coercive fields Ec also increased with switching cycles. There is a
correspondence between the changes of E_c and P_r, i.e., while the polarization decreases,
the coercive field E_c increases, which is consistent with the results obtained by other
researchers.[4][6][11] It is noticed that the ground sample fatigued earlier and faster than the
samples with polished and etched surfaces. The same experiments were also carried out
using sine wave field at the frequencies of 100 Hz and 200 Hz, no apparent difference
were observed. Fig.3(a) and (e) show the weak field dielectric constant as a function of
temperature for a sample with polished surfaces before and after the fatigue test
respectively. One can see a substantial decrease of the dielectric constant in the fatigued
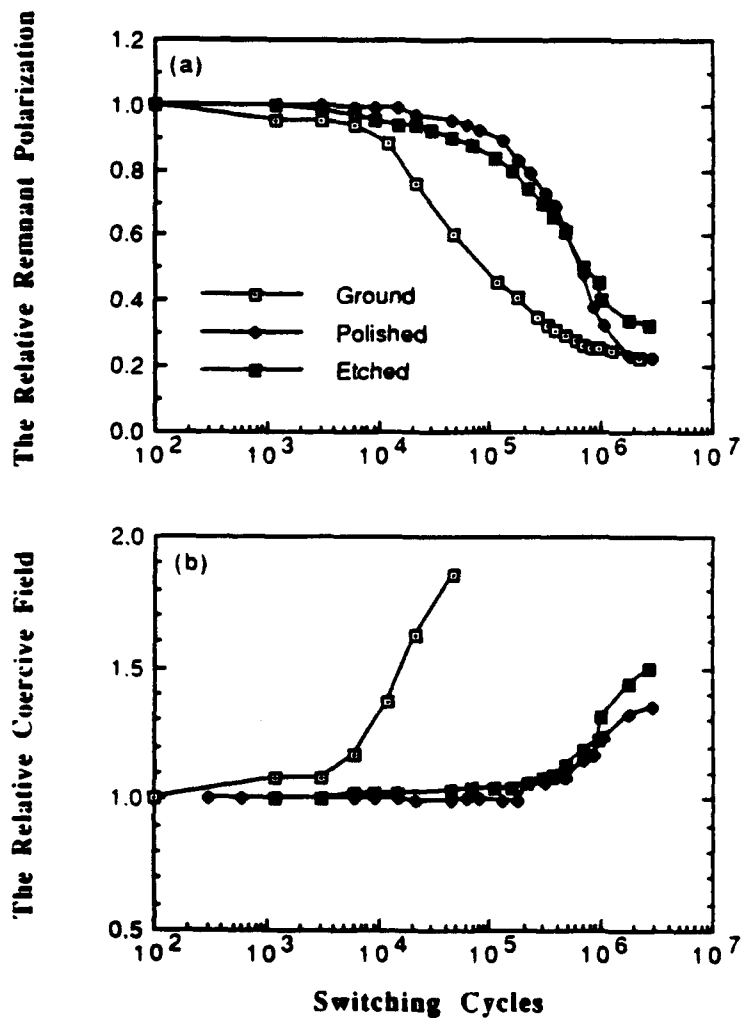
Fig.1   (a) The changes of relative remnant polarization P_r with switching cycles, and (b)

the changes of the relative coercive field E_c with switching cycles, at a frequency of

10 Hz for the conventionally cleaned PLZT 7/68/32 specimens.
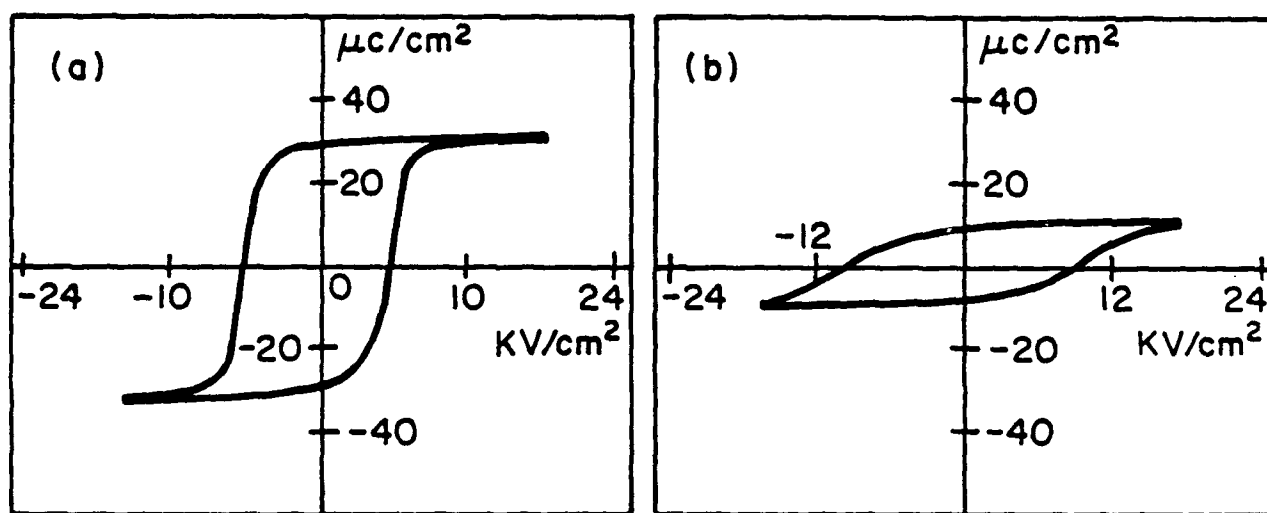
Fig.2 (a) and (b) are the typical hysteresis loops after 10^3 and $3*10^6$ switching cycles respectively for a conventionally cleaned PLZT 7/68/32 sample with ground surfaces at a frequency of 10 Hz.
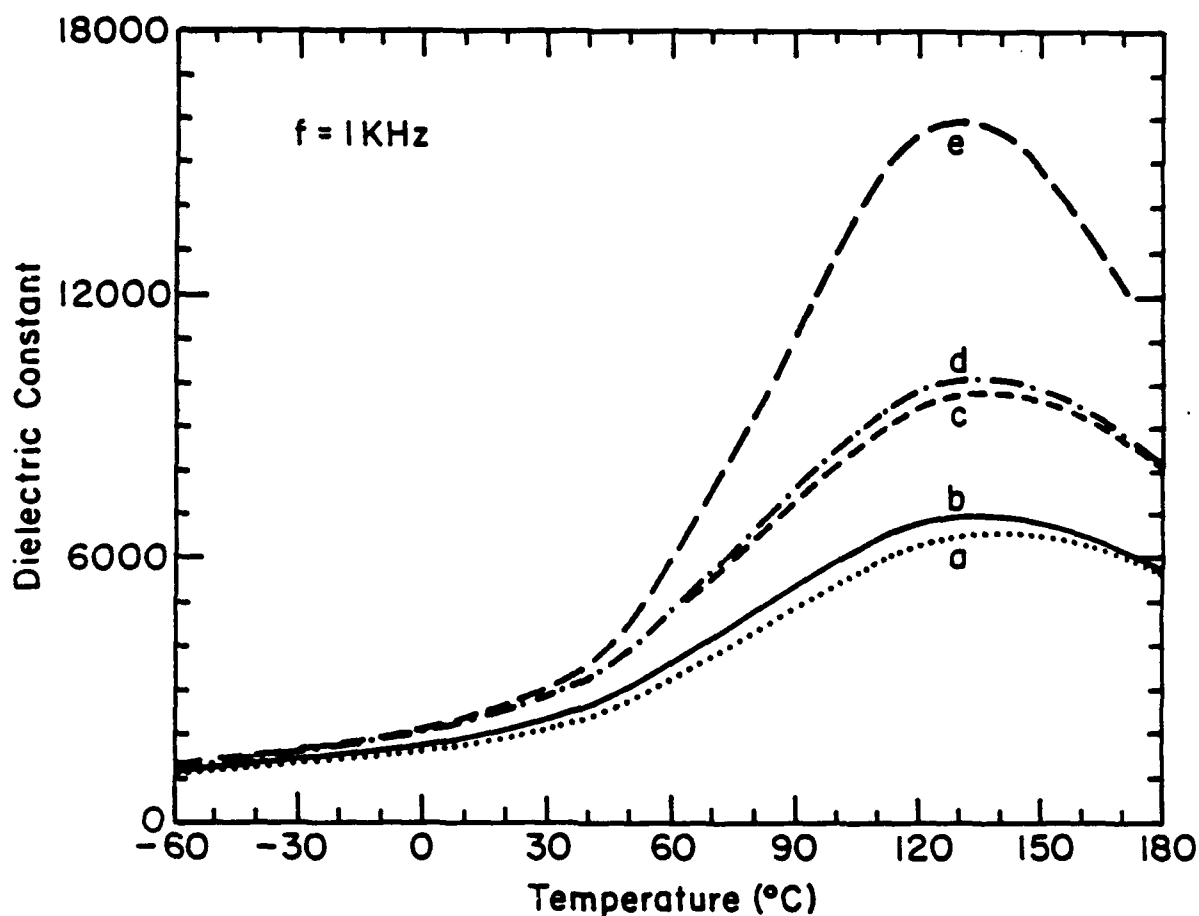
Fig.3 Temperature dependence of the dielectric constant for a conventionally cleaned sample with polished surfaces. (a) Fatigued sample; (b) fatiqued sample after heat treatment at 300 °C for 3 hours. (c) fatiqued sample after heat treatment at 600 °C for 1 hour. (d) a 15 μm thick layer was ground off from each side of the sample. (e) results from a virgin non-fatigued sample.

sample. Samples with the other two types of surfaces have similar results which are not show here.

3.2 Fatigue in PLZT Specimens Cleaned by Improved Procedure.

Fig.4 shows the changes of the polarization and coercive field with switching cycles for samples cleaned by improved procedure. The experiments were carried out at a frequency of 100 Hz. Samples with all the three types of surfaces did not show any fatigue even after 10^8 switching cycles. We can see this more clearly from the two hysteresis loops in Fig.5, which were recorded at 10^3 and 2×10^8 switching cycles in a ground sample, the same results were also obtained from samples with the other two types of surfaces. This is a very important finding which leads to much deeper understanding on the nature of the fatigue behavior in ferroelectrics. We can conclude from these experimental results that the fatigue shown in Fig.1 is purely extrinsic, i.e., caused by dirty surfaces. The actual lifetime of PLZT 7/68/32 ceramics with grain size less than 5 μm is much longer than that shown in Fig.1. We can also conclude that the surface roughness does not change the fatigue characteristic of a ceramic (Fig.4) but the surface preparations have significant effects on the observed fatigue behavior due to the organic contaminants being trapped at the ceramic-electrode interfaces, because a large electric field(15-40 kv/cm) is constantly applied on the sample during switching experiments, which will interact with the contaminates. We will elaborate this point in the following section.

Although these experimental results can not be used as a proof to discredit the validity of other previous explanations on fatigue in terms of internal domain behavior, we can at least conclude that the fatigue in fine grain PLZT 7/68/32 is caused by the ceramic-electrode interface as shown in Fig.6, which can be eliminated with an improved cleaning procedure described in this paper. This finding is very encouraging for many prospective applications of ferroelectrics.

9
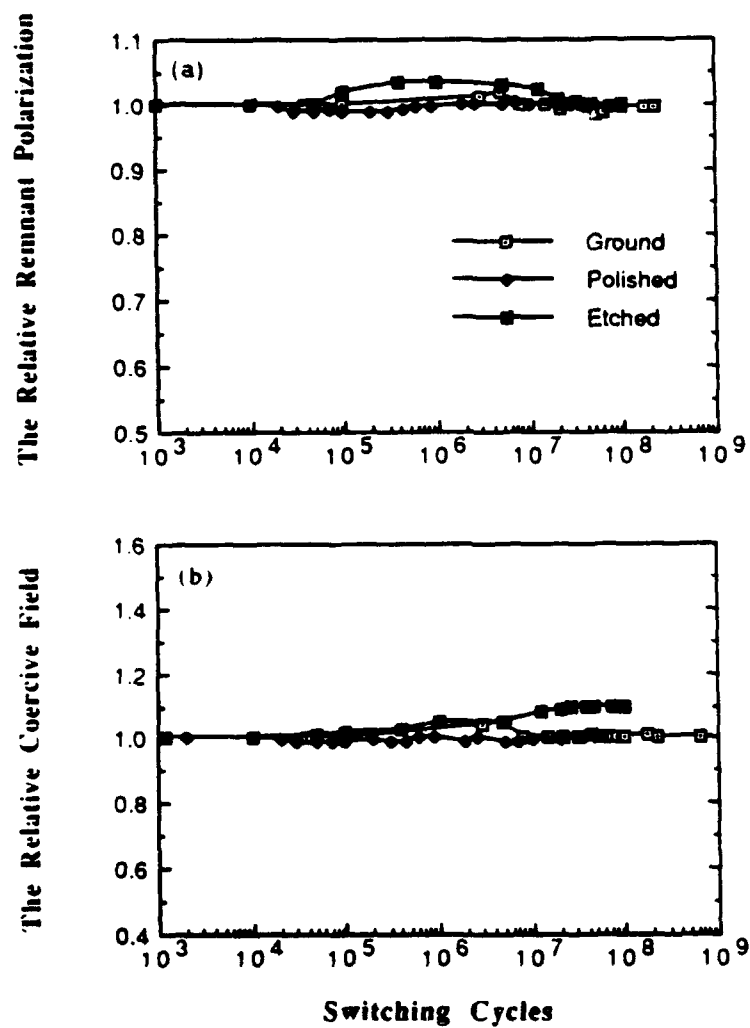
Fig.4. (a)The relative polarization, and (b) the relative coercive field versus

switching cycles for a specimen cleaned by improved procedure at a frequency of
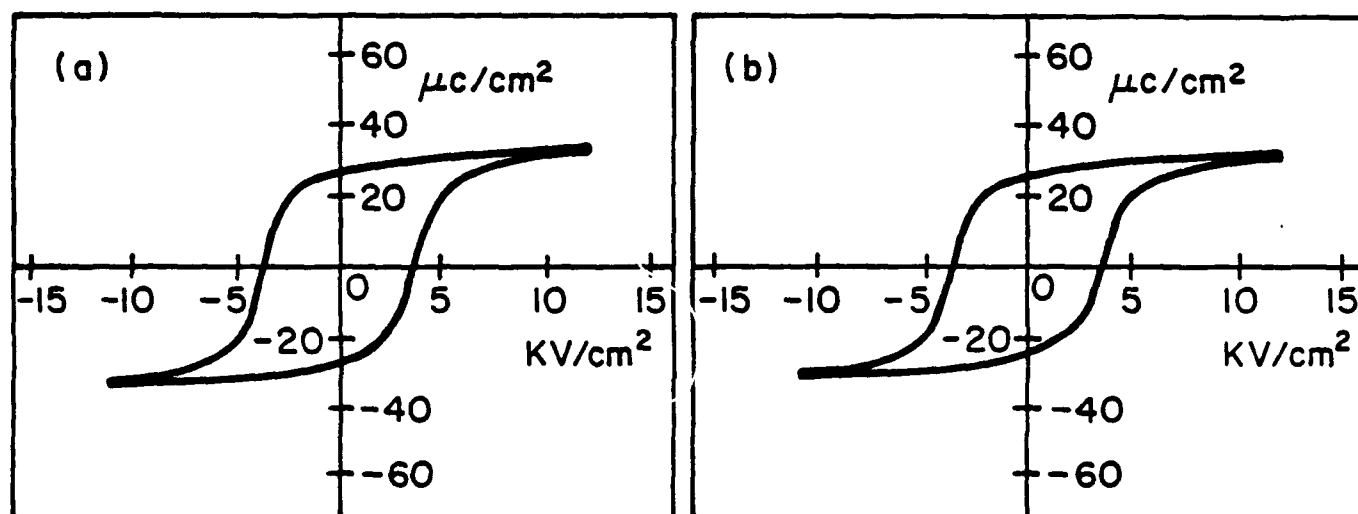
100 Hz.

Fig.5 Typical hysteresis loops of a sample cleaned by improved procedure at a frequency of 100 Hz. (a) after 10^3 switching cycles, (b) after $2 \cdot 10^8$ cycles.

11
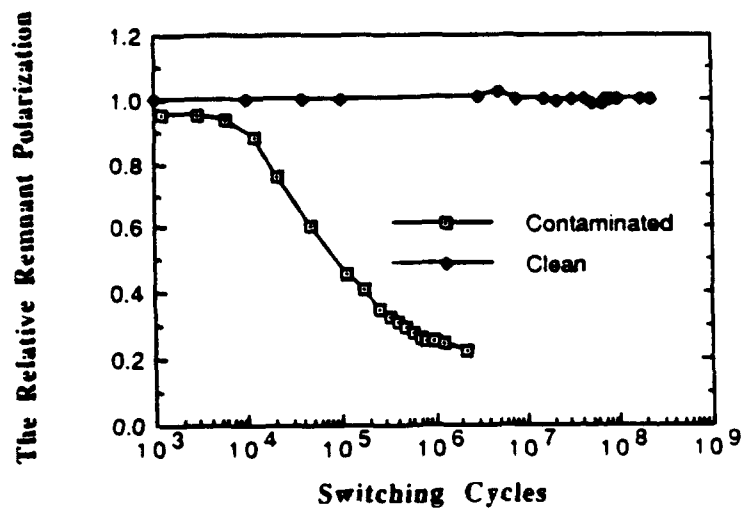
Fig.6   Comparison of the fatigue behavior in a contaminated sample and a clean sample.

3.3 Fatigue Originated from Surface Contamination.

A. Deterioration of the ferroelectric-electrode interface under high AC field.

In fatigue experiments the possible sources of contaminants are: abrasive residue from grinding process; residue of solvents(water, alcohol or acetone); water in the air; residue of the bonding glue from cutting process; skin grease from finger touch. Without further cleaning these contaminants are left on the surfaces of specimens, being sandwiched between the sample surface and the electrode, producing a poor interface contact. The effects of solvents and skin grease were further examined in the following experiments. First, the samples were etched by H_3PO_4 acid to remove the abrasive residues and skin grease, then the following surface treatments were given to three different samples:

a)   sample 1 was washed by water and acetone, then rubbed both surfaces by fingers;

b)   sample 2 was washed by water and acetone, then let it dry in the air;

c)   sample 3 was washed by water and acetone, then heat treated in a furnace at 500 °C for 1 hour (free from contamination).

Fig.7 shows the results from fatigue tests on these samples using a 100 Hz sine wave AC field. The remnant polarization of sample 3 did not decrease at all after 10^8 switching cycles, only E_c increased slightly. (In the etched samples E_c shows slight increase at the beginning and then becomes stable). P_r of sample 2 fatigued to 85% of its initial value after 10^8 switching cycles and E_c increased about 18%. Sample 1 was the worst among the three samples, its P_r reduced to 30% of the initial value, and E_c increased 50% after only 2×10^6 cycles. Since the three samples only differ in surface treatments, these discrepancies in fatigue results could only be explained in terms of the different degree of surface contamination. We can now understand why the fatigue rate was faster for the ground sample than samples with the other two type of surfaces as shown in Fig.1, because of the surface roughness, the ground sample was contaminated the most in the conventional preparation process.
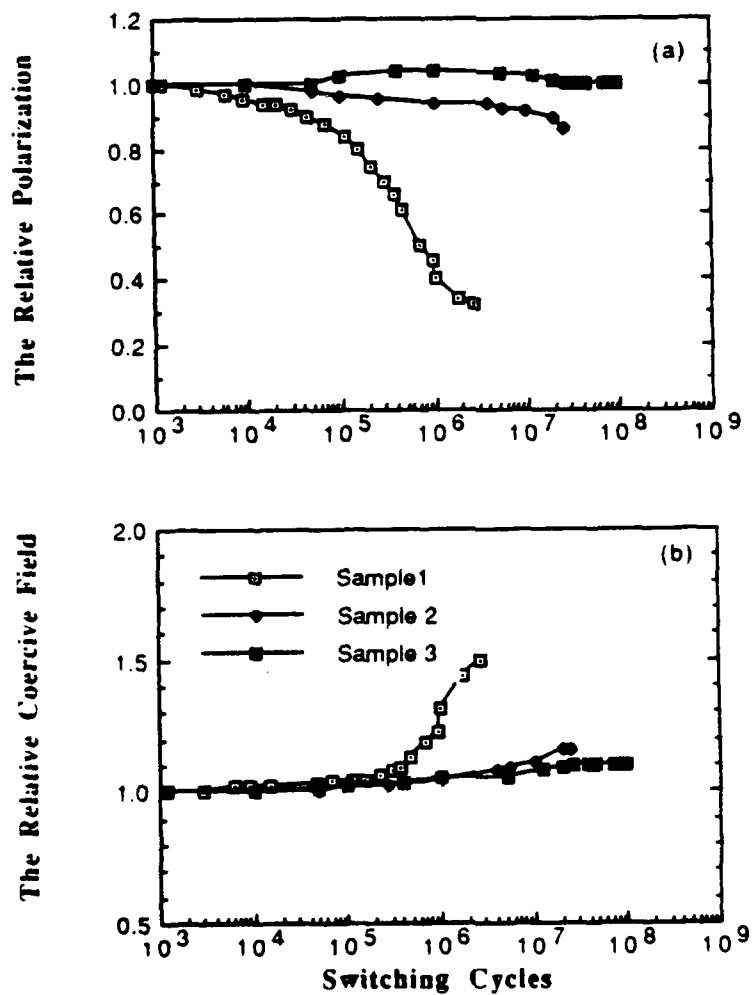
Fig.7 The contamination effects on the fatigue behavior. Sample 1 was contaminated by solvent and skin grease; sample 2 was contaminated by solvent; sample 3 was cleaned by improved procedure.

Although the experiments clearly indicate that the fatigue is initialized at the interface between the surface and electrode, the actual mechanism is still not clear yet because the reactions of organic contaminants under high AC field at the interface are very complicated. A few possible explanations for what might have happened at the interface are:[12][13] 1) electrochemical reaction, such as ionization of contaminants, reduction of the chemical composition near the sample surface; 2) corona, high voltage can ionize water and organics, causing partial discharge which leads to a time related continuous degradation of the dielectric property; 3) contact deterioration effect, residue of solvents and skin grease prohibit a direct contact of the metal electrode with the sample surface, resulting a poor contact. When a poor contact occurs, a large field is applied to the contaminant layer which has much smaller dielectric constant than the sample, causing electrochemical reaction, resulting a partial failure of the contact which then lead to an inhomogeneous field distribution, this field inhomogeneity in turn initiates the microcrackings in the specimen. Among the three factors, the third one may be the most important.

B. The nature of the fatigue by surface contamination.

From previous discussions it is no doubt that the fatigue was initiated at the sample surfaces. Next question we want to ask is whether the fatigue behavior only reflects surface damage or it also indicate interior failure. To answer this question we have measured the bulk dielectric constant as a function of temperature for the fatigued sample at a frequency of 1 kHz, the results are shown in Fig.3 curve (a). The maximum temperature in the measurement was 190 °C which is above the Curie temperature(130 °C for PLZT 7/68/32). Compared with the results measured before fatigue test, curve (e) in Fig.3, we can see a drastic decrease of the dielectric constant especially close to the Curie temperature region. Different heat treatments were applied to this fatigued sample to see if the fatigued sample could be repaired. Curve (b) in Fig.3 is the temperature dependence of the dielectric constant measured after the fatigued sample went through a heat treatment at 300 °C for 3

15

hours, only partial recovery was achieved. The sample then experienced further heat treatment at 600 °C for 1 hour, further improvements were observed as shown in curve (c) of Fig.3, but the dielectric constant still did not recover to its initial value, which means that part of the damage is permanent. In order to investigate the depth of the damage from surface initiated fatigue, the sample was then ground off a 15 μm thick layer from each surface and re-electroded using sputtering technique. The measured results are shown in curve (d) in Fig.3, no further improvement was achieved which indicates that the fatigue damage has propagated to the interior of the sample.

The high field properties, i. e., the remnant polarization P_r and the coercive field E_c, were also measured after each heating, re-electroding, and thinning. The results are listed in Table 1. One can reach the same conclusion as for the weak field dielectric measurements from the results in Table 1. We conclude from this study that the fatigue, although started at the ceramic-electrode interface, has caused permanent damage to the whole body of the sample, thermal treatment can only achieve partial recovery.

Previously, fatigue in ferroelectrics was explained as due to the stabilization of domain walls.[1][5][8] The fatigue caused by domain pinning usually can be recovered by heating the samples to paraelectric phase.[5][8] In our experiments, total recovery did not occur even after the fatigued sample has been heated to as high as 600 °C which is 470 °C higher than the Curie temperature. Therefore, the fatigue we have observed could not be due to the domain wall pinning, instead, we believe that the intergranular microcracking is responsible for the non-recoverable fatigue initiated by surface contamination. Scanning Electron Microscopy was performed on a fatigued sample(Fig.8 a) and non-fatigued sample(Fig.8 b) with ground surfaces. The samples were etched using H_3PO_4 acid to remove gold electrodes. On the micrographs in Fig.8, we can see some of the grinding damages and etch-pits for the non-fatigued sample, while for the fatigued sample we see a lot of grains without grinding damages and etch-pits. This means that a whole layer over these grains was peeled off during etching, which indicates that the bonding between

16
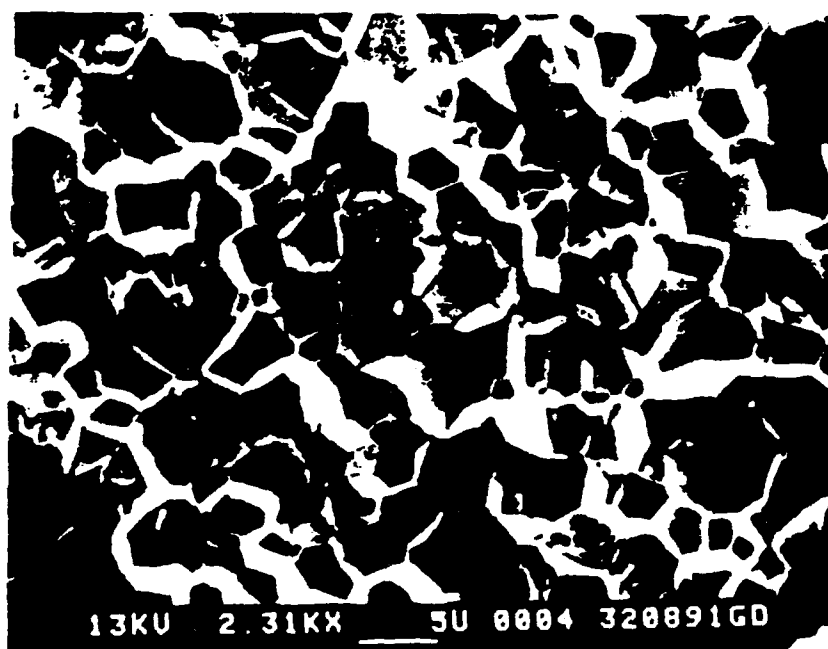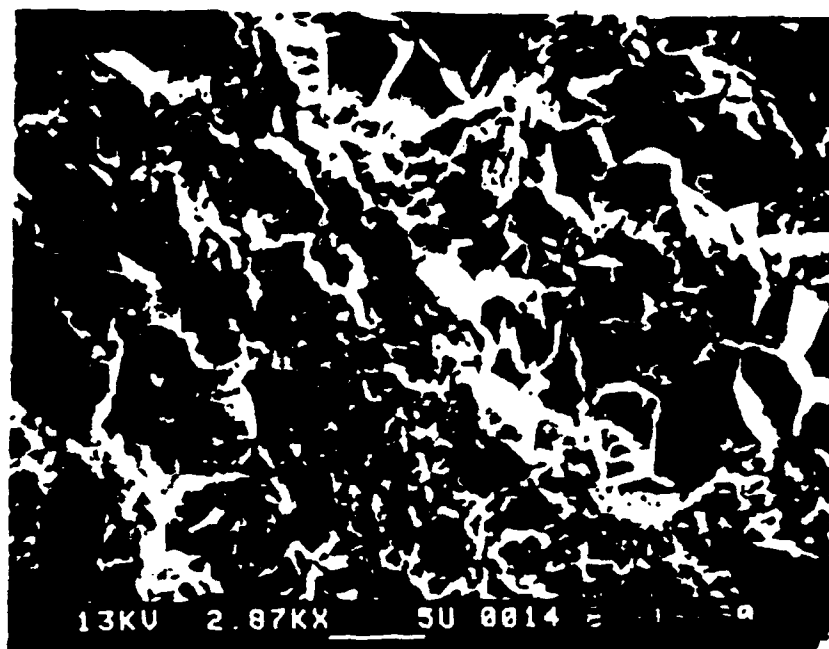
Fig.8   SEM photograph taken from a fatigued sample after about a 1 μm surface layer being removed by etching.

grains was weakened during fatigue test. In addition, some cracks around grain boundaries are clearly visible in Fig.8 (a), but no large cracks were observed either on the surfaces or on the cross section of the fatigued sample.

Poor contact between ceramic and electrode can cause non-uniform field distribution as shown in Fig.9. The highest field concentration occur at the edges of the contaminates as indicated by the letters A, B, and C on the figure. Chemical reactions will happen in the contaminates under high field, which will destroy the intimate contact between the electrode and the ceramic, causing the effective applied field strength in the underneath ceramic to become smaller. One can refer to the schematic drawing of the field flux lines in the figure to understand the physical picture. Because ferroelectrics are both piezoelectric and electrostrictive, large strain is generated during switching. In PLZT ceramics the field induced strain can be as large as 0.1% or more.[14] When the deterioration of the interface occurred during fatigue experiment the regions under good contact with the electrode were under larger field, while the regions under deteriorated interface effectively experience much smaller field, hence these two regions can not be switched simultaneously, which generate stress concentrations at the boundaries between the switched regions and the non-switched regions. As we know that the grain boundaries have weaker mechanical strength than that of the grains, intergranular microcracking could be produced by these stress concentrations, which initiates the fatigue behavior. Optical micrograph of a fatigued sample shows that this is indeed the situation (see Fig.10). The micrograph was taken from a fatigued sample after the electrodes being carefully removed, we found that some of the regions were changed from transparent to opaque, but some regions remain to be transparent. The darkness represents the degree of damages in the sample, in general, the worse is the fatigue the less are the transparent regions. Using this microcracking mechanism one can explain reasonably well the results in Table 1.

Based on the discussions above, we suggest that the fatigue initiated by surface contamination in hot pressed PLZT 7/68/32 ceramics is though microcracking at the

Table I Comparison of the remnant polarization and the coercive field for a PLZT 7/68/32 sample before and after fatigue, and after heating, re-electroding and thinning treatments.

	Remnant Polarization $(\mu c/cm^2)$	Coercive Field (kv/cm)
Before fatigue	27.0	5.0
After fatigue	6.0	6.8
After 190 ºC heating	11.5	8.0
After 300ºC heating	19.2	10.4
After 600 ºC heating	22.4	7.3
After removal of 15μm from each side	22.5	7.2
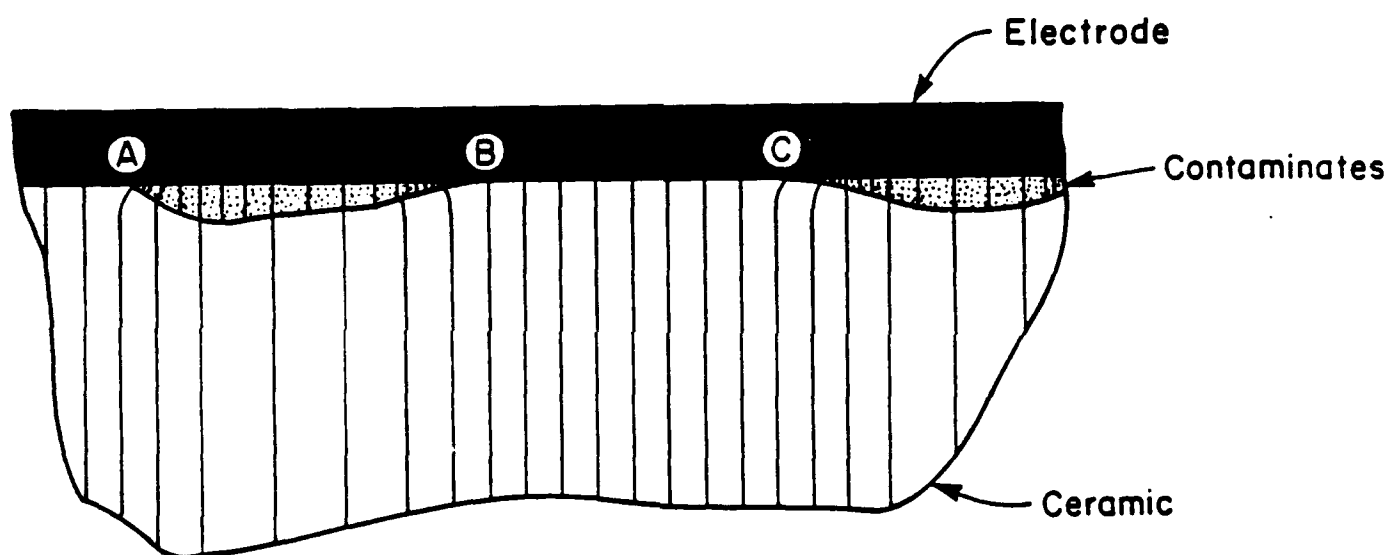
Fig.9   Schematic plot of the inhomogeneous electric field concentrations at the ceramic-electrode interface in a contaminated sample.
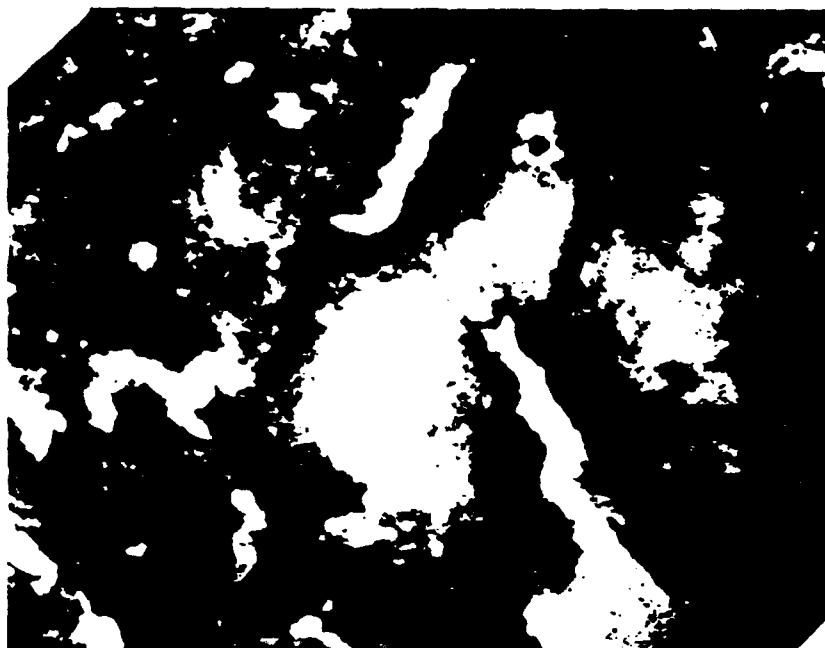
Fig.10 Optical micogragh taken from a fatigued sample. The darkness indicates the degree

of mechanical damage or stress concetrations. The transparant regions are non-

fatigued portions still left in the sample.

boundaries of the switched and non-switched regions near the ceramic-electrode interface, which extends quickly into the interior of the ceramic.

IV. SUMMARY AND CONCLUSIONS

A systematic study has been carried out on the influence of surface conditions on the fatigue behavior of hot pressed PLZT 7/68/32 ceramics with grain size less than 5μm. It is found that the observed fatigue which occurred within 10^5 switching cycles is actually caused by surface contamination. These surface contaminates cause deterioration of the contact between ferroelectric and electrode, resulting an inhomogeneous field distribution in the specimen inducing microcrackings at the grain boundaries. The applied field then will be concentrated across those cracks parallel to the electrode, which effectively raise the coercive field and lower the polarization. The conventional cleaning method is proved to be not appropriate for specimens used under high AC field. This surface contamination initiated fatigue can be eliminated though an improved surface cleaning procedure, our results show that the ferroelectric properties of PLZT 7/68/32, such as the polarization and the coercive field, can be preserved for more than 10^8 switching cycles if the surfaces are cleaned properly, which is a very encourage finding for some potential applications based on the polarization reversals.

Contrary to some reported results.[5][8] we found that the fatigue damages are permanent and are throughout the entire sample. The fatigued properties i.e., the reduction of the polarization and the dielectric constant, and the increase of the coercive field can be partially recovered though thermal treatment, however, a complete recovery is not possible.

At last we like to point out that the results obtained here are applicable only for small grain ceramics, the fatigue mechanism in large grain systems is completely different.[15]

22

ACKNOWLEDGEMENT

REFERENCES

1. Malcolm McQuarrie, J. Appl. Phys., **24**, 1334 (1953).

2. W. J. Merz and J. R. Anderson, Bell Lab. Record, **33**, 335(1955).

3. J. R. Aderson, G. W. Brady, W. J. Merz and J. P. Remeika, J. Appl. Phys., **26**, 1387 (1955).

4. G. W. Taylor, J. Appl. Phys., **38**, 4697(1967).

5 W. C. Stewart and L. S. Cosentino, Ferroelectrics, **1**, 149(1970).

6. D. B. Fraser and J. R. Maldonado, J. Appl. Phys., **41**, 2172(1970).

7. K. Carl, Ferroelectrics, **9**, 23(1975).

8. Ennio Fatuzzio and W. J. Merz, "Ferroelectricity", North-Holland Publishing Company, INC New York, 1967, pp102-104.

9. Richard Williams, J. Phys. Chem. Solids, **26**, 399(1965).

10. A. Yu. Kudzin and T. V. Panchenko, Sov. Phys. Sol. State, **14**, 1599(1972).

11. W. R. Salaneck, Ferroelectrics, **4**, 97(1972).

12. Carl J. Tautscher, "Contamination Effects on Electronic Products", Marcel Dekker, INC., New York. Basel. Hong Kong, 4-5(1991).

13. K. L. Mittal, "Treatise on Clean Surface Technology" Vol **1**, Plenum Press, New York and London, 182(1987).

14. W. Y. Pan, Q. M. Zhang, Q.Y. Jiang And L. E. Cross, Ferroelectrics, **88**, 1(1988).

APPENDIX   10

Title: Fatigue Effects in High Strain Actuators

Authors: L. Eric Cross
          Qiyue Jiang
          Materials Research Laboratory
          The Pennsylvania State University
          University Park, PA 16802

ABSTRACT

In all ceramic piezoelectric and electrostrictive actuator materials, the basic mechanism coupling electric and elastic properties is electrostriction i.e. the strain x_{ij} is related to the components of the Polarization P_kP_l by the relation:

$$x_{ij} = Q_{klij} \, P_kP_l$$

where the Q_{klij} are electrostriction constants in polarization notation. For the different piezoelectric and electrostrictive ceramics, P_k and P_l may be made up of combinations of spontaneous and induced polarizations and changes of P can also be effected by both domain and by phase changes. In all perovskite structure based systems however the Q_{klij} are 'proper' constants (not morphic) and do not change widely within a given composition family. Thus it is clear that to achieve large shape change (strain) it is essential to be able to induce large changes in polarization.

We have demonstrated in earlier studies (1)(2) that in Lead lanthanum zirconate titanate (PLZT) family of ceramics at compositions which are in the spin glass phase at room temperature, large polarization changes and large strain changes can be induced by a nano to macrodomain phase change driven by electric field.

For PZLTs, the fatigue effects which occur in all high strain systems and limit the number of useful strain cycles driven are particularly accessible to study. In this work we demonstrate:

(i)   That initial fatigue which occurs in the composition 7 : 68 : 32 at $\sim 10^5$ cycles is due to improper electroding procedures.

(ii)   That in hot pressed transparent ceramics of the same compositions with grain size less that 5 μm and no visible pores or micro voids, there is not fatigue for $\sim 10^9$ cycles of strain up to 0.4%.

(iii)   For a similar composition which is not hot pressed and contains a normal ceramic pore distribution (ρ actual/ρ theoretical ~ 97 to 98%) fatigue sets in at $\sim 10^4$ to 10^5 cycles.

(iv)   In large grain samples, a different failure mechanism occurs due to the development of micro-cracks which evolve into macro-cracks rupturing the sample.

Different compositions of PLZT and of Lead Magnesium Niobate : lead titanate solid solution show micro to macrodomain transition down to liquid nitrogen temperature. Evidence for strain and fatigue effects in these materials will also be presented.

(1) INTRODUCTION

To describe the electro-elastic interactions in insulating crystalline dielectric materials it is customary to use the phenomenological equations involving the piezoelectric and electrostrictive deformations induced by electric fields in the form

$$x_{ij} = s_{ijkl}X_{kl} + d_{mij}E_m + g_{mnij}E_mE_n \qquad (1)$$

where
- x_{ij} are components of the induces strain
- X_{ij} components of the applied electric field
- E_mE_n components of the applied electric field
- s_{ijkl} the elastic compliance tensor
- d_{mij} the piezoelectric tensor
- g_{mnij} the electrostriction tensor.

In simple linear dielectrics, alternative forms may be written transposing stress and strain, polarization and field and all constants are related by simple transformations. For the nonlinear ferroelectric related dielectrics which are essential for achieving high strain behaviour the relation between E and P is highly nonlinear, often hysteretic and the "constants" dmij and gmnij are strong functions of both field and temperature. In such materials systems it is simpler to describe the elasto-dielectric behaviour using

$$x_{ij} = s_{ijkl}X_{kl} - b_{mij}P_m - Q_{mnij}P_mP_n \qquad (2)$$

where
- P_m, P_n are components of electric polarization
- b_{mij} the piezoelectric tensor now in polarization notation
- Q_{mnij} the electrostriction tensor again in polarization form.

In both equations (1) and (2) the Einstein summation convention is assumed. For (2) however, the coefficients b and Q are now found to be largely independent to temperature and to have similar values in the same structure families.

For bulk samples, the polarization levels which can be induced by realizable electric fields below dielectric breakdown are such that even in very high permittivity ferroelectric or paraelectric dielectrics the constants b and Q do not permit the induction of strains much above 3 $\cdot 10^{-4}$. In ferroelectric crystals however, spontaneous polarizations occur which are order to magnitude larger and in some cases induce strain $\sim 1.5.10^{-1}$.

In looking for new electro-elastic actuators which can control strains much larger than conventional piezoelectric and electrostrictive ceramics it is then natural to look for materials in which P_s the spontaneous polarization can be controlled.

In earlier studies (1)(2) two different types of phase switching actuators were demonstrated.

- Systems which could be switched by electric field from antiferroelectric (P=0) to strongly ferroelectric (P = Ps) inducing strains up to 0.8%.

- Compositions in the lead lanthanum zirconate titanate (PLZT) family which settle into a spin glass state (P = 0) at the working temperature, but can be switched to a ferroelectric state (P = P_s) which induced strains up to 0.5%.

For all ferroic systems, whether ferroelectric, ferroelastic (shape memory) or ferromagnetic where large strains are switched by inducing or reorienting spontaneous strain, there must be concern as to possible mechanisms which may degrade performance on repeated actuations, problems which may stem from a number of different causes but are often lumped together under the heading of fatigue.

It is the purpose of this paper to summarize work on fatigue mechanisms in high strain phase switching actuators which has been carried on the Materials Research Laboratory at Penn State over the last four years.

(2) STUDIES OF FATIGUE IN PLZT PHASE SWITCHING CERAMICS

Previous studies of high strain actuators have explored compositions in the PLZT system chosen near to the morphotropic phase boundary. In describing the PLZT compositions it has become conventional to use the notation X/Y/Z where Y/Z is the ratio of the mole fraction of zirconia to titania, and x is the model fraction of Lanthanum substituted into the solid solution. Thus for example on 9/65/35 composition has 65% Zirconia to 35% titania with 8 mole% of Lanthanum added. For the compositions explored the maximum switchable strain was over 0.5%. The strain vs field relation is hysteretic, but the strain levels induced are strictly proportional to the square of the inducing polarization. Thus, by current control it is possible to "dial" a specific displacement and the actuator can be left remanent at any chosen strain level. Compositions and dielectric and strain data from the earlier study (2) are listed in Table 1 and the compositions identified on the phase diagram in figure 1.

In any study of the mechanical properties of ceramics at high strain levels, the flaw population which may initiate mechanical failure is critical since the PLZTs can be hot pressed to very near theoretical density and good optical transparency, indicating the complete absence of larger scattering centers with dimensions near to the wavelength of light, they appear to be an ideal vehicle for fatigue studies. With the close correspondence between polarization and induced strain, strain fatigue may be monitored by continuous observation of the polarization levels and only needs to be checked at intervals along the degradation curve.

Initial studies using a 7:68:32 PLZT compositions were however most disappointing (fig. 2) with the material showing severe fatigue after only some 10^4 cycles. A first question which must be answered is whether the fatigue is a surface or a volume phenomenon, does it occur at the electrode:ceramic interface or is it distributed through the volume of the sample. The simple experiment shown in figure 3 answered the question unequivocally for this initial fatigue. For the experiment a square cross section sample rod was cut from the transparent ceramic, polished and cleaned and silver electrodes applied to all surfaces. To separate the major surfaces the edges were beveled leaving two orthogonal electrode pairs (1:2 and 3:4 in fig. 2). With switching field applied between the 1:2 pair polarization was degraded following the curve in figure 3b. The field was then transferred to the 3:4 pair, now clearly if degradation is a volume effect the 3:4 field will be seeing already degraded material, however figure 3c shows that the 3:4 electrodes repeat almost exactly the degradation cycle observed with 1:2, as it they were starting from virgin material. Clearly the observed fatigue is a surface effect. Switching back to the 1:2 electrode pair the sample is still fatigued, however, removing the electrode and re-applying brings the sample back to the unfatigued virgin state.

The strong suspicion is that the problem is at the dielectric: electrode interface. Roughening the surface to promote adhesion, polishing or even chemically etching modified but did not radically improve fatigue (fig. 2). A treatment which did however eliminate fatigue up to more than 10^8 switching cycles is illustrated in figure 4. The sample was cleaned ultrasonically, then etched in hot phosphoric acid, rinsed and dried at 500°C for ~ 1 hour (fig. 4a). Etching with air drying (fig. 4b) improved the sample with respect to conventional surface preparation (fig. 4c), but the high temperature heat treatment was essential to eliminate fatigue (fig. 5).

Table 1

Dielectric, Polarization and Strain Data for a Number of Spin Glass to Ferroelectric Phase Switching Composition in the PLZT Family at Compositions Close to the Morphotropic Phase Boundary.

Comp.	T_m (°C)	K_m	K_{25}	Ec (kv/cm)	Pr (uc/cm²)	$x_t(10^{-3})$	$x_l(10^{-3})$	x_m/x_t
8/67/33	99	12000	5500	2.6	21	0.91	2.5	0.1
8/65/35*	106	11350	4600	3.6	20	0.82	2.3	0.32
8/63/37	114	11300	4500	4.7	21	0.76	1.9	0.32
7/65/35	140	15000	3000	4.5	28.4	1	3.1	0.7
7/62.5/37.5*	160	16000	2900	5	27.2	1.2	3.7	0.64
7/60/40	172	17000	3000	6.3	26.2	1.2	3.8	0.4
7/58/42	180	17300	2600	8	22	1.1	3.2	0.39
7/56/44	190	17200	2200	10	22	0.94	2.3	0.4
6/62/38	196	19000	2100	5	31	1.45	4.1	0.58
6/60/40*	204	18000	2000	5.6	29.5	1.35	4.7	0.57
6/58/42				7.45	29	1.32	3.9	0.53
5/60/40	230	19000	1600	6.52	32	0.79	4.2	0.53
5/58.5/41.5*				6.41	34	1.24	4.5	0.59
5/56/44				8.5	32.1	1.6	5.4	0.56
4/57/43*				7.47	35.2	1.26	3.0	0.6
4/55/45				10	29.5	1.21	2.9	0.55

* MPB compositions: x_t: Transverse strain induced at 15 kv/cm. x_l: Longitudinal strain induced at 15 kv/cm. x_m: Transverse remanent strain. T_m: Temp. of dielectric maximum. K_m: Maximum dielectric constant. K_{25}: Dielectric constant at 25°C.
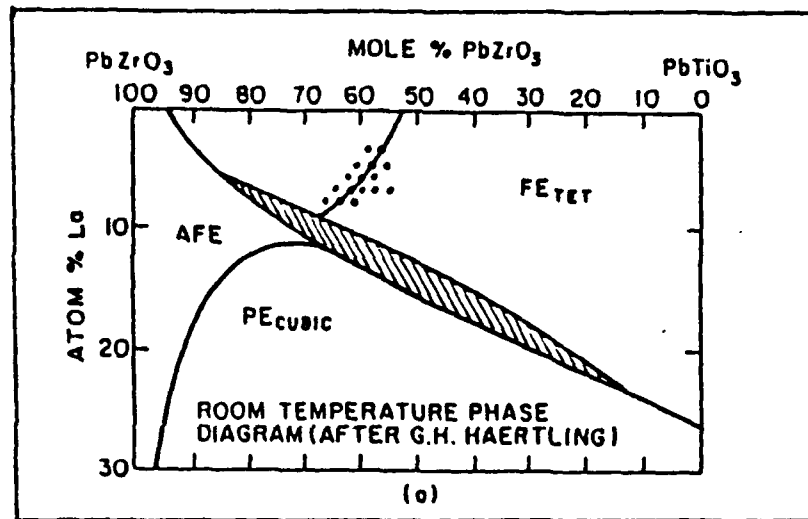
Fig. 1 Identification on the PLZT composition phase diagram of the compositions with properties summarized in Table 1. Dots on the diagram indicate the compositions studied.
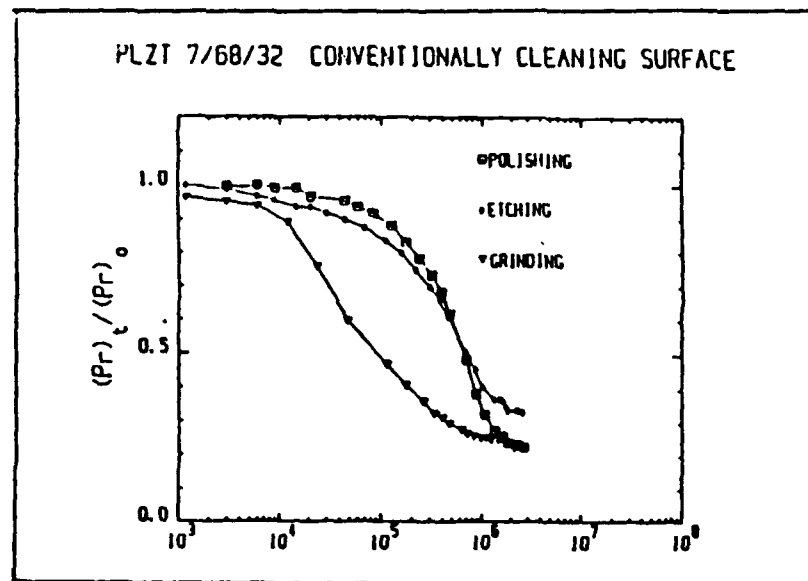
Fig. 2 Early fatigue data for a hot pressed transparent 7/68/32 PLZT composition using sputtered gold electrodes deposited upon polished, etched or ground surfaces after conventional cleaning with organic solvents and distilled water.

That the degradation effect is associated with a surface impedance is suggested by weak field dielectric studies. Using an 8.4/65/35 composition which has a very high dielectric permittivity near 90°C Qiyue Jiang has shown that on thinning a conventionally prepared sample the effective peak permittivity appears to decrease figure 6: just the effect to be expected if there is a capacitive series impedance. If however the electrode is applied immediately after appropriate heat treatment, there is no change in apparent peak permittivity down to less than half the thickness of the conventionally prepared sample (fig. 7).

A most important question concerns the possible role of the high perfection of the hot pressed transparent ceramic. To test the importance an almost identical 7/65/35 composition was prepared by conventional sintering ~97-98% theoretical density, yielding the normal opaque ceramic body. Switching studies compared to the hot pressed body now show degradation begins at $10^4 \sim 10^5$ cycles and is severe by 10^9 cycles (fig. 8) even though identical electroding procedures were used. Studies have shown that this degradation is a volume phenomenon and cannot be restored by reelectroding.

For the hot pressed theoretically dense samples it may be asked whether the ceramic grain size is important in fatigue. The 7:68:32 composition used for the data in figure 4 had a grain size of order 3 μmeters. Heat treating the sample it was possible to grow the grains to ~30 μmeter. Again it appears that severe fatigue is induced by 10^5 ~10^6 cycles of field (fig. 9).

That the fatigue behaviour is a complex overlay of several competing mechanisms is evident from studies using 8.4:65:35 compositions. Frequently with this composition, even though the induced strain at saturation is less than in the 7:68:32 composition, the ceramic often failed catastrophically by cracking after only some 10^7 ~10^8 cycles (fig. 10).

(3) LOW TEMPERATURE STUDIES

An interesting potential application for the hysteretic high strain actuator is in precise position control for large space based telescope mirrors. For a completely active system, the power requirements for many banks of position control actuators could be prohibitive. In the phase switching actuator, if the composition is properly designed polarization switching can be very fast, so that banks of actuators could be serviced by a single power supply which would only be required to update the actuator against aging and system drift. For such systems however it would clearly be necessary for the actuator to be in initimate contact with the mirror, whose surface would probably be at space ambient temperature ~100°K, i.e. - 173°C. Thus it is important to know how polarization controlled high strain actuators would behave at low temperature.

In the spin-glass type switching systems it is important to explore the freezing temperature as a function of composition. From such studies which will be reported elsewhere it was clear that the 9.5/65/35 PLZT and pure lead magnesium niobate (PMN) would be adequately square hysteretic. For the PLZT, polarization and strain curves taken at -132°C are shown in figure 11. Clearly strains up to ~2·5.10^{-3} can be retained remanently in this temperature. Pure PMN at -140°C (fig. 12) has a rather less square hysteresis loop and the strain level is now less then 2.10^{-3}.

In both the PLZT composition (fig. 13) and the PMN (fig. 14) full switching up to 10^7 cycles only leads to very small fatigue. If the actuator were used in a static deflection situation and only updating pulses were applied we believe this level of fatigue would be acceptable for practical situation. Clearly if the actuator has to be continuously exercised across the full strain range further improvement will be necessary.
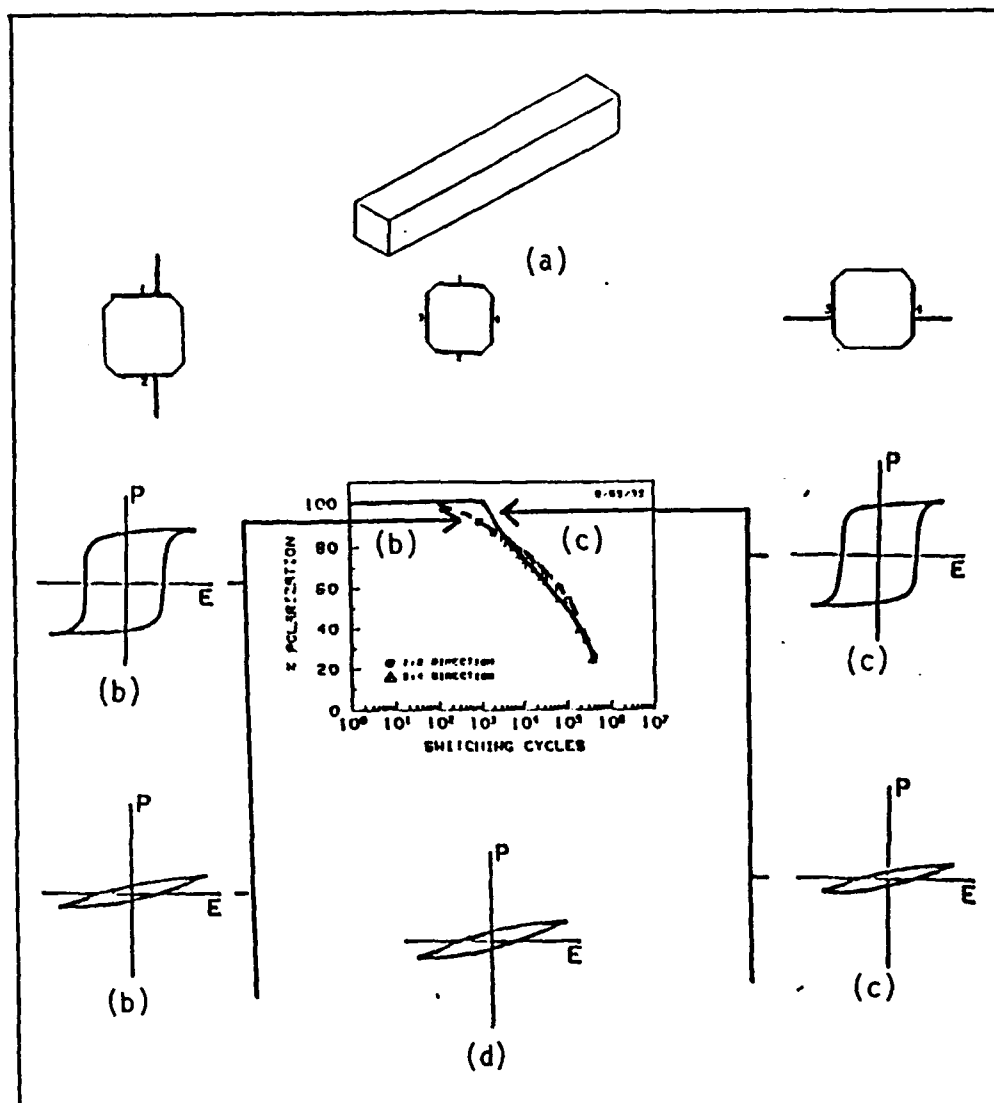
Fig. 3   Experimental configuration used to demonstrate that early fatigue is a surface not a volume related problem.

(a)   Square cross section sample of 8.4/65/35 PZT electroded on the major surfaces, but with the edges beveled to separate 1:2 and 3:4 electrode pairs.

(b)   Modification of the dielectric hysteresis and polarization degradation for fields in the 1:2 direction.

(c)   Modification of hysteresis and polarization with field cycling for fields in the 3:4 direction. Note that for 3:4 degradation again starts as if for a virgin sample.

(d)   Returning field to either 1:2 or 3:4 electrode pairs after fatigue the sample remains in the fatigued state.
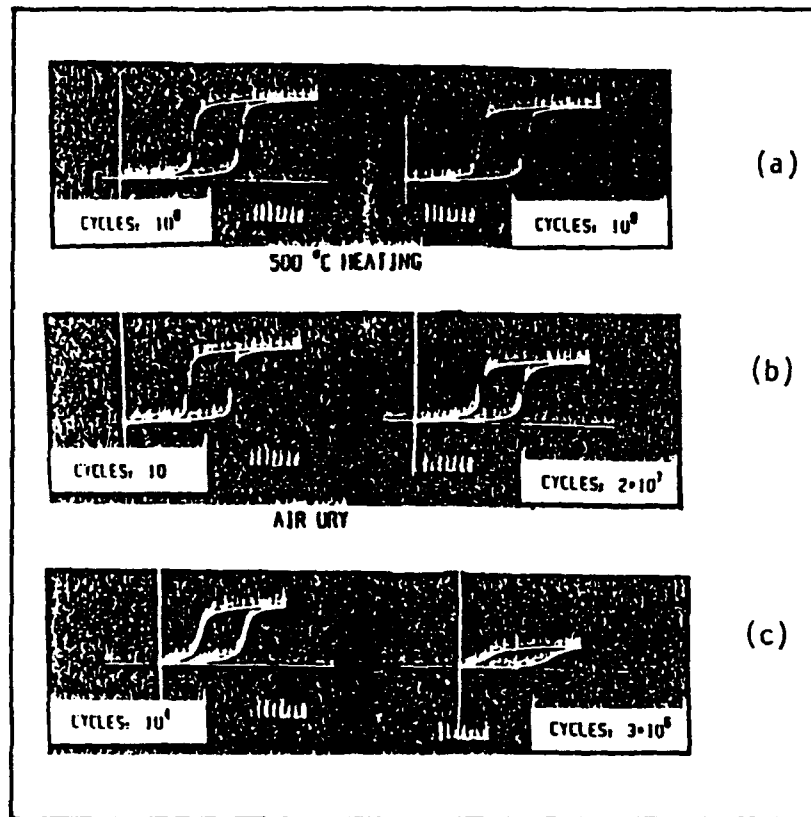
Fig. 4   Hysteresis behaviour showing the effects of different surface treatments on a hot pressed transparent 7:68:32 PLZT before sputter deposition of gold electrodes.

(a)   For maximum resistance to fatigue the treatment involves etching in hot phosphoric acid, rinsing in distilled water then heat treating to 500°C for one hour immediately before electrode deposition.

(b)   Fatigue evident at 2.10^7 cycles after phosphoric acid etch, rinsing and drying without heat treatment.

(c)   Severe fatigue associated with electrodes applied to conventionally prepared PLZT surfaces.
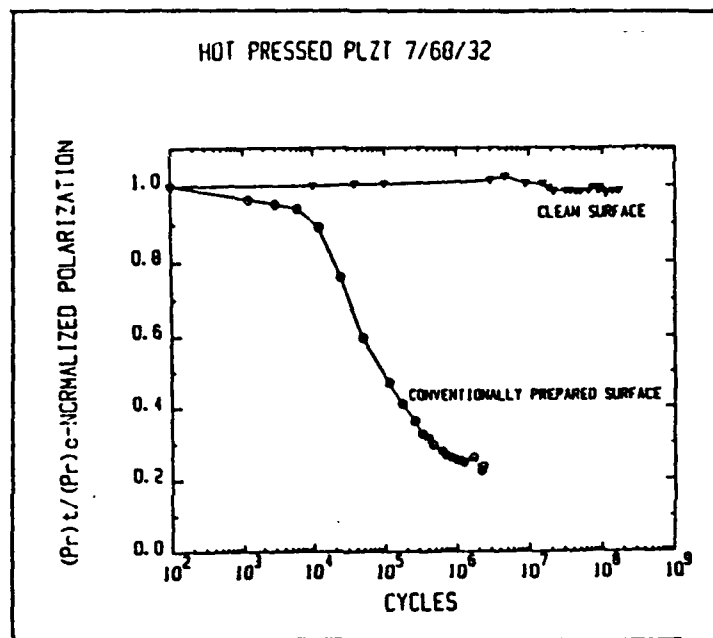
Fig. 5 Comparison of fatigue life for a PLZT 7:68:32 composition with etched and heat treated surfaces and with conventionally prepared surfaces.
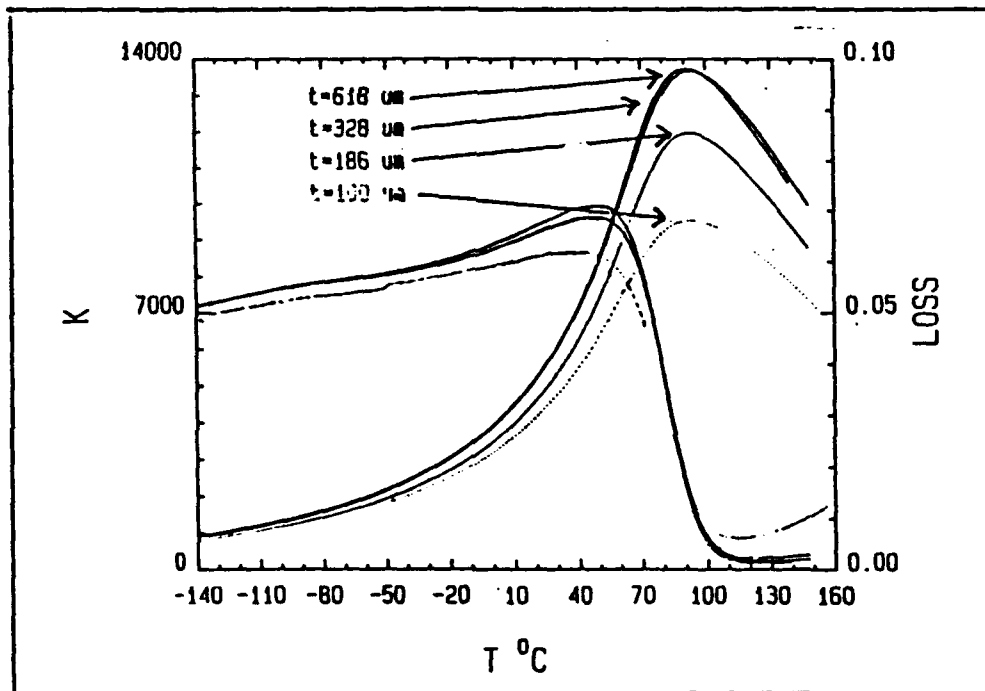
Fig. 6 Weak field dielectric permittivity as a function of temperature in 8 -4/65/35 PLZT with polished and conventionally cleaned surfaces as a function of sample thickness. Note that at 100 μm thickness there is severe degradation of the apparent peak permittivity due to series capacitive impedance.
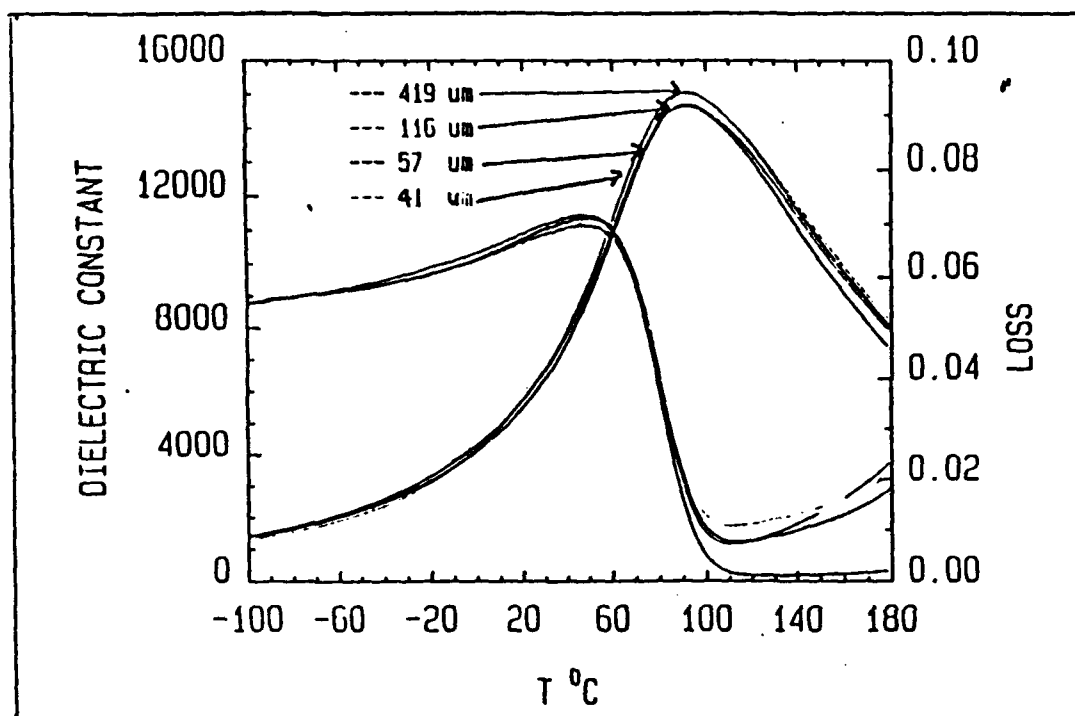
Fig. 7   Weak field permittivity of a similar 8·4:65:35 PLZT composition with
         etched heat treated surfaces. Note that there is no evidence of a series
         impedance at the surface for samples down to 41 μm thick.
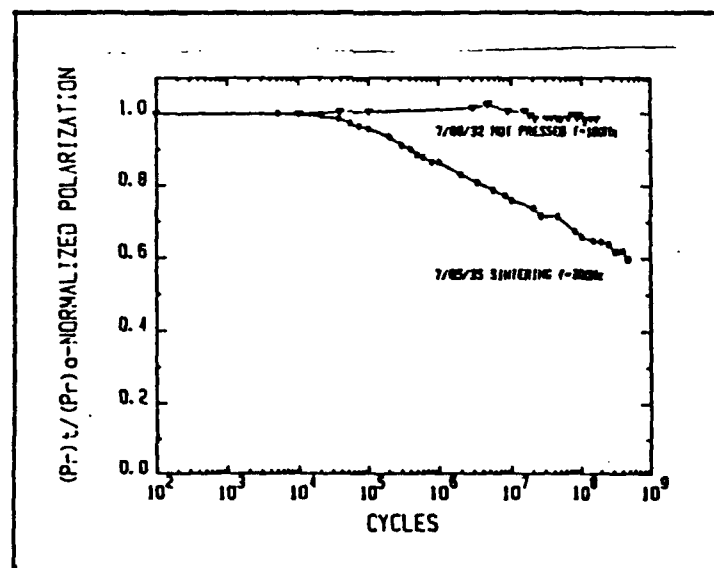
Fig. 8   Comparison of the fatigue behaviour between hot pressed theoretically
         dense 7:68:32 and a conventionally sintered 7/65/35 composition Curves
         were taken using the same electrode treatments. Damage in the 7/65/35
         compositions could not be rejuvenated by re-electroding and appeared a
         volume phenomenon.
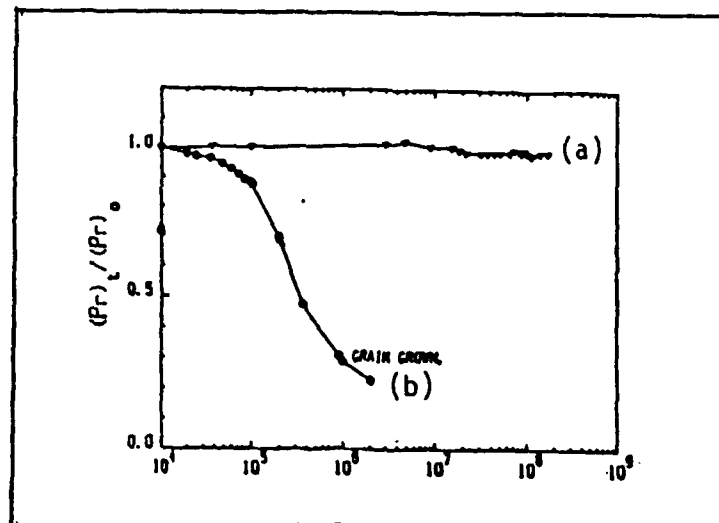
Fig. 9   Effects of ceramic grain size on fatigue (a) 7/68/32 PZT with grain size ~3
μmeters; (b) 7/68/32 PZT grain grown to size ~30 μmeters.
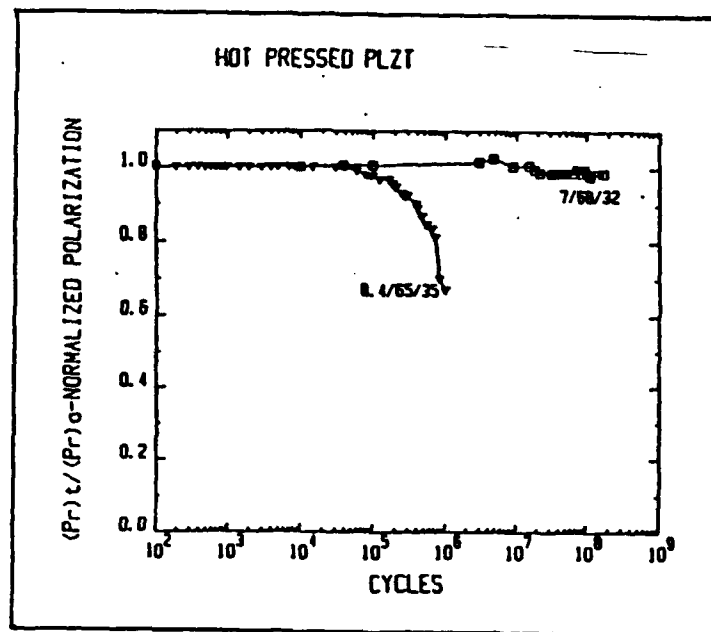
Fig. 10   Fatigue in a 7/68/32 composition as compared to that in an 8-4/65/35
composition. Note that the 804/65/35 undergoes lower strain excursions
than the 7/68/32 composition, but thouth it has similar grain size and the
same electrode treatment it fails catastrophically by cracking after only
10^6 cycles.

(4) SUMMARY AND CONCLUSIONS

For high strain phase switching actuators based upon spin glass like compositions in the PLZT family it has been shown that the fatigue effects which limit the number of useful strain switching cycles involve a number of phenomena

For hot pressed theoretically dense optically transparent ceramics, the electrode structure has been shown to be critical if premature fatigue is to be avoided. For sputtered gold electrodes, etching in phosphoric acid followed by a high temperature heat treatment immediately before electrode application was shown to yield fatigue free performance up to 10^9 cycles. Conventional ceramics of ~97-98% theoretical density made by conventional sintering could not be made fatigue free. The grain size and the composition of the ceramic were also shown to play a major role in determining the lifetime. In general finer grain ceramics as expected had longer fatigue lifetimes, however composition is a more sophisticated variable and failure does not appear to be directly keyed to strain performance.

Initial low temperature studies have shown that hysteretic (dial-a-displacement) actuators can be developed to work at temperatures ~-140°C. Fatigue at 10^7 cycles is quite small and for simple updating to maintain a near constant static displacement present materials will be quite adequate.

In many high strain applications it will be necessary to use multilayer systems with cofired electrodes so as to achieve adequate displacements at low terminal voltages. It will be important to repeat these types of fatigue studies for system with cofired internal electrodes.
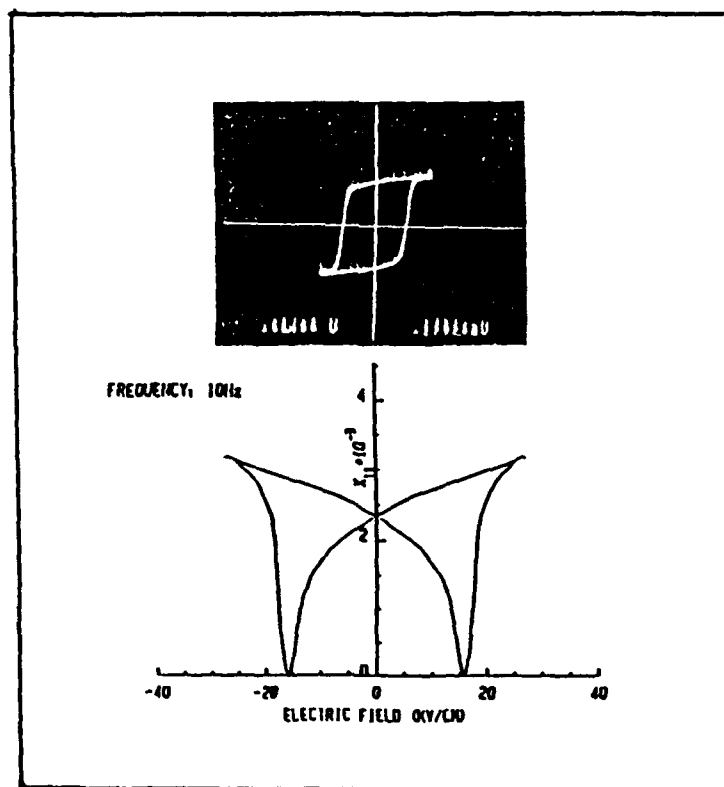
Fig. 11   Low temperature polarization and strain cycles in a 9·5/65/35 PLZT. Frequency 10 Hz, Temperature -132°C, Cycling field 30 KV/cm.
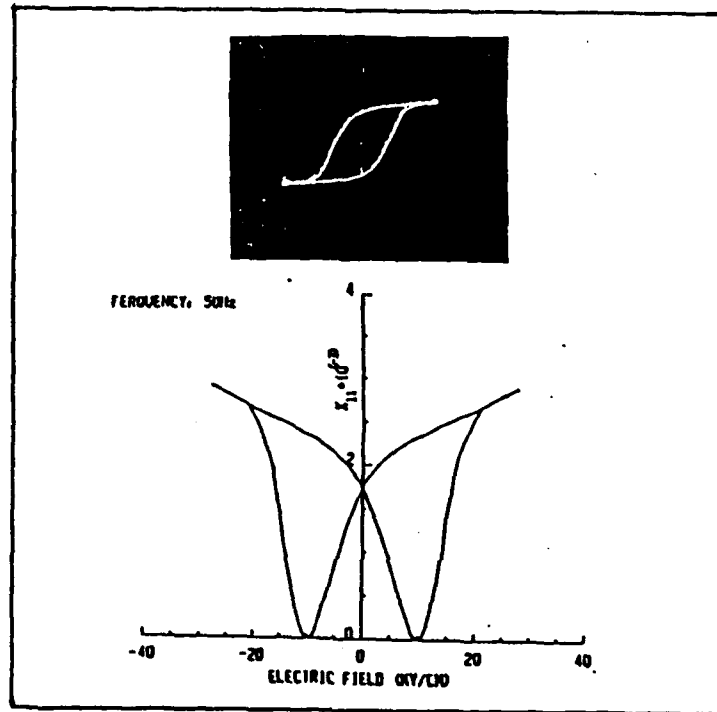
Fig. 12   Low temperature polarization and strain curves in pure Lead magnesium niobate (PMN).

10² CYCLES   10⁷ CYCLES
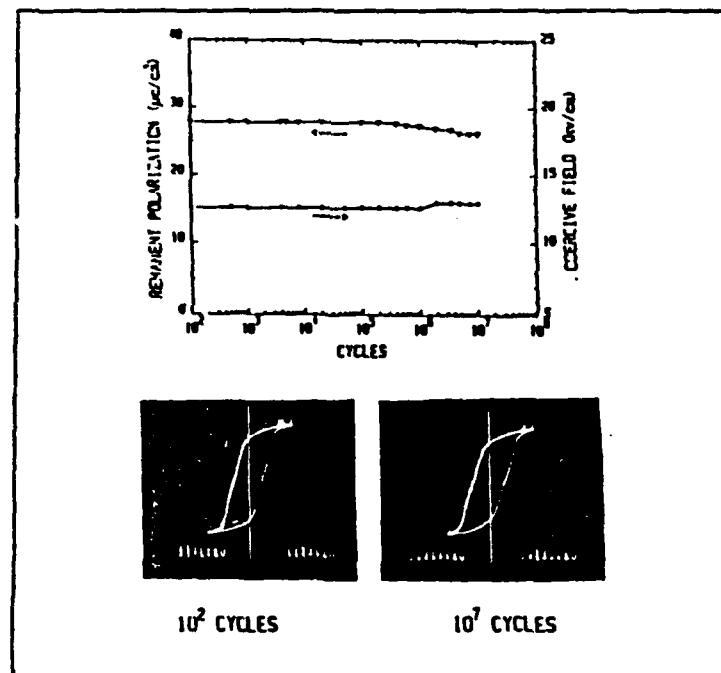
Fig. 13   Fatigue in the 9·5/65/35 PLZT under high field cycling under a frequency of 160 Hz at -140°C.
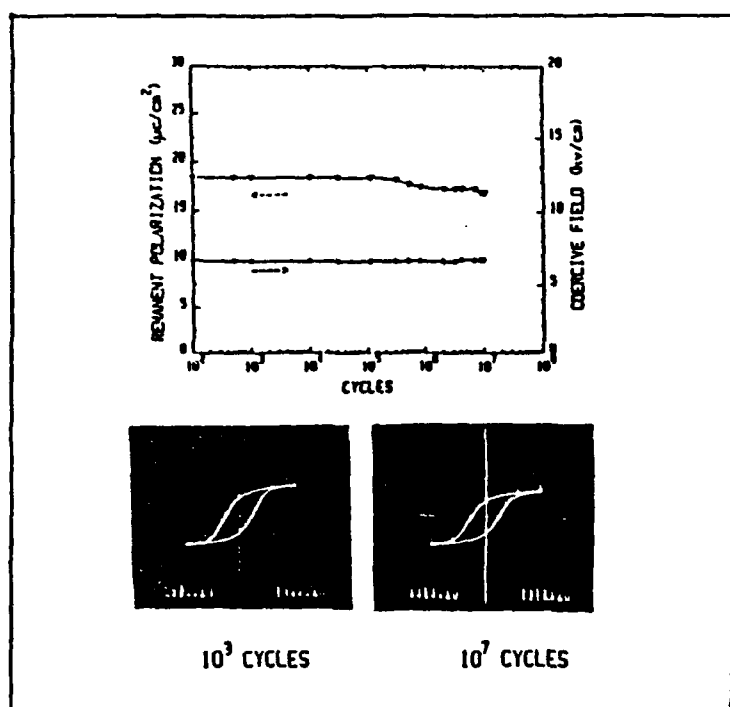
Fig. 14   Fatigue in pure PMN under high cyclic field of 100 Hz applied at -140°C.

REFERENCES

1. W. Y. Pan, C. Q. Dam, Q. M. Zhang and L. E. Cross. "Large Displacement Transducers based on Electric Field Forced Phase Transitions in the Tetragonal $(Pb_{0.97} La_{0.02})(Ti, Zr, Sn)O_3$ Family of Ceramics." J. Appl. Phys. **66** (12), 6014-6023 (1989).

2. L. E. Cross. "Polarization Controlled High Strain Actuators." First Joint US:Japan Conference on Adaptive Structures. Editors B. K. Wada, J. L. Fanson, K. Miura, Technomic Publishing, Lancaster (1991), p. 807.

APPENDIX 11

ACOUSTIC EMISSION IN FERROELECTRIC LEAD TITANATE CERAMICS: ORIGIN AND RECOMBINATION OF MICROCRACKS

V. SRIKANTH and E. C. SUBBARAO†

Materials Research Laboratory, The Pennsylvania State University, University Park, PA 16802, U.S.A.

Abstract—Lead titanate doped with niobium forms solid solutions of the type $Pb_{1-x/2}(Ti_{1-x}Nb_x)O_3$ where $x = 0.02$ and 0.05. The ferroelectric Curie temperature of these solid solutions is around 465°C, compared to 490°C for $PbTiO_3$, at the cubic-tetragonal phase change. The lattice distortions at and below the Curie temperature generate internal stresses, leading to microcracking. The microcracking in lead titanate ceramics is detected by acoustic emission methods as a function of heating to and cooling from various temperatures upto 800°C. From this study it is concluded that microcracking is primarily triggered by the sudden lattice parameter changes at the Curie temperature on cooling and that it is enhanced by the anisotropic thermal expansion below the transition. The healing of microcracks is a gradual process and escapes direct detection by the acoustic emission methods. An indication of the recombination of microcracks on heating has been obtained by the total number of acoustic emission counts in samples cooled from various temperatures and also from fixed temperatures after different periods.

1. INTRODUCTION

Single phase ceramic materials may exhibit micro-cracking on cooling from high temperatures either due to anisotropic axial thermal expansion (if they have non-cubic crystal structure) [1, 2] or due to phase transitions. A material with anisotropic thermal expansion behavior undergoes contraction (or expansion) by varying extents in different crystallographic directions during cooling, setting up internal stresses, which may lead to intergranular or transgranular ruptures if the internal stresses exceed the fracture stress of the material. Aluminum titanate, which possesses anisotropic axial thermal expansion, was the first ceramic material in which an unusual linear thermal expansion behavior is reported [3]. On heating a sintered ceramic aluminum titanate, it contracts upto a certain temperature and then expands. On cooling from the peak measuring temperature, it contracts, as expected, down to a certain temperature when it begins to expand on further cooling, thus exhibiting a hysteresis in its thermal expansion behavior. Buessem [4, 5] was the first to explain these experimental facts by invoking micro-cracking on cooling and healing on heating. On cooling a sample from a high temperature, it contracts normally until the microcracking becomes severe enough to cause overall expansion masking the normal contraction. On heating such an aluminum titanate ceramic from room temperature, the pre-existing microcracks heal (or recombine) causing an

apparent contraction masking the true expansion. When the shrinkage of the sample due to healing of microcracks becomes less than the normal expansion, a net overall expansion is measured on further heating. While this is a plausible explanation and has since been invoked to account for similar behavior in other materials, not much direct (microscopic or other) evidence has so far been available for intergranular or transgranular fractures on cooling as well as healing of microcracks on heating, in such materials. However, many single phase anisotropic ceramics have been shown to exhibit similar linear thermal expansion as aluminum titanate and these include magnesium dititanate [6, 7], pseudobrookites [8], niobium pentoxide [9], titania [10], alumina [11], sodium zirconium phosphate family [12], among others, many of which possess low (or near zero) overall thermal expansion over a certain temperature range.

Though healing or recombination of pre-existing microcracks has been postulated to explain the thermal expansion behavior on heating and the thermal shock characteristics of non-cubic single phase ceramics [4, 6, 13–17], not much direct evidence for the same has so far been obtained.

Acoustic emissions are transient elastic waves arising from the rapid release of energy within a material due to any microdeformation process such as micro-cracking, crystallographic phase transition etc. These can be detected by piezoelectric transducers mounted on the sample while it is heated and cooled over the desired temperature range.

Acoustic emission is a convenient tool to study microcracking in ceramics [18–21] and has already been used in the case of aluminum titanate [22, 23].

---

†Permanent address: Tata Research Development and Design Center. 1 Mangaldas Road. Pune 411001, India.

sodium zirconium phosphates [24], and niobia [25] to detect microcracking due to anisotropic thermal expansion during cooling.

It has been known that as the grain size decreases in polycrystalline non-cubic ceramics, strength increases sharply, and this behavior is associated with the suppression of microcracking at small grain sizes. The average grain size corresponding to microcracking is called the critical grain size, G_{cr}. The initial explanation of a critical grain size from microcracking was put forward by Clarke [26] and extended by others [7, 8, 10, 27-33]. In the theoretical models, the equation for the critical grain size usually takes the form

$$G_{cr} = \frac{k \cdot f}{E(\Delta T \cdot \Delta \alpha_{max})^2} \qquad (1)$$

where k is a function of the grain geometry, f is the fracture surface energy, E is the Young's modulus, ΔT is the temperature change and $\Delta \alpha_{max}$ is the maximum difference in the axial thermal expansion coefficients. This implies that microcracking in a ceramic may not occur for grain sizes less than G_{cr}.

From the above, it is seen that microcracking due to anisotropic thermal expansion of non-cubic polycrystalline materials has been quite extensively investigated. On the other hand, microcracking in ceramics due to phase transitions is studied only in the case of some ferroelectrics [27] and more recently in superconducting $YBa_2Cu_3O_{7-x}$ [34]. Ferroelectrics undergo a phase transition (e.g. cubic-tetragonal) at the Curie temperature. In the case of lead titanate, $PbTiO_3$, the variation of lattice parameters, tetragonal distortion (c/a), unit cell volume and linear dimensional change of a ceramic are plotted in Fig. 1 as a function of temperature through the phase change at the Curie point, 490°C [35, 36]. At room temperature, $a = 0.3894$ nm and $c/a = 1.063$ for $PbTiO_3$.

The large tetragonal distortion and the volatility of PbO at the sintering temperature makes it difficult to produce dense sintered polycrystalline $PbTiO_3$. However, introduction of 2-5% Nb enables the production of dense, strong lead titanate ceramics [37]. A number of other additions have also been tried [38-40]. Matsuo and Sasaki [40] found that some additions resulted in average grain size in the range of 0.8-1.5 μm whereas others gave average grain sizes of 10-80 μm. They established that the poor mechanical strength of lead titanate ceramics is due to the intergranular cracking arising from grain boundary stresses set up by the anisotropic thermal expansion coefficients along the a and c directions of the tetragonal phase i.e. below the Curie temperature in ceramics with grain size > 1-3 μm, with complete crumbling when grain size ≈ 10 μm. Mechanically strong lead titanate ceramics are interesting because of its high Curie temperature and first order ferroelectric transition.

In the present work, microcracking in Nb-doped $PbTiO_3$ ceramics is studied during heating and cooling through the phase transition via the acoustic emission method. An effort is made to delineate the
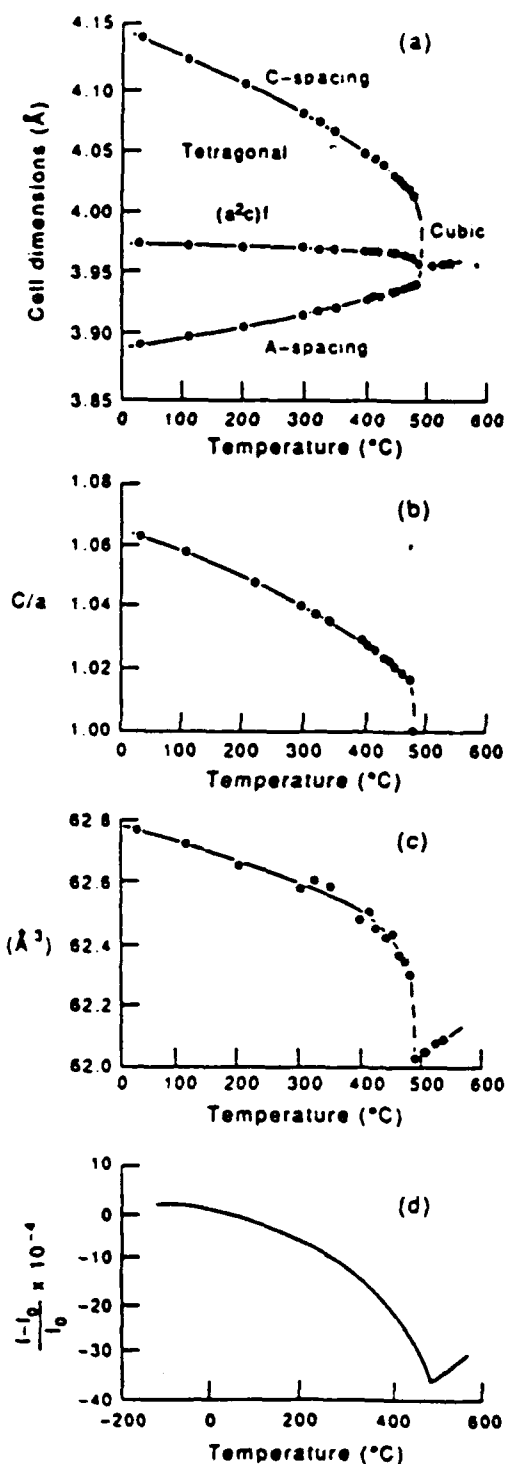
Fig. 1. Variation of (a) lattice parameters, (b) tetragonal distortion (c/a), (c) unit cell volume and (d) linear dimensional change ($\Delta l/l$) of a ceramic as a function of temperature for $PbTiO_3$ (Ref. [35]).

role of the phase transition and the gradual lattice parameter changes with temperature below the phase change, on the microcracking. Evidence for recombination of microcracks on heating is also sought.

2. EXPERIMENTAL

2.1 Specimen preparation

Compositions of $Pb_{1-1.2}(Ti_{1-x}Nb_x)O_3$ with $x = 0.02$ and 0.05 were prepared from reagent grade PbO, TiO_2 and Nb_2O_5. The oxide powders were mixed in a ball mill for 24 h using poly-ethylene jar, calcined at 1100°C for one hour. The calcined powders were ground and pressed into circular disks of 1" dia. and 0.2" thick. The disks were sintered at 1180°C for 15 min in a covered platinum crucible.

2.2. Characterization

The density was obtained from weight and dimensions. The phase identification and lattice parameters (from 200 and 002 reflections) was determined by X-ray diffraction using Cu K_t radiation. The micro-structure was observed from the scanning electron micrographs (TSI-60) of fractured surfaces of sintered samples. The linear thermal expansion of ceramic rods ($0.5 \times 0.5 \times 2$ cm) was measured using a Harrop dilatometer during heating to 600–800°C and cooling to about 100°C, using heating and cooling rates of about 4°C/min.

2.3. Acoustic emission

The Nb-doped $PbTiO_3$ ceramic rod. about $3 \times 5 \times 20$ cm, is attached with a high temperature cement to a 30 cm long alumina rod. which served as a waveguide. The other end of the alumina rod is joined to a transducer using a water soluble ultra-sonic couplant. The sample is placed inside a tube furnace and a chromel-alumel thermocouple posi-tioned near the sample monitors the temperature. The furnace temperature was raised at the rate of 10°C/min up to the range of 425–800°C. The maxi-mum temperature was maintained for 15 min (except in one experiment where the sample was held at 600 and 800°C for periods of 10, 100 and 1000 min), before cooling at the rate of 5°C/min. Below 300°C. the power to the furnace was turned off and a natural cooling rate applies. The transducer employed has a center frequency of 500 kHz (in a range of 300–700 kHz). The electrical signal output from the transducer is amplified. filtered and processed through a train of instrumentation. consisting of an amplifier discriminator. totalizer and rate meter mod-ules, to obtain "total AE counts" and "count rate (counts/5°C)" data. The discriminator triggers a pulse whenever the amplifier output exceeds a certain adjustable threshold. The details of the system here are described earlier [24, 34].

3. RESULTS AND DISCUSSION

3.1. Samples

The density of $Pb_{1-1.2}(Ti_{1-x}Nb_x)O_3$ ceramics is 6.66 g/cc for $x = 0.02$ and 7.30 g/cc for $x = 0.05$. representing 84% and 92% of theoretical density, respectively, which are comparable to those of Ref. [37]. The X-ray diffraction pattern of $Pb_{0.97}Ti_{0.98}Nb_{0.02}O_3$ is single phase tetragonal with $a = 0.3886$, $c = 0.4118$ nm and $c/a = 1.059$, which is slightly smaller than that of $PbTiO_3$ ($c/a = 1.063$). The $Pb_{0.975}Ti_{0.95}Nb_{0.05}O_3$ sample was mostly
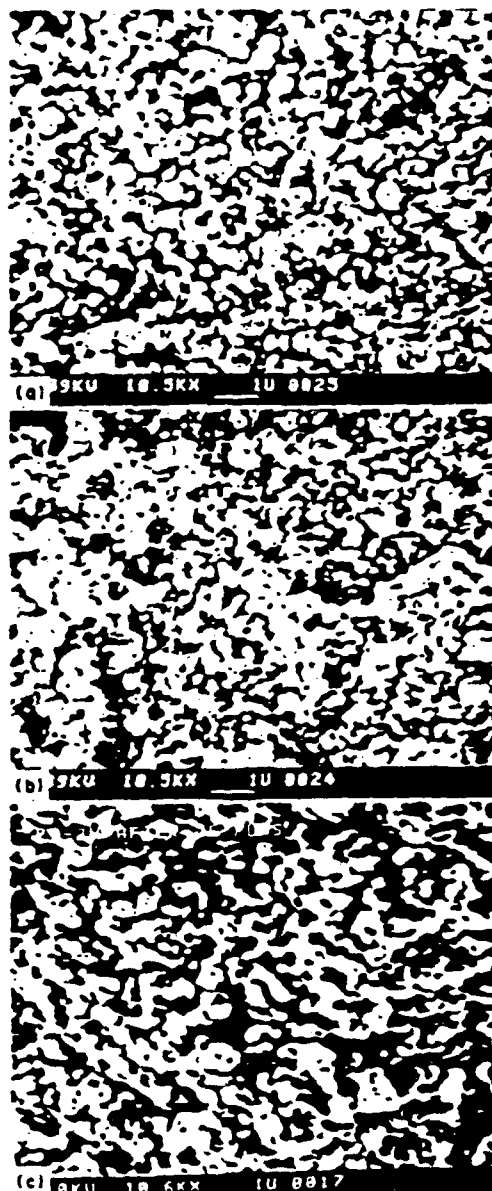
Fig. 2 Scanning electron micrographs of the fracture sur-faces of (a) $Pb_{0.97}Ti_{0.98}Nb_{0.02}O_3$ and (b) $Pb_{0.975}Ti_{0.95}Nb_{0.05}O_3$ ceramics. (c) Same as (a), but after several cycles of heat-ing cooling for acoustic emission measurements.
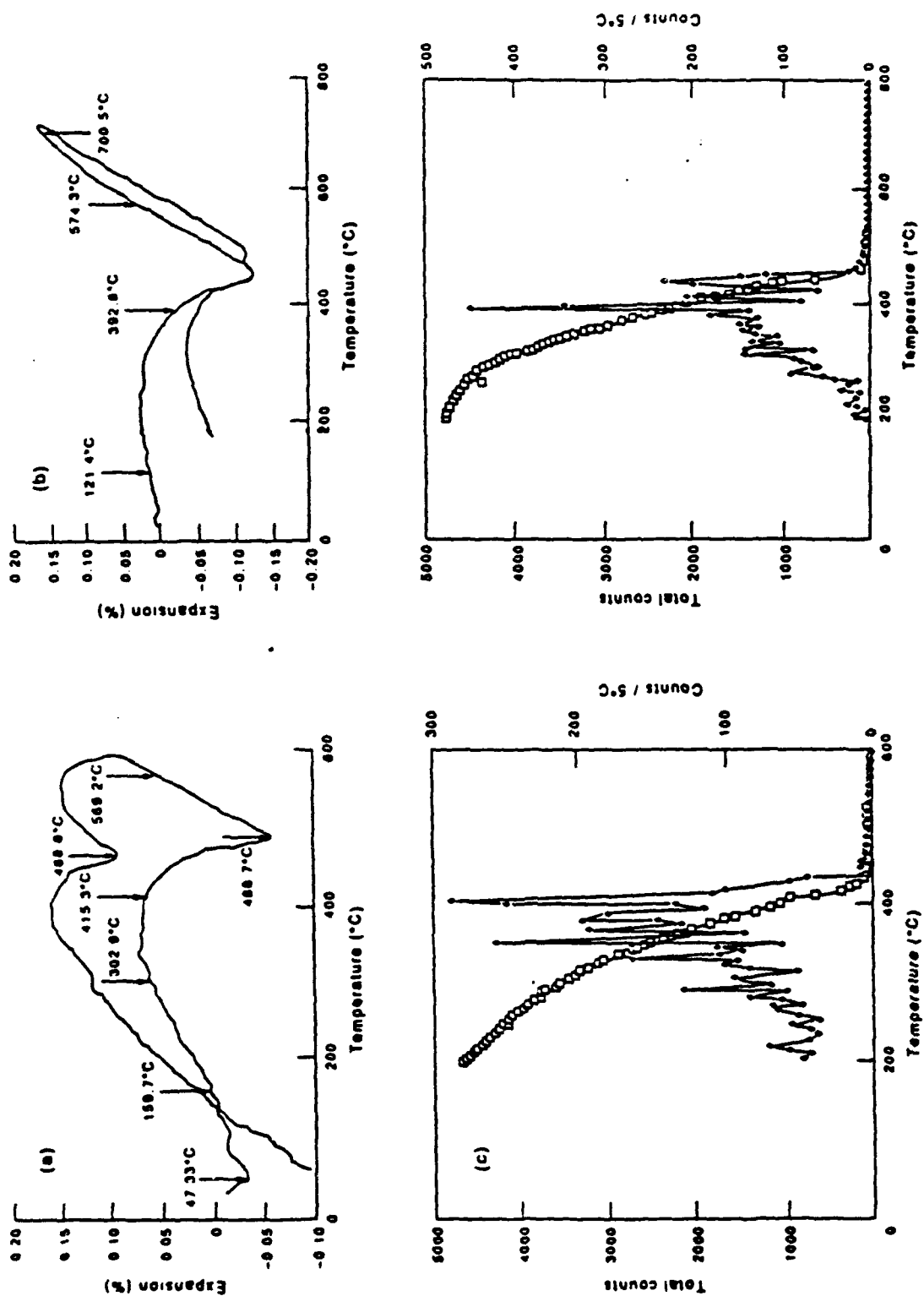
Fig. 3. Linear thermal expansion of (a) $Pb_{0.97}Ti_{0.88}Nb_{0.01}O_3$ and (b) $Pb_{0.97}Ti_{0.88}Nb_{0.01}O_3$ ceramics during heating and cooling. The corresponding acoustic emission data (total counts and counts/5°C) during cooling for these two compositions are given in (c) and (d), respectively.

perovskite with $a = 0.3894$, $c = 0.4106$ nm and $c/a = 1.054$ (which again is slightly smaller than that for the 2% Nb composition), while a trace of an unidentified second phase was also present. Thus, the solubility limit of Nb in $PbTiO_3$ is between 2 and 5% [37]. The scanning electron micrographs (Fig. 2) show the average grain size to be $0.2-0.3\,\mu m$ for the two $PbTiO_3$ samples with 2 and 5% Nb. The small grain size is significant, since the tendency of $PbTiO_3$ to crystallize as small crystals during sintering is reported to be one of the obstacles in producing dense, strong $PbTiO_3$ ceramics [40]. The unexpectedly good strength of the present samples is no doubt due to their small grain size, below the value for spontaneous cracking [40, 27].

3.2. Dilatometry and acoustic emission

The thermal expansion behavior of the 2% Nb-doped $PbTiO_3$ ceramics (Fig. 3) on heating shows a small expansion upto about 400°C and then contracts sharply upto the transition temperature (489°C) before it starts to expand normally. On cooling from about 600°C, it contracts down to the phase change (469°C) and then begins to expand first steeply down to about 400°C, followed by gradual contraction down to room temperature. The 5% Nb doped $PbTiO_3$ ceramics essentially behaves in a similar manner, showing very little length change upto about 300°C, followed by a steep contraction up to the transition point (450°C) and finally expanding in the normal manner, on heating. On cooling, the normal contraction is observed down to the transition points (about 490° and 450°C), below which the sample expands down to about 300°C, followed by slight contraction at lower temperatures. The two minima, in agreement with the results of Ref. [37], are attributed to a non-equilibrium condition with two compositions having slightly different Nb contents. The sharp dimensional changes (expansion followed by contraction) starting at the cubic-tetragonal phase change down to room temperature is noteworthy. A single sharp dielectric constant maximum was reported at about 465°C in the $x = 0.02$ sample, while two minima were observed in the $x = 0.05$ sample [39], in support of the thermal expansion data.

The acoustic emission data for these two samples are also included in Fig. 3. On heating, no significant acoustic emission events are detected between room temperature and 600°C for a sample with $x = 0.02$. On the other hand, intense acoustic emission activity was observed during cooling. For example, the $x = 0.02$ sample exhibited significant number of acoustic emission signals starting at 473°C on cooling from 600–800°C (Fig. 4). The AE activity continues down to at least 200°C. The data for the $x = 0.05$ sample were essentially similar.

3.3. Origin of microcracks

During cooling, AE is detected at the transition temperature, around 470°C (Fig. 4) and continues

down to at least 200°C (Fig. 5). It may be recalled that the cubic a parameter suddenly undergoes a sharp increase to become the c axis and a decrease to become the a axis of the tetragonal phase at the Curie point, causing considerable internal stresses. These internal stresses are partly relieved by the creation of ferroelectric domains (particularly of the 90° type) and partly by the initiation of microcracks. Therefore, the appearance of significant AE signals at about 470°C is attributed to the initiation of microcracks due to the sudden lattice parameter changes at the Curie point. The most intense AE is observed between 450° and about 250°C. This may be accounted for by the following: As the sample is cooled from the transition temperature to lower temperatures, an anisotropic thermal expansion (c axis expansion and the a axis contraction) takes place (Fig. 1). This is
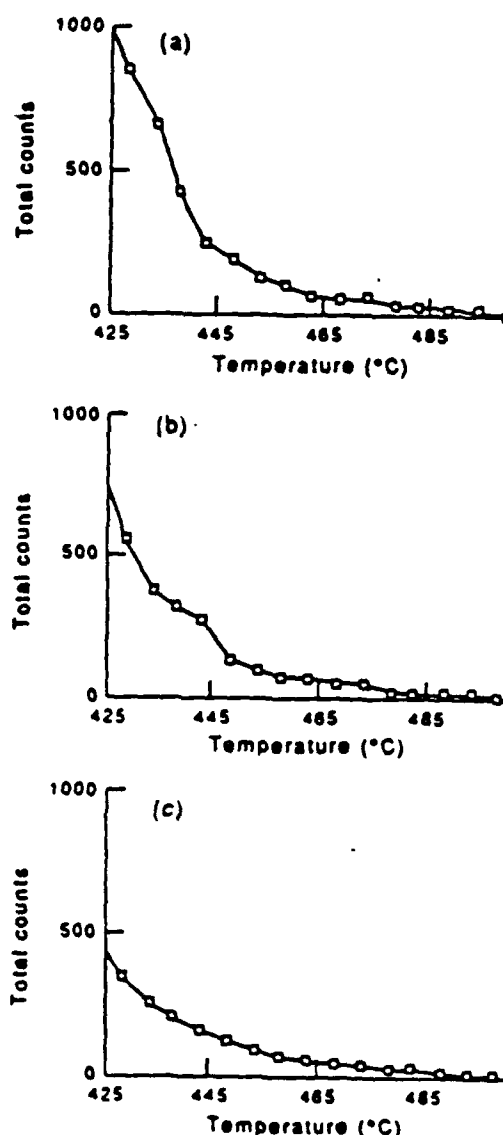
Fig. 4. Acoustic emission on cooling $Pb_{0.98}Ti_{0.98}Nb_{0.02}O_3$ ceramic from (a) 300, (b) 700 and (c) 600°C. The temperature 500–425°C is shown on an expanded scale.

apparent from the dilatometric data also (Fig. 3). Thus the AE behavior during cooling is attributed to the dimensional changes resulting from the variation of lattice parameters with temperature.

The fact that microcracking arises from anisotropic lattice parameter changes with temperature is confirmed by the two following experiments: In one, hardly any AE signals were detected between the
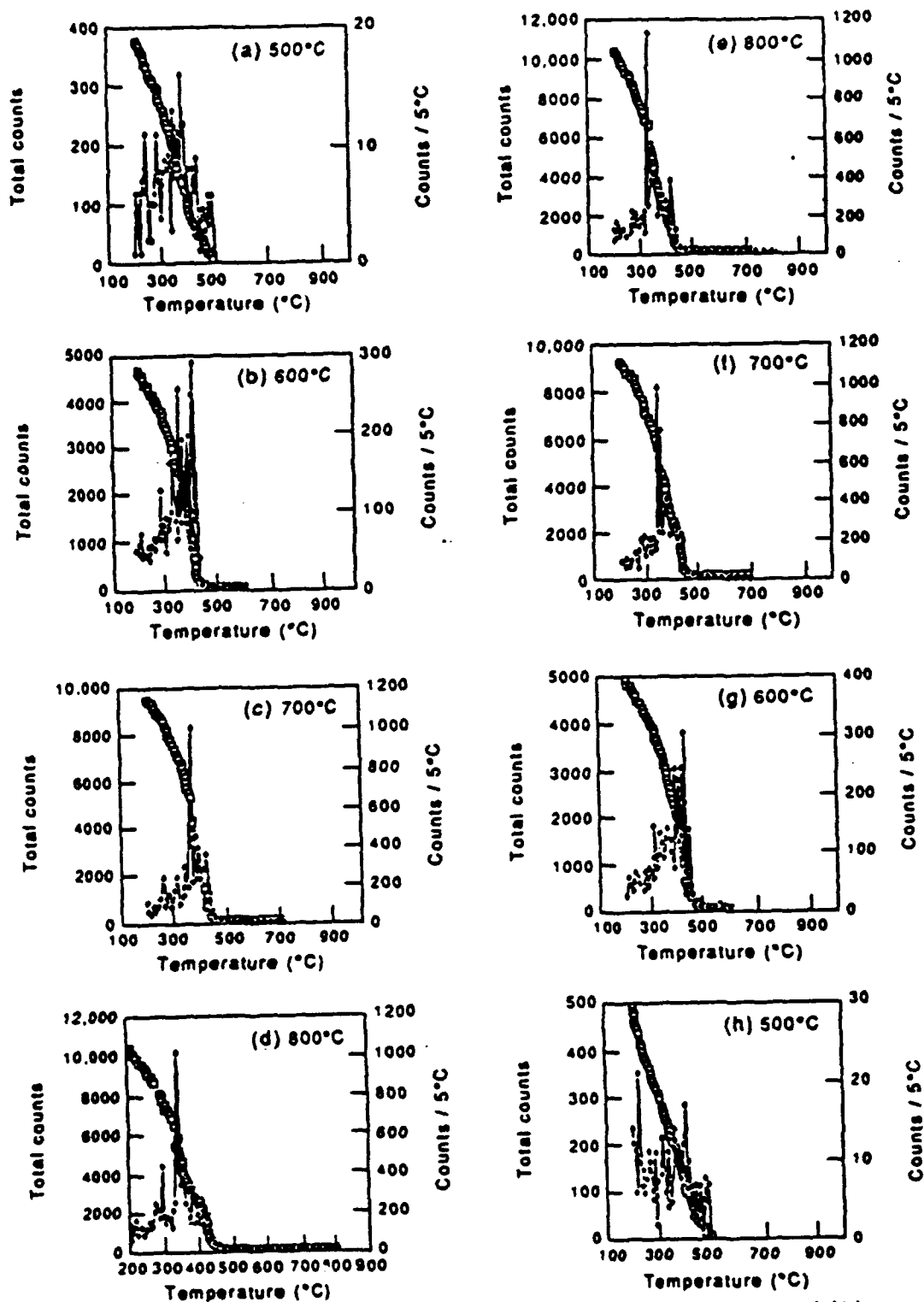
Fig. 5. Acoustic emission, during cooling to 200°C of Pb$_{9}$..Ti$_{9}$..Nb$_{9}$O, ceramic from successively higher temperatures: (a) 500, (b) 600, (c) 700, and (d) 800 C and also from successively lower temperatures: (e) 800, (f) 700, (g) 600 and (h) 500 C.
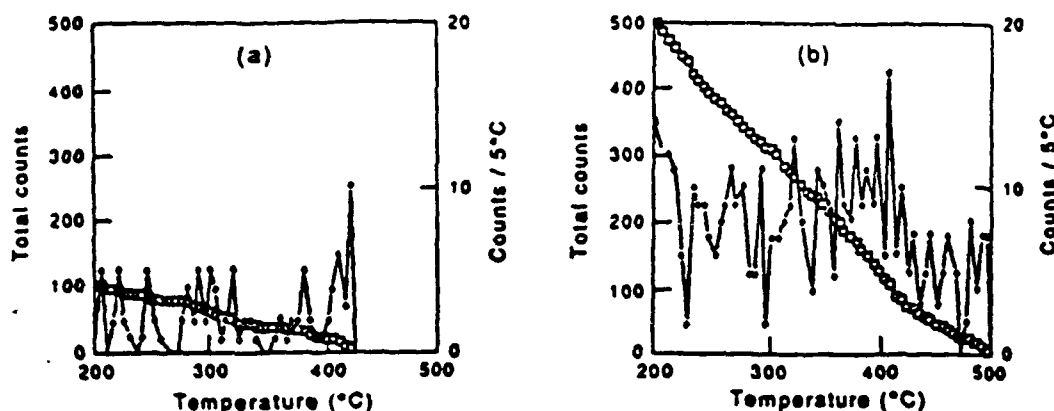
Fig. 6. Acoustic emission on cooling $Pb_{0.99}Ti_{0.98}Nb_{0.02}O_3$ ceramic from (a) 425 and (b) 500°C.

maximum temperature of the experiment (from 500 to 800°C) and the Curie temperature (Fig. 5), clearly indicating that no microcracking (and therefore no AE activity) takes place on heating or cooling in the cubic phase region, as expected [Figs 3(c.d) and 5]. In the second experiment, when the sample was heated to and cooled from 425°C, slightly below the cubic-tetragonal transition temperature, much less AE activity (about 100 counts) was detected, compared to the samples heated and cooled from above 500°C (about 500 counts) (Fig. 6), suggesting that the sudden lattice parameter changes at the Curie temperature really trigger the microcracking, which is enhanced by the anisotropic thermal expansion as the sample is cooled below the transition temperature. The scanning electron micrograph of a sample which had undergone several heating/cooling cycles through the phase transition shows intergranular fractures [Fig. 2(c)] which are absent in the same sample before such thermal cycling [Fig. 2(a)].

3.4. Recombination of microcracks

Only minor acoustic activity is observed as the sample is heated through the phase transition (Fig. 7) compared to the intense AE signals during cooling of the same sample (Fig. 5). This may imply that crack
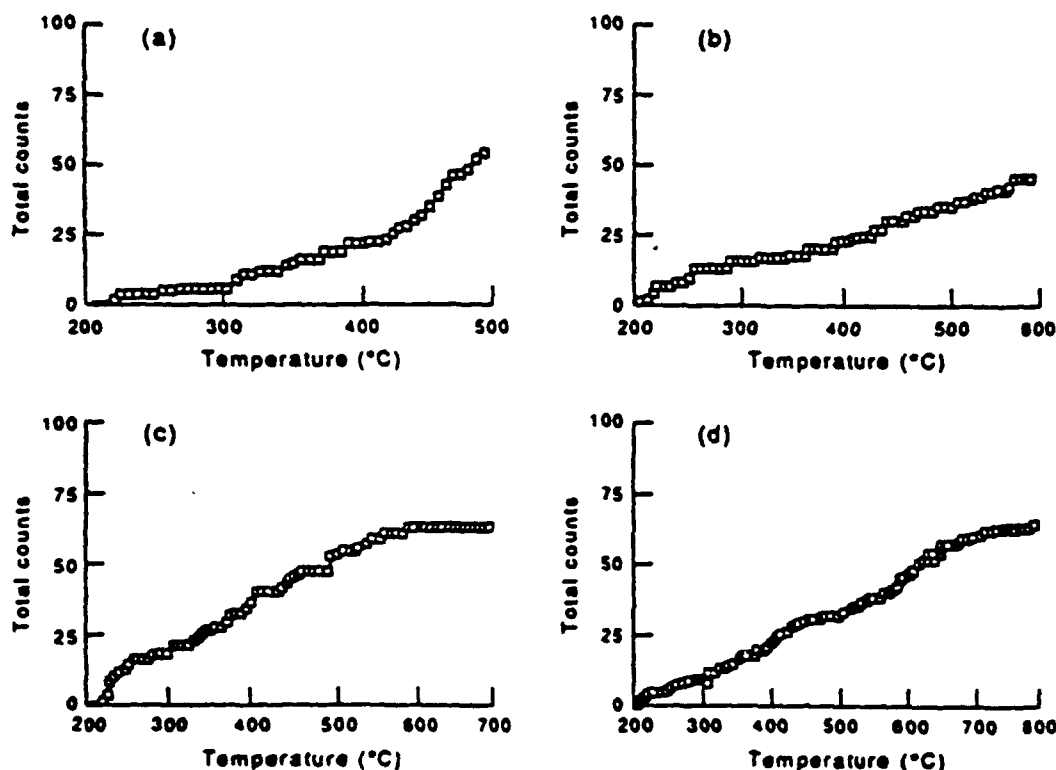
Fig. 7. Acoustic emission on heating $Pb_{0.99}Ti_{0.98}Nb_{0.02}O_3$ ceramic from 200°C to successively higher temperatures: (a) 500. (b) 600. (c) 700 and (d) 800°C.

heating is a gradual process and is therefore not amenable for detection by AE methods.

However, AE data were collected on a sample of $Pb_{0.99}Ti_{0.98}Nb_{0.02}O_3$ ceramic as it was subjected to heating cooling cycles, in which it was heated to successively higher temperatures (500, 600, 700 and 800°C) but cooled to 200°C between successive heatings [Fig. 5(a)–(d)], in order to study the effect of maximum temperature experienced by the sample on the extent of microcracking during cooling. The heating and cooling rates have been kept constant at 10 and 5°C/min, respectively. It may be noticed that the total number of counts (essentially all of them in the temperature range from the transition point to 200°C) as well as the count rate were larger, the higher the maximum temperature to which the sample has been heated and from which it has been cooled. For example, as the maximum temperature experienced by the sample increased from 500 to 800°C, the total AE counts increased from about 400 to over 10,000 and the count rate (per 5°C) increased from less than 20 to over 1000. This experiment was repeated in which the maximum temperature experienced by the sample was successively lowered (800–700 to 600–500°C) with cooling to 200°C between successive cycles. The AE data in this case [Fig. 5(e)–(h)] were nearly identical to those obtained in the first experiment in which the successively higher maximum temperatures were employed [Fig. 5(a)–(d)]. The relationship between the total number of counts and the maximum temperature to which the sample was exposed is essentially linear in the temperature range of 500–700°C (Fig. 8). This may be explained as follows: The number of AE counts may be taken as the number of fresh microcracks occurring in a sample. Healing or recombination of pre-existing microcracks may be assumed to be a function of the temperature to which the sample is heated. Therefore, the microcracks in more of the grains may be healed by heating it to a higher temperature (and therefore offer themselves as potential sites for fresh microcracking) than when it is
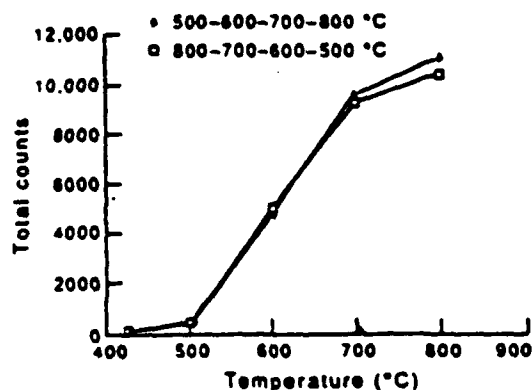
Fig. 8. Total AE counts on cooling $Pb_{0.99}Ti_{0.98}Nb_{0.02}O_3$ ceramic to 200 C as a function of maximum temperature to which the sample was exposed.
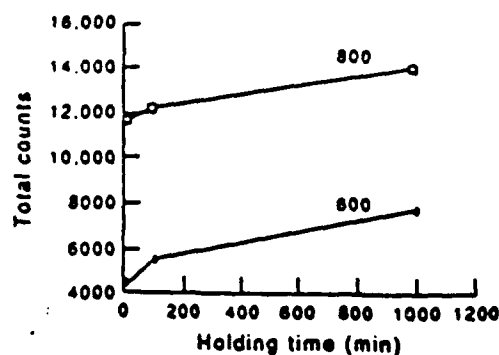
Fig. 9. Total AE counts on cooling $Pb_{0.99}Ti_{0.98}Nb_{0.02}O_3$ ceramic to 200°C from 600 and 800°C, as a function of holding time at 600 and 800°C.

heated to a lower temperature. As a result, the number of fresh microcracks occurring (and thus the number of AE counts) increases with the temperature to which the sample is heated. This explanation is confirmed by the fact that the number of AE counts decreased when the sample was cooled to 200°C successively from 800, 700, 600 and 500°C [Fig. 5(e)–(h)]. It may be noted (Fig. 8) that the total counts on cooling a sample from 800°C are only slightly more than those when it is cooled from 700°C, which may mean that much of the recombination of microcracks is completed by heating to 700°C. Further, very few AE counts were obtained when the sample was cooled from 425°C, which is below the cubic–tetragonal transition temperature, compared to samples cooled from above the transition temperature (Figs 6 and 8), as pointed out earlier.

The healing of microcracks has been shown above to be a function of the temperature to which the sample has been heated (Fig. 8). In order to examine the influence of holding (or annealing) time on the recombination of microcracks, samples held at 600 and 800°C for 10, 100 and 1000 min were cooled to 200°C, while AE data were obtained (Fig. 9). The recombination of microcracks appears to be more rapid in the first 100 min compared to longer periods, both at 600 and 800°C. Further, in the time span studied, the rate of healing of microcracks was faster at 600°C (nearly doubled between 10 and 1000 min). In other words, the holding time was more important at 600°C than at 800°C for the healing of microcracks. This also means that many of the microcracks which can recombine do so as soon as the temperature reaches 800°C and not many more do so by holding the sample at 800°C for long periods, whereas the holding time does play a more significant role at lower annealing temperatures such as 600°C.

4. CONCLUSIONS

Microcracking in $Pb_{0.99}Ti_{0.98}Nb_{0.02}O_3$ ceramic, arising from tetragonal distortion at the cubic–tetragonal phase transition (at about 469°C) and becoming

enhanced by the anisotropic changes of the tetragonal lattice parameters on cooling below the transition, are detected by acoustic emission measurement. Appearance of significant AE activity starts at or near the phase transition and the AE count rate reaches a peak at 50–100°C below the transition temperature. Very few AE signals are detected during heating (indicating that healing of microcracks is a gradual process, not amenable to detection by AE methods) and during heating or cooling of the sample in the cubic phase regime. Only a small number of AE counts were detected when the sample was heated to and cooled from 425°C, well below the transition temperature, indicating the important role of the sudden lattice distortion at the ferroelectric Curie temperature as the prime trigger for the microcracking process. The AE activity continues as the sample is cooled below the Curie temperature due to the microcracking caused by the anisotropic thermal expansion behavior of the tetragonal phase. The extent of healing increases with increasing temperature to which the sample is heated and consequently the number of fresh microcracking events (and the AE counts) increase with increasing temperature experienced by the sample. The extent of recombination of microcracks increases substantially with holding time of the sample at 600°C, whereas holding time does not play an important role for a sample heated to 800°C.

REFERENCES

1. A. G. Evans, *Acta metall.* 26, 1845 (1978).
2. V. Tvergaard and J. W. Hutchinson, *J. Am. Ceram. Soc.* 71, 157 (1988).
3. W. R. Buessem, N. R. Thielke and R. V. Sarakauskas, *Ceramic Age* 60, 38 (1952).
4. W. R. Buessem, in *Mechanical Properties of Engineering Ceramics* (edited by W. W. Kriegel and H. Palmour III) p. 127. Interscience, New York (1961).
5. W. R. Buessem and F. F. Lange, *Interceram* 15, 229 (1966).
6. E. A. Bush and F. A. Hummel, *J. Am. Ceram. Soc.* 41, 189 (1958).
7. J. A. Kuszyk and R. C. Bradt, *ibid* 56, 420 (1973).
8. J. J. Cleveland and R. C. Bradt, *ibid* 61, 478 (1978).
9. W. R. Manning, O. Hunter Jr. F. W. Calderwood and D. W. Stacy, *ibid* 55, 342 (1972).
10. H. P. Kirchener and R. M. Grover, *ibid* 53, 232 (1970).
11. J. E. Blendell and R. L. Coble *ibid* 65, 174 (1982).
12. R. Roy, and D. K. Agrawal, *A. Rev. Mater. Sci.* 19, 59 (1989).
13. F. F. Lange and T. K. Gupta, *J. Am. Ceram. Soc.* 53, 54 (1970).
14. F. F. Lange and K. C. Radford, *ibid* 53, 420 (1970).
15. B. J. Hockey in *Fracture Mechanics of Ceramics* (edited by R. C. Bradt, A. G. Evans, D. P. H. Hasselman and F. F. Lange), Vol. 6, p. 637. Plenum Press, New York (1983).
16. T. K. Gupta, *Adv. Ceram.* 10, 750 (1984).
17. L. Wagner, S. Lee and J. C. M. Li, *Scripta metall.* 19, 361 (1985).
18. A. G. Evans and M. Linzer, *A. Rev. Mat. Sci.* 7, 179 (1977).
19. A. G. Evans, *J. Am. Ceram. Soc.* 58, 239 (1975).
20. J. Noone and R. L. Mehan, in *Fracture Mechanics of Ceramics* (edited by R. C. Bradt, D. P. H. Hasselman and F. F. Lange) Vol. 1, p. 201. Plenum Press, New York (1974).
21. Y. Fu and A. G. Evans, *Acta metall.* 33, 1515 (1985).
22. R. E. Wright, *J. Am. Ceram. Soc.* 55, 54 (1972).
23. Y. Ohya, Z. Nakagawa and K. Hamano, *ibid* 70, C184 (1987).
24. V. Srikanth, E. C. Subbarao, D. K. Agrawal C.-Y. Huang and G. V. Rao, *ibid* 74, 060 (1991).
25. V. Srikanth, E. C. Subbarao and G. V. Rao.
26. F. J. P. Clarke, *Acta metall.* 12, 139 (1964).
27. R. W. Rice and R. C. Pohanka, *J. Am. Ceram. Soc.* 62, 559 (1979).
28. R. W. Rice, S. W. Freimen and P. F. Becher, *ibid* 64, 345 (1981).
29. R. W. Rice and S. W. Freimen, *ibid* 64, 350 (1981).
30. F. J. Parker and R. W. Rice, *ibid* 72, 2364 (1989).
31. R. C. Pohanka, R. W. Rice and B. E. W.... er Jr, *ibid* 59, 71 (1976).
32. V. D. Krstic, *ibid* 67, 589 (1984).
33. R. McPherson, *J. Aust. Ceram. Soc.* 3, 43 (1967).
34. E. C. Subbarao and V. Srikanth, *Physica* C171, 449 (1990).
35. G. Shirane and S. Hoshino, *J. phys. Soc. Japan* 6, 265 (1951).
36. F. Jona and G. Shirane, *Ferroelectric Crystals*. McMillan, New York (1962).
37. E. C. Subbarao, *J. Am. Ceram. Soc.* 43, 119 (1960).
38. T. Y. Tien and W. G. Carlson, *ibid* 45, 567 (1962).
39. Y. Matsuo, M. Fujimura and H. Sasaki, *ibid* 48, 111 (1965).
40. Y. Matsuo and H. Sasaki, *ibid* 49, 229 (1966).

APPENDIX 12

Materials Research Laboratory, Pennsylvania State University, University Park[1])

Morphotropic Phase Boundary in the Pb(Zr$_x$Ti$_{1-x}$)O$_3$ System

By

M. Fukuhara[2]), A. S. Bhalla, and R. E. Newnham

The ionic polarizabilities in Pb(Zr$_x$Ti$_{1-x}$)O$_3$ compositions are calculated by the Clausius-Mossotti-Lorentz-Lorentz equation. The resultant gap of the polarizability appearing at the morphotropic phase boundary (MPB) composition suggests the phase transition boundary to be due to the electrostatic long-range dipole moment. Semiconducting and phonon softening of PZT near MPB compositions may be arrived at from screening of the long-range dipole–dipole interaction by electrons.

Es werden die ionaren Polarisierbarkeiten von Pb(Zr$_x$Ti$_{1-x}$)O$_3$ mit Hilfe der Clausius-Mossotti-Lorentz-Lorentz-Beziehung berechnet. Die resultierende Polarisierbarkeitslücke bei der Komposition der morphotropen Phasengrenze (MPB) läßt vermuten, daß die Phasenübergangsgrenze durch das langreichweitige elektrostatische Dipolmoment hervorgerufen ist. Nahe der MPB-Komposition ist Halbleitung sowie ein Aufweichen der Phononmoden bei Abschirmung der langreichweitigen Dipol–Dipol-Wechselwirkung durch Elektronen möglich.

1. Introduction

Since Jaffe et al. [1, 2] found enhanced piezoelectric effects, such as maximum electromechanical coupling coefficient and dielectric susceptibility, for compositions near the morphotropic phase boundary[3]) (MPB) between the tetragonal and rhombohedral ferroelectric phases in the Pb(Zr$_x$Ti$_{1-x}$)O$_3$ solid solution (PZT) system, PZT ceramics are now the main materials in modern piezoelectric technology. For these compositions, there are fourteen possible poling directions over a very wide temperature range, explaining why the piezoelectric coefficients are largest near the MPB [3]. Once the phase boundary was considered as the composition where these two phases were present in equal quantity [4], Benguigui and coworkers [5] have suggested the coexistence of the two phases in MPB over the region of 15 mol%, but Isupov [6] has reported a possible existence of an extended region of the MPB composition. Subsequent investigations by Kakegawa et al. [7] and Multani et al. [8] have proved that no coexistence of the two phases occurs in any range of composition without compositional fluctuation, using wet-dry combination and sol-gel techniques, respectively. Nakamura [9] has also pointed out that the MPB is the phase boundary of the first-order transition tetragonal and rhombohedral phases. However, even if the MPB is a monoboundary separating two ferroelectric phases, there is still the question of why the MPB appears at a specified composition in the complete solid solution system. Our overall interest lies in an inquiry into the origin of the MPB in terms of lattice dynamics. Previous work [10 to 13] has been carried out on this subject using Raman techniques, but it is not completely clear yet, as far as we know.

---

[1]) University Park. PA 16802, USA.

[2]) Present address: Toshiba Tungaloy, Research Department for Tool Development, 7-1, Tsukagoshi, Saiwai-Ku, Kawasaki 210, Japan.

[3]) This is used to denote an abrupt structural change within a solid solution with variation in composition [2]. That the boundary cannot be crossed by changing temperature is important in PZT.

2. Appearance of MPB and Relief of Lattice Strain

In order to answer the question, the charactertistics of the MPB are reviewed as follows:
1. The boundary appears as a vertical line and does not depend on temperature [4, 14].
The temperature independence is not common in other ferroelectric systems. In general,
the subsolidus boundaries in binary solid-solution regions show a half ellipse shape such
as the σ-phase in Fe-Cr alloys. 2. The orthorhombic ferroelectric phase is not found among
the perovskite oxide systems in which the morphotropic boundaries occur. For this reason,
Newnham [3, 15] has suggested the instability or suppression of the orthorhombic phase
due to the symmetry hierarchy. 3. The morphotropic boundaries are relatively common in
Pb-based perovskites, more than in other perovskite phase diagrams [3]. A Pb^{2+} ion favors
pyramid bonding which is common in the tetragonal and rhombohedral perovskite, under
its lone-pair $6s^2$ electron configuration [16]. The bonding calls for an asymmetrical position
which is the result of the deformation of the Pb^{2+} ion. Thus, the high permittivity in the
tetragonal side is a consequence of the high polarizability of the (Ti, Zr)–O chains
perpendicular to the spontaneous polarization along [001] directions (Fig. 4 in [16]). 4. The
dielectric constant, piezoelectric d strain coefficients, and electromechanical coupling factor
k have their highest values just on the tetragonal side of the structural transition [17], while
the piezoelectric g-constants maintain their high values into the rhombohedral field [4]. 5.
The tetragonal distortion. $(c/a) - 1$, in tetragonal range shows a minimum value near the
MPB [2, 18]. In order to make clear it, the strain S_i in the direction of spontaneous
polarization at room temperature was calculated in both tetragonal and rhombohedral
regions, using the general formula [14, 19]

$$S_i = Q_{ij}P_j^2,\qquad\qquad\qquad (1)$$

where P_j is the spontaneous polarization and Q_{ij} the electrostrictive coefficient. For this
calculation, the latest data at 298 K by Haun et al. [20, 21] were used. These results are
shown in Fig. 1. The strain (3.0%) of $PbTiO_3$ decreases almost linearly with increasing
zirconate content to the MPB composition and reversely increases in the $PbZrO_3$-rich
region over the composition. This suggests that the domains near the MPB are most easily
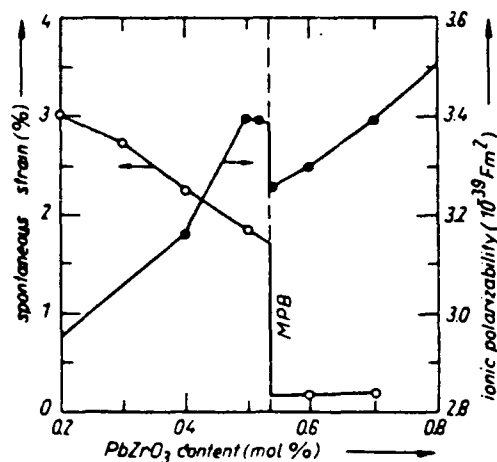
Fig. 1. Compositional dependence of the strain
in the direction of spontaneous polarization
and ionic polarizability for $Pb(Zr_xTi_{1-x})O_3$

aligned for poling due to the relief of the strain. Therefore, it is very difficult to explain the appearance of the MPB based on the 15% strain limit according to the Hume-Rothery rule which predicts structural stability limits based on ionic mismach considerations [22].
6. The local maxima of electric conductivity (10^{-8} to 10^{-6} $(\Omega\,cm)^{-1}$ at the Curie point) exist for the compositions close to the MPB [23]. These values and their positive temperature coefficient in conductivity indicate semiconducting character.

These six characteristics yield clues as to the reason why the morphotropic boundary appears at $x = 0.535$ [24]. We first consider physical causes of the dielectric anomaly near the MPB.

According to the Lyddane-Sachs-Teller (LST) relation [25]

$$\frac{\omega_T^2}{\omega_L^2} = \frac{\varepsilon(\infty)}{\varepsilon(0)}. \tag{2}$$

if $\varepsilon(0) \to \infty$, a characteristic of ferroelectricity, ω_T would be zero[*]), where $\varepsilon(0)$ is the static dielectric constant, $\varepsilon(\infty)$ is the high-frequency limit of the dielectric function, and ω_T and ω_L are transverse and longitutional optic phonon frequencies, respectively. Hence, by analogy we infer that a singularity in dielectric constant at the MPB may be related to the soft modes with $\omega_T \to 0$. Indeed, Pinczuk [10], Burns and Scott [11], and Bauerle et al. [13] have observed that the "soft" ω_T mode frequency decreases with increasing zirconate content in the tetragonal region and goes to zero at the MPB. However, no optical soft mode exists in the rhombohedral phase; all (Ti, Zr)–O chains are spontaneously polarized due to the formation of triangular Pb–O structures [16]. Therefore, these characteristics at either side of the MPB indicate that the Pb^{2+} ion in cubo-octahedral sites plays an important role for the lattice softening and the polarization which are responsible for the appearance of the MPB. The occurrence of the MPB might therefore be connected with relief of the lattice strain, especially shear strain.

3. Ionic Polarizability Gap at MPB

Goldschmidt has established that, for a given structure, the possibility of substitution in isomorphous oxides is limited to a certain range of ion sizes and polarizability[5]) [26], so the chief factor underlying the appearance of the MPB would be the influence of composition, especially ratio of Zr to Ti, on the ionic polarizability. To our knowledge, however, there is no system with phase transition boundary due to the polarizability. The effects of the ionic size and electronegativity will be negligible for the components close to the MPB. Since, moreover, it is known that the PZT is a ferroelectric solid solution without vacancy like K(Ta, Nb)O$_3$ [27], we can omit an oxygen vacancy effect. Thus, the ionic polarizability α_i contributing to the MPB composition is calculated by the Clausius-Mossotti-Lorentz-Lorentz equation under extremely small short-range repulsive force [28],

$$\frac{N_0\alpha}{3\varepsilon_0} = \frac{\varepsilon_s - 1}{\varepsilon_s + 2} \frac{M}{\varrho} = \frac{n^2 - 1}{n^2 + 2} \frac{M}{\varrho}, \tag{3}$$

---

[*]) Burns and Scott [12] have reported that displacive ferroelectrics such as Pb$_{1-x}$La$_x$Ti$_{1-x}$O$_3$ ($x < 0.24$) do not behave according to the accepted LST theory. However, it is probably out of question for this study because of A site occupation of La against Zr of B site in perovskite ABO$_3$ compound [11].

[5]) Polarizability describes the lability of these electrons when induced from their normal positions, while the polarization describes the position of the outer electrons with reference to the atomic nuclei.

where Avogadro's number $N_0 = NM/\varrho = 6.023 \times 10^{23}$, ε_s is the relative dielectric constant, ε_0 the dielectric constant of vacuum, n the refractive index, provided that the local Mosotti field applies to the $Pb(Zr, Ti)O_3$ crystal. In fact, the O^{2-} ions in ferroelectric perovskite-structure crystal do not necessarily have cubic symmetry and the local field factors turn out to be unusually large [29].[6]) However, the crystal symmetry of the compositions near the MPB seems to be close to the cubic environment and the quadrupole and octupole polarizabilities of ions will be small [31, 32], since the soft mode in ferroelectric transition is actually characterized by a negative contribution by the long-range dipole–dipole interaction [33]. Thus, we write the molar polarizability of PZT in the form

$$\frac{\varepsilon_s - 1}{\varepsilon_s + 2} = \frac{N}{3\varepsilon_0} (\alpha_{e\cdot} + \alpha_{e\cdot} + \alpha_i), \tag{4}$$

where $\alpha_{e\cdot}$ and $\alpha_{e\cdot}$ are the electronic polarizabilities of the positive and negative ions, respectively. At optical frequencies, we arrive at the approximate formula

$$\frac{n^2 - 1}{n^2 + 2} = \frac{N}{3\varepsilon_0} (\alpha_{e\cdot} + \alpha_{e\cdot}), \tag{5}$$

because of $\alpha_i = 0$. Thus, we can obtain α_i by subtraction of (5) from (4) [34].

Here we use the ceramic dielectric constant data at 4.2 K [20] and single-crystal refractive index data at room temperature. It is expected that the low temperature dielectric data freeze out the thermally activated contributions such as domain wall and defect effects to the dielectric properties [20]. The refractive indices of the solid solution $Pb(Zr, Ti)O_3$ may not differ so much from intermediate values of $PbTiO_3$ ($n = 2.6$) [35] and $PbZrO_3$ ($n = 2.2$) [36] crystals, so these indices are interpolated with linear allocation of these values for $PbTiO_3$ and $PbZrO_3$ [37]. The numbers of each ion per unit cell (m^3) are $1/5ab^2$ and $1/3.5a^3(1 - 3\cos^2\theta + 2\cos^3\theta)^{1/2}$ (θ is the rhombohedral angle) for tetragonal and rhombohedral regions, respectively. In the rhombohedral case, we take a covalency of alternating $(Ti-Zr)O_3$ and PbO_3 dipoles which align with the [111] direction (Fig. 5 in [16]) into consideration and ignored the effect of the $(Zr, Ti)-O$ chains, because the $(Zr, Ti)-O$ chains retain only minor significance for the ferroelectricity as a result of the reduced titanium content [16]. The unit cell volumes of the solution $Pb(Zr_xTi_{1-x})O_3$ are calculated using room temperature lattice parameters of pure homogeneous polycrystalline samples from sol-gel derived powders [7], since the parameters are almost constant in the temperature region from 4.2 K to room temperature [38].

Ionic polarizabilities for $Pb(Zr_xTi_{1-x})O_3$ solid solution are also presented in Fig. 1, where a gap of the polarizability appears near the MPB composition ($x = 0.535$). This gap suggests that appearance of the MPB arises from the difference of large-range dipole moments between the tetragonal and rhombohedral ferroelectric crystals. If so, the MPB in PZT would be the first case of the phase transition boundary due to polarizability.

4. Strain Relief and Band Crossing

As mentioned in review [6], the PZT ceramics near the MPB behave as semiconductor and show an increase of conductivity. This variation is quite analogous to the composition-induced semiconductor–insulator (S–I) transition in ferroelectric $(BaTiO_3)_{1-y}(R_2O_3)_y$

---

[6]) The detailed calculation must use the general quantum-mechanical formula for a localized system, taking the occupied and available excited orbitals into consideration [30].

APPENDIX   13

(R: Sm, Gd, and Ho, $0.0015 < y < 0.003$) [39]. The conduction in the PZT is by a band transport mechanism, by a charge transfer process such as occurs in lithium-doped NiO [40], or by an exchange process through the anions. Although the question of whether a conduction band exists in PZT cannot be answered at the present time, it probably results from a change in band overlap with a structure change. If two bands either cross or uncross as a function of an external variable such as pressure, then the S-1 transition will occur [41]. Amin et al. [42] have reported that the tetragonal-rhombohedral phase transition can be induced in the morphotropic PZT compositions by the application of a relatively small hydrostatic pressure, because the ferroelectric properties are related to a hydrostatic stress on the ions in the B position of the perovskite ABO_3 compound [43]; the position of the MPB moves towards $PbZrO_3$ and $PbTiO_3$ compositions with increasing compressive and tensile hydrostatic pressure, respectively [42]. Therefore, there is a possibility that the two bands cross due to the relief of strain in phase transition from tetragonal to rhombohedral on the MPB composition. There are several materials such as Ca [44], Yb [45], and CdS [46] in which a band uncrossing does occur with increasing pressure.

On the other hand, the tetragonal-rhombohedral phase transition is directly connected with the softening of the lowest ω_T phonon, as described above. Thus, the PZT near the MPB composition has two contradictory characteristics, semiconduction and softening of ω_T phonon. For this reason, the effect of screening of the long-range dipole-dipole interaction by the electrons might be dominant over that of the short-range, by the positive Coulomb forces, and of the "chemical" effects by introducing either impurities or oxygen vacancies [47].

Judging from these discussions, the coupling of the electronic system to lattice distortions would be sufficiently strong and the relevant phonon mode would be sufficiently "soft". In order to explain simultaneously both behaviors of the dielectric permittivity and the conductivity in the composition near MPB on the basis of quantum mechanics, the lowest Hartree-Fock state for the transition must involve a combination of a lattice distortion and an oscillatory electronic polarization. The detailed study will be addressed in the next paper. In addition, assuming from these discussions, it will be difficult to get single PZT crystals with MPB composition, as pointed out by Ikeda and Fushimi [48].

Acknowledgement

References

[1] B. JAFFE, R. S. ROTH, and S. MARZULLO, J. appl. Phys. 25, 809 (1954).
[2] B. JAFFE, R. S. ROTH, and S. MARZULLO, J. Res. Nat. Bur. Standards 55, 239 (1955).
[3] R. E. NEWNHAM, Rep. Progr. Phys. 52, 123 (1989).
[4] B. JAFFE, W. R. COOK, and H. JAFFE, Piezoelectric Ceramics. Academic Press, London 1971 (p. 136).
[5] L. BENGUIGUI, Solid State Commun. 19, 979 (1976).
    P. ARI-GUR and L. BENGUIGUI, Solid State Commun. 15, 1077 (1974).
[6] V. A. ISUPOV, Solid State Commun. 17, 1331 (1975).
    V. A. ISUPOV, Soviet. Phys.—Solid State 22, 98 (1980).
    V. A. ISUPOV, Ferroelectrics 46, 217 (1983).
[7] K. KAKEGAWA, J. MOHRI, K. TAKAHASHI, H. YAMAMURA, and S. SHIRASAKI, Bull. Chem. Soc. Japan 5, 717 (1976).
    K. KAKEGAWA, J. MOHRI, S. SHIRASAKI, and K. TAKAHASHI, Solid State Commun. 24, 769 (1979).
[8] M. S. MULTANI, S. G. GOKARN, R. VIJAYARAGHAVAN, and V. R. PALKAR, Ferroelectrics 37, 652 (1981).

44*

[9] T. Nakamura, Bull. Ceram. Soc. Japan 14, 894 (1979).
[10] A. Pinczuk, Solid State Commun. 12, 1035 (1973).
[11] G. Burns and B. A. Scott, Solid State Commun. 13, 417 (1973).
[12] G. Burns and B. A. Scott, Phys. Rev. Letters 25, 1191 (1070).
[13] D. Bäuerle, Y. Yacoby, and W. Richter, Solid State Commun. 14, 1137 (1974).
[14] A. Amin, M. J. Haun, B. Badger, H. McKinstry, and L. E. Cross, Ferroelectrics 65, 107 (1985).
[15] R. E. Newnham, in: Phase Diagrams, Ed. A. M. Alper, Vol. V, Academic Press, New York 1978 (p. 46).
[16] W. Heywang and H. Thomann, Annu. Rev. Mater. Sci. 14, 27 (1984).
[17] T. B. Weston, A. H. Webster, and V. M. McNamara, J. Canad. Ceram. Soc. 36, 15 (1967).
[18] G. Shirane and K. Suzuki, J. Phys. Soc. Japan 7, 333 (1952).
E. Sawaguchi, J. Phys. Soc. Japan 8, 615 (1953).
[19] M. J. Haun, Z. O. Zhuang, E. Furman, S. J. Jang, and L. E. Cross, J. Amer. Ceram. Soc. 72, 1140 (1989).
[20] M. J. Haun, Z. Q. Zhuang, E. Furman, S. J. Jang, and L. E. Cross, Ferroelectrics 99, 45 (1989).
[21] M. J. Haun, E. Furman, S. J. Jang, and L. E. Cross, Ferroelectrics 99, 63 (1989).
[22] W. Hume-Rothery and G. V. Raynor, The Structure of Metals and Alloys, The Institute of Metals, London 1954 (p. 101).
[23] J. Dudek and Z. Wróbel, Ferroelectrics 18, 161 (1978).
Z. Wróbel, phys. stat. sol. (a) 45, K67 (1978).
[24] K. Kakegawa, J. Mohri, S. Shirasaki, and K. Takahashi, Bull. Chem. Soc. Japan 4, 692 (1985).
[25] C. Kittel, Introduction to Solid State Physics, 6-th Ed., John Wiley & Sons, New York 1986 (p. 275, 380).
[26] S. T. Bowden, The Phase Rule and Phase Reactions, Macmillan & Co, New York 1954 (p. 167).
[27] M. Nakahira, Crystal Chemistry, Kodan-Sha, Tokyo 1973 (p. 207).
[28] A. R. Von Hippel, Dielectrics and Waves, Chapman & Hall, New York 1954 (p. 98).
[29] J. C. Slater, Phys. Rev. 78, 748 (1950).
J. M. Luttinger and L. Tisza, Phys. Rev. 70, 954 (1946).
[30] S. T. Pantelides and W. A. Harrison, Phys. Rev. B 13, 2667 (1976).
[31] P. W. Langhoff and R. P. Hurst, Phys. Rev. 139, 1415 (1967).
P. W. Langhoff, M. Karplus, and R. P. Hurst, J. chem. Phys. 44, 505 (1966).
[32] G. D. Mahn, Solid State Commun. 33, 797 (1980).
G. D. Mahn, Solid State Ionics 1, 29 (1980).
[33] J. D. Axe and G. Shirane, Phys. Today September, 32 (1973).
[34] K. Okazaki, Exercise on Electrical Engineering Materials, 8-th Ed., Gakken, Tokyo 1988 (p. 77).
[35] J. Kobayashi and N. Yamada, Memories School Sci. Engng., Waseda Univ. 23, 111 (1959).
[36] F. Jona, G. Shirane, and R. Pepinsky, Phys. Rev. 97, 1584 (1955).
[37] S. Fushimi and T. Ikeda, J. Phys. Soc. Japan 20, 2007 (1965).
[38] M. J. Haun, E. Furman, H. A. McKinstry, and L. E. Cross, Ferroelectrics 99, 27 (1989).
[39] V. J. Tennery and R. L. Cook, J. Amer. Ceram. Soc. 44, 187 (1961).
[40] A. J. Bosman and C. Crevecoeur, Phys. Rev. 144, 763 (1966).
[41] D. B. McWhan and J. R. Remeika, Phys. Rev. 177, 1063 (1969).
[42] A. Amin, R. E. Newnham, and L. E. Cross, Phys. Rev. B 34, 1595 (1986).
[43] M. Troccaz, P. Gonnard, Y. Fetiveau, L. Eyrand, and G. Grange, Ferroelectrics 14, 679 (1976).
[44] F. P. Bundy and K. J. Dunn, in: Physics of Solids under High Pressure, Ed. J. S. Schilling and R. N. Shelton, North-Holland Publ. Co., Amsterdam 1981 (p. 402).
[45] N. H. March, in: Advance in High Pressure Research, Vol. 3, Ed. R. S. Bardley, Academic Press, London 1969 (p. 284).
D. Jerome and M. Rieux, Solid State Commun. 7, 957 (1969).
[46] H. G. Drickamer, Solid State Phys. 17, 55 (1965).
[47] H. Uwe and T. Sakudo, Ferroelectrics 52, 205 (1983).
[48] T. Ikeda and S. Fushimi, J. Phys. Soc. Japan 17, 1202 (1962).

Theory of tetragonal twin structures in ferroelectric perovskites with a first-order phase transition

Wenwu Cao and L. E. Cross

Materials Research Laboratory, The Pennsylvania State University, University Park, Pennsylvania 16802

A three-dimensional Landau-Ginzburg model has been constructed to describe the tetragonal twin structures resulting from a first-order O_h-C_{4v} proper ferroelectric phase transition in perovskites. The model takes into account the nonlinear and nonlocal characteristics of the polarization (order parameter) as well as the electromechanical coupling. Quasi-one-dimensional (Q1D) analytic solutions for the space profiles of the order parameter are obtained for a 180° twin and for a charge-neutral 90° twin with a special choice of parameters. Without the presence of interfacial defects, such as dislocations, the Q1D solutions require the support of inhomogeneous mechanical constraints. Elastic deformation and dimensional changes associated with the twin structures, and their implications on the piezoelectric effect in ferroelectric ceramics, are also addressed.

I. INTRODUCTION

Many important ferroelectric materials, such as $PbTiO_3$, $BaTiO_3$, $(Pb_{1-x}r_x)TiO_3$ [PZT], etc., have perovskite structure (ABX_3).[1] The prototype phase is cubic with symmetry group O_h, which transforms to a ferroelectric tetragonal (C_{4v}) or rhombohedral (C_{3v}) structure upon cooling. In certain materials there are several low-temperature ferroelectric phases, so that the stable structure of a material depends on the given temperature range.

These thermally induced structural phase transitions are usually displacive, and there are several low-temperature variants associated with each phase transition. For instance, there are six and eight variants in the tetragonal and rhombohedral phases, respectively, upon transforming from cubic. These variants are energetically equivalent; therefore, twinning between these variants is a common phenomenon under natural conditions. For single crystals with free boundary conditions, twinning may be eliminated through (electric or mechanical) field-induced domain switching between these low-temperature variants. However, twinning cannot be eliminated for a confined system, such as grains in a ceramic, because unit-cell distortions are usually associated with these ferroelectric transitions, domain switching could generate large elastic energy. Although, for some materials, a single phase may be achieved under a very large electric field, twinning will reappear when the external field is removed in order to release some of the elastic strain so as to minimize the total system energy. For other materials, twinning cannot be driven out by the electric field before the solid is shattered.

The existence of these twinning structures often changes the mechanical and electrical properties of a ferroelectric material substantially. There are considerable experimental studies being carried out in this regard[2,3] and some phenomenological theories were also developed.[4-6] However, in order to understand the physical process associated with the twinning phenomenon, one has to go down to the microscopic level to see how the lattices move in forming a twin structure and how they interact with each other. To this end, it is essential to know the structure of a twin boundary, including its stable space profile, energy density, and associated elastic distortions. In this paper, we will calculate these physical properties for a ferroelectric twin boundary by using a Landau-Ginzburg type of continuum theory. The problem we are dealing with is a first-order cubic to tetragonal proper ferroelectric transition, which appears in systems such as $BaTiO_3$, $PbTiO_3$, and some PZT compositions.

There are six tetragonal variants upon transforming from cubic; they can form three different kinds of twinning structures: (1) 180° twins, for which the polarizations in the two domains have the same magnitude but in opposite directions, (2) 90° twin with a charge-neutral domain wall, for which the polarizations in the two domains are (almost) perpendicular to each other with head to tail configuration, and (3) 90° twin with a charged domain wall, for which the polarizations in the two domains are perpendicular to each other and with either head-to-head or tail-to-tail configurations. It has been verified that the third kind of twin structure is unstable and will transform into the second kind with a zigzag twin boundary.[7]

Several authors[8-10] have attempted to model the structure of ferroelectric domain walls by using the Landau-Ginzburg theory; however, those models are either one dimensional or three dimensional with gradient terms in the free-energy expansion not obeying the symmetry requirement. Moreover, the focusing point was on the first kind (180°) of twins only. It has been pointed out that a one-dimensional model is not adequate for describing a three-dimensional solid.[11] A quasi-one-dimensional (Q1D) solution can be obtained only under certain constraints when unit-cell distortions are involved. We have taken all of these points into account in our three-dimensional model described in this paper, which can give a full description of both the first and the second

kind of domain walls mentioned above. Analytic expressions of the order-parameter profiles for a 180° twin and a 90° twin were derived, although special parameters were chosen in order to get the 90° twin solution. The boundary conditions and the associated shape change were also addressed in our model. The expansion coefficients in the free-energy equation (2.1) can be determined experimentally, which enables one to apply the present model to a real system.[12]

This paper is divided into six sections. We introduce the theoretical model in Sec. II. Sections III-V are the solutions for the tetragonal phase with a homogeneous structure, 180° twin, and 90° twin, respectively. Section VI contains the summary and conclusions.

II. THEORETICAL MODEL

The order parameter for describing the O_h-C_{4v} proper ferroelectric phase transition is the polarization vector **P**. The free-energy density, which is invariant under O_h symmetry, can be written as

$$F(P_i,P_{i,j},\eta_{kl})=F_L(P_i)+F_{el}(\eta_{kl})$$
$$+F_c(P_i,\eta_{kl})+F_G(P_{i,j}) . \qquad (2.1)$$

We should emphasize here that **P** is the material measure of polarization which ensures the invariant nature of the free energy.[13] The first term in Eq. (2.1) is the Landau-Devonshire free energy:

$$F_L(P_i)=\alpha_1(P_1^2+P_2^2+P_3^2)+\alpha_{11}(P_1^2+P_2^2+P_3^2)^2+\alpha_{12}(P_1^2P_2^2+P_2^2P_3^2+P_1^2P_3^2)+\alpha_{111}(P_1^6+P_2^6+P_3^6)$$

$$+\alpha_{112}[P_1^4(P_2^2+P_3^2)+P_2^4(P_1^2+P_3^2)+P_3^4(P_1^2+P_2^2)]+\alpha_{123}P_1^2P_2^2P_3^2 , \qquad (2.2)$$

where α_{11} is negative for describing a first-order transition. The second term in Eq. (2.1) is the elastic energy of the system,

$$F_{el}(\eta_{kl})=\frac{C_{11}}{2}(\eta_{11}^2+\eta_{22}^2+\eta_{33}^2)+C_{12}(\eta_{11}\eta_{22}+\eta_{11}\eta_{33}+\eta_{22}\eta_{33})+2C_{44}(\eta_{12}^2+\eta_{13}^2+\eta_{23}^2) . \qquad (2.3)$$

$\eta_{kl}=\frac{1}{2}(u_{k,l}+u_{l,k})$ $(k,l=1,2,3)$ is the linear elastic strain tensor which serves as a secondary order parameter here, u_k is the component of elastic displacement, C_{ij} are the second-order elastic constants. The third term in Eq. (2.1) represents the coupling between the primary and the secondary order parameters:

$$F_c(P_i,\eta_{kl})=-q_{11}(\eta_{11}P_1^2+\eta_{22}P_2^2+\eta_{33}P_3^2)-q_{12}[\eta_{11}(P_2^2+P_3^2)+\eta_{22}(P_1^2+P_3^2)+\eta_{33}(P_1^2+P_2^2)]$$

$$-2q_{44}(\eta_{12}P_1P_2+\eta_{13}P_1P_3+\eta_{23}P_2P_3) , \qquad (2.4)$$

q_{ij} are the electrostrictive constants. The fourth term in Eq. (2.1) is the gradient energy of the lowest-order compatible with the cubic symmetry, which has the invariant form

$$F_G(P_{i,j})=\frac{1}{2}g_{11}(P_{1,1}^2+P_{2,2}^2+P_{3,3}^2)$$

$$+g_{12}(P_{1,1}P_{2,2}+P_{1,1}P_{3,3}+P_{2,2}P_{3,3})$$

$$+\frac{g_{44}}{2}[(P_{1,2}+P_{2,1})^2+(P_{1,3}+P_{3,1})^2$$

$$+(P_{2,3}+P_{3,2})^2] . \qquad (2.5)$$

All the expansion coefficients in Eqs. (2.2)-(2.5) are assumed to be independent of temperature except α_1 in Eq. (2.2), which signifies that the transition is proper ferroelectric.

For convenience we define the following new constants:

$$\hat{C}_{11}=C_{11}+2C_{12} , \qquad (2.6a)$$

$$\hat{C}_{22}=C_{11}-C_{12} , \qquad (2.6b)$$

$$\hat{q}_{11}=q_{11}+2q_{12} , \qquad (2.7a)$$

$$\hat{q}_{22}=q_{11}-q_{12} . \qquad (2.7b)$$

They are the bulk and shear elastic constants and electrostrictive constants, respectively.

III. STATIC EQUILIBRIUM CONDITIONS AND THE HOMOGENEOUS SOLUTIONS

The static equilibrium conditions can be derived from the total energy expansion by using variational method, which gives rise to the Euler equations for the primary and secondary order parameters:

$$\frac{\partial}{\partial x_j}\left[\frac{\partial F}{\partial P_{i,j}}\right]-\frac{\partial F}{\partial P_i}=0 \quad (i,j=1,2,3) , \qquad (3.1)$$

$$\sigma_{ij,j}^{tot}=\frac{\partial}{\partial x_j}\left[\frac{\partial F}{\partial \eta_{ij}}\right]=0 \quad (i,j=1,2,3) . \qquad (3.2)$$

The Cauchy stress tensor σ_{ij}^{tot} includes contributions from the pure elastic response and the electrostrictive effect.

In order to avoid the complication of defects, we only consider the case for which no dislocations and disclinations are generated in the structural phase transition, which means that the following compatibility relations[14] must also be satisfied:

$$\epsilon_{ikl}\epsilon_{jmn}\eta_{ln,km}=0 \quad (i,j,k,l,m,n=1,2,3) , \qquad (3.3)$$

where ϵ_{ikl} is the permutation symbol (or Levi-Civita density).

For a homogeneous system, all physical quantities are uniform in space, hence, Eq. (3.3) becomes trivial and Eqs. (3.1) and (3.2) reduce to the following simple equations:

$$\frac{\partial F}{\partial P_i} = 0 , \qquad (3.4)$$

$$\sigma_{ij}^{\text{tot}} = \text{const} = 0 . \qquad (3.5)$$

We have set the constant in Eq. (3.5) to zero, assuming that the system being studied is free of external stresses.

Equations (3.4) and (3.5) can be easily solved, there are four different temperature ranges which we will discuss separately. It is customary to assume that α_1 depends linearly on temperature, i.e., $\alpha_1 = \alpha_0(T - T_0)$, where α_0 is positive definite, then the solutions for the homogeneous system are the following.

(i) For $T > T_1$ where

$$T_1 = T_0 + \frac{\alpha_{11}'^2}{3\alpha_0\alpha_{111}} ,$$

$$\alpha_{11}' = \alpha_{11} - \frac{\hat{q}_{11}^2}{6\hat{C}_{11}} - \frac{\hat{q}_{22}^2}{3\hat{C}_{22}} ,$$

$$P_i = 0, \quad \eta_{ij} = 0 \quad (i,j = 1,2,3) , \qquad (3.6)$$

only the cubic phase exists.

(ii) For $T_1 > T > T_c$, where $T_c = T_0 + \alpha_{11}'^2/4\alpha_0\alpha_{111}$, there are two solutions:

(a) $P_i = 0, \quad \eta_{ij} = 0 \quad (i,j = 1,2,3)$ \qquad (3.7)

and

(b) $\mathbf{P} = (\pm P_0, 0, 0), (0, \pm P_0, 0), (0, 0, \pm P_0)$ \qquad (3.8)

with

$$P_0 = \left[\frac{-\alpha_{11}' + (\alpha_{11}'^2 - 3\alpha_1\alpha_{111})^{1/2}}{3\alpha_{111}} \right]^{1/2} , \qquad (3.9)$$

$$\eta_\parallel = \frac{P_0^2}{3} \left[\frac{\hat{q}_{11}}{\hat{C}_{11}} + \frac{2\hat{q}_{22}}{\hat{C}_{22}} \right] , \qquad (3.10)$$

$$\eta_\perp = \frac{P_0^2}{3} \left[\frac{\hat{q}_{11}}{\hat{C}_{11}} - \frac{\hat{q}_{22}}{\hat{C}_{22}} \right] , \qquad (3.11)$$

$$\eta_{ij} = 0 \quad (i \neq j) . \qquad (3.12)$$

Here $\eta_\parallel$ and $\eta_\perp$ are the normal strain components in the directions parallel and perpendicular to the tetragonal axis in each of the three tetragonal states, respectively.

Solution (a) represents a thermodynamically stable cubic phase and (b) indicates that an additional tetragonal metastable phase also exists in this temperature region. This metastable phase can be stabilized to become the ferroelectric phase with further cooling. T_c is the phase-transition temperature at which the free energies of the

cubic and tetragonal phases are equal.

(iii) For $T_c \geq T > T_0$, solutions (a) and (b) in (ii) exist, but in this temperature region the tetragonal phase becomes thermodynamically stable and the cubic phase becomes metastable.

(iv) For $T < T_0$, only the tetragonal phase exists [solutions (b) in (ii)].

IV. 180° TWIN SOLUTION

Twinning exists because of the coexistence of several energetically degenerate variants in the low-temperature phase. The domain wall represents a transition region between two tetragonal variants, where the lattice structure is distorted, so that the formation of domain walls introduces inhomogeneity to the system. The 180° twins represent one kind of inhomogeneous structure, which consists of two variants whose polarizations are 180° out of phase. The tetragonal axes of these two domains are the same. A continuous space profile of a 180° twin can be obtained by solving Eqs. (3.1)–(3.3) under specified boundary conditions. Taking, for example, the two variants $(0, 0, \pm P_0)$ to form a [100] 180° twin, the boundary conditions are

$$\lim_{x_1 \to \pm\infty} P_3(x_1) = \pm P_0 , \qquad (4.1)$$

$$\lim_{x_1 \to \pm\infty} \sigma_{ij}^{\text{tot}}(x_1) = 0 \quad \text{for } ij = 11, 22, 33 , \qquad (4.2)$$

$$\sigma_{ij}^{\text{tot}}(x_1) = 0 \quad \text{for } ij = 23, 13, 12 . \qquad (4.3)$$

Here Eq. (4.1) states that the polarization component $P_3(x_1)$ should match one of the two values corresponding to the two variants far from the domain wall; Eqs. (4.2) and (4.3) represent, respectively, that the system is free from mechanical stresses in the homogeneous region $(|x_1| \to \infty)$ and there are no shear stresses in the entire system.

We assume a Q1D solution exists and make the following ansatz for the primary and secondary order parameters,

$$\mathbf{P} = (0, 0, P_3(x_1)) , \qquad (4.4)$$

$$\eta_{ij} = \eta_{ij}(x_1) . \qquad (4.5)$$

Substituting Eqs. (4.4) and (4.5) into Eqs. (3.1)–(3.3) generates a second-order nonlinear differential equation for $P(x_1)$

$$2\alpha_1^+ P_3 + 4\alpha_{11}^+ P_3^3 + 6\alpha_{111} P_3^5 - g_{11} P_{3,11} = 0 \qquad (4.6)$$

with

$$\alpha_1^+ = \alpha_1 - \left[\frac{\hat{C}_{22}}{C_{11}} q_{12}\eta_\perp + \left(q_{11} - \frac{C_{12}}{C_{11}} q_{12} \right)\eta_\parallel \right] , \qquad (4.7)$$

$$\alpha_{11}^+ = \alpha_{11} - \frac{q_{12}^2}{2C_{11}} . \qquad (4.8)$$

Equation (4.6) has a kink solution[15] which satisfies the boundary condition (4.1)

$$P_3(x_1) = \frac{P_0 \sinh(x_1/\xi_{180})}{[A + \sinh^2(x_1/\xi_{180})]^{1/2}} , \qquad (4.9)$$

where $\sinh(y)$ is the hyperbolic sine function and

$$\xi_{180} = \frac{\sqrt{g_{11}}}{P_0(6\alpha_{111}P_0^2 + 2\alpha_{11}^+)^{1/2}} , \qquad (4.10a)$$

$$A = \frac{(3\alpha_{111}P_0^2 + \alpha_{11}^+)}{(2\alpha_{111}P_0^2 + \alpha_{11}^+)} . \qquad (4.10b)$$

The elastic strain field associated with the 180° twin solution can be derived from Eqs. (3.2) and (3.3) together with the Q1D solution (4.9),

$$\eta_{22} = \eta_\perp , \qquad (4.11a)$$

$$\eta_{33} = \eta_\perp , \qquad (4.11b)$$

$$\eta_{11} = \eta_\perp - \frac{q_{12}}{C_{11}} \frac{P_0^2}{1 + A^{-1}\sinh^2(x_1/\xi_{180})} , \qquad (4.11c)$$

$$\eta_{12} = 0 , \qquad (4.11d)$$

$$\eta_{13} = 0 , \qquad (4.11e)$$

$$\eta_{23} = 0 . \qquad (4.11f)$$

The kink solution (4.9) gives the continuous space profile of polarization for a 180° twin in the tetragonal phase. A planar domain wall which bridges the $(0,0,-P_0)$ and $(0,0,P_0)$ states is located at $x_1 = 0$ in our coordinate system. Note that the strain components Eqs. (4.11a)–(4.11f) were derived under the assumption that the twin structure is free of defects, i.e., the distortion caused by the presence of a domain wall is purely displacive, no atoms are lost or gained in forming the twin. It can be seen from Eqs. (4.11a)–(4.11f) that all the strain components of a twin structure are the same as those for a single domain tetragonal system except η_{11} [Eq. (4.11c)]. In other words, the distortion caused by the Q1D domain wall is only in the x_1 direction. The displacement u with respect to the cubic structure can be easily integrated from Eqs. (4.11a)–(4.11d),

$$u = \begin{vmatrix} \eta_\perp x_1 + \Delta u \\ \eta_\perp x_2 \\ \eta_\parallel x_3 \end{vmatrix} \qquad (4.12)$$

with

$$\Delta u = -\frac{q_{12}}{C_{11}} P_0^2 \xi_{180}\xi_1 \text{arctanh} \left[\frac{1}{\xi_1}\tanh(x_1/\xi_{180})\right] , \qquad (4.13)$$

$$\xi_1 = \left[3 + \frac{\alpha_{11}^+}{\alpha_{11}P_0^2}\right]^{1/2} . \qquad (4.14)$$

Since the electrostrictive constant q_{12} is usually negative, there is an expansion in the x_1 dimension associated with

the 180° wall, with the amount of

$$\Delta L_1 = -2\frac{q_{12}}{C_{11}}\xi_1\xi_{180}\text{arctanh}\left[\frac{1}{\xi_1}\right] . \qquad (4.15)$$

It was proved[11] that the dimensional changes are correlated under the elastic compatibility constraints, Eq. (3.3). Therefore, in order to sustain the displacive change in the x_1 direction without affecting the other two dimensions, we need to apply inhomogeneous stresses on the lateral surfaces; these required stresses are

$$\sigma_{22}^{\text{tot}} = \frac{(\hat{C}_{22}/C_{11})q_{12}P_0^2}{1 + A^{-1}\sinh^2(x_1/\xi_{180})} , \qquad (4.16)$$

$$\sigma_{33}^{\text{tot}} = \frac{[q_{11} - (C_{12}/C_{11})q_{12}]P_0^2}{1 + A^{-1}\sinh^2(x_1/\xi_{180})} . \qquad (4.17)$$

It is interesting to compare the 180° twin solution here with the antiphase solution obtained in Ref. 16. Although the forms representing the coupling between the order parameter and the elastic strain were taken to be identical (determined by the cubic symmetry) in the two cases, the underlying physics is different. For the antiphase solution, the rotation axes of the octahedra are the same in the two domains divided by an antiphase boundary, which implies that the tetragonal axis must be perpendicular to the antiphase boundary plane; but, for the 180° ferroelectric twin discussed here, charge neutrality is a prerequisite to ensure a stable static configuration, which means that the polarization vectors and, hence, the tetragonal axes of the two domains are parallel to the twin boundary plane. As a consequence of this difference, the normal-surface stresses required in the two lateral directions for supporting the Q1D solutions become distinct for the 180° ferroelectric twin but are the same for the antiphase solution. Another obvious difference between the two cases is the functional form of the order-parameter profile: a ϕ^4-type kink (second-order phase transition) in Ref. 16 but a ϕ^6-type kink (first-order phase transition) in this paper. In addition, since the coupling constants q_{11} and q_{12} (B_1 and B_2 in Ref. 16) have opposite sign, the antiphase boundary induces shrinkage but the 180° twin boundary causes expansion in the dimension along the twin (antiphase) boundary normal.

There is a certain amount of energy stored in the 180° domain wall. We define the energy density per unit area for a single domain wall to be E_{180}, which is a function of temperature only and is given by

$$E_{180} = \int_{-\infty}^{\infty} (F - F_0)dx_1 . \qquad (4.18)$$

Here F_0 is the energy density of a homogeneous system at a given temperature. The integration of Eq. (4.18) can be carried out by substituting the solutions (4.9)–(4.11) into Eq. (2.1). After some algebra, a closed form can be obtained,

$$E_{180} = \left[\frac{2g_{11}}{\alpha_{111}}\right]^{1/2}\left\{\frac{\alpha_{11}^+}{2}P_0\left[3P_0^2 + \frac{\alpha_{11}^+}{\alpha_{111}}\right]^{1/2} - \left[\frac{\alpha_{11}^{+2}}{4\alpha_{111}} - \alpha_1^+\right]\text{arcsinh}\frac{P_0}{(2P_0^2 + \alpha_{11}^+/\alpha_{111})^{1/2}}\right\} . \qquad (4.19)$$
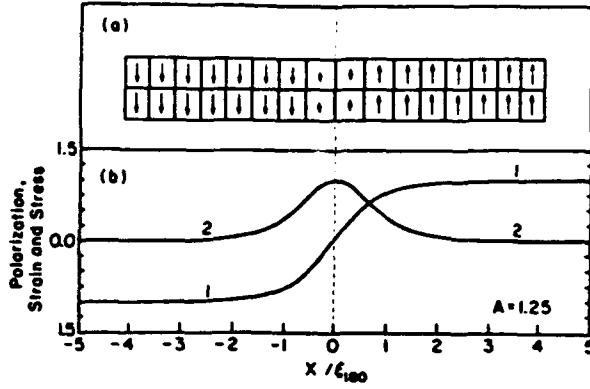
FIG. 1. 180° twin solution. (a) Illustration of polarization and unit-cell distortion in a 180° twin structure represented by a continuum solution. (b) Space profile of normalized polarization P/P_0 (curve 1) and normalized inhomogeneous components of strain $-(C_{11}/q_{12}P_0^2)(\eta_{11}-\eta_\perp)$, and stresses $(C_{11}/\hat{C}_{22}q_{12}P_0^2)\sigma_{22}^{tot}$ and $[q_{11}-(C_{12}/C_{11})q_{12}]^{-1}P_0^{-2}\sigma_{33}^{tot}$ (curve 2).

For $T < T_c$, $E_{180°}$ is positive definite (see arguments below), so that a twin structure has higher energy compared to a single domain structure. As mentioned above, external constraints are needed to stabilize base twin solution; these are often provided by surface stresses or intergranular interaction in a polycrystal (or ceramic) system. It should be pointed out that defects play a very important role in stabilizing the twin structures in a real system, but it is beyond the scope of this paper.

In Fig. 1(b) are plots of polarization, strain, and stress profiles in dimensionless form, each physical quantity has been rescaled with a different scaling factor. The polarization and unit-cell distortion represented by the solutions are illustrated in Fig. 1(a).

V. 90° TWIN SOLUTION

The other type of stable twin structure in the tetragonal phase besides the 180° twin is the 90° twin, which consists of two domains whose tetragonal axes (or polarizations) are (almost) perpendicular to each other. Since the twin structure with charged twin boundary (with polarizations head-to-head or tail-to-tail) has additional Coulomb energy, only the twin structure with charge neutral boundary (head-to-tail configuration) is a stable configuration for the 90° twin.

We consider a twin structure of the two following variants: $\mathbf{P}_1 = (P_0,0,0)$ and $\mathbf{P}_2 = (0,P_0,0)$, with the twin boundary oriented in [110]. It is convenient to work in a new coordinate system (s,r,x_3) which is a 45° rotation of the x_1-x_2 plane around x_3. The two coordinate systems, the structure and the polarization configurations, are shown in Fig. 2. We choose a system with its dimension along the s coordinate much larger than the other dimensions in order to set up the boundary conditions $(L_s \sim \infty \gg L_r, L_3)$, and assume that the space profile of the polarization vector of the system is quasi-one-dimensional, i.e., it depends on the space variable s only. Our goal is to seek solution of the kind $\mathbf{P} = [P_1(s), P_2(s), 0]$ for the 90° twin structure, which satisfies the boundary conditions

$$\lim_{s \to -\infty} \mathbf{P} = (P_0,0,0)$$

and

$$\lim_{s \to +\infty} \mathbf{P} = (0,P_0,0) .$$

In order to use this Q1D nature to our advantage, we will convert all quantities into the new coordinate system, the polarization becomes $\mathbf{P} = [P_s(s), P_r(s), 0]$, and the free energy of this 90° twin can be written as

$$F_{90°} = \alpha_1(P_s^2 + P_r^2) + \alpha_{11}(P_s^2 + P_r^2)^2 + \frac{\alpha_{12}}{4}(P_s^2 - P_r^2)^2 + \alpha_{111}(P_s^2 + P_r^2)^3 + \frac{\alpha_{112} - 3\alpha_{111}}{4}(P_s^4 - P_r^4)(P_s^2 - P_r^2)$$

$$+ \frac{G_{ss}}{2}P_{s,s}^2 + \frac{G_{rs}}{2}P_{r,s}^2 + F_{el}(\eta_{kl}) + F_c(P_s,P_r,\eta_{kl}) \quad (k,l = r,s,x_3) , \tag{5.1}$$

where

$$G_{ss} = (g_{11} + g_{12} + 2g_{44})/2 , \tag{5.2a}$$

$$G_{rs} = (g_{11} - g_{12})/2 , \tag{5.2b}$$

$F_{el}(\eta_{kl})$ and $F_c(P_s,P_r,\eta_{kl})$ are the elastic and coupling energies [Eqs. (2.3) and (2.4)], respectively, in the new coordinate system.

The boundary conditions as $s \to \pm\infty$ are, for the polarization and strain components, respectively,

$$\lim_{s \to \pm\infty} P_s = \frac{P_0}{\sqrt{2}} , \tag{5.3a}$$

$$\lim_{s \to \pm\infty} P_r = \pm\frac{P_0}{\sqrt{2}} , \tag{5.3b}$$

$$\lim_{s \to \pm\infty} \eta_{rr} = \lim_{s \to \pm\infty} \eta_{ss} \tag{5.3c}$$

$$= (\eta_\parallel + \eta_\perp)/2 , \tag{5.3d}$$

$$\lim_{s \to \pm\infty} \eta_{sr} = \pm(\eta_\parallel - \eta_\perp)/2 . \tag{5.3e}$$

In addition, there should be no mechanical constraints in the single domain states $(s \to \pm\infty)$ and no shear stress in the x_3 direction. These arguments lead to the mechanical boundary conditions

$$\lim_{s \to \pm\infty} \sigma_{ij}^{tot}(s) = 0 \quad (i,j = r,s,x_3) , \tag{5.4}$$

$$\sigma_{s3} = \sigma_{r3} = 0 . \tag{5.5}$$

The compatibility relations (3.3) give three nontrivial
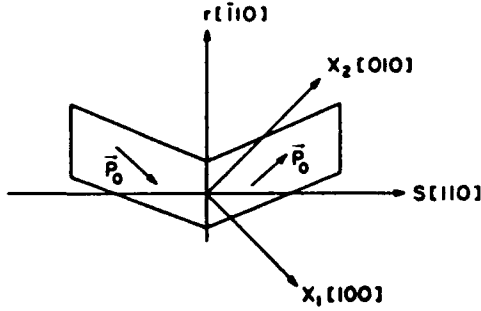
FIG. 2. (001) cross section of a 90° twin crystal with a twin boundary at $s=0$. The orientation of the new and old axes are shown in the figure, and the directions of the polarizations in the two domains are also indicated.

constraints for the twin solution. They are, in the new coordinate system,

$$\eta_{rr,ss}=0 , \tag{5.6a}$$

$$\eta_{33,ss}=0 , \tag{5.6b}$$

$$\eta_{rs,ss}=0 . \tag{5.6c}$$

These equations (5.6a)–(5.6c) together with the boundary conditions (5.3) and (5.5), can determine four of the six independent strain components; they are

$$\eta_{r3}=\eta_{s3}=0 , \tag{5.7a}$$

$$\eta_{rr}=\tfrac{1}{2}(\eta_{\parallel}+\eta_{\perp}) , \tag{5.7b}$$

$$\eta_{33}=\eta_{\perp} . \tag{5.7c}$$

These four components are constants in space since the quantities $\eta_{\parallel}$ and $\eta_{\perp}$ are functions of temperature only. The other two of the six independent strain components are inhomogeneous and strongly coupled to the primary order parameter. From Eq. (3.2) and the boundary conditions (5.4), we have

$$\eta_{rs}=(\hat{q}_{22}/\hat{C}_{22})P_sP_r , \tag{5.8}$$

$$\eta_{ss}=\tfrac{1}{2}(\eta_{\parallel}+\eta_{\perp})$$
$$-\frac{1}{2C_{ss}}\{(q_{11}+q_{12})[P_0^2-(P_s^2+P_r^2)]$$
$$-q_{44}(P_s^2-P_r^2)\} , \tag{5.9a}$$

where

$$C_{ss}=\frac{C_{11}+C_{12}}{2}+C_{44} . \tag{5.9b}$$

By using these strain solutions and the definitions of $\eta_{\parallel}$ and $\eta_{\perp}$, we can explicitly write the equilibrium conditions (3.1) in the rotated coordinate system:

$$G_{ss}P_{s,ss}=2\alpha_1^sP_s+4\alpha_{11}^sP_s^3+4\alpha_{11}^{sr}P_sP_r^2$$
$$+\tfrac{1}{2}(\alpha_{111}+\alpha_{112})P_s^5+(15\alpha_{111}-\alpha_{112})P_s^3P_r^2$$
$$+\tfrac{1}{2}(15\alpha_{111}-\alpha_{112})P_sP_r^4 , \tag{5.10a}$$

$$G_{rs}P_{r,ss}=2\alpha_1'P_r+4\alpha_{11}'P_r^3+4\alpha_{11}^{sr}P_rP_s^2$$
$$+\tfrac{1}{2}(\alpha_{111}+\alpha_{112})P_s^5+(15\alpha_{111}-\alpha_{112})P_r^3P_s^2$$
$$+\tfrac{1}{2}(15\alpha_{111}-\alpha_{112})P_rP_s^4 , \tag{5.10b}$$

where

$$\alpha_1^s=\alpha_1-\left[\frac{1}{3}\frac{\hat{q}_{11}^2}{\hat{C}_{11}}+\frac{1}{6}\frac{\hat{q}_{22}^2}{\hat{C}_{22}}\right.$$
$$\left.-\frac{(q_{11}+q_{12})(q_{11}+q_{12}+q_{44})}{4C_{ss}}\right]P_0^2 , \tag{5.11a}$$

$$\alpha_1'=\alpha_1-\left[\frac{1}{3}\frac{\hat{q}_{11}^2}{\hat{C}_{11}}+\frac{1}{6}\frac{\hat{q}_{22}^2}{\hat{C}_{22}}\right.$$
$$\left.-\frac{(q_{11}+q_{12})(q_{11}+q_{12}-q_{44})}{4C_{ss}}\right]P_0^2 , \tag{5.11b}$$

$$\alpha_{11}^s=\alpha_{11}+\frac{\alpha_{12}}{4}-\frac{(q_{11}+q_{12}+q_{44})^2}{8C_{ss}} , \tag{5.11c}$$

$$\alpha_{11}'=\alpha_{11}+\frac{\alpha_{12}}{4}-\frac{(q_{11}+q_{12}-q_{44})^2}{8C_{ss}} , \tag{5.11d}$$

$$\alpha_{11}^{sr}=\alpha_{11}-\frac{\alpha_{12}}{4}-\frac{(q_{11}+q_{12})^2-q_{44}^2}{8C_{ss}}-\frac{\hat{q}_{22}^2}{2\hat{C}_{22}} . \tag{5.11e}$$

In general, Eqs. (5.10a) and (5.10b) have to be solved numerically. All the coefficients may be determined from dielectric, electrostrictive, and elastic measurements, and from phonon dispersion curves for a given system. We will show this numerical procedure elsewhere.[12]

Putting the quantitative individual characters of each specific system aside in the following, we will abstract the common features of a 90° twin solution by choosing some of the parameters to special values. For instance, if

$$\alpha_{11}^{sr}=0 , \tag{5.12}$$

$$15\alpha_{111}=\alpha_{112} , \tag{5.13}$$

then we can obtain analytic solutions for P_s and P_r from Eqs. (5.10a) and (5.10b),

$$P_s=\frac{1}{\sqrt{2}}P_0 , \tag{5.14a}$$

$$P_r=\frac{1}{\sqrt{2}}P_0\frac{\sinh(s/\xi_{90})}{[B+\sinh^2(s/\xi_{90})]^{1/2}} , \tag{5.14b}$$

where

$$\xi_{90}=\frac{1}{P_0}\left[\frac{G_{rs}}{6\alpha_{111}P_0+\alpha_{11}'}\right]^{1/2} . \tag{5.15a}$$

$$B=\frac{6\alpha_{111}P_0^2+\alpha_{11}'}{4\alpha_{111}P_0^2+\alpha_{11}'} . \tag{5.15b}$$

The two inhomogeneous strain components, Eqs. (5.8) and (5.9), now become

$$\eta_{rs} = (\hat{q}_{22}/2\hat{C}_{22})P_0^2 \frac{\sinh(s/\xi_{90})}{[B+\sinh^2(s/\xi_{90})]^{1/2}} , \quad (5.16a)$$

$$\eta_{ss} = \frac{1}{2}(\eta_{\parallel}+\eta_{\perp})$$

$$- \frac{P_0^2}{4C_{ss}}(q_{11}+q_{12}-q_{44})\frac{1}{1+B^{-1}\sinh^2(s/\xi_{90})} . \quad (5.16b)$$

Equation (5.16a) describes the shape change (or bending) caused by the 90° twinning and Eq. (5.16b) indicates a dimensional change in the s direction with the total amount of

$$\Delta L_s = -\frac{\xi_{90}P_0^2}{2C_{ss}}(q_{11}+q_{12}-q_{44})$$

$$\times \left[\frac{B}{B-1}\right]^{1/2} \ln(\sqrt{B}+\sqrt{B-1}) . \quad (5.17)$$

Note the mathematical forms of Eqs. (4.15) and (5.17) are interconvertible. The two position-dependent normal strain components, which are required to support the Q1D solution, are given by

$$\sigma_{rr}^{tot} = \frac{P_0^2}{4C_{ss}}[2C_{44}(q_{11}+q_{12})+(C_{11}+C_{12})q_{44}]$$

$$\times \frac{1}{1+B^{-1}\sinh^2(s/\xi_{90})} , \quad (5.18a)$$

$$\sigma_{33}^{tot} = \frac{P_0^2}{4C_{ss}}[-C_{44}(q_{11}-q_{44})+(C_{11}+2C_{44})q_{12}]$$

$$\times \frac{1}{1+B^{-1}\sinh^2(s/\xi_{90})} . \quad (5.18b)$$

Similar to Eqs. (3.18) and (3.19), the energy density stored in this 90° domain wall can be obtained from the analytic solution, (5.14a) and (5.14b),

$$E_{90°} = \left[\frac{G_{rs}}{2\alpha_{111}}\right]^{1/2}\left[\frac{\alpha_{11}'P_0}{4}\left[3P_0^2+\frac{\alpha_{11}'}{2\alpha_{111}}\right]^{1/2} - \left[\frac{\alpha_{11}^2}{16\alpha_{111}}-\alpha_1'\right]\text{arcsinh}\frac{P_0}{(2P_0^2+\alpha_{11}'/2\alpha_{111})^{1/2}}\right] . \quad (5.19)$$

For a static configuration, $E_{90°}>0$, which may not be obvious from Eq. (5.19) but can be proved to be true for more general cases. According to definition we can write the energy density of the 90° domain wall as

$$E_{90°} = \int_{-\infty}^{\infty}[F(P_i,P_{i,j})-F_L(P_0)]ds$$

$$= 2\int_{-\infty}^{\infty}[F_L(P_i)-F_L(P_0)]ds . \quad (5.20)$$

Here Eqs. (5.10a) and (5.10b) have been used, $F_L(P_i)$ is the Landau energy which has a minimum value $F_L(P_0)$ for $T < T_c$, i.e., $F_L(P_i) > F_L(P_0)$ for $P_i \neq P_0$, therefore the integral in Eq. (5.20) is a positive value, hence, $E_{90°}>0$. The same argument also applies to $E_{180°}$ obtained in Sec. IV.

Figure 3(a) illustrates the 90° ferroelectric twin structure and the associated elastic distortion. In the twin boundary region, not only the rotation of polarization vector occurs, the magnitude of the polarization also changes in space as shown in Fig. 3(b). For the special choice of parameters, Eqs. (5.12) and (5.13), the magnitude of polarization is

$$|P| = P_0\left[\frac{(B/2)+\sinh(s/\xi_{90})}{B+\sinh(s/\xi_{90})}\right]^{1/2} \leq P_0 , \quad (5.21)$$

which is less or equal to the polarization in the single-phase region. For other choices of the parameters, or in real system, Eq. (5.21) may not be true.

VI. SUMMARY AND CONCLUSIONS

Based on Landau-Ginzburg theory, a continuum model has been developed for the twin structure in tetragonal
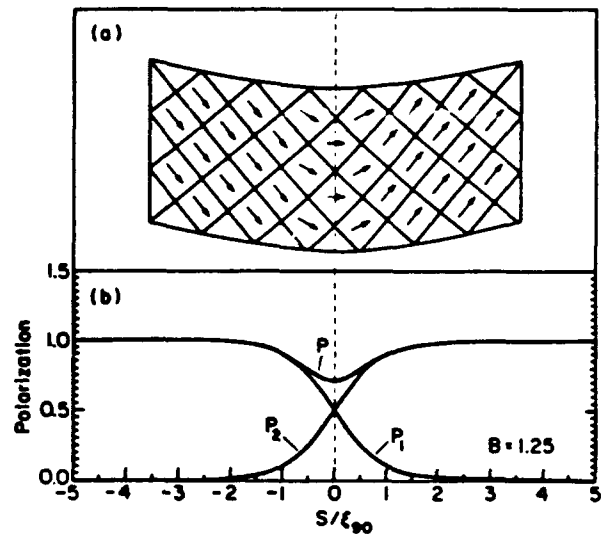

FIG. 3. 90° twin solution. (a) Illustration of the polarization variation and unit-cell distortion. (b) Space profiles of the normalized polarization components P_1, P_2, and the magnitude P, the parameters have been set to satisfy Eqs. (5.12) and (5.13).

ferroelectric perovskites, which is a three-dimensional ϕ^6 model with the primary order parameter chosen to be the material measure of polarization. Under the assumption of a coherent interface, the model can describe the O_h-C_{4v} first-order proper ferroelectric phase transition and gives rise to the space profiles of a 180° twin and a 90° twin with charge-neutral twin boundary.

The ferroelectric phase transitions are often accompanied by unit-cell distortions (in certain cases the distortions could be very large); therefore, a proper ferroelectric is usually an improper ferroelastic. The second-order improper ferroelastic phase transition has been addressed in Ref. 16; that model can also describe a second-order ferroelectric phase transition with proper physical constraints, such as the orientational relationship between tetragonal axes of domains and the twin boundary. For the same reason, the ferroelectric ϕ^6 model developed in this paper may also be generalized to describe other improper ferroelastic systems.

It is interesting to see that the coupling of the order parameter to strain has different effects in the case of second-order and first-order phase transitions.[11,17] The transition temperature is the same for the former, but will be shifted for the latter resulting from this coupling and the imposed boundary conditions.

Due to the nonlocal coupling of the polarization, the domain walls acquire finite width. In addition, as shown in Fig. 3(a), the crystallographic symmetry is lower in the 90° domain-wall region. At the domain-wall center, the structure is quasiorthorhombic, which implies that the 90° domain walls are natural nucleation sites for the tetragonal-orthorhombic transition if the orthorhombic phase happens to be the next low-temperature thermodynamically stable phase.

We have also proved in Sec. V that both 180° and 90° domain walls contain positive energy, so that the existence of a stable Q1D twin structure must be supported by either inhomogeneous (internal or external) stress distribution or by defects. In a ceramic system the stresses are provided by intergranular coupling. This implies that the stress concentration at the grain boundaries is inho-

mogeneous.

An important application of any ferroelectric material is based on its piezoelectric effect. Strictly speaking, the macroscopic piezoelectric effect comes from two different origins: For a single domain single crystal, the induced strain is due to the direct coupling of the polarization to the unit-cell distortion, which, in our case, is proportional to the square of polarization. Therefore, the intrinsic piezoelectric constants are proportional to the product of the electrostrictive constants and the components of spontaneous polarization. For a multidomain system, such as a ceramic, there are additional contributions from the motion of 90° domain walls, which can be understood from Fig. 3(a). We can clearly see a shape change associated with the misalignment of polarization vectors in the two domains. A lattice movement of an entire domain in the direction parallel to the twin boundary plane can be generated by the motion of a 90° domain wall along its normal direction. We define this additional piezoelectric effect as the "orientational effect," it is extrinsic in nature. The strength of this effect is determined by the degree of unit-cell distortion (relative to the cubic structure) and the maximum distance which a domain wall can move without breaking the atomic coherency. Except in a single domain single crystal, these two effects exist simultaneously and interact with each other. In order to analyze this complicated process, one must know the detailed structure in the domain-wall region, which is one of the achievements of the present work. We will show in a forthcoming paper[12] how to determine those expansion coefficients from experiments so as to quantify the atomic displacements in a ferroelectric twin structure for a specific system.

ACKNOWLEDGMENTS

[1]M. E. Lines and A. M. Glass, *Principles and Applications of Ferroelectrics and Related Materials* (Clarendon, Oxford, 1979).

[2]E. K. W. Goo, R. K. Mishra, and G. Thomas, J. Appl. Phys. 52, 2939 (1981).

[3]P. G. Lucuta and V. Teodoresu, Appl. Phys. A 37, 237 (1985).

[4]Von Cieminski, C. Kleint, H. Beige, and R. Hoche, Ferroelectrics 109, 95 (1990).

[5]L. Pardo, J. Mendida, A. Gonzalez, and J. De. Frutos, Ferroelectrics 94, 189 (1990).

[6]G. Arlt, Ferroelectrics 76, 451 (1987).

[7]C. A. Randall, D. J. Barber, and R. W. Whatmore, J. Mater. Sci. 22, 925 (1987).

[8]V. A. Zhirnov, Zh. Eksp. Teor. Fiz. 35, 1175 (1958) [Sov. Phys. JETP 35, 822 (1959)].

[9]I. I. Ivanchik, Fiz. Tverd. Tela (Leningrad) 3, 3731 (1961) [Sov. Phys. Solid State 3, 2705 (1962)].

[10]L. N. Bulaevskii, Fiz. Tverd. Tela (Leningrad) 5, 3183 (1963) [Sov. Phys. Solid State 5, 2329 (1964)].

[11]W. Cao, G. R. Barsch, and J. A. Krumhansl, Phys. Rev. B 42, 6396 (1990).

[12]W. Cao (unpublished).

[13]G. R. Barsch, B. N. N. Achar, and L. E. Cross, Ferroelectrics 35, 187 (1981).

[14]E. A. N. Love, *A Treatise on the Mathematical Theory of Elasticity* (Dover, New York, 1944), p. 49.

[15]F. Falk, Z. Phys. B 51, 177 (1983).

[16]W. Cao and G. R. Barsch, Phys. Rev. B 41, 4334 (1990).

[17]J. Lajzerowicz, Ferroelectrics 35, 219 (1981).

APPENDIX 14

The extrinsic nature of nonlinear behavior observed in lead zirconate titanate ferroelectric ceramic

Shaoping Li, Wenwu Cao, and L. E. Cross
Materials Research Laboratory, The Pennsylvania State University, University Park, Pennsylvania 16802

The nonlinear electric and electromechanical responses of lead zirconate titanate $Pb(Zr_xTi_{1-x})O_3$ ceramics to an external ac electric field have been measured under different driving levels. The onset of measurable nonlinearity is observed to be accompanied by the appearance of hysteresis loops. This lossy nature suggests that the nonlinearities in a ferroelectric ceramic are generated by the domain-wall motion. In addition, aging experiments and the bias field dependence of the threshold field (onset of nonlinearity) all indicate the extrinsic nature of the nonlinear behavior of ferroelectric ceramics. A phenomenological theory of Arlt, Dederichs, and Herbiet [Ferroelectrics 74, 34 (1987)] has been extended to include the nonlinear contributions. With only 90° wall vibration being considered, the theory leads to some basic understanding of the experimental results.

I. INTRODUCTION

The study of the nonlinear behavior of piezoceramic materials is very important because ferroelectric ceramics are now widely used to make transducers, resonators, actuators, motors, sonars, etc. One of the limitations for practical use of these ceramic products is their nonlinear behavior, which occurs at higher driving levels. In order to optimize the performance of these ceramic devices, it is essential to understand the origin of the nonlinear properties in ferroelectric ceramics. Recent developments in the fabrication of ferroelectric thin films open up the possibility of utilizing these nonlinear properties, because now the nonlinear response can be observed under voltage as small as a few fractions of a volt. In fact, some applications of the nonlinear properties have already been made, for example, convolvers and correlators for microwave acoustic devices,[1-3] frequency mixers and frequency doublers. Therefore, the study of nonlinear effects in ferroelectric ceramics is not only scientifically interesting, but also technically important.

The physical origin of most phenomena observed in a ferroelectric ceramic is, in general, quite complex. For instance, the piezoelectric effect consists of two parts, the intrinsic[4] and the extrinsic piezoeffects.[5,6] The intrinsic effect refers to the homogeneous (unit cell) deformation caused by the electric field, and the extrinsic effect represents the elastic deformation caused by the motions of non-180° domain walls (partially domain switching) and the interphase interfaces.[7] It is believed that the piezoelectric effect of a ferroelectric ceramic comes mainly from extrinsic contributions at a relatively low to moderate driving level. Studies on barium titanate, $BaTiO_3$, and lead zirconate titanate (PZT), $Pb(Zr_xTi_{1-x})O_3$,[8] show that the extrinsic effect contributes 60%–70% of the piezomoduli observed experimentally. Microstructural analyses[9,10] reveal that a large number of 90° domain walls are present in ferroelectric ceramics, which strongly affect their electromechanical behavior.[11,12]

A number of researchers have looked at the nonlinear-ities of ferroelectrics.[13-15] However, most of the studies were focused on the intrinsic effect. The extrinsic effect is very complicated, because it involves interactions of several length scales, i.e., the interactions between ions, domains, and even different phases (such as in PZT). Therefore, it is very difficult to develop a detailed microscopic theory to account for the extrinsic effect. Arlt, Dederichs, and Herbiet[5,6] have proposed a formal phenomenological theory dealing with linear electromechanical properties related to 90° domain-wall motion, which might be a possible route to avoid some of the unnecessary complications. In this paper we will try to address the nonlinear effects resulting from a 90° domain-wall motion by using a similar idea. More importantly, we will present some experimental results which can provide evidence for the extrinsic nature of the nonlinearities in ceramics. It has been found that these nonlinearities are mainly from the nonlinear motion of non-180° domain walls.

II. EXPERIMENTS

A series of experiments were carried out on both soft and hard PZT systems. The instruments employed include an optical interferrometer,[16] HP4192 LF impedance analyzer, HP3586 spectrum analyzer, multifrequency LCR meter (HP4275A), a modified Sawyer–Tower circuit, and a strain gauge (Kyoan KRF-02(C1-11).

The piezoelectric constants d_{33}, d_{31}, and d_{15} of soft PZT were measured versus ac field strength at a frequency of 200 Hz. The results are shown in Fig. 1. Figure 2 shows the field dependence of ac dielectric constants ϵ_{11} and ϵ_{33} of soft PZT at 200 Hz. One can clearly see in Figs. 1 and 2 that these quantities depend strongly on the field strength. In addition, it is observed that the losses (both mechanical and electric) also increase with field strength as shown in the insert of Fig. 2 (hysteresis loop). The appearance of a hysteresis loop accompanying the onset of nonlinearity suggests that the source of these nonlinearities might come from the nonlinear response of the domain walls to external field, because domain-wall motion is known to be a
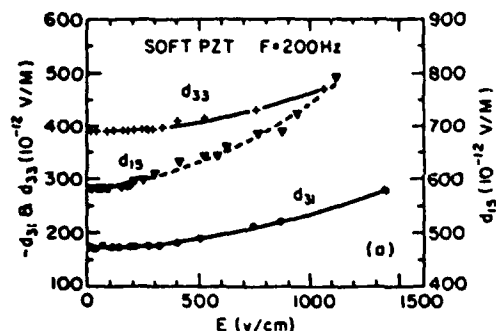
FIG. 1. Electric-field dependence of piezoelectric coefficients for d_{31}, d_{33}, and d_{15}.

FIG. 3. The threshold field of the dielectric constant ϵ_{33} for a poled soft PZT ceramic as a function of positive dc bias field and temperature. The frequency of the applied field is 200 Hz.

strong lossy process.[17,18] Observing Figs. 1 and 2, we find there is a relatively flat region in each of the curves, which implies that linear relations (d_{ij} and ϵ_{ij} are independent of applied field) between the applied electric field and the induced strain or polarization hold for small values of the field strength. We have defined a threshold field E_t at which $\Delta d/d(\Delta\epsilon/\epsilon) > 2.5\%$–$5\%$; the range of the percentages are based upon the uncertainties of the experiments. E_t signifies the onset of measurable nonlinearity. In general, the threshold field E_t is influenced by temperature, composition, frequency of the applied field, dc bias field, and time. E_t is a relative measure and may differ for different physical quantities. As an example, we show in Fig. 3 the change of the threshold field for ϵ_{33} with respect to temperature and dc bias field for a soft PZT sample. E_t increases with bias dc field. This is because the bias field shifts the working point of the poled ceramic toward a more saturated region on the P-E hysteresis loop. Looking at the microstructure, the domains are in better alignment under the bias field, and the domain walls become more difficult to move, which will reduce the extrinsic contribution. Hence the overall dielectric and piezoelectric constants become smaller; at the same time, the loss and nonlinearity are also substantially reduced. It is believed that the nonlinearity from the intrinsic contribution is very small. Therefore, when the domain-wall motion is "pinned" by the bias field, E_t becomes much larger; i.e., the

onset of measurable nonlinearity requires much larger field strength. Similarly, lowering temperature can also "freeze" the domain-wall motion, because the potential well of the low-temperature phase becomes deeper so that the energy barrier for domain switching becomes higher. Therefore, E_t will decrease with temperature as shown in Fig. 3. The clue for the extrinsic nature of nonlinearities observed in PZT ceramics is the drastic increase of dielectric loss accompanying the onset of nonlinearity as shown in Fig. 4. It is also shown in Fig. 4 that the loss decreases with frequency, reflecting the delayed response of the domain-wall motion to the high-frequency electric field.

In order to further the understanding of this matter, we have analyzed the spectrum of the response signals in both electric and electrochemical measurements, which are shown in Figs. 5(a) and 5(b). In Fig. 5(a) the electric field is parallel to the poling direction. When $E > E_t$, the output signal contains both odd and even harmonics, and a small asymmetric hysteresis loop was observed (note, that the maximum electric field strength is $0.57E_c$, where E_c is the coercive field of the ceramic used in the experiments). In Fig. 5(b) the electric field is perpendicular to the poling direction. For $E > E_t$, only odd harmonics were observed, and the small hysteresis loop observed is symmetric. An

FIG. 2. Electric-field dependence of dielectric coefficients ϵ_{11} and ϵ_{33}. The two inserts are the P-E relations at low and high electric fields, respectively.
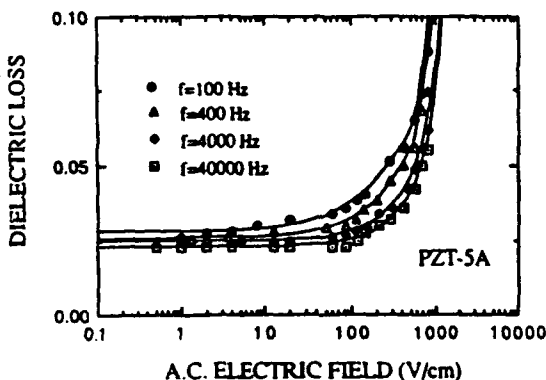
FIG. 4. Dependence of dielectric loss tan δ on the amplitude of the external ac field at different frequencies.

TABLE I. The magnitude of output voltage for the second and third-harmonic components under different ac electric-field strength. E_c is the coercive field.

The ac electric field	$0.008E_c$	$0.1E_c$	$0.39E_c$	$0.57E_c$	$0.64E_c$
The magnitude of V_1-V_2 (dB)	no higher harmonics detected	3.8	2.9	2.4	1.9
The magnitude of V_1-V_3 (dB)	no higher harmonics detected	2.5	2.3	2.2	2.4

important finding from the spectral analyses was the correspondence between the nonlinearity and dielectric loss (the area of the hysteresis loop), which is given in Table I and Fig. 6. At very low electric field, the system is practically linear and no loss was observed. When the field strength increases, the magnitudes of the second and third harmonics increase, and the area of the hysteresis loop (loss) is also enlarged. As a comparison, we have also included the hysteresis loop for field strength close to E_c in Fig. 6. One can see that for $E > E_c$ the hysteresis loop again becomes symmetric. This observation enables us to identify that the origin of the nonlinearity is truly extrinsic, i.e., due to the nonlinear response of domain wall.

Figure 7 shows the x-ray-diffraction (XRD) profiles of (002) and (200) peaks for plate PZT samples of different orientations. It can be seen from Fig. 7(a) that when the normal direction of the platelet is perpendicular to the poling direction, the (200) peak is much higher than the (002) peak. Conversely, for samples with the normal direction of the platelet parallel to the poling direction [Fig. 7(b), the (002) peak is much higher than (200) peak.

FIG. 6. The asymmetric P-E hysteresis loops at different field level for a poled soft PZT sample. The loss (area of the loop) increases with the applied field, and the loop becomes more asymmetric for $E < E_c$

Figure 7(c) is for an unpoled sample. Since there is no preferred orientation, the intensity of (200) peak is about twice as that of (002) peak. Structurally speaking, all of the tetragonal variants are equivalent. For a poled ceramic, only the relative volume ratio of the variants $[P_0,0,0]$ and $[0,0,P_0]$ is different in the directions parallel and perpen-

FIG. 5. Spectral analyses of the output voltage of dielectric (or piezoelectric) responses. (a) Electric field parallel to the poling direction. The amplitude of the ac field is $0.57E_c$. (b) Electric field perpendicular to the poling direction. The amplitude of the ac field is $0.7E_c$
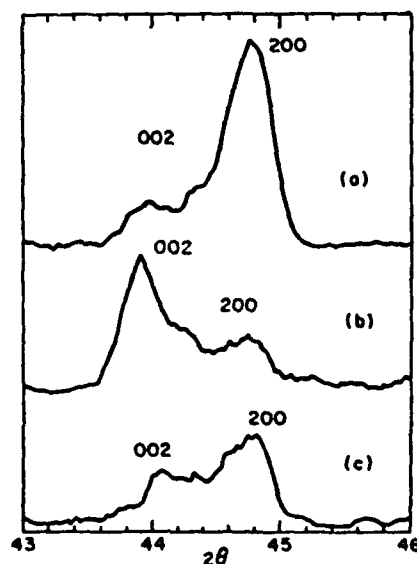
FIG. 7. XRD (002) and (200) peaks for unpoled and poled soft PZT ceramic. (a) X-ray intensity profile of a poled ceramic plate sample with its normal direction perpendicular to the poling direction. (b) X-ray intensity profile of a poled ceramic plate sample with its normal direction parallel to the poling direction. (c) X-ray intensity profile of an unpoled ceramic sample.
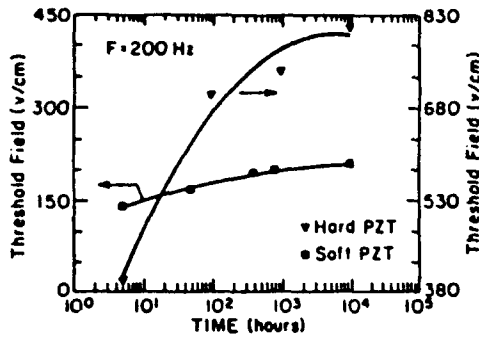
FIG. 8. The threshold field of the peizoelectric coefficients d_{33} for both poled soft and hard PZT ceramics as a function of aging time.

FIG. 9. A basic element of 90° twin in tetragonal ferroelectric ceramics. The relative orientation of unprimed and primed coordinate systems is characterized by the Euler angles (Θ, Φ, Ψ). The z-axis is the poling direction, n is the normal direction of the twin boundary.

dicular to the poling direction, which can only affect the extrinsic process. However, as shown in Figs. 1 and 2, the physical quantities observed in the directions parallel and perpendicular to the poling direction are quite different. They differ not only in the magnitude, but also the onset of nonlinearities (E_t). This fact provides another piece of evidence for the nonintrinsic origin of the nonlinearities in ceramics, because E_t would be the same in the two directions if the nonlinear effect is intrinsic.

It is known that the aging effect of ferroelectric ceramics is related to the reduction of non-180° domain-wall mobility. The aging experiments shown in Fig. 8 provide further proof for the extrinsic nature of the nonlinearities found in ferroelectric ceramics. The increase of E_t (reduction of nonlinearity) with time can be understood as having the same physical origin as that of the aging effect, i.e., the decrease of domain-wall mobility. In addition, the fact that a stronger time dependence of the threshold field occurs in hard PZT rather than in soft PZT is also consistent with the aging phenomena observed in these ceramics.

From the above experimental results, we conclude that the nonlinear phenomena observed in ferroelectric ceramics (PZT, for example) is mainly caused by the nonlinear motion of non-180° domain walls, or is extrinsic in nature.

III. PHENOMENOLOGICAL THEORY

Arlt and co-workers[5,6] have developed a phenomenological theory to calculate the contributions of 90° domain-wall vibrations for a linear system. The basic element is a twin plate shown in Fig. 9. The changes in the dielectric and piezoelectric quantities induced by the domain-wall displacement Δl can be described in terms of Δl and the Euler angles Θ, Φ, and Ψ. For example, the change of the electric dipole moment of this basic element can be expressed as

$$\delta P_i = \Delta l \, A P_0 f_i (\Theta, \Phi, \Psi), \quad (1)$$

where

$$f_1 = (\cos \Theta \sin \Phi \sin \Psi - \cos \Psi \cos \Phi),$$

$$f_2 = - (\cos \Psi \sin \Phi + \cos \Theta \cos \Phi \sin \Psi),$$

$$f_3 = - \sin \Psi \sin \Theta,$$

P_0 is the spontaneous polarization, and A is the area of the vibrating domain wall per unit volume. Similarly, the induced strain is given by

$$\delta \eta_\alpha = \Delta l \, A S_0 F_\alpha \quad (\alpha = 1\text{--}6), \quad (2)$$

in which

$$F_1 = 2(\sin \Theta \cos \Psi \cos \Phi \sin \Phi$$
$$ - \cos \Theta \sin \Theta \sin^2 \Phi \sin \Psi),$$

$$F_2 = - 2(\sin \Theta \cos \Psi \cos \Phi \sin \Phi$$
$$ + \cos \Theta \sin \Theta \cos^2 \Phi \sin \Psi),$$

$$F_3 = 2\cos \Theta \sin \Theta \sin \Psi,$$

$$F_4 = (\cos \Theta \cos \Psi \sin \Phi + \cos^2 \Theta \sin \Psi \cos \Phi$$
$$ - \sin^2 \Theta \sin \Psi \cos \Phi),$$

$$F_5 = \cos \Theta \cos \Psi \cos \Phi - \cos^2 \Theta \sin \Psi \sin \Phi$$
$$ + \sin^2 \Theta \sin \Psi \sin \Phi,$$

$$F_6 = (\sin \Theta \cos \Psi \sin^2 \Phi + 2 \sin \Theta \cos \Theta \sin \Psi$$
$$ \times \cos \Phi \sin \Phi - \sin \Theta \cos \Psi \cos^2 \Phi),$$

S_0 is the spontaneous strain representing the unit-cell distortion in the tetragonal phase. It has been shown[19,20] experimentally that the 90° domain-wall motion is highly nonlinear. Therefore, the potential energy of a displaced domain wall may be expanded as a polynomial function of the domain-wall displacement Δl:

$$U = U_0 + \frac{C_1}{2} \Delta l^2 + \frac{C_2}{3} \Delta l^3 + \frac{C_3}{4} \Delta l^4$$

$$ + \text{higher-order terms,} \quad (3)$$

where U_0 is the rest energy of a domain boundary, which is assumed to be independent of domain-wall motion. The presence of the cubic term in Eq. (3) describes the asymmetric feature of the domain-wall motion in a poled ceramic. Following Fousek and Brezina[21], the differential equation for the forced vibration of a 90° domain wall in a poled ceramic may be expressed as follows:

$$Am\,\Delta\ddot{l} + Ab\,\Delta\dot{l} + A\frac{\partial U}{\partial\Delta l} = -\left(\frac{\partial W_E}{\partial\Delta l} + \frac{\partial W_M}{\partial\Delta l}\right), \qquad (4)$$

where m represents the effective mass of the domain wall, b is the damping constant, and $W_E(\delta P_i)$ and $W_M(\delta U_{ij})$ are the induced electric and mechanical energies, respectively. The physical origins of the restoring force, damping, and effective mass have been discussed by several groups.[22-25] Hence, we will not give further details here.

If we only consider the first three terms of $\partial U/\partial\Delta l$, Eq. (4) becomes

$$Am\,\Delta\ddot{l} + Ab\,\Delta\dot{l} + AC_1\,\Delta l + AC_2\,\Delta l^2 + AC_3\,\Delta l^3$$

$$= -\left(\frac{\partial W_E}{\partial\Delta l} + \frac{\partial W_M}{\partial\Delta l}\right). \qquad (4')$$

Under certain conditions, one can get approximate solutions for Eq. (4'). For example, assume that the nonlinear terms are small, i.e.,

$$C_1\,\Delta l \gg C_2\,\Delta l^2, C_3\,\Delta l^3.$$

We may use a perturbation method[26] to derive an approximate solution for Δl and, hence, to get the expressions for δP_i and $\delta\eta_\alpha$.

In the following we will analyze only the domain-wall movement under an ac electric field $\mathbf{E} = \mathbf{E}_0\exp(j\omega t)$. The frequency ω of the applied field is usually much smaller than the resonance frequency of the domain wall, $\omega_0 = \sqrt{C_1/m}$, which is in the gigahertz range.[21] For example, the ac electric field used in our experiments is only 200 Hz. If we divide Eq. (4') by C_1, then for a system with strong damping we can neglect the first term on the left hand side, which has the coefficient of (ω^2/ω_0^2). The remaining first-order differential equation is the same as that for a relaxation system. The approximate solution for Δl up to the third order is given by

$$\Delta l = \Delta l^0 - \frac{C_2(\Delta l^0)^2}{C_1(1 + 2j\omega\tau)}$$

$$- \frac{(\Delta l^0)^3}{C_1(1 + 3j\omega\tau)}\left(C_3 - \frac{2C_2^2}{C_1(1 + 2j\omega\tau)}\right), \qquad (5)$$

$$\Delta l^0 = \frac{e^{j\omega\tau}}{2C_1(1 + j\omega\tau)}\left(P_0\sum_{i=1}^{3} f_i E_{0i}\right). \qquad (6)$$

Here, $\tau = b/C_1$ is the relaxation time.

The total induced polarization ΔP_i and strain $\Delta\eta_\alpha$ by the 90° domain-wall motion in a poled tetragonal ferroelectric ceramic may be derived as follows: First, substitute the solution (5) into Eqs. (1) and (2). Then, assume an angular distribution function $Z(\Theta)$ for the twin boundary orientation and integrate those quantities over the entire range of Euler angles. The final results may be written in the following form:

$$\Delta\eta_\alpha = (\Delta d_{\alpha k} + \Delta Q_{\alpha ik}E_i)E_k + \Delta G_{\alpha klj}E_kE_lE_j, \qquad (7)$$

$$\Delta P_i = [\Delta\epsilon_{ij} + \Delta\Gamma_{ikj}E_k]E_j + \Delta H_{iklm}E_kE_lE_m$$

$$(i,j,k = 1,2,3; \alpha,\beta,\gamma = 1\text{-}6), \qquad (8)$$

where E_k are the components of electric field, and the corresponding coefficients are given below.

If we define the Euler angle integration

$$\int d\Omega = \int_0^{2\pi} d\phi \int_0^{2\pi} d\Psi \int_0^\pi d\theta, \qquad (9)$$

the induced linear piezoelectric and dielectric coefficients $\Delta d_{i\alpha}$ and $\Delta\epsilon_{ij}$, respectively can be written as the following integrals:

$$\Delta d_{k\alpha} = \int S_0 P_0 K(\omega) f_k F_\alpha Z(\Theta) d\Omega, \qquad (10)$$

$$\Delta\epsilon_{kl} = \int P_0^2 K(\omega) f_k f_l Z(\Theta) d\Omega, \qquad (11)$$

where

$$K(\omega) = \int_0^\infty \frac{Ag(\tau)d\tau}{2C_1(1 + j\omega\tau)}. \qquad (12)$$

Here, we have assumed a distribution function $g(\tau)$ for the relaxation time.[5,6] The integrations with respect to Φ and Ψ can be carried out immediately, which give rise to the nonzero independent components of these tensor coefficients:

$$\Delta d_{\kappa\alpha} = \begin{bmatrix} 0 & 0 & 0 & 0 & \Delta d_{15} & 0 \\ 0 & 0 & 0 & \Delta d_{15} & 0 & 0 \\ \Delta d_{31} & \Delta d_{31} & \Delta d_{33} & 0 & 0 & 0 \end{bmatrix}, \qquad (13)$$

$$\Delta\epsilon_{kl} = \begin{bmatrix} \Delta\epsilon_{11} & 0 & 0 \\ 0 & \Delta\epsilon_{11} & 0 \\ 0 & 0 & \Delta\epsilon_{33} \end{bmatrix}. \qquad (14)$$

As indicated in Eqs. (7) and (8), the domain-wall motion also contributes to the nonlinear coefficients, including the electrostrictive constants $\Delta Q_{ij\alpha}$ and the nonlinear dielectric constants $\Delta\Gamma_{ijk}$. These quantities are given by the following integrals:

$$\Delta Q_{ki\alpha} = \int S_0 P_0^2 K'(\omega) f_k f_i F_\alpha Z(\Theta) d\Omega, \qquad (15)$$

$$\Delta\Gamma_{lki} = \int P_0^3 K'(\omega) f_l f_k f_i Z(\Theta) d\Omega, \qquad (16)$$

where

$$K'(\omega) = \int_0^\infty \frac{C_2 A g(\tau)d\tau}{4C_1^3(1 + j\omega\tau)^2(1 + 2j\omega\tau)}. \qquad (17)$$

Similarly, we can derive the expressions for the higher-order piezoelectric and dielectric constants $\Delta G_{\alpha dijkl}$ and ΔH_{ijkl}, respectively:

$$\Delta G_{\alpha klj} = \int S_0 P_0^3 K''(\omega) F_\alpha f_k f_l f_j Z(\Theta) d\Omega, \qquad (18)$$

$$\Delta H_{lkim} = \int P_0^4 K''(\omega) f_l f_k f_i f_m Z(\Theta) d\Omega, \qquad (19)$$

where

$$K^*(\omega) = \int_0^\infty \frac{Ag(\tau)}{4C_1^4(1+j\omega\tau)^3(1+3j\omega\tau)}$$

$$\times \left(\frac{C_2^2}{C_1(1+2j\omega\tau)} - \frac{C_3}{2} \right) d\tau. \qquad (20)$$

Similarly, one can derive the induced strain and polarization by the domain-wall movement under a stress field.[27]

IV. DISCUSSIONS AND SUMMARY

When $T_a = 0$, Eqs. (7) and (8) give the induced strain $\Delta\eta_a$ and polarization ΔP_i induced by the 90° domain-wall motion, respectively, in a poled ferroelectric ceramic. If the electric field E is in the same direction as that of the remanent polarization, Eqs. (7) and (8) become

$$\Delta\eta_3 = \Delta d_{33}E + \Delta Q_{333}E^2 + \Delta G_{3333}E^3, \qquad (21)$$

$$\Delta P_3 = \Delta\epsilon_{33}E + \Delta\Gamma_{333}E^2 + \Delta H_{3333}E^3. \qquad (22)$$

However, when the field E is perpendicular to the remanent polarization, Eqs.(7) and (8) reduce to

$$\Delta\eta_5 = \Delta d_{15}E + \Delta G_{1115}E^3, \qquad (23)$$

$$\Delta P_1 = \Delta\epsilon_{11}E + \Delta H_{1111}E^3. \qquad (24)$$

Equations (21)–(24) reveal that the nonlinearities are different for the two situations. The fact that there is no second harmonic when the electric field is perpendicular to the polarization [Eqs. (23) and (24)] agrees with the experiment results shown in Fig. 5. It needs to be pointed out that the model here cannot explain why the field strength has a much stronger effect on the magnitude of the second (even) harmonic than that of the third (odd) harmonic (see Table I), which might indicate that the extrinsic contribution not only comes from 90° domain-wall motion, but also from other sources, such as oscillating interphase interfaces and localized phase transitions.

To summarize, we have measured the nonlinear behavior of several PZT ceramic systems. Several important results were obtained, which include the following.

(1) The increase of nonlinear effects is accompanied by an increase in loss.

(2) Nonlinear effects can be reduced by applying a dc bias field or decreasing the temperature.

(3) Nonlinearity is found to decrease with time, and this aging effect is much stronger in hard PZT than in soft PZT.

From these results, we conclude that the nonlinear effects found in ferroelectric ceramic is extrinsic in nature. Even though the extrinsic nonlinear effects could be orders of magnitude larger than the intrinsic nonlinearities, prac-

tical applications of these nonlinear properties might be limited by the loss generated from the domain-wall motion.

The extension of the phenomenological theory of Arlt and co-workers by including higher-order terms in the energy function [Eq.(3)] shows a certain degree of success for describing the nonlinear ferroelectric ceramic system. Nevertheless, there are still some experimental results which could not be explained by the model. This implies that the actual extrinsic process is more complicated than just the motion of 90° domain walls. At least for PZT systems with compositions close to the morphotropic phase boundary (the one we have used in the experiments), oscillating interphase and/or a localized transition between the tetragonal and rhombohedral phases definitely contribute substantially to the extrinsic process.

[1] R. Lee and J. F. Vetelino, Proc. IEEE Ultrason. Symp. 2, 741 (1987).

[2] E. A. Kraut, T. C. Lim, and B. R. Tittman, Ferroelectrics 3, 247 (1972).

[3] See articals in Acoustic Surface Waves, edited by A. Oliner (Springer, New York, 1978).

[4] A. F. Devonshire, Philos. Mag. 40, 1040 (1949).

[5] G. Arlt, H. Dederichs, and R. Herbeit, Ferroelectrics 74, 37 (1987).

[6] G. Arlt and H. Dederichs, Ferroelectrics 29, 47 (1980).

[7] V. A. Isupov, Sov. Phys. Solid State 18, 529 (1976).

[8] A. G. Luchaninov, A. V. Shil'Nikov, L. A. Shuvalov, and I. JU. Shipkova, Ferroelectrics 98, 123 (1989).

[9] E. K. W. Goo, R. K. Mishra, and G. Thomas, J. Appl. Phys. 52, 2939 (1981).

[10] P. G. Lucuta and V. Teodoresu, J. Appl. Phys. A 37, 237 (1985).

[11] J. Von Cieminski, C. Kleint, H. Beige, and R. Hoche, Ferroelectrics 109, 95 (1990); L. Pardo, J. Mendida, A. Gonzalez, and J. De. Frutos Ferroelectronics 94, 189 (1989).

[12] G. Arlt, Ferroelectrics 76, 451 (1987).

[13] H. Beige and G. Schmidt, Ferroelectrics 41, 39 (1982).

[14] M. D. Bryant and R. F. Keltie, Sensors Actuators 9, 95 (1986); 9, 105 (1986).

[15] A. F. Litvin, M. M. Pikalev, V. A. Doroshenko, and V. Z. Borodin, Ferroelectrics 51, 159 (1984).

[16] Q. M. Zhang, W. Y. Pan, and L. E. Cross, J. Appl. Phys. 63 2492 (1988).

[17] J. O. Gentner, P. Gerthsen, A. Schmidt, and R. E. Send, J. Appl. Phys. 49, 4485 (1978); and P. Gerthsen, K. H. Hardtl, and N. A. Schmidt, J. Appl. Phys. 51, 1131 (1980).

[18] L. Benguigui, Ferroelectrics 7, 315 (1974).

[19] J. Fousek and B. Brezina, Czech J. Phys. B 10, 511 (1960).

[20] J. Fousek and B. Brezina, Czech. J. Phys. B 11, 344 (1960).

[21] J. Fousek and B. Brezina, J. Phy. Soc. Jpn. 19, 830 (1964).

[22] V. S. Postnikov, V. S. Pavlov, and S. K. Turkov, Phys. Chem. Solids 31, 1785 (1970); Izv. Akad. Nauk. 31, 1845 (1967).

[23] V. S. Postnikov, V. S. Pavlov, S. A. Gridnev, and S. K. Turkov, Sov. Phys. Solid State 10, 1267 (1968).

[24] J. G. Smits, IEEE Trans. Sonics Ultrason. SU-23, 168 (1976).

[25] R. E. Nettleton, J. Phys. Soc. Jpn. 22, 1375 (1967).

[26] A. H. Nayfeh, in Perturbation Methods (Wiley, New York, 1973).

[27] S. Li, W. Cao, and L. E. Cross (unpublished).

APPENDIX   15

ELECTROMECHANICAL NONLINEARITY OF FERROELECTRIC CERAMICS AND RELATED NON-180º DOMAIN WALL MOTIONS

Shaoping Li, Wenwu Cao, R.E. Newnham and L. E. Cross

Materials Research Laboratory,

The Pennsylvania State University, University Park, PA 16802

ABSTRACT

Using an optical interferometer and other experimental techniques, the mechanical and dielectric response of lead zirconate titanate $Pb(Zr_xTi_{1-x})O_3$ ceramics to an *a.c.* electric field have been investigated directly. The experimental results demonstrate the importance of the domain wall motion in generating the electromechanical nonlinearities in ferroelectric ceramics. A phenomenological theory has been extended to describe the extrinsic contributions to the piezoelectric, elastic and dielectric properties. These effects can be attributed to both the linear and nonlinear vibrations of non-180^0 domain walls in ferroelectric ceramics. The proposed theory shows qualitative agreement with the experimental results.

I. INTRODUCTION

Electromechanical nonlinearity in ferroelectric ceramics is an important problem in modern ultrasonic engineering. Ferroelectric ceramics are widely used as transducers, resonators, actuators, motors, and capacitors which represent a very large segment of the electroceramic's market. One of the limitations of ferroelectric transducers for practical use is the nonlinear effect which occur at high driving level [1-6], in fact ferroelectric ceramics are the strongest known nonlinear piezoelectric materials[7]. In recent years, techniques for fabricating ferroelectric thin films have made great progress, which open up the possibility of utilizing the nonlinearities of ferroelectric ceramics in conjunction with integrated circuits, because significant nonlinear phenomena can be observed in thin films even under a few hundred milivolts. In practical applications, the nonlinearity of ferroelectric ceramics are used to influence the performance of microwave acoustic devices such as convolvers and correlators[7-9]. The so-called "smart ceramics"[10] incorporating sensors and actuators also exploit the nonlinear properties of ferroelectric ceramics. In short, on certain occasions, one wants to avoid the nonlinearities, while on other occasions one wants to benefit from them. Therefore, from a technological point of view, it is important to study the nonlinear electromechanical properties in ferroelectric ceramics so as to optimize the choice of piezoceramics for making transducers, actuators, resonators, ultrasonic motors and other acoustic devices, as well as to develop new types of nonlinear electronic devices such as frequency mixers and doublers, and piezoelectric thin film devices.

The piezoelectric effects in ferroelectric ceramics are caused by two mechanisms:
(1) The intrinsic piezoelectric effect [11-12] which is associated with the deformation of each unit cell of the ferroelectric material under an electric field.

(2) The extrinsic piezoelectric effect [13-15] that, for example in lead zirconate titanate
(PZT) system, refers to the motion of non-180^0 domain walls and the movement of the
interphase phase boundary between the tetragonal and rhombohedral phase regions[16].
It is believed that the piezoelectric effect in polycrystalline ferroelectrics is caused not only
by the ionic displacement in connection with the change of the polarization magnitude, but
also by the movements of domain walls and interphase boundaries. Studies on materials
such as $BaTiO_3$ and PZT [17] have shown that as much as 60% - 70% of the piezoelectric
moduli values may originate from the extrinsic contributions. In fact , the performance of
many transducers, actuators and capacitors are based on the control of domain structures
under the applied electric field. Microstructural investigations [18-20] have also shown that
the poled ferroelectric ceramics contain a large number of
non-180^0 domain boundaries which strongly affect their electromechanical behavior [21-
27]. These domain structures give rise to complex linear and nonlinear behavior which is
very sensitive to the quality of the sample, its defect concentration as well as the external
boundary conditions.

Even though the investigation on the electromechanical nonlinearity in ferroelectrics
has been carried on for the last three decades, most of the studies [28-30] are based on
thermodynamic theory only, without considering the dynamics of domain walls. Very little
work[31,32] has been done to describe the behavior of electromechanical nonlinearity in
terms of domain wall motion, even though domain wall motion plays a dominant role over
a wide range of external field levels, and the frequency response of domain wall motions
spans a range from almost zero hertz to the microwave regime. Moreover, a number of
ambiguities remain in this area due to the lack of sufficient information about the
relationship between electromechanical coefficients and the motions of non-180^0 domain
walls and the movement of interphase boundaries.

The objective of this paper is to evaluate the linear and nonlinear elastic, dielectric, and
piezoelectric coefficients arising from the domain wall motions, and to form a tentative

model based on the observed linear and nonlinear effects so as to gain some physical insight into the relationship between domain wall motions and nonlinear electromechanical properties in ferroelectric ceramics. In sections II and III, we present a general description of the electromechanical properties arising from the non-180^0 domain wall motions in the ferroelectric ceramic. In section IV, we show some experimental results which characterize the dynamic electromechanical response of the PZT frroelectric ceramics. Some of the experimental results strongly support our approach to the problem.

II THEORETICAL

2.1. Domain and Interphase Structures

In a $Pb(Zr_xTi_{1-x})O_3$ system with composition near the morphotropic phase boundary (MPB), the tetragonal and rhombohedral phases coexist. Therefore, besides the 180^0 domain wall , there are 70.5^0, 109.5^0 and 90^0 domain walls. Also interphase boundaries between the two phases exist. Here, we do not discuss the case for 180^0 domain walls. The 180^0 domain wall motion does not significantly affect the piezoelectric and electromechanical properties because the spontaneous deformations of the antiparallel domain are the same. In order to investigate systematically the relationship between linear piezoelectric effect and the non-180^0 domain wall motions in ferroelectric ceramics, Arlt et.al.[13,14] first presented a phenomenological model for the vibrating 90^0-domain walls to describe the linear piezoelectric behavior of ferroelectric ceramics under electric fields and mechanical stresses. We have generalized this model to describe the nonlinear effects resulting from the vibrating 90^0-domain walls [33].

Here, we will try to model non-180^0 domain wall motions for the cases of rhombohedral phase and interphase conversion between the tetragonal and rhombohedral regions, respectively. As we know, the symmetry of the ferroelectric phase G_f is fully determined by the symmetry of the parent phase G_p. In other words, the spontaneous

polarization has the equal probability to lie in all the equivalent directions prescribed by the prototypic from which the ferroelectric is derived. From phenomenological theory [12], we can find eight energetically equivalent variants in rhombohedral ferroelectric stable states of *PZT* system as following:

$$I. (P_1, P_2, P_3) \quad II. (P_1, P_2, -P_3) \quad III. (-P_1, P_2, P_3) \quad IV. (P_1, -P_2, P_3)$$

$$V. (-P_1, P_2, -P_3) \quad VI. (P_1, -P_2, -P_3) \quad VII. (-P_1, -P_2, P_3) \quad VIII. (-P_1, -P_2, -P_3) \quad (1)$$

where $P_1^2 = P_2^2 = P_3^2 = P_0^2/3$. P_0 is the spontaneous polarization. Accordingly, the spontaneous strain under zero stress condition can be written as :

$$s_{11} = s_{22} = s_{33} = (Q_{11} + 2Q_{12}) P_0^2/3 \qquad (2)$$

$$s_{12} = Q_{44} P_1 P_2, \quad s_{12} = Q_{44} P_2 P_3, \quad s_{12} = Q_{44} P_1 P_3$$

Obviously, the normal components of s_{ii} are the same for all of the orientation states, and the shear components of the spontaneous strain tensor in the corresponding states of Eq.(1) have the following forms:

$$I(VIII) \ S_{12} = S_{23} = S_{31} = \frac{Q_{44}}{3} P_0^2 \ ; \quad II(VII) \ S_{12} = -S_{23} = -S_{31} = \frac{Q_{44}}{3} P_0^2$$

$$III(VI) \ S_{12} = -S_{23} = S_{31} = \frac{-Q_{44}}{3} P_0^2 \ ; \quad IV(V) \ S_{12} = S_{23} = -S_{31} = \frac{-Q_{44}}{3} P_0^2 \qquad (3)$$

According to the crystallographic relations, these eight low temperature variants will form 180^0, 70^0 and 110^0 twin structures. For instance, the polarization vectors in a twin structure between states *(I)* and *(VI)* form a angle θ,

$$\theta \ ([111],[1\text{-}1\text{-}1]) = \cos^{-1}\left(\frac{-1}{3}\right) \approx 110^\circ$$

The twin boundary is then called 110^0 domain wall. We choose primed and unprimed coordinate systems for a basic piezoelectric element as shown in Fig.1, which contains a single 110^0 domain wall and separates the polarization states *(I)* and *(VI)*. In the primed system, domain wall is located in $z'= 0$ plane [24]. Δl is the displacement of the domain wall and A is the area of the vibrating domain wall per unit volume. A displacement Δl of the domain wall gives rise to a change in the electric dipole moment δP_i in the volume $\Delta l A$ [34,35],

$$\overrightarrow{\delta P'} = \frac{2}{\sqrt{3}} \Delta l \ A \ P_0 \begin{bmatrix} 1 \\ 1 \\ 0 \end{bmatrix} \qquad (4)$$

The Δl also induces a change in the elastic dipole moment,

$$\widetilde{\delta U'} = \Delta l \ A \ S_0 \begin{bmatrix} 0 & 0 & 1 \\ 0 & 0 & 1 \\ 1 & 1 & 0 \end{bmatrix} \qquad (5)$$

where, $\quad S_0 = \dfrac{Q_{44}}{3} P_0^2$

P_o and S_o are the spontaneous polarization and strain, respectively, in the rhombohedral phase. Finally, in the unprimed coordinate system, we can get:

$$\delta P_i = \Delta l \ A P_0 \ f_i (\Theta, \Phi, \Psi) \qquad (6)$$

and,

$$\delta U_{ij} = \Delta l \ A S_0 \ F_{ij} (\Theta, \Phi, \Psi) \qquad (7)$$

where $f_1 = [\ cos\Phi(cos\Psi - sin\Psi) - cos\Theta sin\Phi(sin\Psi + cos\Psi) \ ]$, $f_2 = [sin \ \Phi(cos\Psi - sin\Psi) + cos\Theta cos\Phi(sin\Psi + cos\Psi)]$, $f_3 = sin\Theta(cos\Psi + sin\Psi)$; *and*

$F_{11} = 2sin\Theta sin\Phi[cos\Psi cos\Phi(cos\Psi - sin\Psi) - sin\Phi cos\Theta(cos\Psi + sin\Psi)]$,

$F_{22} = -2sin\Theta cos\Phi[sin\Phi(cos\Psi - sin\Psi) + cos\Theta cos\Phi(cos\Psi + sin\Psi)]$,

$F_{33} = 2cos\Theta sin\Theta(sin\Psi + cos\Psi)$,

$F_{13} = sin\Phi(cos\Psi + sin\Psi)[cos^2\Theta - sin^2\Theta] + cos\Theta cos\Phi(cos\Psi + sin\Psi)$,

$F_{23} = cos\Theta[sin\Phi(cos\Psi - sin\Psi) + cos\Phi cos\Theta(cos\Psi + sin\Psi)] - sin^2\Theta cos\Phi[cos\Psi + sin\Psi]$,

$F_{12} = sin\Theta(cos\Psi - sin\Psi)$.

Next, let us discuss the case of interphase conversion in the ferroelectric ceramic. It is known [15] that the tetragonal (T) and rhombohedral (R) ferroelectric phases coexist in PZT system of compositions near the MPB. According to SEM, SAED and TEM investigation of the domain structure in PZT ceramics with composition near the MPB, there exists an alternating T and R phase layers, which is similar to the 90^0 domain structure in the tetragonal distorted ceramics. Based on experimental results, Lucuta proposed[19,20] a succession model of ferroelectric domains $T_1RT_2RT_1$, due to the coexistence of a R domain between the two different oriented T domains as shown in Fig.2. In the case of the occurrence of a rhombohedral phase between the 90^0 domains, the polarization direction in an alternating sequence is: [001] --- [111] --- [010] ---[111] --- [001] corresponding to a repetitive domain succession $T_1RT_2RT_1$ ... The interphase boundary conversion will induce changes in the electric and elastic dipole moments. Considering the polarization along [111] direction in a R domain converts into the polarization along [001] direction in a T domain, the induced electric and elastic dipole moments in the primed coordinate system will be:

$$\vec{\delta P'} = \Delta l \, A \, P_0 \begin{bmatrix} \dfrac{1}{3} \\ \dfrac{1}{3} \\ \dfrac{-2}{3} \end{bmatrix} \qquad (8)$$

and,

$$\widetilde{\delta U'} = \Delta l \; A \; \begin{bmatrix} u_{11} u_{12} u_{13} \\ u_{21} u_{22} u_{23} \\ u_{31} u_{32} u_{33} \end{bmatrix} \tag{9}$$

where, $u_{12} = u_{13} = u_{23} = u_{21} = u_{31} = u_{32} = \dfrac{Q_{44}}{3} P_0^2$;

$$u_{11} = u_{22} = \dfrac{(Q_{11} - Q_{12})}{3} P_0^2 \; ; \; u_{33} = \dfrac{-2(Q_{11} + Q_{12})}{3} P_0^2$$

Note: here we assume that the magnitude of the spontaneous polarization in the rhombohedral phase is equal to that in the tetragonal phase, and all the coefficients Q_{11}, Q_{12}, and Q_{44} are the same in both phases. Finally, in the (x, y, z) coordinate system, the changes of electric and elastic dipole moments can be written as:

$$\delta P_i = [\widetilde{R_{ij}}] [\delta P'_i] \; ; \qquad [\delta U_{ij}] = [\widetilde{R_{ij}}] [\delta U'_{ij}] [R_{ij}] \tag{10}$$

$$[R_{ij}] = \begin{bmatrix} \cos\Psi & \sin\Psi & 0 \\ -\sin\Psi & \cos\Psi & 0 \\ 0 & 0 & 1 \end{bmatrix} \begin{bmatrix} 1 & 0 & 0 \\ 0 & \cos\Theta & \sin\Theta \\ 0 & -\sin\Theta & \cos\Theta \end{bmatrix} \begin{bmatrix} \cos\Phi & \sin\Phi & 0 \\ -\sin\Phi & \cos\Phi & 0 \\ 0 & 0 & 1 \end{bmatrix}$$

2.2 The Model

Generally speaking, the domain wall motion may be accomplished by a succession of steps starting at initiating nuclei [36,37], but in the case of the non-180^0 domain wall sidewise motions, this may not be exactly true [38]. The entire ceramic specimen is a complex electromechanical system, each individual domain wall in different grains has different orientations and different boundary conditions. The movements of the domain walls are not independent, there are strong interactions between them. The microscopic process for individual domain wall motion is rather complicated and not well understood. However, if we are only interested in the macroscopic effect resulting from the collective motion of domain walls, the microscopic details of each individual domain may be neglected.
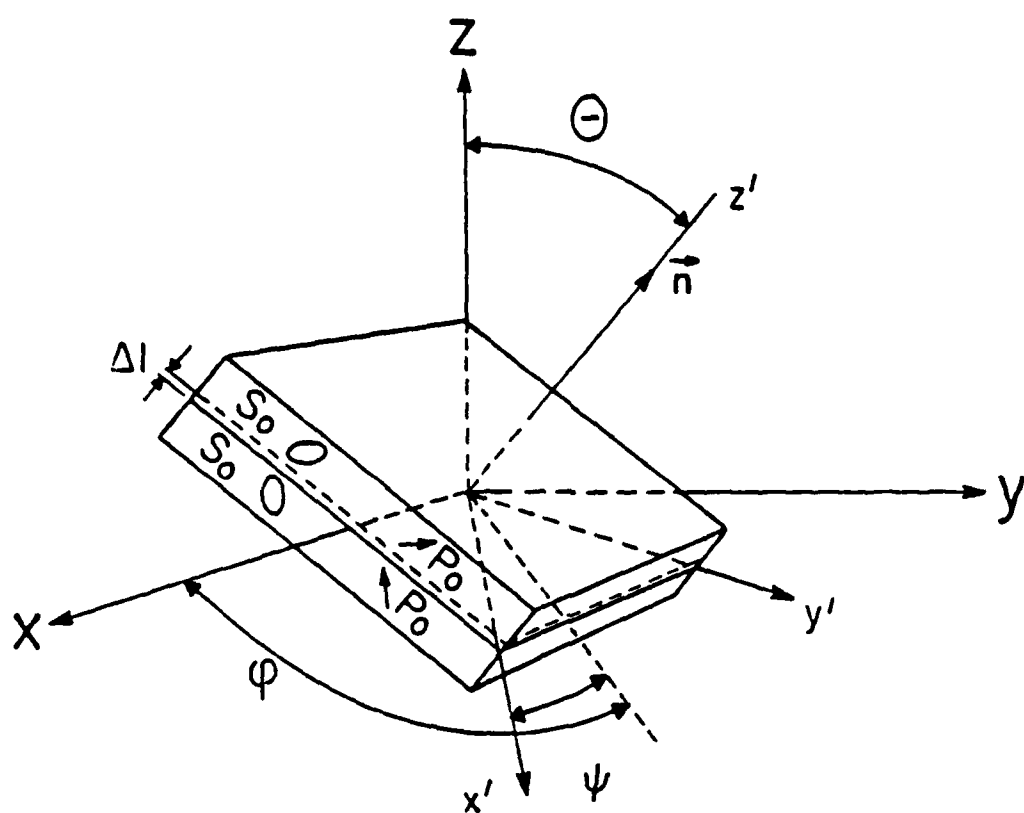
Fig.1.(a) A basic element of a twin stucture in a rhombohedral ferroelectric ceramic.
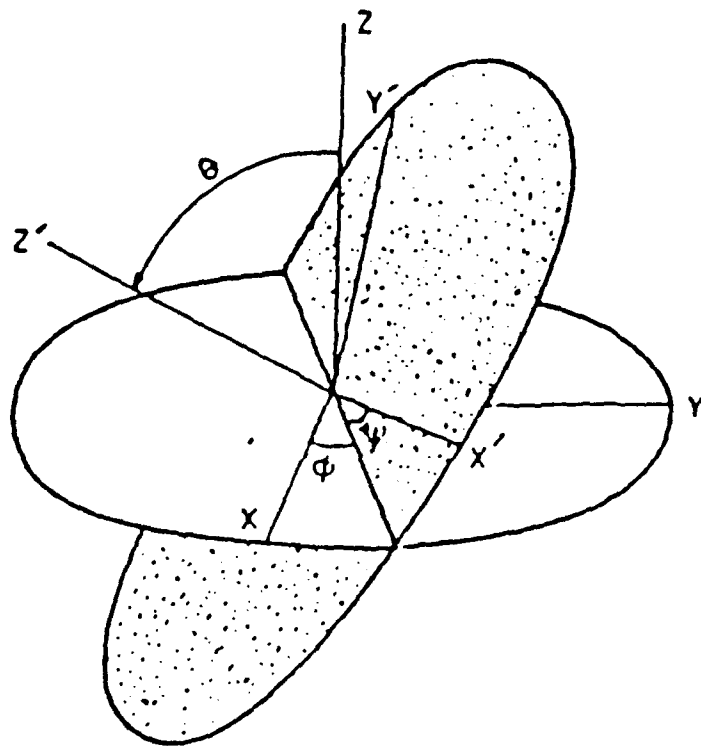
Fig.1.(b) The unprimed and primed coordinate systems. The relative orientation is characterized by the Eulerian angles (ϕ, ψ, θ).
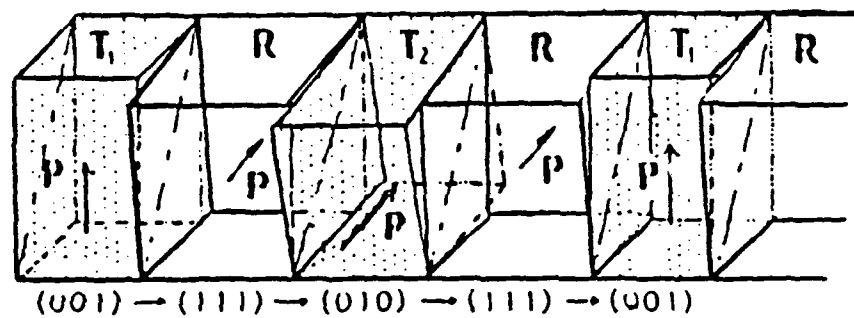
Fig.2. (a) Packing model of T-R twin-related domains along (011) habit plane explains the coexistence of T and R ferroelectric phases in PZT at MPB (After Lucuta 1989 Ref.(20)).
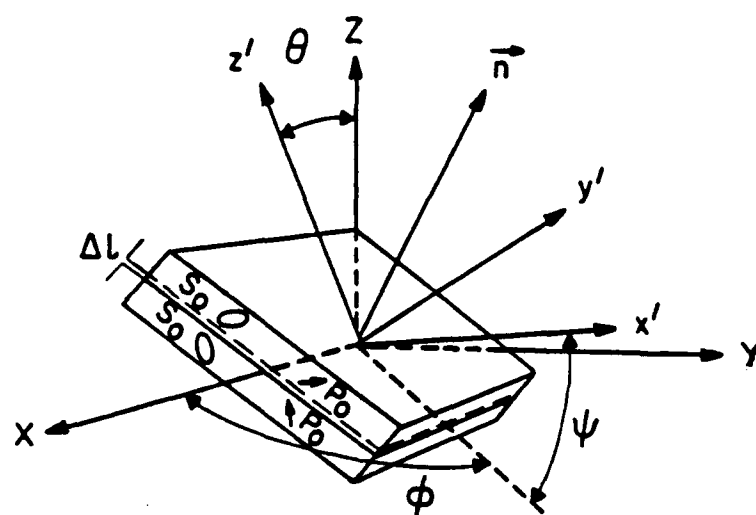
Fig.2.(b) The basic element of interphase boundary in PZT system at MPB
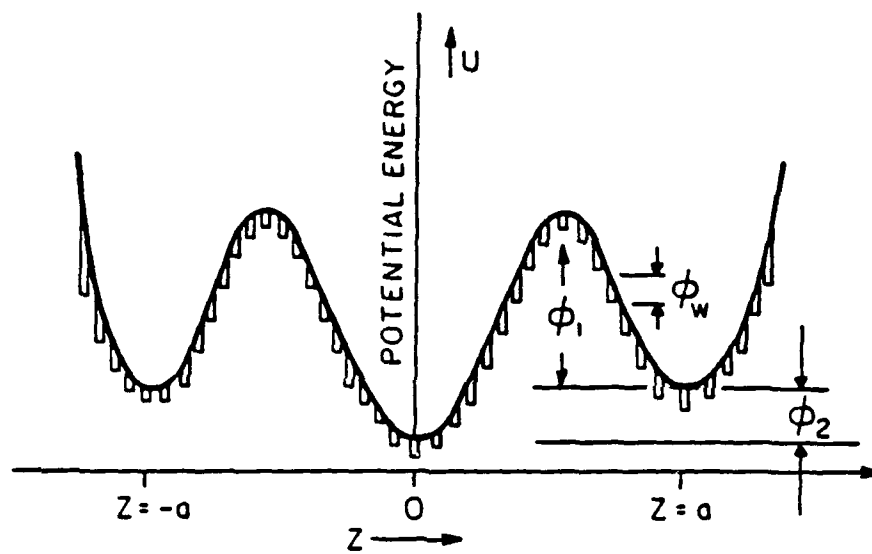
Fig.3. Schematic plot of the nergy potential for non-180⁰ domain wall motion in PZT ceramics.

In the present analysis, we assume that the average displacement of domain wall in a certain direction is quasi-one dimensional , i.e., the wall plane moving as a whole without blending and stacking effects. Fig.3. shows the variation of the wall energy as a function of wall position in a ceramic sample. The height of the potential barrier $(\Phi_1+\Phi_2)$ is the minimum energy required for the wall to relocate from depoling state to poled state. Φ_2 is the amount of the elastic energy which can be relieved during the domain wall switching back to depoling state. Φ_w is the height of potential barrier for a non-180^0 domain wall going across one lattice distance.

In a depolarized ceramic sample, all domain walls are randomly orientated, and the distribution of domain walls possess the symmetry of ∞/mm. Obviously, domain walls are located at the minima of the potential energy ($z = 0$).

When an external ac field is applied, the domain wall will oscillate. However, as long as the magnitude of the domain wall vibration is not very large, the macroscopic potential energy for domain wall motions is symmetric with respect to z axis, i.e: $U(\Delta z) = U(-\Delta z)$. The situation is different for a poled ceramic. During poling process, domain walls will overcome certain energy barrier, and move in the new equilibrium position. As shown in Fig.(3), the new positions are metastable states ($z = a$, or $z = -a$). After the field is removed, the distribution of orientation of the domain walls becomes conical in the poled samples. The potential for domain wall motion is no more symmetric in the poled state, i.e. $U(\Delta z-a) \neq U(\Delta z+a)$.

It also has been shown [39,40] experimentally that the domain wall motion in poled ceramic is highly nonlinear. Therefore, the potential energy for the domain wall motion may be expanded as a polynomial function of the domain wall displacement:

$$U = U_0 + C_1 \Delta l^2 + \frac{C_2}{3}\Delta l^3 + \frac{C_3}{4}\Delta l^4 + \text{higher- order terms} \quad (11)$$

where U_o is the rest energy of a domain boundary, which is assumed to be independent of the domain wall motion. The presence of the third power term describes the asymmetric feature of the domain wall motion in a ferroelectric ceramic. The odd terms will be zero if domain wall vibrations take place around the center of potential energy of the domain wall. Therefore, the differential equation of the forced vibration of a non-180^0 domain wall in a ferroelectric ceramic may be expressed as follows [13,14,38] :

$$Am\Delta\ddot{l} + Ab\Delta\dot{l} + \frac{\partial U}{\partial \Delta l} = -(\frac{\partial W_E}{\partial \Delta l} + \frac{\partial W_M}{\partial \Delta l}) \quad (12)$$

where m represents the effective mass of the domain wall. b is the damping constant. The third term is the restoring force. W_E and W_M are the energies of the induced average electric and elastic dipoles $<\delta P_i>$ and $<\delta U_{ij}>$ by the electric field and stress, respectively, which may be written as

$$-(\frac{\partial W_E}{\partial \Delta l} + \frac{\partial W_M}{\partial \Delta l}) = (\sum <\delta P_i> E_i e^{jw_1 t} + \sum <\delta U_j> T_j e^{jw_2 t}) \quad (13)$$

In general, we have $\omega_1 \neq \omega_2$. The physical origins of the restoring force, damping effects and effective mass have been discussed separately by several scientists [36-45]. If we consider only the first three terms of the restoring force, Eq.(12) becomes

$$Am\Delta\ddot{l} + Ab\Delta\dot{l} + 2A C_1 \Delta l + AC_2 \Delta l^2 + AC_3 \Delta l^3 = -(\frac{\partial W_E}{\partial \Delta l} + \frac{\partial W_M}{\partial \Delta l}) \quad (12')$$

This equation implies that the nature of the extrinsic nonlinear properties in ferroelectric ceramics resides in the interrelationship between the amplitude of the non-180^0 domain wall vibration and the stiffness of the materials. The condition

$$C_1 \Delta l >> C_2 \Delta l^2, \quad C_3 \Delta l^3$$

allows one to employ a perturbation method [46] for approximately solving Eq.(12') in order to obtain the induced polarization δP_i and strain δU_{ij} accompanying domain wall motions. The detailed approximated solution can be seen in Ref.[33]. According to Fousek and Brezina[38], the resonant frequency of domain walls is much higher than the frequencies used in our experiments, which are less than 1 MHz. Thus, the inertia term can be neglected. This means that such the damping is sufficiently strong that Eq.(12') can be simplified to a relaxation equation.

III. LINEAR AND NONLINEAR COEFFICIENTS

We now consider the linear and nonlinear dielectric, piezoelectric, and elastic properties associated with the 110^0 domain wall motion in ferroelectric ceramics. The average induced polarization and strain can be calculated by averaging δU_{ij} and δP_i over all domain wall orientations in the sample [13,14]. $\Delta P_i = <\delta P_i>$, and $\Delta U_{ij} = <\delta U_{ij}>$ may be expressed as:

$$\Delta P_i = [\Delta\varepsilon_{ik} + \Delta r_{ijk} E_j] E_k + [\Delta d_{im} + \Delta e_{ilm} T_l] T_m + 2\Delta Q_{ijl} E_j T_l$$
$$+ \Delta H_{ijkp} E_j E_k E_p + \Delta G_{ijkl} E_j E_k T_l + ...$$

$$\Delta U_l = [\Delta d'_{kl} + \Delta Q'_{ijl} E_i] E_j + [\Delta S_{ln} + \Delta S_{lmn} T_m] T_n + 2\Delta e'_{lkm} E_k T_m$$
$$+ \Delta G'_{ijkl} E_i E_j E_k + \Delta W_{ijnl} E_i E_j T_n + ...$$

where $i, j, k, p = 1, 2, 3$ and $l, n, m = 1, 2, 3, 4, 5, 6$ (14)

In this expressions, ΔP_i is the total induced average polarization, ΔU_l is the average strain component in Voigt notation. T_n is the stress, and E_k is the electric field.
The values of $\Delta d_{kl} = <\delta d_{kl}>$ are the extrinsic piezoelectric constants of a ceramic sample:

$$\Delta d_{kl} = \int_0^{2\pi} d\phi \int_0^{2\pi} d\psi \int_0^{\pi} \frac{1}{\sqrt{3}} S_o P_o K(\omega_i) f_k F_l Z(\Theta) d\Theta \qquad (15)$$

where: $F_1=F_{11}$, $F_2=F_{22}$, $F_3=F_{33}$, $F_4=F_{23}$, $F_5=F_{13}$, $F_6=F_{12}$, and,

$$K(\omega_i) = \int_0^\infty \frac{A\, g(\tau)\, d\tau}{2C_1\, (1+j\omega_i\tau)}$$

Note: Δd_{kl} depends on ω_2, the frequency of the applied elastic field, and $\Delta d'_{kl}$ depends on ω_1, the frequency of the applied electric field. $g(\tau)$ is the relaxation time distribution [13,14] assuming there exist more than one relaxation time. $Z(\Theta)$ is the distribution function of domain wall orientations obtained during the poling process. All quantities having the Δ symbol are caused by 110^0 domain wall vibrations only. The values of $\Delta s_{ln} = \langle \delta s_{ln} \rangle$ and $\Delta \varepsilon_{ik} = \langle \delta \varepsilon_{ik} \rangle$ are the extrinsic elastic, and dielectric parameters of the ceramic:

$$\Delta s_{1n} = \int_0^{2\pi} d\phi \int_0^{2\pi} d\psi \int_0^\pi S_0^2 K(\omega_2) F_1 F_n Z(\Theta) d\Theta \qquad (16)$$

$$\Delta \varepsilon_{ik} = \int_0^{2\pi} d\phi \int_0^{2\pi} d\psi \int_0^\pi \frac{1}{3} P_0^2 K(\omega_1) f_i f_k Z(\Theta) d\Theta$$

where $\Delta Q_{ijl} = \langle \delta Q_{ijl} \rangle$ (electrostrictive coefficients) and $\Delta r_{ijk} = \langle \delta r_{ijk} \rangle$ (nonlinear dielectric coefficients) can be expressed as follows:

$$\Delta Q_{ij1} = \int_0^{2\pi} d\phi \int_0^{2\pi} d\psi \int_0^{\pi} \frac{-2}{3} S_o P_o^2 \, K'(\omega_1, \omega_2) \, f_i \, f_j \, F_l \, Z(\Theta) \, d\Theta \qquad (17)$$

$$\Delta Q'_{ij1} = \int_0^{2\pi} d\phi \int_0^{2\pi} d\psi \int_0^{\pi} \frac{-2}{3} S_o P_o^2 \, K'(\omega_1) \, f_i \, f_j \, F_l \, Z(\Theta) \, d\Theta$$

Where:

$$K'(\omega_1) = \int_0^{\infty} \frac{2 \, C_2 \, A \, g(\tau) \, d\tau}{[4C_1]^3 (1+2j \, \omega_1 \tau)(1+j \, \omega_1 \tau)^2} \quad ;$$

$$K'(\omega_1, \omega_2) = \int_0^{\infty} \frac{2 \, C_2 \, A \, g(\tau) \, d\tau}{[4C_1]^3 (1+j[\omega_2+\omega_1]\tau)(1+j \, \omega_1 \tau)(1+j \, \omega_2 \tau)} \quad .$$

and,

$$\Delta r_{ijk} = \int_0^{2\pi} d\phi \int_0^{2\pi} d\psi \int_0^{\pi} -2P_o^3 \, K'(\omega_1) \, f_i \, f_j \, f_k \, Z(\Theta) \, d\Theta \qquad (18)$$

Here, we should point out that the contributions of domain wall motion to the electrostrictive coefficients ΔQ_{ijl} and the nonlinear dielectric coefficients Δr_{ijk} have the same physical origin as those of the electro-optical coefficients and elasto-optical coefficients. In fact, in hot pressed transparent PLZT ceramics the changes of the remnant polarization give rise to changes in the birefringence Δn [47-50] because of the non-180^0 domain reversal induced by an external field.

The electroacoustic coefficients $\Delta e_{klm} = \langle \delta e_{klm} \rangle$ (the coefficients of the nonlinear piezoelectric effect) describe the change in the velocity of elastic waves, and are given by:

$$\Delta e'_{klm} = \int_0^{\pi} d\phi \int_0^{2\pi} d\psi \int_0^{\pi} \frac{-2}{\sqrt{3}} P_0 S_0^2 \, Z(\theta) \, K(\omega_2) \, f_k \, F_l \, F_m \, d\theta \qquad (19)$$

$$\Delta e_{klm} = \int_0^{\pi} d\phi \int_0^{2\pi} d\psi \int_0^{\pi} \frac{-2}{\sqrt{3}} P_0 S_0^2 \, Z(\theta) \, K(\omega_1, \omega_2) \, f_k \, F_l \, F_m \, d\theta$$

In some materials [7], the extrinsic contribution to the electroacoustic effect (change in velocity of sound under an applied electric field) may be two orders of magnitude larger than the intrinsic contribution. The third order elastic coefficients $\Delta S_{lmn} = \langle \delta S_{lmn} \rangle$ are:

$$\Delta S_{lmn} = \int_0^{2\pi} d\phi \int_0^{2\pi} d\psi \int_0^{\pi} -S_0^3 \ Z(\Theta) \ K(\omega_2) \ F_l F_m F_n \ d\Theta \qquad (20)$$

There are twenty one non-vanishing coefficients. The expressions for the higher order nonlinear piezoelectric coefficients $\Delta G_{ijkl} = \langle \delta G_{ijkl} \rangle$ and dielectric coefficients $\Delta H_{ijkp} = \langle \delta H_{ijkp} \rangle$ are given by the following integrals:

$$\Delta G'_{ijkl} = \int_0^{2\pi} d\phi \int_0^{2\pi} d\psi \int_0^{\pi} \frac{1}{3\sqrt{3}} S_0 \ P_0^3 \ K''(\omega_1) \ f_i \ f_j \ f_k \ F_l \ Z(\Theta) \ d\Theta$$

$$\Delta G_{ijkl} = \int_0^{2\pi} d\phi \int_0^{2\pi} d\psi \int_0^{\pi} \frac{1}{3\sqrt{3}} S_0 \ P_0^3 \ K''(\omega_1, \omega_2) \ f_i \ f_j \ f_k \ F_l \ Z(\Theta) \ d\Theta \qquad (21)$$

Where:

$$K''(\omega_1) = \int_0^{\infty} \left\{ \frac{2C_2^2 \ A \ g'(\tau)}{[4^4 C_1^5] \ (1+2j\omega_1\tau)(1+3j\omega_1\tau)(1+j\omega_1\tau)^3} - \frac{C_3 \ A \ g'(\tau)}{[4^3 C_1^4](1+3j\omega_1\tau)(1+j\omega_1\tau)^3} \right\} d\tau$$

$$K''(\omega_1,\omega_2) = \int_0^{\infty} \left(\frac{2C_2^2 \ [4^4 C_1^5]^{-1} \ A \ g'(\tau)(1+j\omega_1\tau)^{-2}}{(1+2j\omega_1\tau)(1+j[2\omega_1+\omega_2]\tau)(1+j\omega_2\tau)} - \frac{C_3 \ [4^3 C_1^4]^{-1} \ A \ g'(\tau)(1+j\omega_1\tau)^{-2}}{(1+j[2\omega_1+\omega_2]\tau)(1+j\omega_2\tau)} \right) d\tau$$

and,

$$[\Delta H_{ijkp}] = \int_0^{2\pi} d\phi \int_0^{2\pi} d\psi \int_0^{\pi} \frac{1}{9} P_0^4 \ K''(\omega_1) \ f_i \ f_j \ f_k \ f_p \ Z(\Theta) \ d\Theta \qquad (22)$$

Note that all the quantities are frequency dependent. When electric and elastic field are applied simultaneously with different frequencies, one finds the direct and reverse effects have different magnitude, for example, if $\omega_1 \neq \omega_2$, $\Delta d_{kl}(\omega_1) \neq \Delta d_{kl}(\omega_2)$, therefore,

we have used a prime on some of the constants in ΔU_i to indicate their frequency dependence. In general, the contributions from 70.5^0, 109.5^0 and 90^0 twin structures can be all written in the form of Eq.(14) - Eq.(22) except the integration coefficients would be different in each case.

If $T_l = 0$, Eq.(14) becomes:

$$\Delta P_i = \Delta \varepsilon_{ik} E_k + \Delta r_{ijk} E_j E_k + \Delta H_{ijkp} E_i E_k E_p$$

$$\Delta U_l = \Delta d_{ki} E_k + \Delta Q_{ikl} E_i E_k + \Delta G_{ijkl} E_i E_j E_k$$

$$i, j, k, p = 1, 2, 3 \qquad (23)$$

The electric field induced longitudinal strain and polarization arising from the domain wall motion are:

$$\Delta U_3 = \Delta d_{33} E_0 + \Delta Q_{333} E_0^2 + \Delta G_{3333} E_0^3$$

$$\Delta P_3 = \Delta \varepsilon_{33} E_0 + \Delta r_{333} E_0^2 + \Delta H_{3333} E_0^3 \qquad (24)$$

Similarly, the shear strain and related polarization under an applied *a.c.* electric field are described by:

$$\Delta U_5 = \Delta d_{15} E_0 + \Delta G_{1115} E_0^3$$

$$\Delta P_1 = \Delta \varepsilon_{11} E_0 + \Delta H_{1111} E_0^3 \qquad (25)$$

There are no second harmonic and higher even harmonic components in shear vibrations. Therefore, it is expected that the dependence of Δd_{15} and $\Delta \varepsilon_{11}$ on the alternating electric field strength should have different characteristics than those of Δd_{33}, Δd_{31}, and $\Delta \varepsilon_{33}$.

Strictly speaking, under external forces the difference in free energy for the two domains of a twin is[51]:

$$\Delta g = \Delta \varepsilon_{(s)ij} \sigma_{ij} + \Delta P_{(s)i} E_i + \frac{1}{2} \Delta s_{ijkl} \sigma_{ij} \sigma_{kl} + \frac{1}{2} \Delta \kappa_{ij} E_i E_k + \Delta d_{ijk} E_i \sigma_{kl} \qquad (26)$$

where, the first two terms are the differences of the spontaneous strain and polarization of the two domains, representing the primary ferroic effect. The remaining three terms in Δg arise from external force induced differences in elastic compliance, dielectric susceptibility, and piezoelectric coefficients, which

represent the secondary ferroic behavior . In this paper, only the primary ferroic effect is discussed.

IV. EXPERIMENTAL RESULTS AND DISCUSSION

4.1. EXPERIMENTAL PROCEDURE

Several compositions of the PZT solid solution system were selected for this study. The ceramic $Pb(Zr_xTi_{1-x})O_3$ specimens with x= .90, .70, .60, .54, .52, .50, .40, .30, and .15 were prepared by using the sol-gel derived powders. The processing procedure was the same as that described in Ref.[52]. The well sintered ceramic samples were poled at an electric field of 30-65 kV/cm in the temperature range of $100^0 C$ - -$130^0 C$. These poled samples were first checked with a commercial Berlincourt d_{33} meter. Values of the piezoelectric coefficients are listed in Table 1. In addition, some ceramic samples, PZT-501A and PZT-401 which were made by commercial powders form the Ultrasonic Powders Inc, South Plainfield, NJ . And also several of the hard and soft PZT specimens, PZT-5A, PZT-8 and PZT- 4 used in this study are commercial products from Vernitron piezoelectric division, Bedford, OH.

Permittivity- temperature runs were made in a computer-controlled environmental chamber (Delta Design Model 2300) using liquid nitrogen as a cooling agent. Both heating and cooling rates are about $5^0 C/min$. Data were recorded with a digital multimeter controlled by a desk top computer system (Model 9816, Hewlett Packard Inc.). The dielectric response was measured by using a modified Sawyer-Tower circuit and a precision capacitance meter (HP 4275A Multi-Frequency LCR Meter).

The piezoelectric coefficients were measured by both optical interferometry and iterative methods[53,54]. The longitudinal, transverse, and shear strains were measured using a laser interferometer and a strain gauge. The resonance-antiresonance method is widely used for measuring piezoelectric coefficients in weak electric fields at which the

TABLE I. Piezoelectric coefficients for $Pb(Zr_xTi_{1-x})O_3$ ceramics made by sol-gel derived powders. The measurements was made by the commercial Berlincourt meter.

Zr/Ti.	90/10	70/30	60/40	54/46	52/48	50/50	40/60	30/70	15/85
Density (10^3 kg/m^3)	7.44	7.55	7.60	7.62	7.7	7.4	7.6	7.59	7.3
d_{33} (10^{-12} m/V)	?	85-100	100-120	170-200	250-270	100-120	90-100	50-60	?

vibrating system remains linear. However, when the amplitude of the applied field becomes very large, the resonance-antiresonance method is no longer suitable due to the occurrence of nonlinearity. Therefore, interferometry technique was used for measurements under large alternating electric fields. The advantages of the interferometry, apart from its directness, are the simplicity in computational expressions. In addition, the measurements can be carried out under both resonance and non-resonance conditions and are not limited by the amplitude of the external fields. Moreover, a wide range of sample shapes and sizes can be tolerated. In the strain gauge technique, the strain gauge (*Kyowa KRF-02-C1-11*) was attached to the surface of a thin rectangular sample using a polymeric cement (*Kyowa PC-6*). The off-set voltage was amplified through a strain amplifier (Model No. *DPM613B, Kyowa*). The *HP4192 A LF* impedance analyzer was used when employing the resonance technique which has been standardized by *IEEE*[53]. In measuring the nonlinear parameters, a sinusoidal driving field was used for convenience of interpretation. Resistive tuneable low-pass active-filters were used (Package Date 730/740 Series, Frequency Devices, Inc.) in the measurement system. Samples were made as thin as possible in order to achieve high field with low voltage. For larger displacements, Eq.(2) of Ref.[54] is no longer valid, and the cosine term in Eq.(3) of Ref.[54] must be expanded using the Fourier-Bessel expansion. It is important to realize that the nonlinear output signals may be caused by either the nonlinearity of materials or by the distortion of the input signal in the detecting system. There are two ways to avoid the detecting system producing nonlinear output signals. (1) Using quartz as the pre-calibration sample we can subtract the nonlinear contribution of the detecting system. (2) By keeping the thickness of the samples down so that we can get sufficiently large strains while limiting the maximum displacement of the sample to values less than 140 Å.

4.2. RESULTS AND DISCUSSIONS

A *Nonlinear Piezoelectric and Dielectric Coefficients*

Fig.4. shows the piezoelectric constants d_{kl} and the dielectric constants ε_{ii} plotted as a function of applied a.c. field strength. When the magnitude of the applied electric field is below the threshold field E_t, d_{kl} and ε_{ii} remain constant. But beyond the threshold field $(E > E_t)$ d_{ik} and ε_{ij} increase with the amplitude of the a.c. electric field. E_t signifies the onset of measurable nonlinearity, which is not always clearly defined. We use $\Delta d/d$ $(\Delta\varepsilon/\varepsilon)$ > 2.5% - 4 % as the criteria according to different experimental conditions. Generally, E_t depends on frequency, temperature and material properties. For instance, for PZT-501A with F= 200 Hz and T =25^0 C, the threshold field for the piezoelectric coefficient d_{33} is approximately 300 V/cm. Analogously, when the applied field exceeds a certain value, dielectric losses also increase drastically with the amplitude of a.c. electric field[33], but the threshold fields for the loss seem to be smaller than those for the dielectric and piezoelectric coefficients. By using an oscilloscope to follow the polarization (P) and strain (S) under a.c electric field (E) at a given frequency, it was found that the P and S vs E curves are straight lines for small oscillation amplitudes, but the average slope of the hysteresis increases rapidly when the amplitude of the a.c. field exceeds certain values, as shown in the insertion of Fig.4. Since non 180^0-domain wall motion is inherently a lossy process [55-57], the strong correlation between loss and nonlinearity suggests that electromechanical nonlinearity in ferroelectric ceramics originates mainly from the motion of non-180^0 domain walls. Spectrum analyses were made to identify the higher harmonic components in the responses of polarization and strain, it is found [33] that when the direction of a.c. field is perpendicular to the poling direction of the sample, only odd harmonics exist and the shape of the hysteresis loops (both for strain and polarization vs. a.c. electric field) is always symmetric. On the other hand, when the applied electric field E is parallel to the poling direction, both odd and even harmonics exist under large driving field. The shape of hysteresis loop is no longer symmetric. This may be understood from Eqs.(24) and (25). Assuming $E_{ac} = E_0 \cos\omega x$, from Eq.(23), the longitudinal strain is:

$$\Delta U_3 = \Delta d_{33} E_{ac} + \Delta r_{333} E_{ac}^2 + \Delta G_{3333} E_{ac}^3 \qquad (27)$$
$$= Y_o + Y_1 e^{j\alpha t} + Y_{-1} e^{-j\alpha t} + Y_2 e^{2j\alpha t} + Y_{-2} e^{-2j\alpha t} + Y_3 e^{3j\alpha t} + Y_{-3} e^{-3j\alpha t} + ...$$

where

$$Y_o = \Delta r_{333} \frac{E_0^2}{2} \; ; \quad Y_1(\omega) = Y_{-1}(-\omega) = (\Delta d_{33} E_0 + \frac{3\Delta G_{3333} E_0^3}{4})$$

$$Y_2(\omega) = Y_{-2}(-\omega) = \Delta r_{333} \frac{E_0^2}{2} \; ; \quad Y_3(\omega) = Y_{-3}(-\omega) = \frac{\Delta G_{3333} E_0^3}{4}$$

The term $(Y_n e^{jn\alpha t} + Y_{-n} e^{-jn\alpha t})$ represents the component of the nth harmonic oscillation. Based on Eq.(27), we would like to elaborate a few points:

1. The third order term increases the amplitude of the fundamental frequency by an amount of

$$\frac{3\Delta G_{3333} E_0^3}{4}$$

2. The second order harmonic term creates an additional negative bias field which displaces the center of vibration of the domain wall.

3. Both the second and the third harmonic vibrations of non-180° domain walls contribute to the induced longitudinal strain. This implies that the hysteresis loops of both P vs E, and S vs E should be asymmetric when the a.c. field is beyond certain level.

The situation is somewhat different for the shear strain. From Eq.(23), we have

$$\Delta U_5 = \Delta d_{15} E_{ac} + \Delta G_{1115} E_{ac}^3 \qquad (28)$$
$$= Y_o + Y_1 e^{j\alpha t} + Y_{-1} e^{-j\alpha t} + Y_3 e^{3j\alpha t} + Y_{-3} e^{-3j\alpha t} + ...$$

where:

$$Y_o = 0 \; ; \quad Y_1(\omega) = Y_{-1}(-\omega) = \Delta d_{15} E_0 + \frac{3 \Delta G_{1115} E_0^3}{4}$$

$$Y_2(\omega) = Y_{-2}(-\omega) = 0 \; ; \quad Y_3(\omega) = Y_{-3}(-\omega) = \frac{\Delta G_{1115} E_0^3}{4}$$

There is no second harmonic in the shear strain, which is in agreement with the experimental results. Fig.5 shows the relative dielectric permittivity ε_{11} and ε_{33} as well
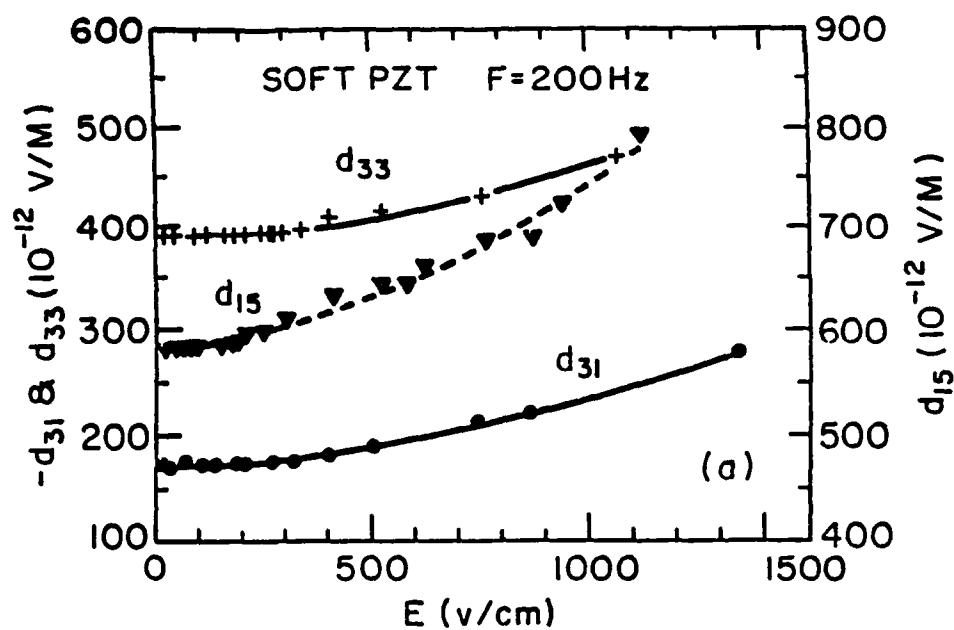
Fig.4. (a). *a.c.* electric field dependence of piezoelectric coefficients for d_{31}, d_{33}, and d_{15}.
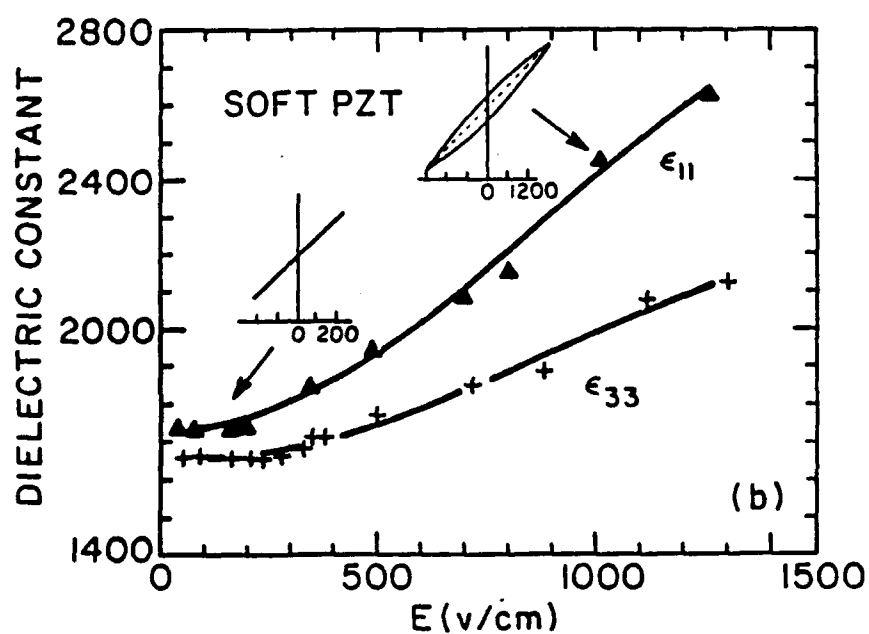
Fig.4.(b). *a.c.* electric field dependence of dielectric coefficients ε_{11}, and ε_{33}.
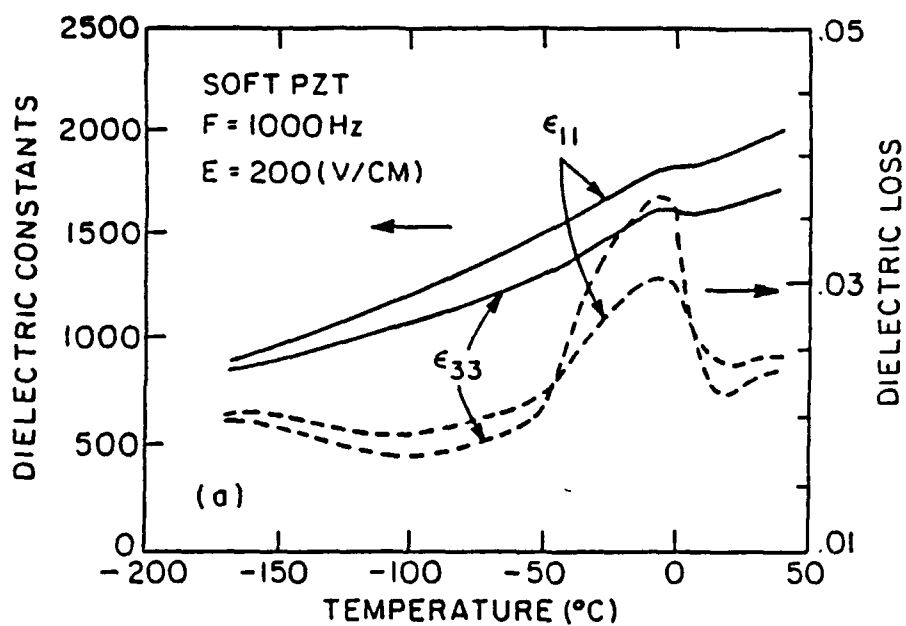
Fig.5.(a) ε_{11} and ε_{33} and their losses as a function of temperature for PZT-501A.
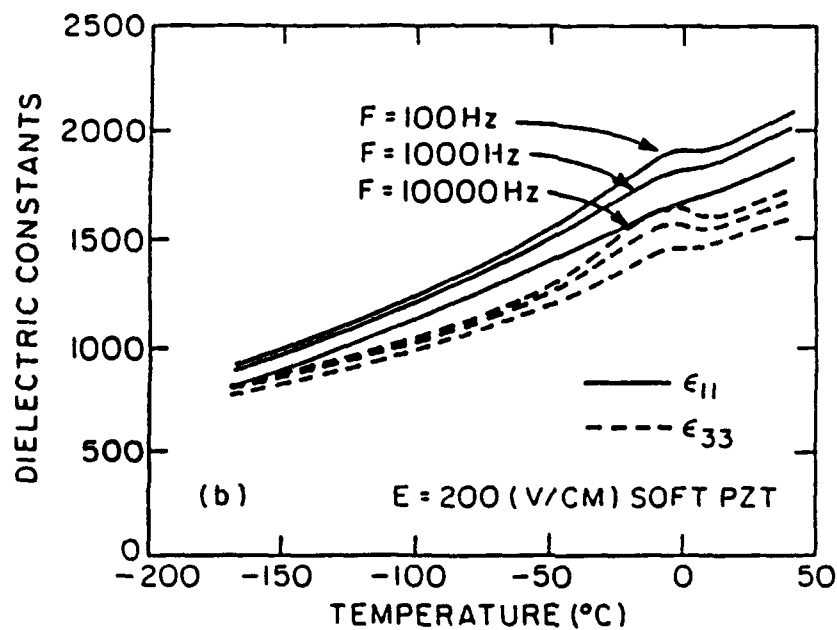
Fig.5. (b) The values of ε_{11} and ε_{33} as a function of temperature for PZT-501A at different frequencies

as their loss tangents as a function of temperature from $-200^\circ C$ to $50^\circ C$ under large a.c. electric fields. Fig.6 shows the dielectric permittivity ε_{33} and its loss versus temperature at different a.c. electric field strength. Clearly, the values of ε_{11} and ε_{33} as well as their losses are quite different at high temperatures, these differences become smaller as temperature decreases. This reveals that part of the difference between ε_{11} and ε_{33} may come from the domain boundary vibrations which will be frozen out at very low temperatures. In Ref.[33], it has been shown that the threshold fields of the piezoelectric coefficients increase with aging time, which is another strong implication that the threshold field is closely related to non-180° domain wall motion, because the reduction of the non-180° domain wall mobility is responsible for the aging phenomena in ferroelectric ceramics[58]. It is also found[33] that the threshold field strengths of the dielectric and piezoelectric coefficients decrease with increasing the magnitude of an applied positive d.c.bias field which provides the pinning to the wall motion. The nonlinearity also decreases with temperature due to the fact that the domain wall becomes less mobile at lower temperatures.

Fig.7 shows the distribution of threshold fields for the piezoelectric coefficients of PZT system with different compositions and dopants. A pronounced minimum value for the threshold field is found at the MPB composition , which reveals that the domain walls have the highest mobility for composition at the MPB. In second order approximation, the extrinsic contributions to the piezoelectric coefficient is given in Eq.(23):

$$d_{kl} = \Delta d_{kl} + \Delta Q_{ikl} E_i + \Delta G_{ijkl} E_i E_j \qquad (29a)$$

Assuming the nonlinearity is purely extrinsic the measured piezoelectric constants $\overline{d_{kl}}$ may be written as:

$$\overline{d_{kl}} = d_{kl(in)} + \Delta d_{kl} + \Delta Q_{ikl} E_i + \Delta G_{ijkl} E_i E_j \qquad (29b)$$

Based on the definition of threshold field strength for $\overline{d_{kl}}$ described earlier , we have:

$$\left|\frac{d_{33} - \left(d_{33(in)} + \Delta d_{33}\right)}{\left(d_{33(in)} + \Delta d_{33}\right)}\right|_{E_t} = \frac{\Delta Q_{333}\, E_t}{d_{33(in)} + \Delta d_{33}} \geq 3\% \qquad (29c)$$

This means that the threshold field E_t is inversely proportional to the ratio of the electrostrictive coefficient and the piezoelectric coefficient. From Eq.(15) and Eq.(17), it is found that $\Delta d_{33} / \Delta Q_{333}$ is proportional to $(C_1)^2 /(P_0 C_2)$. In Ref.[41] the restoring force constant was estimated to be greater than the square of the spontaneous strain $C_1 > (S_0)^2$, and also, $C_1 > C_2$. Therefore, $\Delta d_{33} /\Delta Q_{333}$ can be estimated to be proportional to the spontaneous polarization. Thus from Eq.(29c) one may conclude that the threshold field E_t should also increase with the spontaneous polarization. The experimental data in Fig.7 qualitatively shows this tendency. In addition, the threshold fields E_t for *PZT-8* and *PZT-4* are substantially higher than that of *PZT-5* due to the influence of dopants on the domain wall mobility.

B Electromechanical Nonlinearity Under Resonant Frequency

Some ultrasonic devices are operated at their resonance frequencies. Due to the presence of nonlinearity the performance of these devices will be altered when being driven at high field levels. In this section, we report some of the nonlinear effects under resonant conditions for a PZT-*501*A ceramic . Fig.8 shows that the complex admittance circles at different driving levels. The outer circle (curve*I*) is measured at small-signal conditions, a field level of 1 *V/cm*. The system appears to be a typical linear piezoelectric resonator with very low loss. All the data points fall onto a perfect circle. The inner circle (curve *II*) was measured at a field level of 100 *V/cm*. One can see that the data points obviously deviate from the small circle showing the presence of nonlinearity.

This is expected from the measurements on piezoelectric effects because the relationship between d_{31} and the field strength no longer remains linear under large field, which invalidates the linear assumption made in the measurement technique. Both the
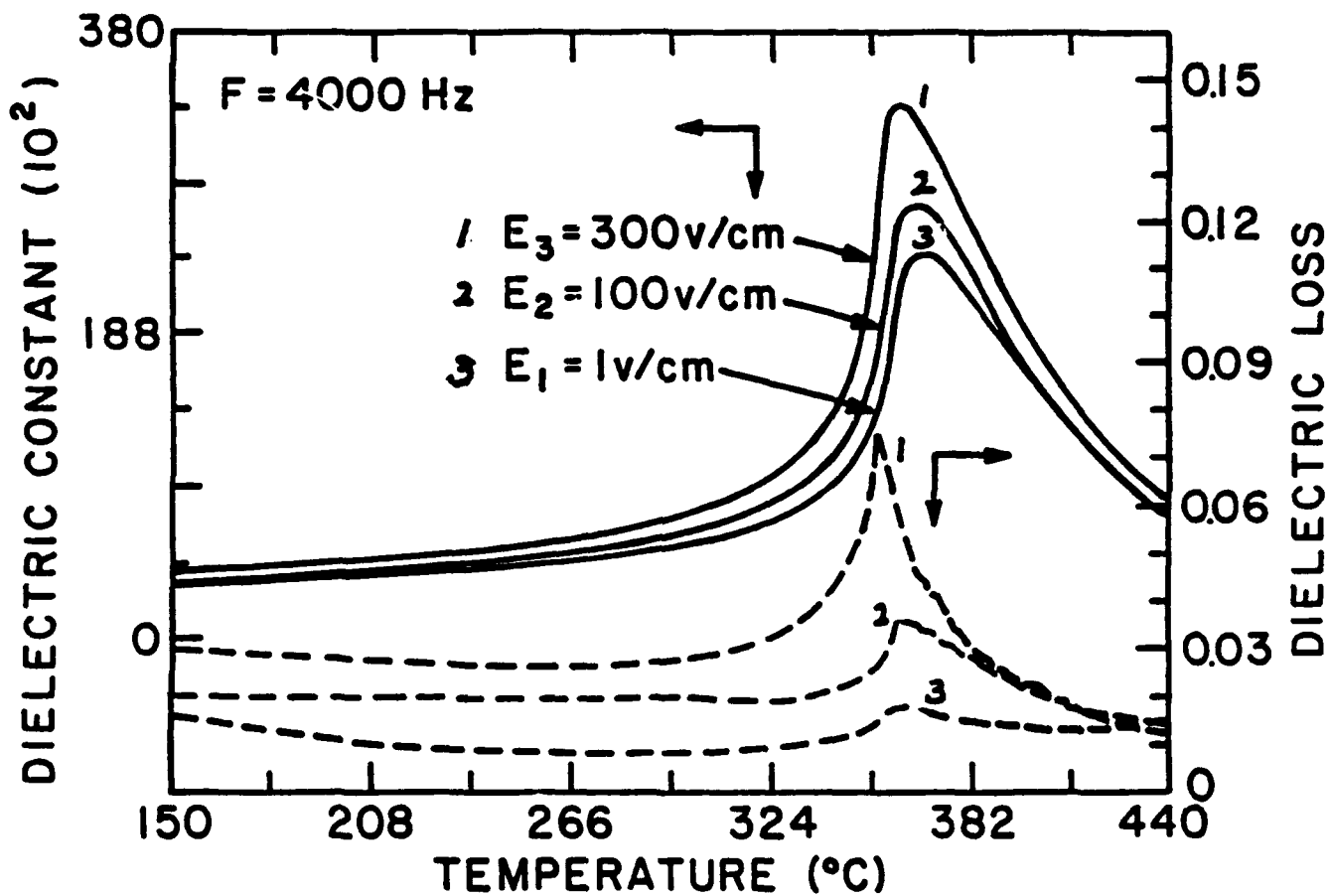
Fig.6. Temperature dependence of ε_{33} and its $tan\delta$ of PZT-*501A* at different magnitudes of *a.c.* fields
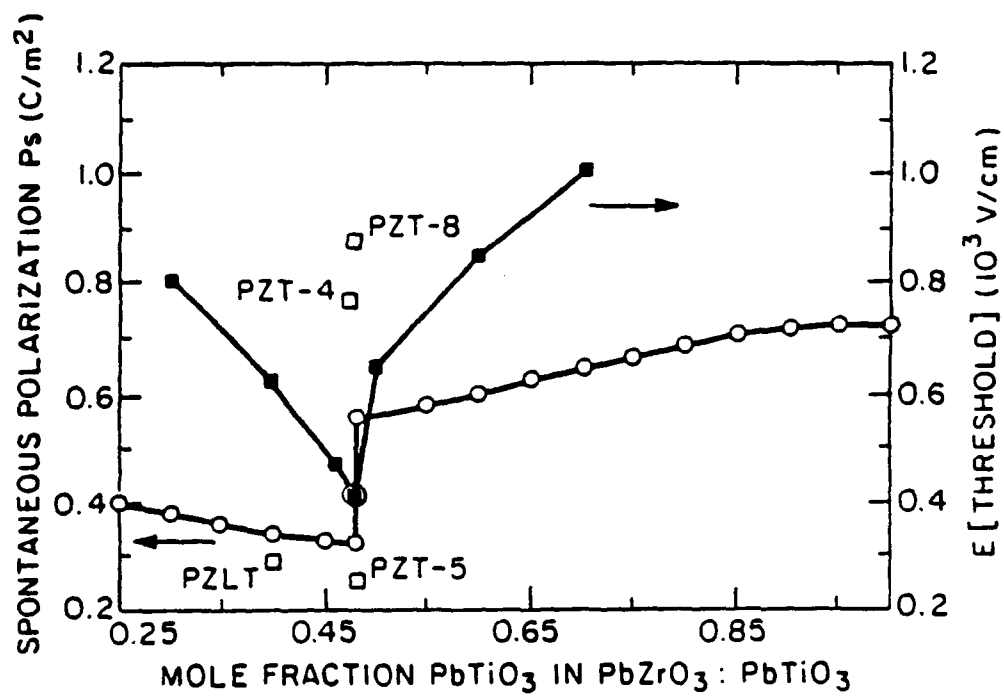
Fig.7. Dependence of the threshold field strength and the spontaneous polarization on the T_i / Z_r ratio for PZT ceramics.
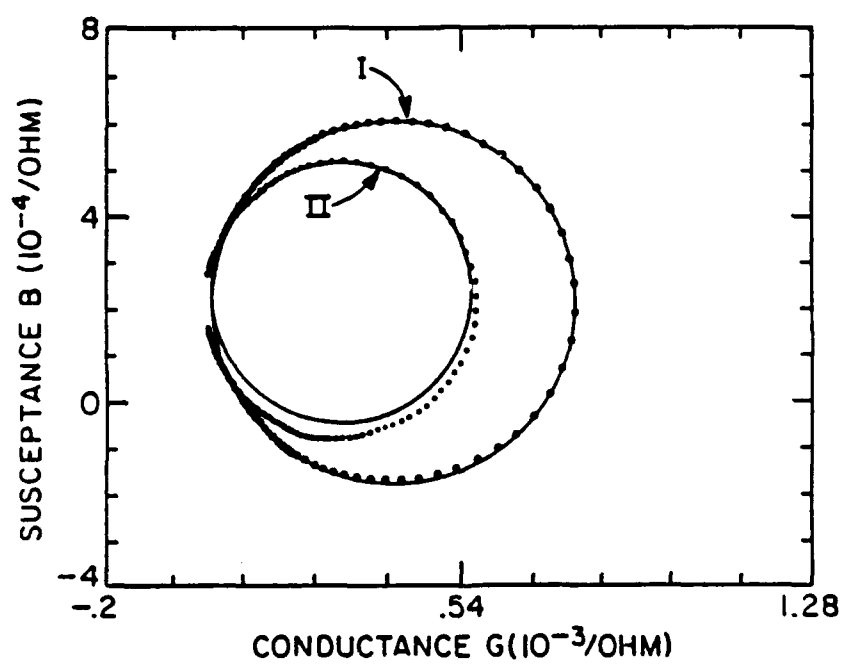
Fig.8. Complex admittance plot of PZT-*501A* bar measured with two different applied field strengths, $E_1 = 1V/cm$ and $E_2 = 100$ V/cm.

magnitudes of $d_{31}[II]$ ($-180 \times 10^{-12} V/m$) and $d_{31}'[II]/d_{31}[II]$ (0.064) which were measured at high driving levels and non-resonant frequencies using an interferometer are larger than those measured at low driving levels, $d_{31}[I]$ ($-176 \times 10^{-12} V/m$) and $d_{31}'[I]/d_{31}[I]$ (0.018). This strongly implies that the nonlinear increase of piezoelectric coefficients causes nonlinear effects at the resonance frequency. We suggest that this nonlinear change of piezoelectric coefficients is originated from the domain wall motion because the increase of (d_{31}'/d_{31}) indicates that the increase of the macroscopic-losses mainly come from domain motions [33]. When the applied field exceeds a certain level, the nonlinear domain wall motions start to contribute to the piezoelectric effect, and the coupling between the vibrations of domain wall and extensional mode causes the nonlinear effects at the resonance frequency. The field dependence of the piezoelectric coefficients will cause the extremum frequencies of the admittance to shift as shown in Fig.9. Fig.9 (a) is the amplitude of the admittance of a PZT - *501A* plate, which was measured with a spectrum analyzer. The resonant frequency f_m shifts towards lower frequencies with increasing applied *a.c.* voltage, but the anti-resonance frequencies f_n do not shift significantly as reported by Uchino et,al.[6]

Interestingly, however, when measuring the absolute value of admittance $|Y|$ of a bar sample with an impedance analyzer, we found that both f_m and f_n shift noticeably to lower frequencies at higher driving level, as shown in Fig.9(b), which may imply that the nonlinearity affects certain vibration modes more severely than to the others. Meanwhile , the experimental results could be affected by the measurement techniques.

Fig.10 and Fig.11 show the dielectric losses and dielectric constants as a function of frequency, respectively, under different field levels near an isolated resonance. It can be seen that the resonance peaks of both the dielectric loss and the dielectric constant move toward lower frequencies with increasing driving level. The dielectric loss in the vicinity of the resonant frequency also becomes larger for the case of higher driving level as shown in Fig.10. It should be noted that when large electric field is applied, nonlinear effects
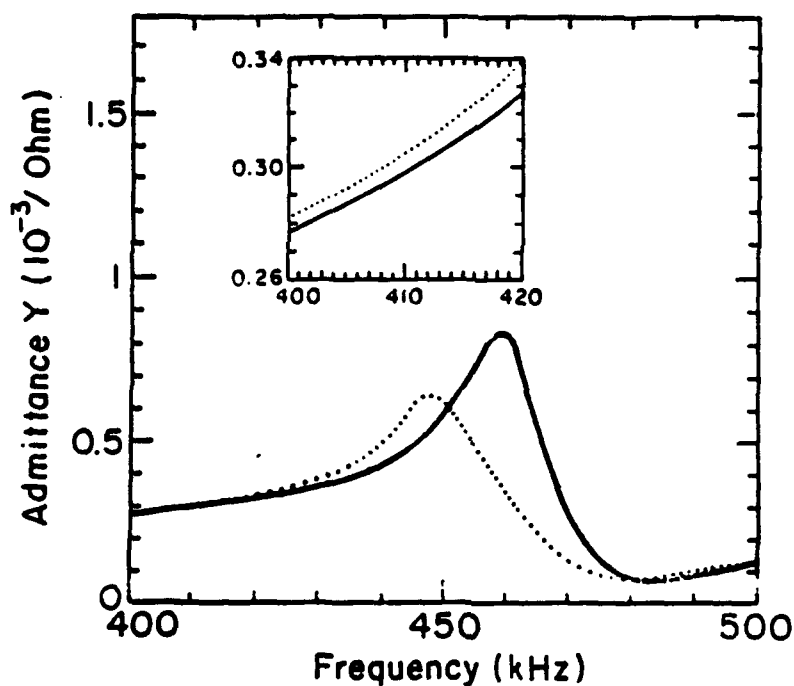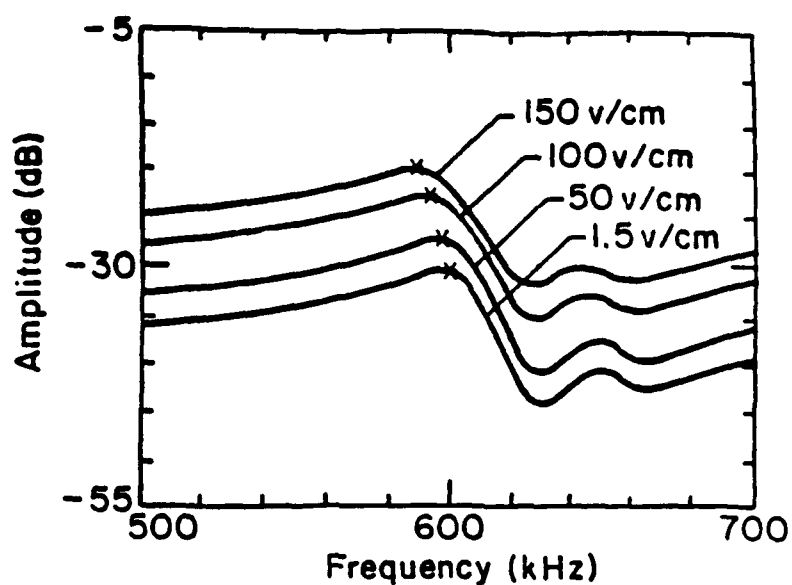
Fig.9. Typical admittance curves measured for the *PZT-501A* samples at different driving

levels. (a) Measured electrical admittance of *PZT-501A* plate at four different

driving levels. (b) Absolute value of admittance |*Y*| for a *PZT-501A* bar at two

driving levels. The soild line and the dash line represent results obtained at field

levels of $E_1 = 1V/cm$ and $E_2 = 100 V/cm$ respectively.
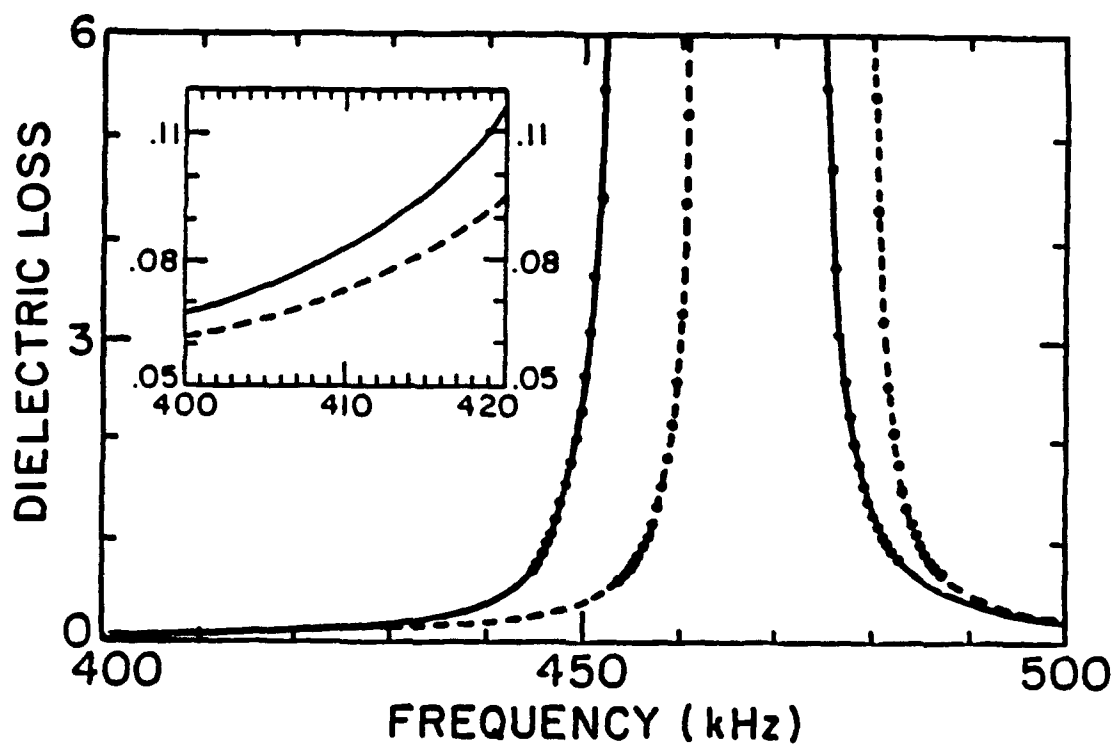
Fig.10. Dielectric losses vs frequency in the vicinity of the resonance frequency with respect to different driving levels for PZT-501A bar. The dash line is for $E_1 =$ 1V/cm and the solid line is for $E_2 =$ 100 V/cm.
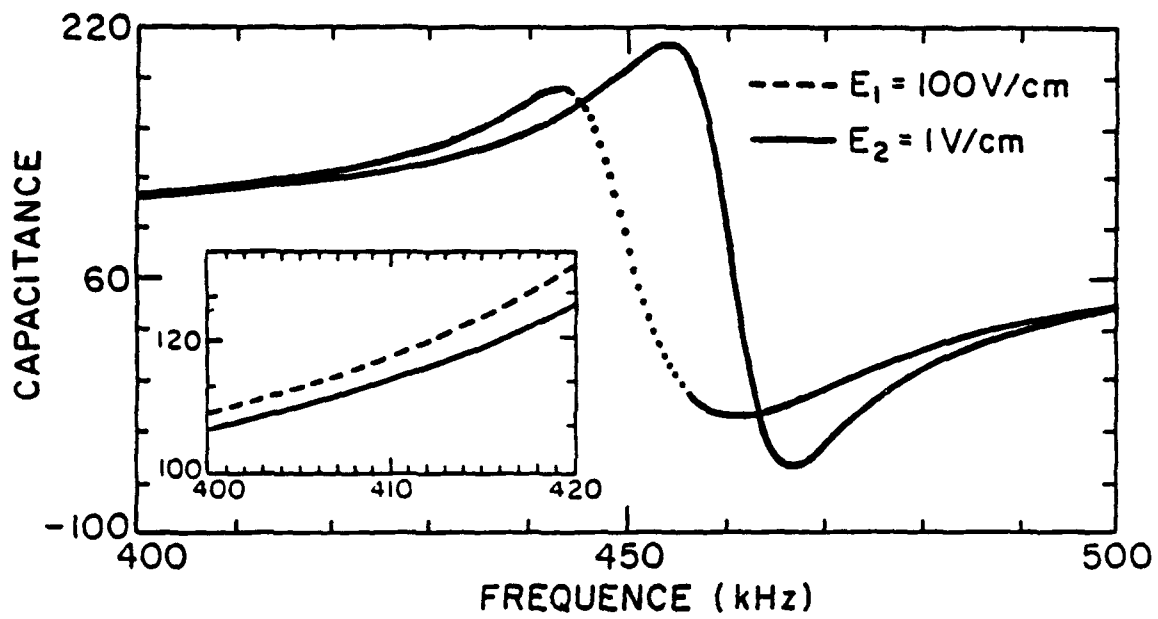
Fig.11. Capacitance of a *PZT-501A* bar vs. frequency in the vicinity of the resonance

frequency at different driving levels.

occur at all frequencies, hence the dielectric loss, dielectric constant and piezoelectric coefficients become larger in all frequency range. Away from the resonance, the motions of non-180⁰ domain walls are the cause for the changes in the dielectric, elastic, and piezoelectric coefficients. At the resonant frequency, changes of these coefficients will cause the shifts of the resonance and anti-resonance frequencies, f_m and f_n. In addition, the mechanical quality factor Q_m and the electromechanical coupling factors K_t will also be affected.

From Ref.[28], in the second order approximation, the shift of the resonant frequency for extensional vibration of an electromechanically excited bar can be written as:

$$\delta\omega_r^D = -\left\{ \frac{32\left[S_{111}^E\right]^2}{9\pi^2 \, S_{11}^E} + \frac{9S_{1111}^E}{32} \right\} \frac{\omega_r^D d_{31}^2 \, E^2 Q^2}{\left[S_{11}^E\right]^2 a^2} \qquad (30)$$

where ω^D_r is the resonant frequency of the extensional mode for a linear system. The frequency of the P_3 maximum is also shifted by the electric field,

$$\delta\omega_r^P = -\left\{ \frac{\left(\epsilon_{333}^T\right)^2}{\epsilon_{33}^T} + \frac{3\epsilon_{333}^T}{4} \right\} \frac{\omega_r^P \, E^2 \, Q^2}{2\epsilon_{333}^T \, a^2} \qquad (31)$$

where ω^P_r is the small-signal resonance frequency. Q is the mechanical quality factor and a is the thickness of the sample. Eqs.(30) and (31) are for single domain single crystal system. For ceramics, there exist additional shifts of the resonant frequencies by domain wall motion. From Eqs.(15)-(21) they can be expressed as:

$$\Delta\omega_r^D = -\left\{ \frac{32\left[\Delta S_{111}\right]^2}{9\pi^2 \, (S_{11(in)} + \Delta S_{11})} + \frac{9\Delta G_{111}}{32} \right\} \frac{\omega_r^D \, (d_{31(in)} + \Delta d_{31})^2 \, E^2 \, Q^2}{(S_{11(in)} + \Delta S_{11})^3 \, a^2} \qquad (32)$$

and

$$\Delta\omega_{\Upsilon}^{P} = -\left\{\frac{[\Delta r_{333}]^2}{\varepsilon_{33(in)} + \Delta\varepsilon_{33}} + \frac{3\Delta H_{3333}}{4}\right\} \frac{\omega_{\Upsilon}^{P} \; E^2 \; Q^2}{2(\varepsilon_{33(in)} + \Delta\varepsilon_{33}) \; a^2} \qquad (33)$$

Here $\varepsilon_{ij(in)}$, $d_{lk(in)}$, and $S_{nm(in)}$ are intrinsic properties. The total shift of these resonance frequencies are the sum of the intrinsic and extrinsic contributions. The above analyses give rise to the relationship between the shifts of the maximum frequency and the damping constant (or losses), restoring force constants, as well as spontaneous polarization and strain. These relations may be used to qualitatively explain the experimental results.

V. SUMMARY

We have measured the dielectric, piezoelectric properties in several compositions of *PZT* system at both high and low field levels. The experimental results show that the domain wall vibrations contribute significantly to the electromechanical nonlinearity in ferroelectric ceramics. The main results are summarized as follows:

(1) A phenomenological model has been extended to evaluate the macroscopic nonlinear parameters associated with non-180^0 domain wall vibrations in ferroelectric ceramics. The theoretical descriptions qualitatively agree with some of the experimental results.

(2) The piezoelectric and dielectric coefficients and losses in the nonlinear regime are much larger than those in the linear regime. The threshold fields of the dielectric and piezoelectric coefficients are strongly affected by the bias field, temperature and compositions.

(3) Both f_m and f_n of the admittance are shifted by the electric field due to the nonlinearity arising from non-180^0 domain wall motion. It has been suggested previously [31] that the nonlinear effects in the resonance frequency region are originated from the collective resonance of domain walls. This opinion is questionable because the resonance frequency of ceramic samples depends upon the sample size and is usually much lower than the

domain wall resonance frequency. However, since the resonance frequency of domain walls is still a disputed topic, further investigation is required. We believe that the nonlinear effects contain both intrinsic and extrinsic contributions, and in a multidomain crystals such as ferroelectric ceramics, the extrinsic contributions play the dominant role in generating these nonlinearities.

ACKNOWLEDGEMENTS

REFERENCES

1.P.Gonnard, L.Eyraud, M.Troccaz and P.Eyraud "Analysis of the Suitability of Piezoceramics for High Power Transducers" Proc. IEEE. Ultrasonics Symposium pp619-623 (1986).

2.Ralph. S. Woollett, and Charles. L. Leblanc, "Ferroelectric Nonlinearities in Transducer Ceramics" IEEE Transactions on Sonics and Ultrasonics, Vol.SU-20, No.1 pp24-31 (1973).

3. D.A. Berlincourt, D.R.Curran and H.Jaffe "Piezoelectric and Piezomagnetic Materials and Their Function in Transducers" Physical Acoustics Vol.1, Part A, Chapter.3, Ed. by W.P. Mason, Academic Press, NY (1964).

4. J.M.Huckabay, Hollis.C.Boehem, and Elmer L. Hixson "Admittance Measurement Accuracies Required to Determine Nonlinear Behavior in Sonar Transducers" IEEE Transactions on Sonics and Ultrasonics , Vol.SU-22, No.2 pp101-104 (1975).

5. K.Lubitz and W.Wersing, "Automatic Performance Testing of Piezoelectric Ceramics for Power Transducers" Ferroelectrics, Vol.40. pp237-244 (1982).

6.K.Uchino, Hiroyasu Negishi and Terukiyo Hirose, "Drive Voltage Dependence of Electromechanical Resonance in PLZT Piezoelectric Ceramics" Jan. J.of Appl. Phys. Vol.28 Supplement 28-2, pp47-49 (1989).

7. R.Lec and J.F.Vetelino, "Influence of An External Electric Field On The Electroacoustic Properties of PZT-4", Proc.IEEE. Ultrasonics Symposium, pp741-745 (1987).

8. E.A.Kraut, T.C.Lim and B.R.Tittmann, " Application of Nonlinear Interactions in Ferroelectric Ceramics to Microwave Signal Processing" Ferroelectrics, Vol.3, pp247-255 (1972).

9. A.Oliver, " Acoustic Surface Waves", Springer, New York. (1978).

10.R.E. Newnham, Q.C.Xu, S.Kumar and L.E. Cross, "Smart Ceramics", Ferroelectrics, Vol.102, pp1-8, (1990).

11. A.F. Devonshire, "Theory of Barium Titanate-Part I", Phil. Mag. 40 pp. 1040-1049 (1949).

12. M.J. Haun, E.Furman, S.J. Jang and L.E. Cross "Thermodynamic Theory of the Lead Zirconate - Titanate Solid Solution System, Part I: Phenomenology" , Ferroelectrics, Vol.99, pp13-25 (1989).

13. G.Arlt, H.Dederichs, and R.Herbiet, " 90^0-domain Wall Relaxation in Tetragonally Distorted Ferroelectric Ceramics" Ferrroelectrics Vol.74, pp37-53 (1987).

14. G.Arlt and H.Dederichs, "Complex Elastic, Dielectric and Piezoelectric Constants by Domain Wall Damping in Ferroelectric Ceramics" Ferroelectrics Vol.29, pp47-50 (1980).

15. P.Gurk, "Contribution of Domain Wall Motion to the Permittivity of Rochelle Salt " Phys. Stat. Sol.(a) 10, pp407-414 (1972).

16. V.A. Isupov, "Characteristics of Coexistence of Tetragonal and Rhombohedral Phases in Piezoelectric Ceramics Based on $PbTiO_3$ and $PbZrO_3$ ", Sov.Phys. Solid State Vol.18 No.4 pp529-534 (1976).

17. A.G. Luchaninov, A.V. Shil'Nikov, L.A.Shuvalov, and I.JU.Shipkova, "The Domain Processes And Piezoeffects In Polycrystalline Ferroelectrics" Ferroelectrics, Vol.98. pp123-126. (1989).

18. E.K.W. Goo, R.K. Mishra, and G.Thomas "Electron Microscopy Study of the Ferroelectric Domains and Domain Wall Structure in $PbZr_{0.52}Ti_{0.48}O_3$", J. Appl.Phys. Vol.52, No.4   pp2939 - 2943 (1981).

19. P.G.Lucuta, V.Teodoresu and F. Vasiliu, "SEM, SAED, and TEM Investigations of Domain Structure in PZT Ceramics at Morphotropic Phase Boundary" Appl. Phys. A37, pp237-242 (1985).

20. P.G.Lucuta, "Ferroelectric-Domain Structure in Piezoelectric Ceramics" J. Am. Ceram. Soc., Vol.72[6], pp933-937 (1989).

21. G.Arlt, "The Role of Domain Wall on the Dielectric, Elastic and Piezoelectric Properties of Ferroelectric Ceramics", Ferroelectrics, Vol.76 pp451-458 (1987).

22. G.Arlt, "Microstructure and Domain Effects in Ferroelectric Ceramics", Ferroelectrics, Vol.91, pp3-7 (1989).

23. R.Herbiet, U.Robels, H.Dederichs, and G.Arlt, "Domain Wall and Volume Contributions to Materials Properties of PZT Ceramics" Ferroelectrics, Vol.98, pp102-121 (1989).

24. E.I. Eknadiosiants, V.Z.Borodin, V.G.Smotrakov, V.V.Eremkin and A.N. Pinskaya, "Domain Structure of Rhombohedral $PbTi_xZr_{1-x}O_3$ Crystals ", Ferroelectrics, Vol.111 pp283-289 (1990).

25. L.Pardo, J.Mendida, A.Gonzalez, and J.De. Frutos "Role of Domains On the Electromechanical Anisotropy of Ca-Modified $PbTiO_3$ Ceramics" Ferroelectrics, Vol.94 pp189-194 (1989).

26. J. Von Cieminski, C.Kleint, H.Beige and R.Hoche "Effects of Internal Mechanical Stress on the Electromechanical Properties of Ferroelectric Ceramics" Ferroelectrics, Vol.109, pp95-100 (1990).

27. D.Berlincourt and H.A.Krueger, "Domain Processes in Lead Titanate Zirconate and Barium Titanate Ceramics" J.of Appl.Phys. Vol.30(11) pp1804-1810 (1959).

28. H.Beige and G.Schmidt, "Electromechanical Resonances for Investigating Linear and Nonlinear Properties of Dielectrics", Ferroelectrics Vol. 41, pp39-49 (1982).

29. M.D. Bryant, and R.F.Keltie, "A Characterization of the Linear and Non-linear Dynamic Performance of a Practical Piezoelectric Actuator, Part.1: Measurements" Sensors and Actuators, 9. pp95-103 (1986).

30. M.D. Bryant, and R.F.Keltie, "A Characterization of The Linear and Non-linear Dynamic Performance of a Practical Piezoelectric Actuator, Part.2. Theory", Sensors and Actuators, 9. pp105-114 (1986).

31. A.F. Litvin, M.M.Pikalev, V.A.Doroshenko, and V.Z. Borodin, "Electromechanical Nonlinearity of Polycrystalline Ferroelectrics Under Resonant Excitation" Ferroelectrics, Vol.51, pp159-171 (1984).

32. H.J. Hagemann, "Loss Mechanisms and Domain Stabilization in Doped BaTiO$_3$ ", J. Phys.C. Vol.11, pp3333-3344 (1978).

33. Shaoping Li, Wenwu Cao, and L.E.Cross, "The Extrinsic Nature of Nonlinear Behavior Observed in Lead Zirconate Titanate Ferroelectric Ceramics" J.Appl. Phys, 69(10) pp7219 -7224 (1991).

34. A.S.Nowick, and W.R.Heller, "Anelasticity and Stress-Induced Ordering of Point Defects in Crystals", Adv. in Phys.12, pp251-298 (1963).

35. A.S.Nowick, and W.R.Heller, "Dielectric and Anelastic Relaxation of Crystals containing Point Defects", Adv. in Phys.14, pp101-164 (1965).

36. R.E. Nettleton, "Effective Mass of 180^0 Domain Wall in Single Crystal Barium Titanate" J.of Physical Society of Japan, Vol.22, No.6, pp1375-1386 (1967).

37. R.C. Miller and G.Weinreich, "Mechanism for the Sidewise Motion of 180^0 Domain Walls in Barium Titanate " Phys. Rev. Vol.117, pp117 (1960).

38. J. Fousek, and B. Brezina, " Relaxation of 90^0-Domain Walls of BaTiO3 and Their Equation of Motion", J. Phy. Soc. of Japan, Vol.19, No.6, pp830-838 (1964); and "Frequency Dependence of the Motion of 90^0 Domain Walls in Barium Titanate" Bulletin of the Academy of Science of the USSR. 28. pp624-628 (1964).

39. J. Fousek,and B. Brezina, "The Movement of Single 90^0 Domain Walls of BaTiO$_3$ in an Alternating Electric Field", Czech.J.Phys.B10, pp511-528(1960), and "The Motion of 90^0 Wedge Domains in BaTiO$_3$ in an Alternating Electric Field", Czech.J.Phys.B11, pp344-359(1961).

40. G.Arlt and N.A. Pertsev, "Force constant and effective mass of 900 domain walls in ferroelectric ceramics", J. Appl. Phys. 70(4) pp2283--2289 (1991)

41. V.S.Postnikov, V.S.Pavlov, and S.K.Turkov, "Internal Friction in Ferroelectrics due to interaction of domain boundaries and Point Deffects", Phys.Chem.Solids, Vol.31, pp1785-1791 (1970).

42. V.S.Postnikov, V.S.Pavlov, and S.K.Turkov, "Internal Friction in $Pb_{0.95}Sr_{0.05}(Zr_{0.53}Ti_{0.47})O_3+3\%PbO$ Ferroelectric Ceramics" Izu.Akad.Nauk. 31. pp1845-1850 (1967).

43. V.S.Postnikov, V.S.Pavlov, S.A.Gridnev, and S.K.Turkov, "Interaction Between 90^0 Domain Walls and Point Defects on the Crystal Lattice in Ferroelectric Ceramics" Soviet Physics-Solid State Vol.10(6) pp1267-1271 (1968).

44. Jan.G.Smits, "Influence of Moving Domain Walls and Jumping Lattice Defects on Complex Material Coefficients of Piezoelectrics" IEEE Transactions on Sonics and Ultrasonics Vol.SU-23, No.3, pp168-174 (1976).

45. J.O.Gentner, P.Gerthsen, A.Schmidt, and R.E.Send, "Dielectric Losses in Ferroelectric Ceramics Produced by Domain Wall Motion", J.Appl.Phys.49(8), pp4485-4489 (1978).

46. A.H. Nayfeh, "Perturbation Methods", John Wiley & Sons Inc. (1973).

47. C.E. Land, and W.D. Smith, Appl. Phys. Lett 23. pp57-60 (1973).

48. I.P.Kaminow, " An Introduction to Electric-optic Devices " Academic Press, New York (1974).

49. J. R. Maldonado and A.H. Meitzler, "Ferroelectric Domain Switching in Rhombohedral- Phase PLZT Ceramics " Ferroelectrics, Vol.3, pp169-175, (1972).

50. C.J. Burfoot, and G.W. Taylor, " Polar Dielectrics and Their Applications " pp304, The Macmilan Press Ltd. (1979).

51. R. E. Newnham, "Domains in Minerals" Amer. Miner. Vol.59, pp906-918 (1974).

52. Z.Q. Zhuang, Michael.J.Haun, Sei-Joo Jang and L.E. Cross, "Fabrication and Characterization of Pure Homogeneous PZT Ceramics from Sol-Gel Derived Powders", Advanced Ceramic Materials, 3[5] pp485-90 (1988).

53. Jan.G. Smits, "Iterative Method for Accurate Determination of the Real and Imaginary Psrts of the Materials Coefficients of Piezoelectric Ceramics" IEEE Transactions on Sonic and Ultrasonics, Vol.SU-23, No.6 pp393-402 (1976).

54. Q.M.Zhang, W.Y. Pan and L.E. Cross, "Laser Interferrometer for the Study of Piezoelectric and Electrostrictive Strains", J. Appl. Phys. 63(8) pp2492-2496 (1988).

55. L.Benguigui, " Ferroelectric Losses in BaTiO3 Produced by the 90^0 Domain Walls" Ferroelectrics, Vol.7. pp315-317, (1974).

56. D.G. Sannikov, " Dispersion in Ferroelectrics" Soviet Physics JETP Vol.14,No.1 pp98-101 (1962).

57. P. Gerthsen, K.H. Hardtl, and N.A. Schmidt, "Correlation of Mechanical and Electrical Losses in Ferroelectric Ceramics" J. Appl. Phys. 51(2) pp1131-1134 (1980).

58.Seiji.Ikegami, and Ichiro Ueda "Mechanism of Aging in Polycrystalline BaTiO3 " J. of the Physical Socity of Japan, Vol.22, No.3. pp725-734 (1967).

APPENDIX 16

Stress and electric displacement distribution near Griffith's type III crack tips in piezoceramics

Shaoping Li, Wenwu Cao and L.E. Cross

Materials Research Laboratory. The Pennsylvania State University. University Park, PA 16802. USA

The inhomogeneous distributions of internal shear stress and electrical field induced by external shear stress or applied electric field around a Griffith's type III crack tip in ferroelectric ceramics have been analyzed. For a linear system. the stress and the electric displacement intensity factors. K_{III} and K_{IV}. respectively. can be expressed in simple analytic forms which account for both electric and mechanical contributions.

The performance of piezoceramics is altered by the presence of cracks, cuts. narrow cavities and similar flaws which may propagate under certain conditions causing eventual destruction of a body as a whole. Today. the problem of mechanical reliability of ferroelectric ceramics becomes increasingly important as the materials are used in more and more sophisticated areas. An updated review about the fracture problem in ferroelectric ceramics was given by Freiman [1]. More recent studies [1–3] show that the mechanical behavior of poled PZT ceramics is greatly affected by the external force induced inhomogeneous distribution of internal stress, and the type of cracks. There exist both electric field and mechanical stress concentration near crack tips. which induces crack propagation and incompatible elastic deformation in ferroelectric ceramics. In usual non-ferroelectric brittle ceramics, the stress intensity factor $K_J (J=I. II. III)$ is related to the stress σ by [4–6]

$$K_J = \sigma Y \sqrt{a}. \tag{1}$$

where a is the crack length. Y is the shape factor of a specimen. For ferroelectric ceramics the expression of eq. (1) needs to be modified due to the piezoelectric effect. Parton et al. [7], have given a general description of the electroelastic plane problem for a piezoelectric medium containing a rectilinear crack, and analyzed in detail the Griffith's type I crack. In this Letter. we discuss the influence of Griffith's type

III crack on electric and mechanical properties in piezoceramics. Relatively simple expressions of the stress and electrical displacement intensity factors K_{III} and K_{IV} have been derived. which can be used to evaluate the mechanical behavior of piezoceramics.

The results derived here may be very helpful in some specific applications. such as transducers with thickness shear vibration mode. mismatch and incompatible deformation between ferroelectric ceramics and substrates under external shearing force in multilayer devices. composite devices and electronic packages.

If a ceramic sample is poled along the x_3 axis. its mechanical, dielectric and piezoelectric properties are described by five elastic moduli. two dielectric and three piezoelectric coefficients. In Voigt notation. the constitutive equations may be written as [7,8]

$$\sigma_{11} = c^E_{11}s_{11} + c^E_{12}s_{22} + c^E_{13}s_{33} - e_{31}E_3. \tag{2a}$$

$$\sigma_{22} = c^E_{12}s_{11} + c^E_{22}s_{22} + c^E_{13}s_{33} - e_{31}E_3. \tag{2b}$$

$$\sigma_{33} = c^E_{13}(s_{11} + s_{22}) + c^E_{33}s_{33} - e_{33}E_3. \tag{2c}$$

$$\sigma_{23} = 2c^E_{44}s_{23} - e_{15}E_2. \tag{2d}$$

$$\sigma_{13} = 2c^E_{44}s_{13} - e_{15}E_1. \tag{2e}$$

$$\sigma_{12} = (c^E_{11} - c^E_{12})s_{12}. \tag{2f}$$

$$D_1 = \epsilon_{11}E_1 + 2e_{15}s_{13}, \tag{2g}$$

$$D_2 = \epsilon_{11}E_2 + 2e_{15}s_{23}, \tag{2h}$$

$$D_3 = \epsilon_{33}E_3 + e_{31}(s_{11} + s_{22}) + e_{33}s_{33}, \tag{2i}$$

where $s_{ij} = \frac{1}{2}(\partial u_i/\partial x_j + \partial u_j/\partial x_i)$ is the elastic strain component; u_j ($j = 1, 2, 3$) is the elastic displacement field, $E_i = \partial\varphi/\partial x_i$, is the electric field strength (the depolarization field is not included), and φ is the electric potential, e_{31}, e_{33} and e_{15} are the piezoelectric coefficients, c_{11}^E, c_{12}^E, c_{13}^E, c_{33}^E and c_{44}^E are the elastic moduli at constant electric field, ϵ_{11} and ϵ_{33} are the dielectric permittivities at constant strain.

For a system under longitudinal shear stress (see fig. 1), the so-called antiplane problem, we have the following conditions [5,6]:

$$u_1 = u_2 = 0, \tag{3a}$$

$$u_3 = u_3(x_1, x_2), \tag{3b}$$
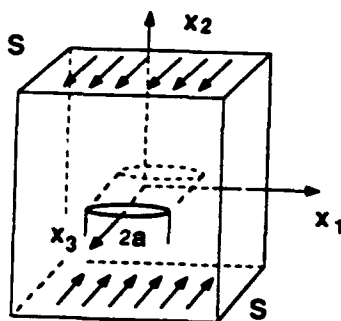
$$\varphi = \varphi(x_1, x_2). \tag{3c}$$

Fig. 1. The Griffith's type III crack in a piezoelectric ceramic. x_3 is the poling direction. Shear stress is applied at $x_2 = \pm L/2$ surface in x_3 axis direction. The electric field is applied along the direction of the x_2 axis.

Eqs. (3a)–(3c) imply that we have a two-dimensional problem and

$$s_{11} = s_{22} = s_{33} = s_{12} = 0, \quad E_3 = 0. \tag{4}$$

Substituting eqs. (4) into eqs. (2) gives

$$\sigma_{23} = 2c_{44}^E s_{23} - e_{15}E_2, \tag{5a}$$

$$\sigma_{13} = 2c_{44}^E s_{13} - e_{15}E_1, \tag{5b}$$

$$D_1 = \epsilon_{11}E_1 + 2e_{15}s_{13}, \tag{5c}$$

$$D_2 = \epsilon_{11}E_2 + 2e_{15}s_{23}. \tag{5d}$$

Considering a system under both mechanical stress and electric field, the Euler and Maxwell equations have the following forms [5–7]:

$$\partial\sigma_{32}/\partial x_2 + \partial\sigma_{31}/\partial x_1 = 0, \tag{6a}$$

$$\partial D_1/\partial x_1 + \partial D_2/\partial x_2 = 0. \tag{6b}$$

Substituting eqs. (5) into eqs. (6) gives

$$c_{44}\nabla^2 u_3 + e_{15}\nabla^2\varphi = 0, \tag{7a}$$

$$e_{15}\nabla^2 u_3 - \epsilon_{11}\nabla^2\varphi = 0. \tag{7b}$$

Generally speaking, the determinant of eqs. (7a) and (7b) is non-zero, i.e.

$$\Delta = \begin{vmatrix} c_{44} & e_{15} \\ e_{15} & -\epsilon_{11} \end{vmatrix} \neq 0.$$

One can easily verify this from the data in table 1 which lists the parameters for the most widely used piezoceramics PZT 65/35, and PZT-4. Therefore, from eqs. (7) one has

$$\begin{pmatrix} \nabla^2 u_3 \\ \nabla^2\varphi \end{pmatrix} = \begin{pmatrix} 0 \\ 0 \end{pmatrix}. \tag{8}$$

We choose the $x_2 = 0$ to be the reference plane for electric potential [$\phi(x_2 = 0) = 0$]. Therefore, the two-

Table 1
The elastic, dielectric and piezoelectric coefficients for PZT 65/35 from ref. [10] and PZT-4 from ref. [11]

Piezoelectric ceramic PZT 65/35		Piezoelectric ceramic PZT-4	
$c_{11}^E = 1.594 \times 10^{11}$ N/m^2	$e_{31} = -6.127$ C/m^2	$c_{11}^E = 13.9 \times 10^{10}$ N/m^2	$e_{31} = -5.2$ C/m^2
$c_{12}^E = 7.385 \times 10^{10}$ N/m^2	$e_{33} = 10.71$ C/m^2	$c_{12}^E = 6.78 \times 10^{10}$ N/m^2	$e_{33} = 15.1$ C/m^2
$c_{33}^E = 1.261 \times 10^{11}$ N/m^2	$e_{15} = 8.387$ C/m^2	$c_{13}^E = 17.43 \times 10^{10}$ N/m^2	$e_{15} = 12.7$ C/m^2
$c_{44}^E = 3.89 \times 10^{10}$ N/m^3	$\epsilon_{11} = 5.66 \times 10^{-9}$ F/m	$c_{33}^E = 11.5 \times 10^{10}$ N/m^2	$\epsilon_{11} = 6.45 \times 10^{-9}$ F/m
$c_{44}^E = 4.276 \times 10^{10}$ N/m^2	$\epsilon_{33} = 2.243 \times 10^{-9}$ F/m	$c_{44}^E = 2.56 \times 10^{10}$ N/m^2	$\epsilon_{33} = 5.62 \times 10^{-9}$ F/m
		$c_{44}^E = 3.06 \times 10^{10}$ N/m^2	

dimensional problem (on $x_3 = 0$ plane) contains one mirror symmetry line (x_2 axis) and the inversion symmetry, thus we only need to study this problem in the first quadrant of the $x_3 = 0$ plane ($x_1 > 0$; $x_2 > 0$), as illustrated in fig. 2. On the x_1 axis we have two boundary conditions for $x_1 > a$:

$$u_3 = 0, \quad \text{when } |x_1| > a; \tag{9a}$$

$$\varphi = 0, \quad \text{when } |x_1| > a. \tag{9b}$$

In addition, the contour of the crack is free of mechanical load and the crack may be considered as a vacuum or air-filled cavity. Since the value ϵ_0/ϵ_1 is very small (ϵ_0 is vacuum permittivity; ϵ_1 is ferroelectric ceramics permittivity), the following boundary conditions also hold on the x_1 axis [7,8]:

$$\sigma_{32} = 0, \quad \text{when } |x_1| \leq a; \tag{10a}$$

$$D_2 = 0, \quad \text{when } |x_1| \leq a. \tag{10b}$$

The strain and the applied electric field strength at $x_2 = L/2$ are S and E_0, respectively. Hence, the boundary conditions at $x_2 = L/2$ are

$$-\partial\varphi/\partial x_2 |_{x_2 = L/2} = E_0. \tag{11a}$$

$$\partial u_3/\partial x_2 |_{x_2 = L/2} = 2S. \tag{11b}$$

As shown in fig. 1, L is the sample dimension in x_2 direction and $2a$ is the width of the cut in x_1 direction with $L \gg 2a$.

The Laplace equation (8) can be solved by using Fourier transformation technique [6]. The solutions for the displacement u_3 and the electric potential φ, which satisfy the boundary conditions of eqs. (10) with arbitrary larger L, are
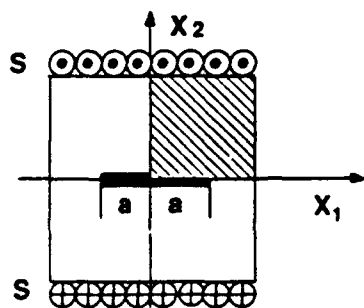
Fig. 2. The $x_3 = 0$ plane which is a cross section of fig. 1. The x_2 axis is a mirror symmetry line.

$$u_3(x_1, x_2) = 2S\left[x_2 + \frac{2}{\pi}\int_0^\infty A(\xi)\, e^{-\xi x_2}\cos(\xi x_1)\, d\xi\right]. \tag{12a}$$

$$\varphi(x_1, x_2) = -E_0\left[x_2 + \frac{2}{\pi}\int_0^\infty B(\xi)\, e^{-\xi x_2}\cos(\xi x_1)\, d\xi\right]. \tag{12b}$$

From eqs. (12) and (10), the unknown functions $A(\xi)$ and $B(\xi)$ can be determined by the Daul integral equations:

$$\frac{2}{\pi}\int_0^\infty \xi[A(\xi), B(\xi)]\cos(\xi x_1)\, d\xi = 1,$$

$$0 \leq x_1 \leq a; \tag{13a}$$

$$\int_0^\infty [A(\xi), B(\xi)]\cos(\xi x_1)\, d\xi = 0, \quad x_1 > a. \tag{13b}$$

The solutions of eqs. (13a) and (13b) are

$$A(\xi) = B(\xi) = (\pi a/2)\, \xi^{-1} J_1(a\xi), \tag{14}$$

where $J_1(a\xi)$ is the first-order Bessel function.

Finally, in order to evaluate the stress and the electrical displacement intensity factors, K_{III} and K_{IV}, we derive the distributions of stress and electric field in the vicinity of a crack tip along the x_1 axis,

$$\sigma_{32}(x_1, 0) = 0, \qquad |x_1| \leq a;$$

$$= \frac{d_1 |x_1|}{\sqrt{x_1^2 - a^2}}, \quad |x_1| > a. \tag{15a}$$

$$D_2(x_1, 0) = 0, \qquad |x_1| \leq a.$$

$$= \frac{d_2 |x_1|}{\sqrt{x_1^2 - a^2}}, \quad |x_1| > a. \tag{15b}$$

Here,

$$d_1 = 2c_{44}^E S - e_{15} E_0, \tag{16a}$$

$$d_2 = \epsilon_{11} E_0 + 2e_{15} S; \tag{16b}$$

d_1 and d_2 are the total stress and electric displacement at $x_2 = L/2$, respectively. Obviously, from eqs. (15) both stress and electric displacement fields diverge at the crack tip and decrease toward asymptotic values d, for $|x_1| \gg a$. According to the defi-

nitions of the stress and the electric displacement intensity factors [6,7], we have

$$K_{\text{III}} = \lim_{x \to a} \sqrt{2\pi(x_1 - a)}\ \sigma_{23}(x_1, 0) = \sqrt{\pi a}\ d_1, \quad (17a)$$

$$K_{\text{IV}} = \lim_{x \to a} \sqrt{2\pi(x_1 - a)}\ D_2(x_1, 0) = \sqrt{\pi a}\ d_2. \quad (17b)$$

Eqs. (17a) and (17b) are analogous to the fracture conditions known for anisotropic materials [5,12], however, here the coefficients d_1 and d_2 contain both mechanical and electric contributions, reflecting the characteristic of piezoelectric materials. It is interesting to note that these two contributions can either be additive or cancel each other in one of the two intensity factors, depending on the relative direction between the applied electric field and the external mechanical load. In other words, the applied electric field (mechanical stress) can either weaken or enhance the stress (electric displacement) concentration in a piezoelectric material. The overall strength of a material is characterized by the critical values of the two intensity factors, K_{III}^c and K_{IV}^c. However, the additive nature of the two contributions in at least one of the intensity factors does not imply that a piezoelectric material is weaker than a non-piezoelec-

tric material, which also depends on the magnitude of K_{III}^c and K_{IV}^c.

References

[1] S.W. Freiman, Ferroelectrics 102 (1990) 381.
[2] F. Kroupa, K. Nejezchleb, J. Rataj and I. Saxl, Ferroelectrics 100 (1990) 281.
[3] B.-C. Shin and H.-G. Kim, Ferroelectrics 100 (1990) 209.
[4] A.G. Evans, Intern. J. Fracture 16 (1980) 485;
 G. Sines, J. Am. Ceram. Soc 59 (1976) 370.
[5] G.P. Cherepanov, in: Mechanics of brittle fracture (McGraw-Hill, New York, 1979).
[6] I.N. Seddon and M. Lowengrub, in: Crack problems in the classical theory of elasticity (Wiley, New York, 1969).
[7] V.Z. Parton and B.A. Kudryavtsev, in: Electromagnetoelasticity piezoelectric and electrically conductive solids, chs. 2 and 4; translated from Russian by E.G. Strel'chenko (Gordon and Breach, New York, 1988).
[8] J. Grindly, in: An introduction to the phenomenological theory of ferroelectricity (Pergamon Press, Oxford, 1970).
[9] I.N. Seddon, in: Fourier transforms (McGraw-Hill, New York, 1959).
[10] P.J. Chen, Acta Mech. 47 (1983) 95.
[11] E.G. Smazhevskaya and N.V. Feldman, in: Piezoelectric ceramics (Soviet Radio, Moscow, 1970), in Russian.

PHENOMENOLOGICAL STUDIES

APPENDIX 17

Stress induced shift of the Curie point in epitaxial $PbTiO_3$ thin films

George A. Rossetti, Jr. and L. Eric Cross

Materials Research Laboratory, Pennsylvania State University, University Park, Pennsylvania 16802

Keiko Kushida

Central Research Laboratory, Hitachi Ltd., Kokubunji, Tokyo 185, Japan

A 50 °C shift in Curie temperature has been observed for c-axis oriented $PbTiO_3$ thin films using x-ray diffraction. An analysis of the electrostrictive strain based on the Devonshire thermodynamic formalism showed that the shift in the Curie point for these films can be plausibly explained by an effective two-dimensional compressive stress of ≈ 400 MPa. The single-domain, single-crystal dielectric susceptibility (η_{33}) and piezoelectric coefficient (d_{33}) were calculated and found to be relatively unaffected, at room temperature, by a compressive stress of this magnitude.

Kushida and Takeuchi[1] have reported excellent piezoelectric properties for highly c-axis oriented $PbTiO_3$ thin films prepared by seeded lateral overgrowth onto Pt electrodes recessed onto a single-crystal $SrTiO_3$ substrate. However, x-ray diffraction measurements[2,3] showed that the cubic-tetragonal phase transition occurred, for some films, at a temperature nearly 50 °C higher than that expected for $PbTiO_3$ single crystals ($T_c \approx 490$ °C).[4] Furthermore, at room temperature, these films were found to be elongated along the c axis, with a c/a axial ratio of 1.076, about 1.2% larger than for pure $PbTiO_3$.

Consideration of the Devonshire thermodynamic formalism[5,6] for ferroelectric perovskites reveals that a two-dimensional stress can be very effective in displacing the Curie temperature. Based on the x-ray data, it is therefore tempting to speculate that the large shift in the Curie point observed for the epitaxial $PbTiO_3$ films is the result of a two-dimensional compressive stress oriented orthogonal

to the c axis. Indeed, simple calculations suggest that lattice and thermal expansion mismatch with the substrate can conceivably result in a large net compressive stress (> 1 GPa). Unfortunately, the contributions to stress relaxation mechanisms from lattice and microstructural imperfections, the film/substrate interface, etc., are unknown, so that it is very difficult to predict with certainty the magnitude of the prevailing stress.

Alternatively, the coefficients of a modified Devonshire energy function for $PbTiO_3$ have been recently determined[7] and shown[8] to satisfactorily predict the shift of the Curie point with hydrostatic stress. In this letter, we use the thermodynamic theory, along with the most recent x-ray results,[3] to show directly that the shift of the Curie point in oriented ferroelectric thin films can be plausibly explained in terms of a two-dimensional stress effect.

The appropriate free-energy function for $PbTiO_3$ is

$$G_1 = \alpha_1(P_1^2 + P_2^2 + P_3^2) + \alpha_{11}(P_1^4 + P_2^4 + P_3^4) + \alpha_{12}(P_1^2P_2^2 + P_2^2P_3^2 + P_3^2P_1^2) + \alpha_{111}(P_1^6 + P_2^6 + P_3^6) + \alpha_{112}[P_1^4(P_2^2 + P_3^2)$$

$$+ P_2^4(P_1^2 + P_3^2) + P_3^4(P_1^2 + P_2^2)] + \alpha_{123}(P_1^2P_2^2P_3^2) - \tfrac{1}{2}s_{11}(X_1^2 + X_2^2 + X_3^2) - s_{12}(X_1X_2 + X_2X_3 + X_3X_1)$$

$$- \tfrac{1}{2}s_{44}(X_4^2 + X_5^2 + X_6^2) - Q_{11}(X_1P_1^2 + X_2P_2^2 + X_3P_3^2) - Q_{12}[X_1(P_2^2 + P_3^2) + X_2(P_1^2 + P_3^2) + X_3(P_1^2 + P_2^2)]$$

$$- Q_{44}(X_4P_2P_3 + X_5P_1P_3 + X_6P_1P_2) \tag{1}$$

where P_i and X_i are the polarization and stress, respectively; α_i, α_{ij}, and α_{ijk} are the dielectric stiffness and higher order stiffness coefficients at constant stress; s_{ij} are the elastic compliances at constant polarization; and Q_{ij} are the cubic electrostrictive constants in polarization notation. The dielectric stiffness constant, α_1, is given a linear temperature dependence based on the Curie–Weiss law

$$\alpha_1 = (T - \theta)/2\epsilon_0 C \tag{2}$$

where C is the Curie constant and θ the Curie–Weiss tem-

perature. All other coefficients are assumed to be independent of temperature and stress, and have the values given previously.[7,8]

In the reduced notation, the tensile stresses are denoted by X_1, X_2, X_3 and the shear stresses by X_4, X_5, X_6. For a two-dimensional stress H, we assign $X_1 = X_2 = H$ and $X_3 = X_4 = X_5 = X_6 = 0$. Following the appropriate sign convention[9] based on Eq. (1), a compressive stress is implied when H is negative.

Equation (1) has two solutions of interest for $PbTiO_3$, corresponding to the prototypic cubic ($Pm3m$) and ferroelectric tetragonal ($P4mm$) states. These are
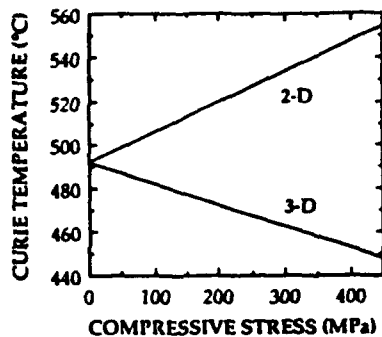
FIG. 1. Calculated shift of the Curie temperature for PbTiO$_3$ subjected to two-dimensional (2-D) compressive stress oriented orthogonal to the c axis and hydrostatic (3-D) compressive stress.

$$P_1^2 = P_2^2 = P_3^2 = 0 \quad (Pm3m),$$

$$P_1^2 = P_2^2 = 0, P_3^2 \neq 0 \quad (P4mm). \tag{3}$$

The spontaneous polarization $(P_s = P_3)$ is determined from the first partial derivative stability condition

$$\delta G_1/\delta P_3 = 0 \tag{4}$$

or

$$P_3^2 = \{ -\alpha_{11} + [\alpha_{11}^2 - 3\alpha_{111}(\alpha_1 - 2Q_{12}H)]^{1/2} \}/3\alpha_{111}. \tag{5}$$

If the polarization dependence of the free energy is to remain unchanged under a constant stress H, a shift ΔT of the transition temperature is required to equate the energies of the cubic and tetragonal states. From Eqs. (2) and (5)

$$\Delta T = 4\epsilon_0 C Q_{12} H. \tag{6}$$

The shift in the Curie point under a hydrostatic stress σ may be similarly derived[8]

$$\Delta T = 2\epsilon_0 C (Q_{11} + 2Q_{12})\sigma. \tag{7}$$

As shown in Fig. 1, since the electrostrictive constant Q_{12} is negative and the sum $(Q_{11} + 2Q_{12})$ is positive,[7] a two-dimensional compressive stress orthogonal to the c axis will shift the Curie point to higher temperatures, while a hydrostatic stress will shift it to lower temperatures. Note that a two-dimensional stress is a factor of
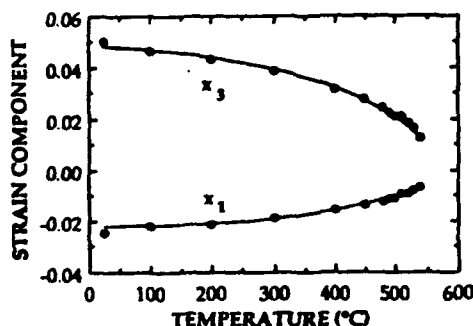

FIG. 2. Measured strain components, x_1 and x_3, vs temperature for a c-axis oriented PbTiO$_3$ thin film.
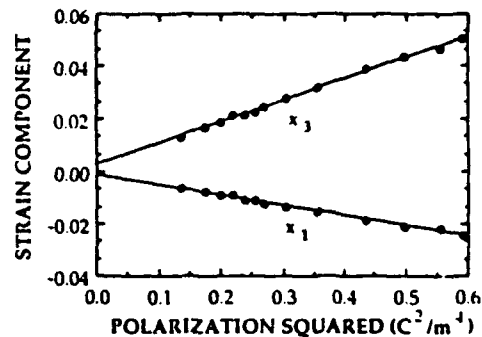
FIG. 3. Measured strain components, x_1 and x_3, for a c-axis oriented PbTiO$_3$ thin film vs the calculated square of the polarization.

$2Q_{12}/(Q_{11} + 2Q_{12}) \approx 1.4$ times more effective at displacing the Curie point than a hydrostatic stress of equal magnitude. If $\Delta T = +50\,°C$ as determined from the x-ray measurements, from Eq. (6) we predict a two-dimensional compressive stress of 350 MPa.

To verify whether such a stress is reasonable, we recall that the strains along the a and c axes can be determined from the lattice constants using

$$x_1 = (a_t - a_c')/a_c' \quad \text{and} \quad x_3 = (c_t - a_c')/a_c' \tag{8}$$

where a_t and c_t are the tetragonal cell constants and a_c' is the equivalent cubic cell constant taken here as $(a_t^2 c_t)^{1/3}$. Using Eq. (8) and the x-ray data,[3] the strain components x_1 and x_3 were calculated over the temperature range of 25 to 540 °C. The results are shown in Fig. 2. From Eq. (1), however, the strain matrix is also given by

$$\delta G_1/\delta X_i = -x_i \tag{9}$$

or for the tetragonal state

$$x_1 = Q_{12}P_3^2 + (s_{11} + s_{12})H, \quad x_3 = Q_{11}P_3^2 + 2s_{12}H. \tag{10}$$

Consequently, plots of the measured strain components against P_3^2, calculated from Eq. (5), should yield straight lines with slopes equal to the assumed electrostrictive constants and intercepts proportional to the assumed stress. Since the constants Q_{11}, s_{11}, and s_{12} are not used in the calculation of either P_3^2 or H [Eqs. (5) and (6)], and since no special relationship between Q_{11} and Q_{12} has been assumed, it can be readily verified whether an analysis based on Eq. (1) is appropriate.

As shown in Fig. 3, a linear relationship between the measured strain components and the calculated polarization squared was in fact obtained. Using Eq. (10), the values of Q_{11}, Q_{12}, and H were determined from the plot using the known values of s_{11} and s_{12} and are compared to

TABLE I. Results of the stress analysis based on Eq. (10).

Quantity	Assumed value	Derived value
$Q_{11}(m^4/C^2)$	0.089	0.081
$Q_{12}(m^4/C^2)$	−0.026	−0.039
H (MPa)	−350	−435[a]

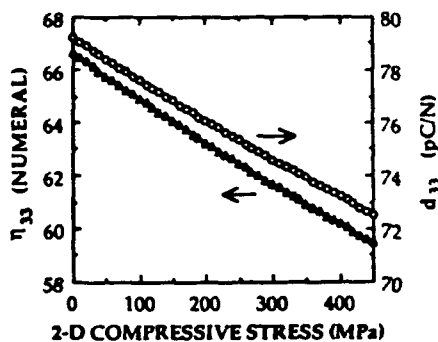[a] Average of the two intercept values.

FIG. 4. Calculated room temperature dielectric susceptibility (η_{33}) and piezoelectric coefficient (d_{33}) of PbTiO$_3$ vs two-dimensional compressive stress.

The dielectric susceptibilities (η_{ij}) and piezoelectric charge coefficients (d_{ij}) may then be obtained from

$$\eta_{ij}=A_{ji}/\Delta \quad \text{and} \quad d_{ij}=b_{kj}\eta_{ik} \tag{12}$$

where A_{ji} is the cofactor and Δ is the determinant of the χ_{ij} matrix. The effect of a two-dimensional compressive stress on the room temperature values of η_{33} and d_{33} is shown in Fig. 4. The results confirm that although a stress of 400 MPa can lead to a substantial shift in the Curie point for the c-axis oriented films, no significant change in the dielectric or piezoelectric properties at room temperature is expected.

the assumed values in Table I. The good qualitative agreement of the expected values with those derived from Fig. 3 suggests that the shift of the Curie point in these films is consistent with an effective two-dimensional compressive stress of approximately 400 MPa.

Considering now the effect of compressive stress on the film properties, appropriate second partial derivatives of Eq. (1) give the reciprocal dielectric susceptibilities (χ_{ij}) and the piezoelectric constants (b_{ij})

$$\delta^2 G/\delta P_i \delta P_j = \chi_{ij} \quad \text{and} \quad \delta^2 G/\delta P_i \delta X_j = -b_{ij} \tag{11}$$

[1] K. Kushida and H. Takeuchi, Appl. Phys. Lett. 50, 1800 (1987).
[2] K. Kushida and H. Takeuchi, Ferroelectrics 108, 3 (1990).
[3] K. Kushida and H. Takeuchi, IEEE Trans., Ultrasonics, Ferroelectrics, and Frequency Control, Special Issue on Ferroelectric Thin Films (to be published November, 1991).
[4] G. A. Samara, Ferroelectrics 2, 277 (1971).
[5] A. F. Devonshire, Philos. Mag. 40, 1040 (1949).
[6] P. W. Forsbergh, Jr., Phys. Rev. 93, 686 (1954).
[7] M. J. Haun, E. Furman, S. J. Jang, H. A. McKinstry, and L. E. Cross, J. Appl. Phys. 62, 3331 (1987).
[8] G. A. Rossetti, Jr., K. R. Udayakumar, M. J. Haun, and L. E. Cross, J. Am. Ceram. Soc. 73, 3334 (1990).
[9] A. Amin, L. E. Cross, and R. E. Newnham, Ferroelectrics 99, 145 (1989).

APPENDIX   18

X-ray and phenomenological study of lanthanum-modified lead zirconate-titanates in the vicinity of the relaxor phase transition region

G. A. Rossetti, Jr. [a] and T. Nishimura

Research Center, Mitsubishi Kasei Corporation, 1000 Kamoshida-cho, Midori-ku, Yokohama 227, Japan

L. E. Cross

Materials Research Laboratory, Pennsylvania State University, University Park, Pennsylvania 16802

X-ray diffraction analyses of chemically derived $Pb_{1-x}La_x(Zr_{0.65}Ti_{0.35})_{1-x/4}O_3$ powders were combined with a phenomenological theory to investigate the corresponding single-crystal thermodynamic properties of compositions approaching the relaxor ferroelectric phase transition region ($x = 0$–0.04). The temperature dependence of the electrostrictive strain component, x_4, could be described by the Landau–Ginsburg–Devonshire phenomenological theory taking $T_c = 357\,°C$ independent of La content (x). The single-domain, single-crystal elastic Gibbs free-energy density was calculated as a function of temperature and composition. The calculated results were discussed in relation to a simple superparaelectric model of relaxor behavior involving the temperature stabilization of noninteracting polar microregions.

I. INTRODUCTION

Ferroelectrics showing relaxor phase transition behavior are of considerable theoretical as well as practical interest. These materials find a variety of applications in ceramic form, particularly as electrostrictive actuators and capacitor dielectrics. The best studied class of relaxor ferroelectrics are compounds and solid solutions of oxides crystallizing with the simple perovskite structure. Although the mechanisms underlying relaxor behavior in the perovskite-based systems are not yet clear, frustration of the normal ferroelectric transition appears to arise in general due to nanostructural lattice imperfections which locally lower, but do not destroy entirely, the translational symmetry. Smolenski[1] first proposed the widely held view that the origin of the symmetry lowering lies in chemical microheterogeneity, which in turn results in a broad distribution of local Curie temperatures. Alternatively, from a series of transmission electron microscope (TEM) studies,[2] it now appears that for the complex $A(B_1B_2)O_3$ perovskite compounds, the origin lies in the coherence length of the long range B-site ordering. Other structural features involving defect dipoles, inhomogeneous order, and incommensurate phase transitions may also play a role in relaxor behavior.[3]

Cross[4] has pointed out that the development of a stable ferroelectric polarization within a postulated microregion of a relaxor crystal requires that the energy barrier separating symmetry equivalent polarization orientation states be sufficient to stabilize the region against thermal agitation. Since ferroelectricity is a cooperative phenomenon, all energies scale with volume. Consequently, by analogy with ferromagnetism, superparaelectric behavior may result if the microregions cannot develop sufficient volume stabilization or electrocrystalline anisotropy energy with respect to other degrees of freedom. Although the superparaelectric model accounts for many of the observed properties of relaxor ferroelectrics, such as the frequency dependence of the permittivity and dielectric aging,[5,6] few quantitative estimates have been reported regarding the microregion size and/or composition dependence of the energy barriers separating equivalent polarization orientation states for actual relaxor crystals.

The Landau–Ginsburg–Devonshire (LGD) free-energy formalism provides a realistic macroscopic thermodynamic description of the single-domain, single-crystal elastodielectric properties of normal (proper) ferroelectric materials.[7] In the absence of suitable quality single-crystal samples, high-temperature cell parameter measurements have proved invaluable in the development of the phenomenological thermodynamic theories for several perovskite ferroelectrics and their solid solutions.[8,9] These measurements establish the temperature dependence of the spontaneous elastic strain, which is related through the electrostrictive strain equations to the spontaneous polarization.[10,11] The spontaneous polarization is the macroscopic order parameter for the paraelectric-ferroelectric (PE-FE) phase transition, and its temperature dependence can be used to determine the higher-order dielectric stiffness coefficients needed to evaluate the elastic Gibb's free-energy density function.

Previous investigations have utilized this approach extensively in phenomenological studies of the $PbZr_yTi_{1-y}O_3$ (PZT) solid solution system.[12,13] In the present work, we extend the x-ray measurements to the relaxor $Pb_{1-x}La_x(Zr_yTi_{1-y})_{1-x/4}O_3$[14] (PLZT) system and consider the compositional series where $y = 0.65$ (also denoted as X/65/35). As judged from the published phase diagram[15] (Fig. 1), compositions in this series begin to exhibit significant relaxor ferroelectric character only for

---

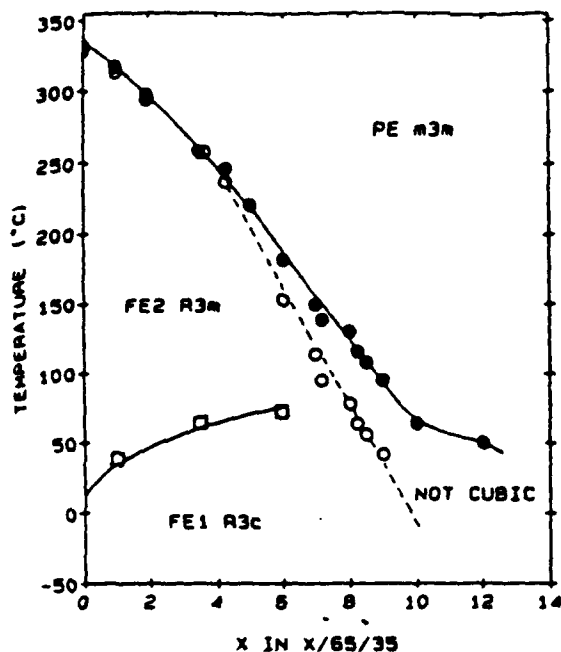[a] Permanent address: Materials Research Laboratory, Pennsylvania State University, University Park, PA 16802.

FIG. 1. Phase diagram for PLZT X/65/35 (after Ref. 15). (●) dielectric susceptibility, (○) dielectric tan δ, (□) longitudinal sound velocity).

$x > 0.04$. In this study, we examine compositions with $x < 0.04$, and show that they are amenable to treatment using the simple LGD formalism. This allows for the evaluation of the single-domain, single-crystal elastic Gibb's free-energy density as a function of temperature and composition in the vicinity of the relaxor phase transition region. The results are discussed in relation to an idealized superparaelectric model of relaxor behavior.

II. EXPERIMENTAL PROCEDURE

PLZT powder samples were prepared from lead acetate trihydrate, lanthanum isopropoxide, zirconium n-butoxide, and titanium isopropoxide according to a modification of a procedure described earlier.[16] All manipulations of the starting chemicals and reaction mixtures were carried out in a glove box under dry nitrogen. Initially, 1:8 (m/m) solutions of the lead compound and of the combined alkoxides in 2-methoxyethanol (2-MOE) were prepared. The Pb solution was dehydrated by boiling and the combined alkoxide was refluxed (≈ 1 h in each case) prior to mixing at approximately 100 °C. The mixed solution was then refluxed until a constant boiling temperature of 124 °C (the boiling point of pure 2-MOE) was attained. At this stage, the H_2O content of the solution, as measured by Karl Fischer titration, had been reduced to < 5 ppm. The refluxed solution was then concentrated, cooled, filtered through a 0.5-μm filter, and adjusted in concentration to 0.6 M. Prior to hydrolysis, 6 mol % Pb in excess of the formula amount was introduced as a dehydrated solution of lead acetate in 2-MOE. The resulting solution was chilled to − 25 °C and excess water for hydrolysis (> 4:1 mol H_2O/mol alkoxide) was added as a 1:2 (vol/vol) solution in 2-MOE. The hydrolyzed solution was gelled by

heating in sealed vials to 80 °C. The gels were then air dried for 2 days at 90 °C, ground in an agate mortar and pestle, and calcined to a maximum temperature of 1100 °C for 1 h with intermediate holds on heating at 250 °C (30 min), 500 °C (2 h), and 800 °C (6 h).

The nominal compositions of the resulting powders were determined from x-ray fluorescence and inductively coupled plasma atomic emission spectroscopy. The residual carbon content was determined from combustion analysis. Particle size and morphology were examined using scanning electron microscopy (SEM). The PE-FE phase transition character was evaluated by differential scanning calorimetry (DSC) performed at a heating rate of 10 °C/min under flowing N_2. X-ray diffraction measurements were carried out on a carefully aligned automated diffractometer employing Cu $K\alpha$ radiation. The temperature stability of the sample hot stage was ±0.1 °C over the measurement range (− 50–300 °C). All analyses of the x-ray data were performed using commercially available software.

Sample homogeneity was assessed from x-ray line broadening measurements. Semiquantitative estimates of the root mean squared (rms) lattice strain and effective crystallite size were obtained based on a modified Warren-Averbach analysis[17] of the (100) and (200) x-ray line profiles using the (100) and (201) reflections of quartz as an external reference standard. The profiles were obtained as step scans using a step size of 0.005° 2θ and count times of 2–10 s to ensure $\approx 10\,000$ counts on the peak maxima. The profiles were corrected for background and $K\alpha_2$ prior to analysis.

The rhombohedral angle (α) was determined as a function of temperature by refinement over four pairs of reflections. The step size (in degrees 2θ) and count time for each pair of reflections were as follows: (111)/(11-1), 0.005°/2 s; (220)/(20-2), 0.01°/5 s; (222)/(22-2), 0.02°/10 s; (420)/(40-2), 0.02°/15 s. Accurate assignment of the peak positions was facilitated by fitting with a Marquardt least-squares routine that properly accounted for the $K\alpha$ splitting. In this routine, the only fixed parameter was the peak width, which was held constant at the room-temperature value. This procedure generally permitted the cell constants to be refined with an absolute angular precision of better than 0.025° 2θ although, especially for the higher La content samples, the relatively broad, low intensity (420)/(40-2) peaks occasionally had to be omitted from the analysis.

III. RESULTS AND DISCUSSION

A. Materials characterization

As shown in Fig. 2, the alkoxy-derived PLZT powders were well crystallized and showed sharp diffraction peaks for the rhombohedral perovskite phase. No secondary phases were detected by x-ray diffraction. Residual carbon from the metalorganic precursors was found to be less than 200 ppm. The final concentration of the volatile Pb component agreed with the expected values to within a few percent. The DSC analyses showed only a flat, featureless
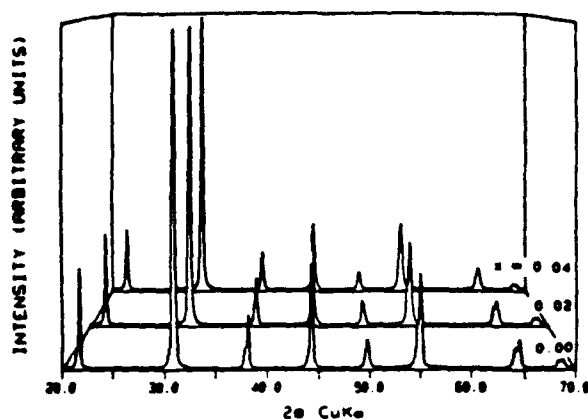
FIG. 2. Powder x-ray diffraction patterns for $Pb_{1-x}La_x$ $(Zr_{0.65}Ti_{0.35})_{1-x/4}O_3$.

baseline in the temperature range of 25–450 °C, consistent with the expectation of second-order phase transition behavior based on previous studies of rhombohedral PZT compositions.[18]

The results of the Warren–Averbach crystallite size/rms lattice strain analysis are shown in Table I. Within the error of the analysis, the effective crystallite size was a constant 53 nm, in good qualitative agreement with the primary particle size determined from direct observation by scanning electron microscopy. The rms strains were also nearly constant, but perhaps increased somewhat as the relaxor phase transition region was closely approached. Although the absolute magnitudes of lattice strains deduced from x-ray line broadening measurements must be interpreted with care, it is interesting to note that the values so obtained are comparable to the electrostrictive shear strain component x_4. In the unmodified PZT system, a nonzero value of the rms strain has been associated with composition fluctuations.[19,20] Table I also shows, however, that the electrostrictive shear strain component, which is related to the rhombohedral angle (α) by[21]

$$x_4 = (90 - \alpha)/90 \qquad (1)$$

decreased markedly with the addition of even small amounts of La. In fact, at room temperature, the relative change of x_4 with La content $(\Delta x_4/\Delta x = -0.023)$ was nearly an order of magnitude larger than the change with Zr content $(\Delta x_4/\Delta y = -0.0025)$ observed for unmodified PZT compositions across the rhombohedral phase field.[21] Since the shear strain is directly related to the spon-

FIG. 3. Spontaneous elastic strain data for $Pb_{1-x}La_x$ $(Zr_{0.65}Ti_{0.35})_{1-x/4}O_3$ $(R3m$ phase). The solid lines represent the best fit to the electrostrictive strain equations taking a composition independent value of $T_c = T_d \approx 357$ °C.

taneous polarization, we might reasonably speculate that small composition variations have a more pronounced effect on the ferroelectric properties of the La-modified materials as compared with pure PZT. At higher temperatures, this effect may become even more important, since measurements on a sample with $x = 0.04$ showed that the rms strain began to exceed the electrostrictive strain above ≈ 250 °C.

B. Temperature dependence of spontaneous strain

The temperature dependence of the electrostrictive strain component x_4 in the region of $R3m$ phase stability is shown for $x = 0.00$, 0.02, and 0.04 in Fig. 3. The terminus of each curve represents the temperature above which the cell parameters could no longer be refined with the desired precision, not the temperature of transition to cubic symmetry. Were a phase change to occur, the large values of the strain prevailing at these temperatures would dictate that it occur by a first-order or nearly first-order transition. Since no latent heat change was detected in this range by DSC, it was concluded that the rhombohedral-cubic phase change occurred by a second-order transition at temperatures higher than those to which a well-defined rhombohedral shear remained evident under interrogation by x-ray wavelength probing radiation.

To investigate this possibility further, the temperature dependence of the spontaneous strain was modeled using

TABLE I. Rhombohedral angle (α), spontaneous strain (x_4), effective crystallite size (D_{eff}), and rms lattice strain $(\langle \epsilon^2 \rangle^{1/2})$ for $Pb_{1-x}La_x(Zr_{0.65}Ti_{0.35})_{1-x/4}O_3$ at 27 °C.

x	α (degrees)	x_4	D_{eff} (nm)	$\langle \epsilon^2 \rangle^{1/2}$	$\langle \epsilon^2 \rangle^{1/2}$ error range
0.00	89.684	0.00351	52.6 ± 1.7	0.00129	0.00123–0.00135
0.01	89.695	0.00339	53.6 ± 1.7	0.00118	0.00112–0.00125
0.02	89.708	0.00324	54.1 ± 2.5	0.00120	0.00111–0.00131
0.04	89.764	0.00262	52.0 ± 1.5	0.00148	0.00142–0.00155

the Landau–Ginsburg–Devonshire (LGD) free-energy formalism. Using reduced tensor notation, an appropriate expression for the elastic Gibbs free-energy density of a ferroelectric of rhombohedral symmetry derived from a cubic prototype of symmetry $Pm3m$ is:[13]

$$G_1 = 3\chi_0(T - T_0)P_3^2 + \xi P_3^4 + \zeta P_3^6 + \beta\theta_3^2 + v\theta_3^4 + \phi P_3^2\theta_3^2 - \tfrac{1}{2}s_{11}(X_1^2 + X_2^2 + X_3^2) - s_{12}(X_1X_2$$

$$+ X_2X_3 + X_3X_1) - \tfrac{1}{2}s_{44}(X_4^2 + X_5^2 + X_6^2) - (Q_{11} + 2Q_{12})(X_1 + X_2 + X_3)P_3^2 - Q_{44}(X_4$$

$$+ X_5 + X_6)P_3^2 - (R_{11} + 2R_{12})(X_1 + X_2 + X_3)\theta_3^2 - R_{44}(X_4 + X_5 + X_6)\theta_3^2, \tag{2}$$

where P_3 is a vector component of spontaneous polarization; θ_3 is a component of the oxygen octahedral tilt angle; X_i is a tensor component of elastic stress; χ_0, ζ, ξ are related to the dielectric stiffness and higher-order stiffness coefficients at constant stress; β, v are related to the octahedral torsion coefficients; ϕ is related to the coupling coefficients between polarization and tilt angle; s_{ij} are the elastic compliances at constant polarization; Q_{ij} are the cubic electrostriction constants in polarization notation; and R_{ij} are the rotostrictive coefficients coupling tilt angle and stress.

Considering initially only the phase of $R3m$ symmetry ($\theta_3 = 0$), from the first partial derivative stability condition

$$\delta G_1/\delta P_3 = 0, \tag{3}$$

the spontaneous polarization for a second-order transition ($T_0 = T_c$) at constant and zero stress is

$$P_3^2 = \{ -\zeta + [\zeta^2 - 9\chi_0(T - T_c)\xi]^{1/2}\}/3\xi \tag{4}$$

with $\chi_0 = 1/(2\epsilon_0 C)$, where C is the Curie constant and ϵ_0 is the permittivity of free space. Rearranging to eliminate the explicit dependence on C and simplifying gives

$$P_3^2 = A\{1 - [1 - B(T - T_c)]^{1/2}\} \tag{5}$$

with $A = -\zeta C/3\xi C$ and $B = 9\xi C/[2\epsilon_0(\zeta C)^2]$. The spontaneous strain ($X_i = 0$) is given by the appropriate partial derivative of Eq. (2)

$$-\delta G_1/\delta X_4 = x_4 = Q_{44}P_3^2. \tag{6}$$

Combining with Eq. (5) yields

$$x_4 = A'\{1 - [1 - B(T - T_c)]^{1/2}\}, \tag{7}$$

where $A' = AQ_{44}$.

Note that the polarization enters in Eq. (6) as the square and so the strain does not depend on the sign of P. Furthermore, fluctuations of the polarization among the symmetry equivalent orientation states are unimportant provided the time spent by the polar vector along the $\langle 111 \rangle$ is long compared to the time spent between states. The strain determined from Eq. (1) therefore reflects the time and space averaged value associated with the net polarization along the symmetry equivalent $\langle 111 \rangle$ orientations for a corresponding hypothetical single crystal of average composition (x).

Equation (7) was used to fit the spontaneous strain data in Fig. 3 using a Marquardt nonlinear regression anal-

ysis with A', B, and T_c as adjustable constants. Taking T_c from the radio frequency dielectric measurements (Fig. 1), values of A' and B could not be found to adequately describe the data for the $x = 0.02$ and 0.04 compositions. Convergence could be achieved for these compositions by allowing A', B, and T_c to vary simultaneously, although for the $x = 0.04$ sample, the value of T_c so obtained had no obvious physical significance and the values of A' and B became unacceptable (i.e., B became very large and $A' \to 0$). The refractive index results of Burns and Dacol,[22] and the x-ray scattering data of Darlington,[23] have shown that the onset of local polarization is independent of x for $x \approx 0.07$–0.095 and occurs at a temperature $T_c \approx 350$–360 °C (following the notation[22] hereinafter termed T_d) of the unmodified PZT end member. Rapid convergence to the fits shown by the solid lines in Fig. 3 that also yielded reasonable values of A' and B was attained using a composition independent value of $T_c = T_d \approx 357$ °C. The excellent fit to the data in Fig. 3 suggests that the onset of local polarization for the lower La compositions ($x < 0.04$) also occurs near 360 °C, and that the relaxor behavior observed for the higher La contents is premonitory from the introduction of even small amounts of La. The values of the fitting constants, A' and B, are given in Table II.

Considering now the phase of $R3c$ symmetry ($\theta_3 \neq 0$), the spontaneous strain becomes

$$-\delta G_1/\delta X_4 = x_4 = Q_{44}P_3^2 + R_{44}\theta_3^2. \tag{8}$$

For the PZT system, R_{44} is negative,[24] and so the rotostrictive contribution to the strain lowers the value relative to electrostriction alone. Apparently, this is also the case for the PLZT compositions studied here. In Fig. 4, the solid lines represent an extrapolation to low temperatures of the electrostrictive strain for the $R3m$ phase according to Eq. (7), while the dashed lines are smoothed fits to the experimental data over the complete measurement range. The points of departure of the data from the calculated lines for electrostriction alone are roughly in agreement with the

TABLE II. Constants used to evaluate Eq. (2).

x	$A'(\times 10^{-4})$	$B(\times 10^{-3})$	$\zeta C(\times 10^{14})$ $(Jm^5 °C/C^4)$	$\xi C(\times 10^{13})$ $(Jm^5 °C/C^4)$
0.00	-3.92	294.4	0.85	4.21
0.02	-7.73	77.73	1.64	4.10
0.04	-25.33	9.92	3.91	2.99

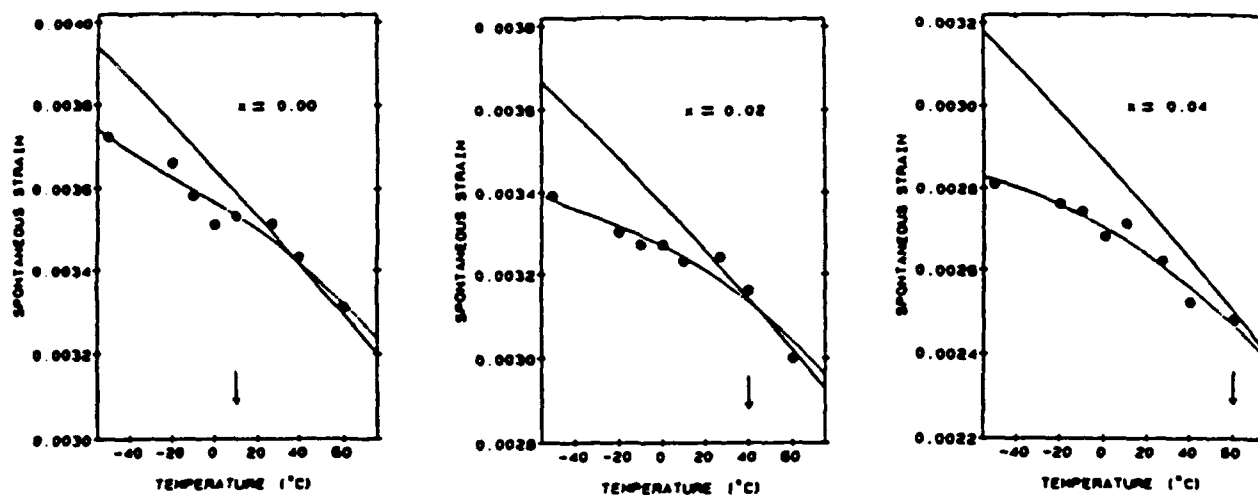FIG. 4. Low-temperature spontaneous strain data for $Pb_{1-x}La_x(Zr_{0.65}Ti_{0.35})_{1-x/4}O_3$. The solid lines are an extrapolation of the electrostrictive strain for the $R3m$ phase. The dashed lines are smoothed fits to the experimental data points over the complete measurement range. The arrows indicate the $R3m - R3c$ phase transition temperatures determined from the acoustic measurements of Ref. 15.

$R3m$-$R3c$ phase transition temperatures determined from acoustic measurements[15] (indicated by the arrows). This result supports the choice of $T_c = T_d$ used in fitting the electrostrictive strain data for the $R3m$ phase.

IV. PHENOMENOLOGICAL ANALYSIS

From the spontaneous strain measurements described above, the spontaneous polarization and single-domain, single-crystal elastic Gibbs free-energy density can be evaluated as a function of composition and temperature up to T_d. It has been demonstrated[23] that Curie–Weiss behavior is obeyed above T_d for a relaxor PLZT 8/65/35 composition, and this is an inherent consequence of the LGD formalism when $T_c \approx T_d$. Equation (2), as applied here, can therefore be used to investigate the macroscopic elastodielectric properties for a hypothetical crystal of average composition (x) undergoing a second-order transition to a Devonshire ferroelectric at T_d. Recognizing that this does not in actuality occur, the deviation from Devonshire behavior is discussed on the basis of an idealized superparaelectric model.[4]

A. Spontaneous polarization

The spontaneous polarization was determined from the x-ray strain measurements and Eq. (6), and is shown for a representative sample with $x = 0.02$ in Fig. 5. The electrostrictive constant Q_{44} in Eq. (6) was taken to be 0.06 m^4/C^2, a typical value for the rhombohedral PZT-based perovskites.[26] The solid line shows the extrapolation of the measured values to T_d using Eq. (5) and the constants from Table II, assuming normal Devonshire behavior. The remanent polarization determined by Haertling[27] from hysteresis loops measured on ceramic samples is also shown in Fig. 5 for comparison. At low temperatures the two measurements are in good agreement, but begin to differ substantially above ≈ 75 °C where the remanent polarization starts to collapse. As discussed earlier, the po-

larization enters in Eq. (6) as the square, and so the differences in the two curves primarily reflect the difference between the reversible macropolarization ($\overline{P}$) and local (rms) polarization ($\langle \overline{P^2} \rangle^{1/2}$). Since the spontaneous polarization is the macroscopic order parameter in Eq. (2), the calculations are expected to approximate the macroscopic elastodielectric properties only at low temperatures where thermally activated processes are frozen out.

B. Free-energy density

Under conditions of constant and zero stress, and neglecting the cell doubling transformation, the elastic Gibbs free-energy density from Eq. (2) becomes
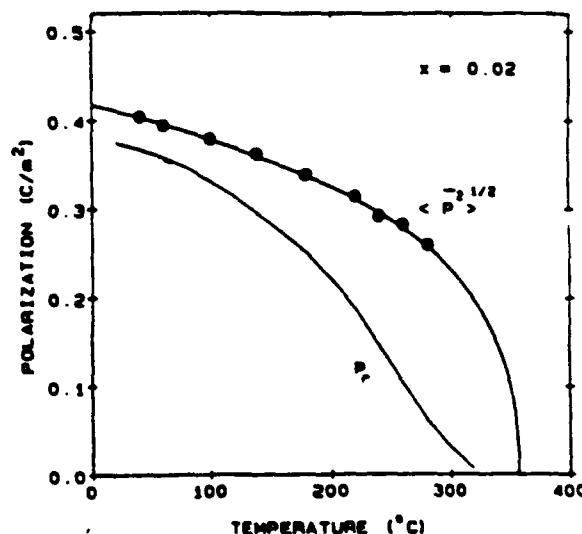

FIG. 5. Polarization plotted against temperature for $Pb_{1-x}La_x(Zr_{0.65}Ti_{0.35})_{1-x/4}O_3$. The data points were determined from spontaneous strain measurements. The solid line represents an extrapolation to T_d based on the phenomenological theory. The curve labeled P_r is taken from the remanent polarization data of Ref. 27.
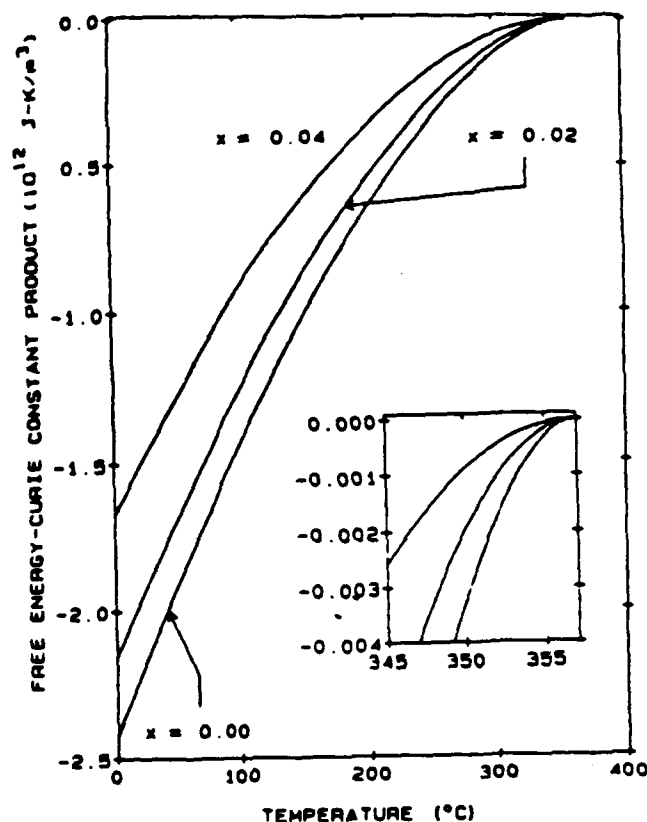
FIG. 6. Free-energy density–Curie constant product plotted against temperature for $Pb_{1-x}La_x(Zr_{0.65}Ti_{0.35})_{1-x/4}O_3$. The inset shows that the strong compositional dependence of the G_1C product is maintained even very close to T_d.

$$G_1 = 3\chi_0(T - T_c)P_3^2 + \zeta P_3^4 + \xi P_3^6. \tag{9}$$

Multiplying Eq. (9) by the Curie constant C, the relative stabilities of the rhombohedral and cubic states can be examined without knowing C explicitly.

$$G_1C = (3/2\epsilon_0)(T - T_c)P_3^2 + \zeta CP_3^4 + \xi CP_3^6. \tag{10}$$

Using Eqs. (5) and (7), the constants ζC and ξC were determined from A', B, and Q_{44}, and are given in Table II. The calculated G_1C product is plotted against temperature for various compositions (x) in Fig. 6. As seen in the figure, G_1C shows a strong composition dependence that is maintained to temperatures very near T_d. Note that at room temperature, the La dependence of G_1C $(\delta G_1C/\delta x)$ found here for PLZT is more than five times stronger than the Zr dependence $(\delta G_1C/\delta y)$ observed for the adjacent rhombohedral PZT compositions in the range of 0/75/25–0/55/45.[28]

The curves of Fig. 6 suggest that increasing the La content at a given temperature strongly decreases the magnitude of the free-energy density and so should quickly lead to a phase of cubic symmetry as $G_1C \to 0$. Taking the isothermal G_1C products for the $R3m$ phase to be approximately linear functions of composition,[28] the La content required to induce the transition was estimated below 75 °C where, judging from Fig. 5, the reversible macropolariza-

tion $(\bar{P})$ approaches the local (rms) polarization $(\langle \bar{P}^2 \rangle^{1/2})$. The calculations indicated that the structure becomes truly cubic at a La content near 13 mol %, in very good agreement with the experimental measurements[15] (Fig. 1). Consequently, application of the simple LGD formalism, with $T_c \approx T_d$, appears to give physically meaningful results for these compositions at low temperatures. At higher temperatures, where the remanent polarization collapses and thermal fluctuations of the order parameter may become important, the macroscopic properties are no longer expected to obey Eq. (2). Instead, as discussed below, the effects of size and composition on the stability of a postulated single-domain polar microregion are investigated in the context of a superparaelectric model.

C. Superparaelectric model

In this model, it is assumed that small deviations from the average composition (x) can localize the polarization to regions on a size scale where thermal fluctuations of the orientation of the polar vector between different permissible variants become possible.[4] Here we inquire as to the stability against thermal agitation of an isolated region in relation to its size, composition, and temperature. These calculations estimate only how the volume stabilization energy of a postulated microregion with symmetry equivalent polarization orientation states compares with the thermal energy. Surface effects, elastic boundary constraints, and interactions between regions are not considered.

The energy barrier H separating symmetry equivalent polarization orientation states is given by

$$H = -nVG_1, \tag{11}$$

where V is the volume per unit cell (≈ 0.064 nm^3), n is the number of unit cells in a postulated microregion, and the free-energy density G_1 may be determined as a function of temperature and composition from Eq. (9) taking $C = 2.0 \times 10^5$ °C.[26] Plots of $-H$ against temperature will therefore have the same shapes as the free-energy density curves of Fig. 6. From Eq. (11) it is obvious that for a given composition, the smaller the value of n, the lower the temperature required to attain stability against thermal agitation. However, since the free energies are strong functions of composition, it is also clear from Fig. 6 that regions most deficient in La will, at any temperature, be the more stable at a given size. This is consistent with the original observation of Burns and Dacol.[22]

To investigate the purely compositional effects further, we find for various postulated microregion sizes n the temperature stabilization difference ΔT for which the energy barriers H for two compositions x and x' become equal to some specified value. The results are plotted for $H = k_B T$ in Fig. 7. At macroscopic sizes, $\Delta T \to 0$, so that an equally stable ferroelectric polarization is expected for all x. As the microregion size is decreased, ΔT increases, eventually increasing exponentially as the size is reduced below 1000 unit cells. Given $V = 0.064$ nm^3, this result implies that, in the lower limit, composition effects become important for microregions with equivalent spherical diameters < 5 nm.
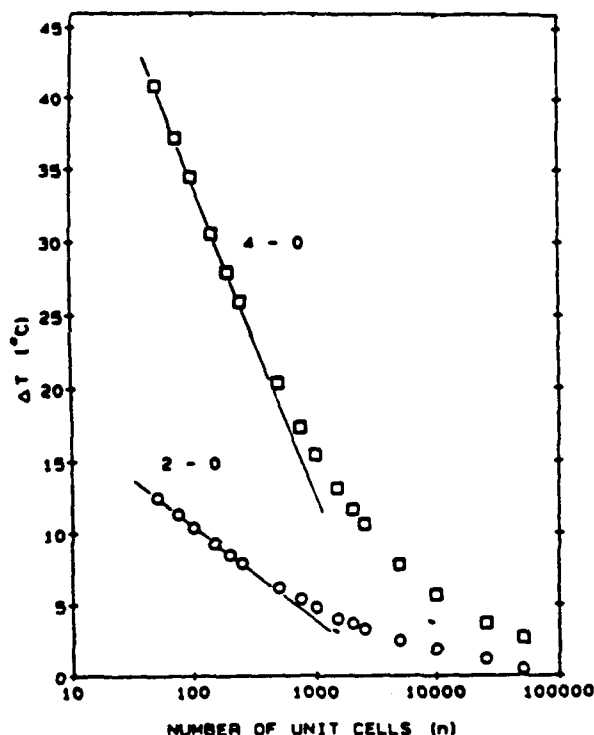
FIG. 7. ΔT plotted against the log of the postulated microregion size n. ΔT is the temperature stabilization difference for which the energy barriers H for two compositions x and x' become equal to $k_B T$. The designations 2-0 and 4-0 refer to the ΔT associated with the compositions $x=0.02$ and 0.04 relative to $x=0.00$.

For noninteracting microregions, however, the polarization flipping frequency is given by

$$\nu = \nu_0 \exp(-H/k_B T), \qquad (12)$$

where ν_0 is characteristic of a softened lattice mode ($\approx 10^{12}$ Hz). Choosing $H = 18k_B T$, the depolarization frequency ν becomes about 15 kHz, which is sufficient to influence the dielectric properties for typical measuring fields at 10 kHz. Repeating the calculations of Fig. 7 using $18k_B T$ as the stability criterion, the microregion size at which composition effects become important is then predicted to be 15 nm. This prediction is consistent with direct TEM observations[29] that place the size of the polar microregions in PLZT 9/65/35 ceramics near 10 nm below 0 °C. Moreover, for the powder samples used in this study, composition variations on this scale are not unreasonable given that the effective crystallite size was found to be substantially larger (50–60 nm). The scale on which composition effects become important relative to size effects alone may be an important factor distinguishing solid solutions with diffuse transitions (broad but not frequency dispersive) from those with relaxor (broad and frequency dispersive) phase transition behavior.

V. CONCLUSIONS

X-ray diffraction analyses of chemically derived $Pb_{1-x}La_x(Zr_{0.65}Ti_{0.35})_{1-x/4}O_3$ (PLZT) powders were

combined with a phenomenological theory to investigate the corresponding single-crystal thermodynamic properties of compositions approaching the relaxor phase transition region ($x=0$–0.04). The results were consistent with the existence of a local (rms) polarization up to ≈ 360 °C independent of composition (x). The predictions of the phenomenological theory regarding the polarization and relative phase stabilities were in good agreement with experimental measurements at low temperatures. At higher temperatures, where thermal fluctuations of the polar vector among the symmetry permitted variants may become important, the calculations were consistent with the notion of compositionally delineated polar microregions in the size range of 5–15 nm.

[1] G. Smolenski and A. Agranovska, Sov. Phys. Sol. State 1, 1429 (1960)
[2] C. A. Randall and A. S. Bhalla, Jpn. J. Appl. Phys. 29, 327 (1990).
[3] C. A. Randall, A. S. Bhalla, T. R. Shrout, and L. E. Cross, J. Mater. Res. 5, 829 (1990).
[4] L. E. Cross, Ferroelectrics 76, 241 (1987).
[5] W. A. Schulze, J. V. Biggers, and L. E. Cross, J. Am. Ceram. Soc. 61, 46 (1978).
[6] W. Pan, E. Furman, G. O. Dayton, and L. E. Cross, J. Mater. Sci. Lett. 5, 647 (1986).
[7] A. F. Devonshire. Philos. Mag. 40, 1040 (1949).
[8] M. J. Haun, E. Furman, S. J. Jang, H. A. McKinstry, and L. E. Cross. J. Appl. Phys. 62, 3331 (1987).
[9] M. J. Haun, T. J. Harvin, M. T. Lanagan, Z. Q. Zhuang, S. J. Jang, and L. E. Cross, J. Appl. Phys. 65, 3173 (1989).
[10] H. D. Megaw and C. N. W. Darlington, Acta Crystallogr. A 31, 161 (1975).
[11] A. M. Glazer, S. A. Mabud, and R. Clarke, Acta Crystallogr. B 34, 1060 (1978).
[12] A. Amin, M. J. Haun, B. Badger, H. A. McKinstry, and L. E. Cross. Ferroelectrics 65, 107 (1985).
[13] M. J. Haun, E. Furman, S. J. Jang, and L. E. Cross, Ferroelectrics 99, 13 (1989).
[14] The B-site vacancy formula is used only to describe the nominal compositions of the samples and is not intended to imply a particular defect structure.
[15] A. Meitzler and H. O'Bryan, Proc. IEEE 61, 959 (1973).
[16] J. B. Blum and S. R. Gurkovich, J. Mater. Sci. 20, 4479 (1985).
[17] B. E. Warren, X-ray Diffraction (Addison—Wesley, Reading, MA, 1969).
[18] M. J. Haun, E. Furman, H. A. McKinstry, and L. E. Cross, Ferroelectrics 99, 27 (1989).
[19] K. Kakegawa, J. Mohri, T. Takahashi, H. Yamamura, and S. Shirasaki, Solid State Commun. 24, 769 (1977).
[20] K. Kakegawa, K. Arai, Y. Sasaki, and T. Tomizawa, J. Am. Ceram. Soc. 71, C-49 (1988).
[21] M. J. Haun, Y. H. Lee, H. A. McKinstry, and L. E. Cross, Adv. X-ray Anal. 30, 473 (1987).
[22] G. Burns and F. Dacol. Phys. Rev. B 28, 2527 (1983).

[23] C. N. W. Darlington, J. Phys. C **21**, 3851 (1988).

[24] M. J. Haun, E. Furman, T. R. Halemane, and L. E. Cross, Ferroelectrics **99**, 55 (1989).

[25] B. Kirsch, H. Schmitt, and H. E. Müser, Ferroelectrics **68**, 275 (1986).

[26] M. J. Haun, Z. Q. Zhuang, E. Furman, S. J. Jang, and L. E. Cross, Ferroelectrics **99**, 45 (1989).

[27] G. H. Haertling, J. Am. Ceram. Soc. **54**, 303 (1971).

[28] M. J. Haun, E. Furman, S. J. Jang, and L. E. Cross, Ferroelectrics **99**, 63 (1989).

[29] C. A. Randall, D. J. Barber, and R. W. Whatmore, J. Microsc. **145**, 275 (1986).